THE ROLE OF FBXO7 IN MITOCHONDRIAL BIOLOGY AND PARKINSON'S DISEASE

Paulina Aiko Rowicka

Gonville & Caius College | Department of Pathology

University of Cambridge

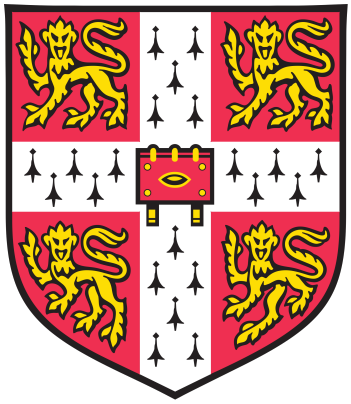

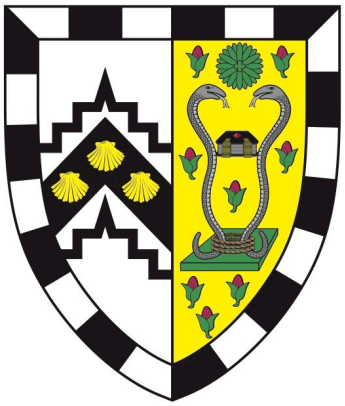

This dissertation is submitted for the degree of

Doctor of Philosophy

2018

ABSTRACT

The Role of FBXO7 in Mitochondrial Biology and Parkinson's Disease

Paulina Aiko Rowicka

Parkinson's disease is a progressive neurodegenerative disorder of the central nervous system, manifesting with both motor and non-motor symptoms. Autosomal recessive mutations in the *FBXO7* gene have been identified to cause a rapidly progressing early-onset form of PD. Canonically, FBXO7 functions as a substrate-recruiting subunit of the SCF-type E3 ubiquitin ligase. However, it also has a variety of other atypical functions, such as cell cycle regulation, proteasome regulation, and mitophagy. The overall aim of this research was to characterise the functional role of FBXO7 in various *in vitro* and *in vivo* PD models. The models examined included *FBXO7* shRNA knockdown SH-SY5Y cell lines, *FBXO7* CRISPR knockout SH-SY5Y cell lines, primary patient fibroblasts with a FBXO7 mutation, and MEFs and tissues from a *Fbxo7* KO mouse. My analysis of fibroblasts from a patient without FBXO7 expression revealed several interesting phenotypes. Briefly, the patient fibroblasts proliferated slower due to increased apoptosis and lower CDK6 and cyclin D1 expression, which led to fewer cells progressing through the G_1 phase of the cell cycle. My experiments showed that these cells also had mitochondrial respiration defects, exhibiting lower basal respiration, ATP production, maximal respiration and spare capacity, in addition to complex I, III and IV deficiencies. Patient fibroblasts also had significantly lower levels of 12S and 16S ribosomal mRNA transcripts, which are necessary for the translation of mitochondrially encoded subunits of complexes I, III, and IV. Similar phenotypes were also observed in MEFs from a *Fbxo7* KO mouse model, indicating conservation between human and mouse FBXO7 in regulating mitochondria, cell death and proliferation. In a tissue-specific KO mouse model of PD, where FBXO7 expression was ablated in the dopaminergic neurons, I analysed proteins regulated by FBXO7 which might be responsible for cell loss in the substantia nigra. I discovered that RPL23, a regulator of MDM2, was ubiquitinated by SCF^{Fbxo7} using K48 chain linkages, promoting its degradation by the proteasome. This suggests that misregulation of the MDM2:p53 axis may underlie the cell loss observed in this conditional *Fbxo7* KO mouse model. In conclusion, these results elaborate on the role of FBXO7 in mitochondrial biology, and identify a new ubiquitination substrate of FBXO7 in a mouse model of PD. It is hoped that by elucidating the potential pathogenic mechanisms of FBXO7 in rare familial forms of the disease, it will be possible to translate findings to the more prevalent sporadic forms of Parkinson's disease as well.

For my Mum and Dad

DECLARATION

This dissertation is the result of my own work and includes nothing which is the outcome of work done in collaboration, except where specified in the text.

None of the material presented has been submitted previously for the purpose of obtaining another degree or qualification at the University of Cambridge or any other University or similar institution.

I also confirm that this thesis does not exceed 60,000 words as stipulated by the School of Biological Sciences.

Paulina Aiko Rowicka

ACKNOWLEDGEMENTS

First and foremost, I would like to thank my supervisor, Dr. Heike Laman, for the opportunity to conduct my PhD in her lab and for her guidance throughout the last four years. I would also like to thank my colleagues from the lab: Dr. Suzanne Randle for always being available for questions, feedback and discussions whenever I had needed, and Dr. Shachi Patel, Lisa Kent and Bethany Mason for their support and friendship.

I must also acknowledge and thank my collaborators: Dr. Suzanne Randle from the Department of Pathology, University of Cambridge (currently based at the Cambridge Institute for Medical Research) and Dr. Simon Stott from the John van Geest Centre for Brain Repair, University of Cambridge, for collaboration on Chapter 5 of this thesis; Drs. Gabrielle Civiletto, Aurelio Reyes and Erika Fernandez-Vizarra from the Mitochondrial Biology Unit, University of Cambridge, for providing advice, protocols, reagents and equipment to conduct some of the mitochondrial assays; Dr. Susan Jones from the Department of Physiology, Development, and Neuroscience, University of Cambridge, for providing advice, protocols, reagents, and equipment for the electrophysiology experiments; and Dr. Shamima Rahman from the UCL Institute of Child Health, Great Ormond Street Hospital, for providing the human fibroblasts for characterisation.

Finally, I would like to thank my family and friends for their endless support and for helping me through the challenging times. I could not have done it without you.

TABLE OF CONTENTS

LIST OF FIGURES

CHAPTER 1 – INTRODUCTION

CHAPTER 3 – CHARACTERISATION OF PATIENT FIBROBLASTS AND MOUSE EMBRYONIC FIBROBLASTS LACKING FBXO7 EXPRESSION

CHAPTER 4 – CHARACTERISATION OF SH-SY5Y *FBXO7* KNOCKDOWN AND KNOCKOUT CELL LINES

CHAPTER 5 – CHARACTERISATION OF *FBXO7* KNOCKOUT MOUSE MODELS

CHAPTER 6 – CONLCUSION

LIST OF TABLES

CHAPTER 1 – INTRODUCTION

CHAPTER 2 – MATERIALS AND METHODS

ABBREVIATIONS

ΔFbox	Mutant Fbxo7 with F-box domain deletion
ATP	Adenosine triphosphate
ATP5A	ATP synthase subunit alpha
bp	Base pair
CDK	Cyclin dependent kinase
cIAP	Cellular inhibitor of apoptosis
CIP	CDK interacting protein
CoQ_1	Coenzyme Q
Cre	cAMP response element
CRISPR	Clustered regularly interspaces short palindromic repeats
CS	Citrate synthase
DAT	Dopamine active transporter
DBH_2	Reduced decylubiquinol
DCFDA	2', 7' –dichlorofluorescin diacetate
DCPIP	Dichlorophenolindophenol
DMEM	Dulbecco's modified eagle medium
DMSO	Dimethyl sulfoxide
DNA	Deoxyribonucleic acid
dNTP	Deoxyribonucleotide triphosphate
EDTA	Ethylenediaminetetraacetic acid
ETC	Electron transport chain
FACS	Fluorescence activated cell sorter
FBXO7	F-box only protein 7
FFA	Free fatty acid
FITC	Fluorescein isothiocyanate
FP	Fbxo7-PI31 dimerisation domain
G_0	Gap phase 0 - quiescence
G_1	Gap phase 1
G_2	Gap phase 2
GAPDH	Glyceraldehyde 3-phosphate dehydrogenase
GeCKO	Genome-scale CRISPR knock out
GFP	Green fluorescence protein
GTPase	Guanosine triphosphate hydrolyse
H1-FBXO7	Mutant helix 1 of Fbxo7 F-box domain
HI-FBS	Heat inactivated foetal bovine serum
HSP	Heavy strand promoter

HURP	Hepatoma up-regulated protein
IB	Immunoblot
IP	Immunoprecipitation
IRES	Internal ribosomal entry site
kb	Kilo base
KD	Knockdown
kDa	Kilo dalton
KO	Knockout
LC3B	Microtubule associated protein 1 light chain 3 beta (MAP1LC3B)
LD	Lipid droplet
LSP	Light strand promoter
M	Mitosis phase
MEF	Murine embryonic fibroblast
MFI	Mean fluorescent intensity
mRNA	Messenger RNA
MSCV	Murine stem cell virus promoter
MT-ATP6	ATP synthase subunit a
MT-CO1	Cytochrome c oxidase subunit 1
MT-CO2	Cytochrome c oxidase subunit 2
MT-CYB	Cytochrome b
mtDNA	Mitochondrial DNA
MT-ND1	NADH-ubiquinone oxidoreductase chain 1
MT-RNR1	12S RNA
MT-RNR2	16S RNA
NADH	Nicotinamide adenine dinucleotide
NDUFB8	NADH:ubiquinone oxidoreductase subunit B8
NDUFS3	NADH:ubiquinone oxidoreductase subunit S3
NES	Nuclear export signal
NF-κB	Nuclear factor-κB
NLS	Nuclear localisation signal
NT	Non-targeting
OCR	Oxygen consumption rate
ORO	Oil red O
OXPHOS	Oxidative phosphorylation
p53	Tumour protein p53
p62	Tumour protein p62
PAM	Protospacer adjacent motif
PARP	Poly ADP-ribose polymerase
PCR	Polymerase chain reaction
PD	Parkinson's disease

PE	Phycoerythrin fluorophore
PI	Propidium iodide
PI31	Proteasome inhibitor 31
PMSF	Phenylmethylsulfonyl fluoride
PPS	Parkinsonian-Pyramidal syndrome
qPCR	Quantitative PCR
qRT-PCR	Quantitative reverse transcription-PCR
R	restriction point
RNA	Ribonucleic acid
RNaseP	Ribonuclease P
RNS	Reactive nitrogen species
ROS	Reactive oxidative species
RPL23	Ribosomal protein L23
RT	Reverse transcriptase
RT-PCR	Reverse transcription-PCR
S	Synthesis phase
SCF	Skp1/Cullin/F-box E3 Ub ligase complex
SDH	Succinate dehydrogenase
SDHB	Succinate dehydrogenase complex iron sulphur subunit B
SDM	Site directed mutagenesis
SDS-PAGE	Sodium dodecyl sulphate polyacrylamide gel electrophoresis
sgRNA	Single guide RNA
shRNA	Short hairpin RNA
SKP	S-phase kinase-associated protein
SNP	Single nucleotide polymorphism
TCA	Tricarboxylic acid
TEFM	Transcription elongation factor, mitochondrial
TF	Transcription factor
TOM20	Translocase of outer mitochondrial membrane 20
Ub	Ubiquitin
Ubl	Ubiquitin like domain
UQCR	Ubiquinol-cytochrome c reductase
UQCRC2	Ubiquinol-cytochrome c reductase core protein II
VDAC1	Voltage dependent anion channel 1
Vec	Vector
WT	Wild-type
Zp3	Zona pellucida glycoprotein 3

CHAPTER 1

INTRODUCTION

1.1. Parkinson's disease

1.1.1. Parkinson's disease overview

Parkinson's disease (PD) is named after James Parkinson, who described its main clinical symptoms in his 1817 "Essay on the Shaking Palsy".[1] In this essay, Parkinson described the Shaking Palsy as "involuntary tremulous motion, with lessened muscular power, in parts not in action and even when supported; with a propensity to bend the trunk forwards, and to pass from a walking to a running pace: the senses and intellects being uninjured."[1] Nowadays, we describe PD as a progressive neurodegenerative disorder of the central nervous system, manifesting not only with motor features but non-motor symptoms as well.[2–4] The most common motor features of PD include bradykinesia, muscle rigidity, tremor and festinating gait.[2–4] Whereas, the main non-motor symptoms are sleep disturbances (REM sleep behaviour disorder), cognitive decline, depression, olfactory deficits, and constipation.[2–4] Sometimes, these non-motor symptoms may precede the onset of motor abnormalities and can therefore provide clues to early pathogenic causes of this disease and lead to earlier diagnosis.[2–4]

The main pathological features of PD were not determined until Arvid Carlsson's 1957 discovery of dopamine as a neurotransmitter.[5] Previously, dopamine was considered to just be a precursor of norepinephrine, and not a neurotransmitter in its own right.[5] The main pathophysiology of PD is the loss of midbrain dopaminergic (DA) neurons in the substantia nigra pars compacta (SNpc) and the presence of α-synuclein cytoplasmic inclusions (Lewy bodies).[2–4] SNpc DA neurons primarily project to the striatum, forming a crucial pathway of modulating information through the basal ganglia.[6] Other non-DA nuclei, such as the locus coeruleus, reticular formation of the brain stem, amygdala and hippocampus, are also affected in PD.[6] Thus, possibly explaining some of the non-motor symptoms of PD. Whilst the mechanisms underlying the SNpc DA neurodegeneration in PD are not yet fully understood, oxidative stress,[7] altered mitochondrial function,[8]

altered proteolysis and inflammatory changes have been implicated (**Fig1.1**).[9] Similarly, a high-throughput study of sporadic PD post-mortem substantia nigra samples showed a significant dysregulation of genes involved in oxidative stress, mitochondrial dysfunction, cell cycle regulation, protein aggregation, dopamine metabolism, synaptic function, and cell trafficking pathways.[10] Another proposed mechanism underlying neurodegeneration in PD is increased excitatory input leading to N-methyl-D-aspartate receptor (NMDAR)-mediated excitotoxicity.[11] Some of these pathways will be discussed in more detail in subsequent sections.

Arvid Carlsson also showed that motor symptoms resulting from a depletion of striatal dopamine (DA) can be alleviated through the oral administration of levodopa (L-DOPA; L-3,4-dihyroxyphenylalanine).[5] L-DOPA is a precursor of DA, which can cross the blood brain barrier and is converted into DA within the central nervous system.[4,5] It is still one of the main PD pharmacotherapies used today.[12] Amazingly, L-DOPA appears to have already been used in traditional Ayurvedic Indian medicine since 1500 B.C. to treat 'Kampavata', a tremor disease that seems to be what we now refer to as PD.[13] In those times, the source of L-DOPA were the seeds of the legume *Macuna pruriens*, which contain high concentrations of the DA precursor.[14] However, as chronic L-DOPA usage may lead to dyskinesias and motor fluctuation side effects, it is now often used in conjunction with DA agonists.[15–17] Other pharmacotherapies that are currently used in the clinic are DA metabolising enzyme inhibitors targeting MAO (monoamine oxidase B) or COMT (cathecol-O-methyltransferase), and Amantadine, which blocks glutamatergic hyperactivity.[12] And many more pharmacological agents are currently in trials. In terms of neurosurgical interventions, ablations (pallidotomy) are being replaced by deep brain stimulation (DBS), which can be considered as a safer reversible type of lesioning.[12] The high frequency electric stimulation is most commonly targeted at the subthalamic nucleus and the internal globus pallidus.[12] Other therapeutic avenues that are currently under intense research are gene- and cell-based therapies.[12]

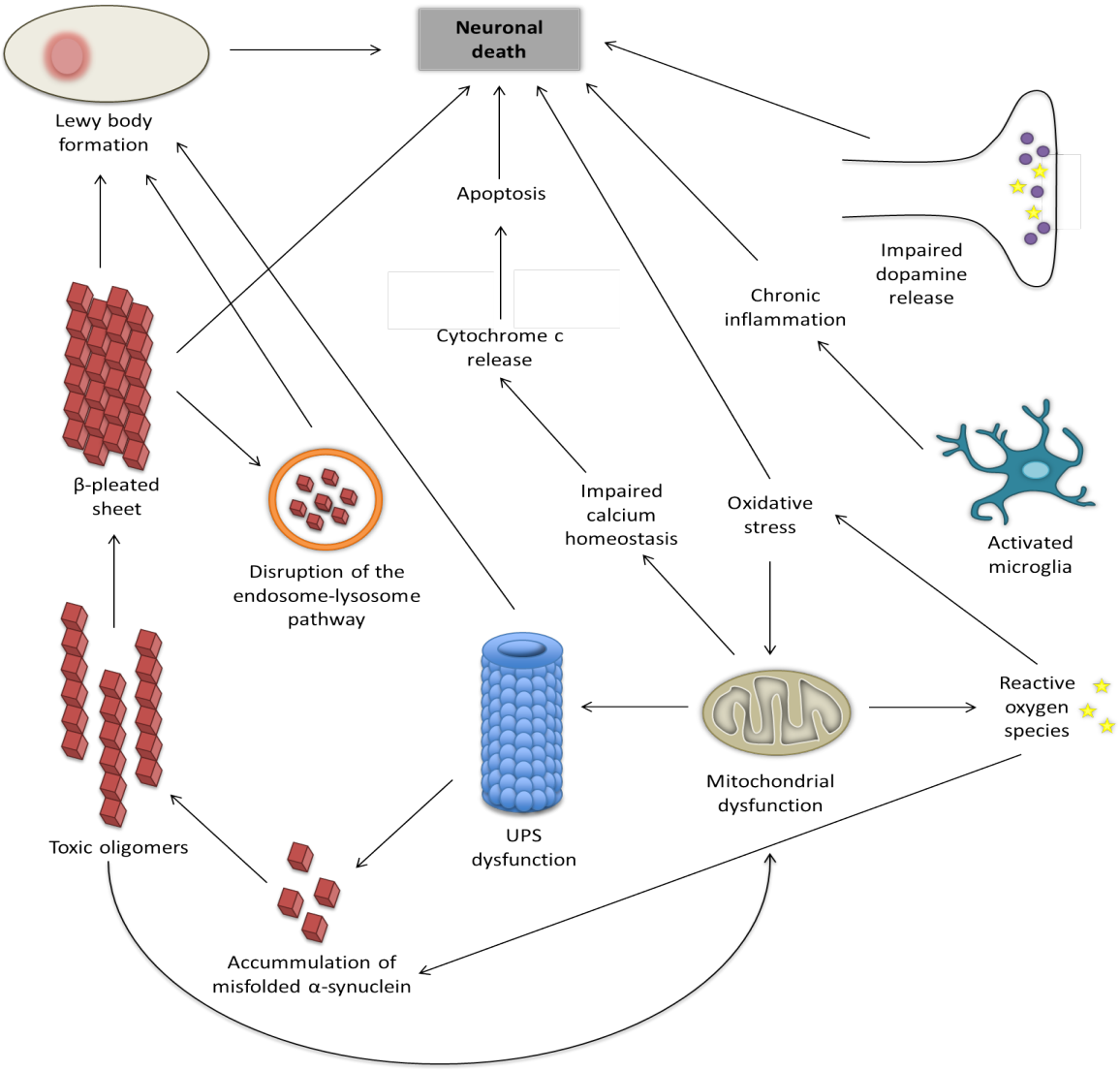

Figure 1.1 – Mechanisms of Parkinson's disease. This schematic shows the main mechanisms leading to cell death in PD, which include UPS (ubiquitin-proteasome system) dysfunction, accumulation of α-synuclein into Lewy bodies, mitochondrial dysfunction, chronic inflammation, increased reactive oxygen species and impaired dopamine release. This figure is based on Przedborski *et al*. (2003)

1.1.2. Genetics of Parkinson's disease

Approximately 10% of PD cases are familial. Numerous autosomal dominant (AD), autosomal recessive (AR) and risk genes implicated in PD have been identified using GW-linkage, exome sequencing or linkage/exome sequencing strategies.[2,3,18,19] A summary of the main identified genes can be found in **Table 1.1**.

The principle genes associated with AD-PD are *SCNA* (α-synuclein), *LRRK2* (leucine-rich repeat kinase 2), and *VPS35* (vacuolar protein sorting-associated protein 35).[2,3,18,19] *SCNA* point mutations and whole-locus duplications or triplications have been identified in PD families.[20,21] Interestingly, *SCNA* duplications present with a more typical clinical phenotype, whereas patients with triplications usually present with an atypical disease progression, including earlier onset and co-occurrence of dementia.[20,21] Thus, there appears to be a dose relationship between the severity of PD progression and α-synuclein levels.[21] Missense *SCNA* mutations can also present with a wide clinical spectrum of onset, disease severity and progression.[22,23] However, they do have similar Lewy body and Lewy neurite neuropathology. As previously mentioned, α-synuclein is the main component of Lewy bodies, the universal pathogenic hallmark of PD, thus providing a direct link between both sporadic and familial forms of the disease.[23,24] *LRRK2* mutations seem to be the most common cause of AD-PD.[25,26] Pathologically, they usually present with Lewy bodies, but sometimes their intracellular inclusions are only tau- or ubiquitin-positive.[23,25,27] Clinically, patients usually present with typical levodopa-responsive PD with an onset at around 50 years of age, albeit progressing less rapidly than other AD cases.[23,25,27] Furthermore, *LRRK2* PD patients also seem to suffer more frequently from dystonia and tremours.[27] *LRRK2* mutations have an incomplete penetrance and seem to be influenced by genetics, external/environmental factors and stochastic events.[23,25,27]

In addition to rare causal mutations, *GBA* (glucosylceramidase beta) has been identified as a moderate risk gene by observing that patients afflicted with Gaucher's disease also present with PD more frequently than expected.[28–32] Clinically, these patients usually have typical PD symptoms.[28] However, it has been also reported that symmetrical onset is more common and that there is a faster progression of cognitive changes, bradykinesia, resting tremor and rigidity.[28]

AR forms of PD can be further subdivided based on their clinical presentations into early-onset typical and juvenile-onset atypical parkinsonism, and mutations in different AR inherited genes have been implicated in both types. The main genes associated with the early-onset typical AR-PD are *PINK1* (phosphatase and tensin homolog-inducible kinase 1), *PRKN* (Parkin), and *DJ-1* (protein deglycase DJ-1).[2,19,23] Mutations in Parkin are the most frequent cause of familial AR-PD cases with an average age of onset in the 30s and usually slow levodopa-responsive disease progression.[33] The brain pathology of these patients is rather heterogeneous, with some exhibiting Lewy bodies while others do not. The typical clinical and pathological presentation is very similar in patients harbouring PINK1 and DJ-1 mutations, apart from the disease usually arising in the 40-50s and 20-30s respecitvely.[34] However, some atypical phenotypes, such as prominent dystonia pyramidal signs in PINK1 families, and psychiatric and dystonic features in DJ-1 families, have also been reported.[35–37]

On the other hand, some of the genes associated with the juvenile-onset atypical AR-PD include *FBXO7* (F-box only protein 7), *ATP13A2I* (ATPase type 13A2), and *PLA2G6* (phospholipase A2, group VI).[2,19,23] These genes usually cause more atypical and severe forms of parkinsonism, together with a variety of other clinical symptoms, some arising already in early childhood.[2,19,23] For instance, mutations in *ATP13A21* and *PLA2G6* cause a juvenile-onset form of levodopa-responsive parkinsonism with pyramidal signs and cognitive and psychiatric phenotypes.[38,39] Pathologically, patients with *PLA2G6* mutations present with widespread LBs, suggesting a link with idiopathic PD.[39] The focus of this thesis is on *FBXO7*, whose autosomal recessive mutations have been identified to cause a rapidly-progressing, early-onset, severe, levodopa-responsive parkinsonism, with additional pyramidal signs.[40,41] Even though the brain pathology of *FBXO7* patients largely remains unknown, the presence of FBXO7 immunoreactivity in Lewy bodies has been reported.[42] The structure and functions of FBXO7 are described in more detail in section 1.5. Investigations into these genes involved in familial PD can reveal crucial clues about the pathogenic mechanisms underlying the disease process at the molecular level of the more common sporadic forms of the disease as well.

Gene (locus)	Inheritance	Clinical phenotype	References
SNCA *(PARK1/4)*	AD	Range from typical to aggressive early-onset	Polymeropoulos *et al.*, 1997[20]
PRKN *(PARK2)*	AR	Early-onset, slow course	Kitada *et al.*, 1998[33]
PINK1 *(PARK6)*	AR	Early-onset, slow course	Valente *et al.*, 2004[43]
DJ-1 *(PARK7)*	AR	Early-onset, slow course	Bonifati et al., 2003[44]
LRRK2 *(PARK8)*	AD	Typical, late-onset	Funayama *et al.*, 2002[25] Zimprich *et al.*, 2004[26]
ATP13A2 *(PARK9)*	AR	Atypical, juvenile-onset	Ramirez *et al.*, 2006[38]
HTRA2 *(PARK13)*	AD/ risk factor	Typical, late-onset	Strauss *et al.*, 2005[45]
PLA2G6 *(PARK14)*	AR	Atypical, juvenile-onset	Paisan-Ruiz *et al.*, 2008[39]
FBXO7 *(PARK15)*	AR	Atypical, juvenile-onset	Shojaee *et al.*, 2008[46] Di Fonzo *et al.*, 2009[41]
VPS35 *(PARK17)*	AD	Typical, late-onset	Zimprich *et al.*, 2011[47] Vilarino-Guell *et al.*, 2011[48]
EIP4G1 *(PARK18)*	AD	Typical, late-onset	Chartier-Harlin *et al.*, 2011[49]

DNAJC6 *(PARK19)*	AR	Atypical, juvenile-onset	Edvardson *et al.*, 2012[50] Koroglu *et al.*, 2013[51]
SYNJ1 *(PARK20)*	AR	Atypical, juvenile-onset	Krebs *et al.*, 2013[52] Quadri *et al.*, 2013[53]
TMEM230 (PARK21)	AD	Typical, late-onset	Deng *et al.*, 2016[54]
CHCHD2 (PARK22)	AD	Typical, late-onset	Funayama *et al.*, 2015[55]
VPS13C (PARK23)	AR/ risk loci	Early-onset, rapid and severe	Lesage *et al.*, 2016[56]
GBA	Risk-gene	Typical, late-onset	Neudorfer et al., 1996[57] Aharon-Peretz et al., 2004[32]

Table 1.1 **– List of main genes associated with Parkinson's disease.** Other chromosomal loci (*PARK3, PARK10, PARK11, PARK12, PARK16*) have been identified to potentially harbour still unknown PD-associated gene. Whether or not *RIC3 (also PARK23)* and *UCHL1 (PARK5)* are associated with PD is still under debate. Genes marked in bold are associated with PD with the highest confidence.

1.1.3. Models of Parkinson's disease

As with most neurodegenerative disease, there is no complete animal or cellular model that recapitulates all PD neuropathology. There are toxic- and genetic-based animal models of Parkinson's disease, both recapitulating varying hallmarks. Rodents have been most widely used due to their conserved neuroanatomy, function and nuclei connectivity when compared with human brains.[58]

One of the classic PD animal models is generated by unilaterally injecting 6-Hydroxydopamine (6-OHDA) directly into the brain, which then enters the cytosol of DA neurons via DAT (dopamine active transporter), auto-oxidises and upregulates oxidative stress.[59–62] A 6-OHDA injection into the SNpc damages around 60% of TH neurons in the area followed by loss of TH-positive terminals in the striatum.[59–62] Whereas, striatal

injections have been mainly used to investigate retrograde degeneration.[59–62] Animal models based on MPTP (1-methyl-4-phenyl-1,2,3,6-tetrahydropyridine) have been shown to recapitulate many of the PD hallmarks in both rodents and primates, including oxidative stress, ROS, energy failure and inflammation.[62–65] MPTP is metabolised to its active and toxic form, MPP^+, by MAO-B (monoamine oxidase-B), which is then taken up by DAT and affects mitochondrial complex I activity.[62–65] However, the Lewy body PD hallmark is missing in non-primate MPTP models.[62–65] The two main pesticide/herbicide models are based on paraquat (*N*,*N*'-dimethyl-4-4-4'-bipiridinium) and rotenone exposure. Paraquat generates hydrogen peroxide and hydroxyl radical ROS, leading to lipid, protein, DNA and RNA damage.[62,66] Importantly for PD research, it also upregulates α-synuclein and induces formation of Lewy-like bodies in SNpc DA neurons.[62,66] Whereas, rotenone-based models seem to recapitulate many PD hallmarks, including Lewy-bodies, oxidative stress, α-synuclein aggregation, inflammation, complex I deficiency, and behavioural and gastrointestinal symptoms.[62,67] One of the disadvantages of using toxin-based models is that they usually represent the disease at its end-stage.[62] More details of how these toxins specifically lead to mitochondrial dysfunction can be found in section 1.2.3.

In addition to the PD toxin models, there are new genetic animal and cellular models being developed based on familial pathogenic mutations. The rationale behind studying these very rare mutations is the expectation that similar pathogenic mechanisms may be involved in both sporadic and familial forms of PD. There have also been examples of studies that try to combine genetic and toxin strategies in a single animal model in an attempt to increase the number of observed PD hallmarks.[67] Genetic-based mouse models of PD rarely develop substantial loss of nigral DA neurons unless the gene of interest is overexpressed or conditionally not expressed in DA neurons.[69] For instance, constitutive independent or triple knockout mouse models of *Pink1*, *Parkin* or *Dj-1* do not display any nigrostriatal degeneration, possibly due to various compensatory mechanisms.[70,71] Whereas, neurodegeneration occurs in the SNpc of a mouse with a conditional *Parkin* knockout.[70,71] *Parkin* KO and *Pink1* KO mice also have mitochondrial respiration dysfunction and increased oxidative damage.[69,72–74] While *Dj-1* KO mice do not present with DA neuronal loss, they do have mild motor dysfunction and abnormal nigrostriatal synaptic physiology.[75–77] Details on the mitochondrial phenotypes found in PD animal models can be found in section 1.2.3. Currently, progressively more rat PD

models are being generated due to their engineering becoming easier.[58] Even though, *Parkin* KO rats show no Lewy bodies, age-dependent DA neurodegeneration, or motor deficits,[78] PARKIN overexpression rescues SNpc neuronal loss in 6-OHDA and α-synuclein over-expression models.[79] *Pink1* KO rats present with DA neuronal loss, various locomotor deficits, mitochondrial dysfunction and α-synuclein aggregates (albeit differing slightly from Lewy bodies).[78,80] *Dj-1* KO rats also present with age-dependent DA neurodegeneration and mitochondrial dysfunction.[78,81] Thus, it seems that in the case of Parkin and PINK loss of function, rat models generally seem to better recapitulate the PD phenotypes of neuronal loss and protein aggregation than mouse models.[58]

Aside from animal models, various cellular models have also been developed to investigate the molecular pathogenesis of PD.[82] These may include short hairpin RNA (shRNA), small interfering RNA (siRNA) and CRISPR cell lines, which are easy to maintain and genetically manipulate. In addition to these advantages, each type of cell line also has its own disadvantages. For instance, primary rodent or human cultures being difficult to maintain, tumour derived cell lines carrying various mutations resulting in immortalisation that can affect signalling pathways, and clonal variation of induced pluripotent stem cells (iPSCs).[83] One of the main difficulties in neurodegeneration research is the limited amount of tissue for study and the fact that the SNpc is almost entirely degenerated at the end-stage of disease. This can be somewhat circumvented by deriving iPSCs from PD patient fibroblasts, and differentiating them into the subtypes of neurons that are affected, which would be midbrain dopaminergic neurons in this case.[84,85] The other types of cellular models, shRNA, CRISPR and patient fibroblasts were used throughout this thesis and will therefore be discussed further in their relevant chapters.

1.2. Mitochondria

1.2.1. Mitochondrial DNA

According to the serial endosymbiotic theory, mitochondria originated from an α-proteobacterium,[86] which explains the existence of a distinct mitochondrial DNA (mtDNA) genome. Human mtDNA is maternally inherited and consists of a 16,569bp circular double-stranded genome (**Fig1.2**).[87] It encodes a total of 37 genes, including 13 proteins of the respiratory chain, 2 ribosomal RNAs (rRNA) and 22 transfer RNAs

(tRNAs).[87] Apart from 16S rRNA, *MT-RNR2* has been described to encode humanin (HN).[88,89] This 24-animo acid mitochondria-associated peptide plays a role in a variety of cellular processes including inflammation, apoptosis, cell survival, substrate metabolism, oxidative stress, and is also considered to be a neuroprotective factor against Alzheimer's disease.[88,89] A list of mtDNA encoded proteins and rRNAs can be found in **Table 1.2** and **Table 1.3** respectively. The other required respiratory chain proteins are encoded by nuclear DNA and imported into the mitochondria.[90] The mitochondrial genome does not have any introns and there are only two non-coding regions, the longer of which contains mtDNA transcription and replication control elements.[91] The mitochondrial genome is composed of the light (L) and heavy (H) strands, each containing the LSP (light-strand promoter) and HSP (heavy-strand promoter) respectively. LSP transcription only produces MT-ND6 mRNA, 8 tRNAs and RNA primers, whereas HSP transcription produces the two rRNAs and the rest of the mRNAs and tRNAs.[92–94] Polycistronic precursor RNAs encompassing the entire strand are initially produced, which are subsequently processed into individual mRNA, rRNA and tRNA.[92–94]

Mitochondrial DNA is replicated and repaired by the nuclear-encoded *POLG* (DNA polymerase gamma).[87,95] Mitochondrial DNA transcription is initiated by POLRMT (mitochondrial DNA-directed RNA polymerase), TFAM (mitochondrial transcription factor A) and TFB2M (mitochondrial transcription factors B2).[96] Another important member of mitochondrial transcription is TEFM (mitochondrial transcription elongation factor), which interacts with the C-terminus of POLRMT.[97] TEFM associates with POLRMT and enhances its activity on ss- and dsDNA templates.[97] Furthermore, it has been shown that knockdown of TEFM decreases levels of mitochondrial transcripts from both L and H strands, resulting in decreased mitochondrial respiration.[97]

Function	Gene	mtDNA strand	mtDNA position
Complex I NADH dehydrogenase subunits 1/2/3/4L/4/5/6	MT-ND1	H	3307-4262bp
	MT-ND2	H	4470-5511bp
	MT-ND3	H	10059-10404bp
	MT-ND4L	H	10470-10766bp (overlap with MT-ND4)
	MT-ND4	H	10760-12137bp (overlap with MT-ND4L)
	MT-ND5	H	12337-14148bp
	MT-ND6	L	14149-14673bp
Complex III Cytochrome b	MT-CYB	H	14747-15887bp
Complex IV Cytochrome c oxidase subunits 1/2/3	MT-CO1	H	5904-7445bp
	MT-CO2	H	7586-8269bp
	MT-CO3	H	9207-9990bp
Complex V ATP synthase F_O subunits 6/8	MT-ATP6	H	8527-9207bp (overlap with MT-ATP8)
	MT-ATP8	H	8366-8572bp (overlap with MT-ATP6)
Humanin	MT-RNR2	H	1671-3229bp

Table 1.2 **– List of mitochondrial encoded proteins**

Function	Gene	mtDNA strand	mtDNA position
12S Small subunit (SSU)	MT-RNR1	H	648-1601bp
16S Large subunit (LSU)	MT-RNR2	H	1671-3229bp

Table 1.3 **– List of mitochondrial encoded ribosomal RNAs**

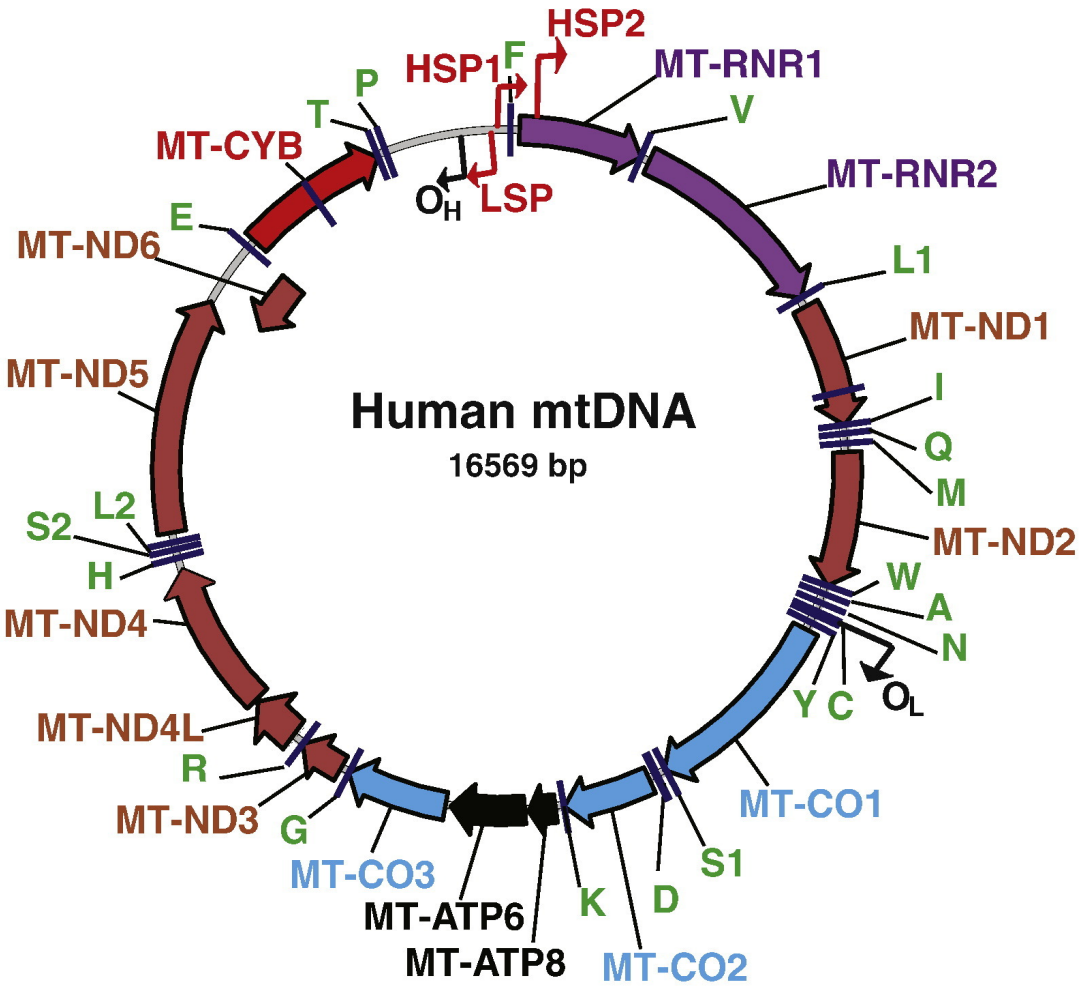

Figure 1.2 – Human mtDNA. Schematic of the human mitochondrial genome according to the Cambridge Reference Sequence. Thin bent black arrows indicate origins and directions of L-strand (O_L) and H-strand (O_H) replication. Thin bent red arrows indication the H-strand promoters (HSP1 and HSP2) and the L-strand promoter (LSP). Brown arrows indicate complex I subunits (MT-ND1, MT-ND2, MT-ND3, MT-ND4L, MT-ND4, MT-ND5 and MT-ND6). Red arrow indicates the complex III subunit MT-CYB. Blue arrows indicate complex III subunits (MT-CO1, MT-CO2 and MT-CO3). Black arrows indicated complex V subunits (MT-ATP6 and MT-ATP8). Purple arrows indicate the 12S small subunit (MT-RNR2) and the 16S large subunit (MT-RNR2). Green letters and bars designate tRNAs. This figure is taken from Shokolenko *et al.* (2015).

1.2.2. Mitochondrial respiration

Mitochondria are known as the powerhouse of the cell, producing ATP via the tricarboxylic acid (TCA) cycle and oxidative phosphorylation (OXPHOS). TCA occurs in the mitochondrial matrix and supplies two substrates for the OXPHOS electron transport chain (ETC), as depicted in **Fig1.3**.[98–100] The ETC is composed of a series of complexes embedded in the inner mitochondrial membrane that transfer electrons via redox reactions and generate a proton gradient which drives ATP synthesis (**Fig1.4**).[101,102] Citrate synthase (CS) is an important enzyme that catalyses the first reaction of the TCA cycle by breaking down Acetyl-CoA into carbon dioxide, water and energy (GTP and NADH).[99] The two TCA-derived points of entry into the ETC is either through complex I via NADH or through complex II via succinate (which is coupled to FAD^+).[103–105] The electrons produced by these redox reactions are routed through their respective complexes to ubiquinone (UQ, coenzyme Q_{10} or CoQ), which acts as a mobile electron carrier, reducing it to ubiquinol (UQH_2).[103–105] The other entry points into the ETC are via the ETF-Q_O (flavoprotein-ubiquinone oxidoreductase) that transfers electrons from fatty acid oxidation and via dihydroorotate reductase within the pyrimidine synthesis pathway.[103–105] Subsequently, complex III oxidises ubiquinol (UQH_2) and the electrons are transferred to complex IV via cytochrome c, a hydrophilic heme protein that is another mobile electron carrier.[103–105] Then, complex IV reduces molecular oxygen to water.[103–105] Throughout this process, protons are actively pumped by complexes I, III and IV into the mitochondrial inter membrane space, which generates the electrochemical gradient potential that is necessary for ATP synthesis by complex V.[106] The ETC is crucial in maintaining mitochondrial membrane potential via the generated proton gradient across the mitochondrial inner membrane.[107]

Complex I (CI, NADH:ubiquinone oxidoreductase, NADH-CoQ reductase, NADH dehydrogenase) is the first, and largest, enzyme of the electron transport chain.[108,109] The mammalian enzyme is located within the inner mitochondrial membrane and consist of 45 subunits in total with 14 established as the core subunits (homologues to the bacterial enzyme); 7 from the mitochondrial genome in the hydrophobic arm and 7 from the nuclear genome in the hydrophilic arm.[108,109] The roles of the remaining subunits have not been fully elucidated, but some appear to be essential for proper assembly and function of the complex.[110] Complex I catalyses the oxidation of NADH, produced by the TCA cycle and β-oxidation, into NAD+ by the non-covalently bound

flavin mononucleotide (FMN).[108,109] Then the 2 electrons are transferred along a series iron-sulphur (FeS) clusters to the ubiquinone binding site to reduce it to ubiquinol.[108,109] Complex I can be inhibited at this step by rotenone, which binds to the ubiquinone binding site.[108,109] These redox reactions ultimately result in 4 protons being transported across the inner membrane, contributing to the proton-motive force that supports ATP production and mitochondrial import/export.[108] As a consequence of its catalytic activity, complex I is also a major producer of superoxides, contributing to oxidative stress.[108,109] Mutations in subunits of complex I cause mitochondrial diseases, including Leigh syndrome (infantile sub-acute necrotising encephalomyelopathy) and Leber's hereditary optic neuropathy.[108,109]

Complex II (CII, succinate dehydrogenase, succinate-CoQ reductase, succinate:ubiquinone oxidoreductase) is the smallest enzyme of the ETC and the only one entirely encoded by nuclear DNA and not acting as a proton pump.[103,111,112] Complex II consists of 4 subunits anchored to the inner mitochondrial membrane.[112] Hydrophilic subunits, SDHA (FAD cofactor) and SDHB (Fe-S clusters), catalyse the oxidation of succinate to fumarate as part of the TCA cycle, which is coupled to the reduction of FAD^+ to $FADH_2$.[103,113] Whereas, as part of OXPHOS, electrons are transferred from succinate via the Fe-S clusters to ubiquinone, which is then reduced to ubiquinol.[113,114] Ubiquinone reduction occurs in two stepwise single electron reactions and also involves the two hydrophobic subunits, SDHC and SDHD.[103] Thus, complex II forms a direct functional link between TCA cycle and electron transport chain as it participates in both of these essential processes.[112] Sometimes these functions are distinguished as the SDH (succinate dehydrogenase) activity and the SQR (succinate:ubiquinone oxidoreductase) activity of complex II respectively.[115] Furthermore, complex II also has a function as a cell death sensor and regulator.[116] A drop in pH or Ca^{2+} influx can cause the SDHA and SDHB subunits to generate excessive ROS, leading to cell death.[116] Mutations in SDHA can also cause Leigh syndrome, whereas mutations in SDHB, SDHC or SDHD result in familial paraganglioma syndrome.[103,117]

Complex III (CIII, cytochrome bc_1 complex, ubiquinone-cytochrome *c* reductase, ubiquinol cytochrome c oxidoreductase) consists of 11 subunits, one of which, cytochrome b, is encoded in the mtDNA and functions as a dimer.[118] This complex is responsible for the Q cycle[119] that involves the redox reactions of ubiquinol (UQH_2) to ubiquinone (UQ) and the reduction of cytochrome c.[120] This is coupled to proton transfer

across the inner mitochondrial membrane, contributing to the proton motive force that is necessary for ATP synthesis.[120] In more detail, ubiquinol (UQH_2) is oxidised at the Q_O site, on the inter-membrane space side, whereas ubiquinone (UQ) is reduced at the Q_i site, on the matrix side of the membrane.[121] The electrons become separated at the Q_O site into two distinct pathways: the high potential pathway leading to cytochrome c reduction and the low potential pathway towards the Q_i site.[122,123] Due to the production of an unstable semiquinone at the Q_i site, a second Q cycle is necessary to complete the process and fully reduce it to ubiquinol.[122,123] These redox reactions ultimately result in 4 protons being transported across the inner membrane, thereby contributing to the proton-motive force. Under basal conditions, a small amount of superoxide anions may be produced through electron leakage to molecular oxygen.[123,124] Antimycin A (AA) is able to inhibit complex III by binding to the Qi site and thereby blocking the ubiquinol oxidation and the resulting electron transfer.[125] This results in increased ROS production[107] and decreased ATP production.[126] Autosomal recessive forms of complex III deficiency are usually very severe multisystem disorders, which result in death during early childhood.[127–130] The defective factors leading to the complex III deficiencies, and thereby the pathogenic mechanisms and symptoms, are very variable.[130] Symptoms may include mitochondrial encephalopathy, Leigh syndrome, hypoglycaemia, and GRACILE syndrome (growth retardation, aminoaciduria, cholestasis, iron overload, lactic acidosis and early death).[127–130]

Complex IV (CIV, cytochrome c oxidase, COX) is the terminal enzyme of the electron transport chain and consists of 13 subunits.[131] Three subunits are encoded in mtDNA and form the catalytic core of the enzyme, containing all the necessary heme and copper prosthetic groups.[132] Whereas, the 10 nuclear-encoded supernumerary subunits are thought to play a role in regulating proton translocation and oxygen consumption.[131] Complex IV catalyses the transfer of electrons from the reduction of cytochrome c to molecular oxygen.[133] Four electrons enter the complex via subunit II and oxygen reduction takes place in the heme a_3/Cu_B centre of subunit I where they are transferred to bound O_2, forming two H_2O molecules and preventing ROS production.[131] Together with complexes I and III, complex IV also acts as a proton pump and transports two protons across the membrane per reaction. Complex IV is considered to be the OXPHOS rate-limiting step as the ATP/ADP ratio controls respiration rate by affecting the phosphorylation of the enzyme.[131,134] Complex IV deficiencies can be a result of

mutations in the subunits and/or in assembly factors of the complex and thereby present with variable clinical phenotypes.[131,133] Complex IV dysfunction may also lead to increased ROS production.[135]

ATP synthase, also referred to as complex V, uses the generated proton gradient from the electron transport chain to synthesise ATP from ADP in the mitochondrial matrix.[136,137] ATP synthase has two functional domains: hydrophilic F_1 that resides in the mitochondrial matrix and hydrophobic F_0 that is bound to the inner mitochondrial membrane.[138] F_1 consists of 5 different subunits and F_0 consists of 6 main subunits and 4 accessory subunits.[138] The net accumulated protons in the intermembrane space flow back into the mitochondrial matrix via the F_0 domain, which subsequently transfers the energy to the F_1 domain where ADP phosphorylation occurs.[138] Oligomycin is able to bind to F_0 subunits and inhibit the translocation of protons within the ATP synthase.[139] ATP synthesis is coupled to mitochondrial respiration.[138] Uncoupler proteins as well as some chemicals, such as CCCP (carbonyl cyanide *m*-chlorophenyl hydrazone), are able to dissipate the protein gradient, and thereby 'uncoupling' ATP synthesis from electron transport and preventing ATP synthesis mediated by oxidative phosphorylation.[138]

Other important proteins that play a role in mitochondrial respiration are VDAC-1 (voltage-dependent anion-selective channel 1) and the TOM (translocase of the outer mitochondrial membrane) and TIM (translocase of the inner mitochondrial membrane) complexes. VDAC-1 is nuclear encoded and forms an ion channel in the outer mitochondrial membrane.[140,141] It links the mitochondria and the rest of the cell by enabling the exchange of metabolites, including ATP.[140,141] VDAC-1 not only plays a role in maintaining the equilibrium of cell metabolism, but also cell death. It regulates the release of apoptotic proteins and over-expression or dysregulation of VDAC-1 can lead to apoptosis. It can therefore be used as a one of the markers of mitophagy.[140,141]

The TOM and TIM complexes are responsible for the translocation of precursor proteins into the mitochondria. The TOM complex is composed of TOM40, TOM20, TOM22, TOM7, TOM5, TOM6, and TOM70.[142,143] The TOM complex is located within the outer mitochondrial membrane and imports all nuclear-encoded precursors into the outer membrane and the intermembrane space.[142,143] TIM23 and TIM22 complexes are the two translocases embedded in the mitochondrial inner membrane.[144] The TIM23 complex is composed of TIM23, TIM17, TIM44, and the mitochondrial Hsp70 protein

(mt-Hsp70), and imports preproteins with a matrix-targeting signal.[144] Whereas, the TIM22 complex is composed of TIM9, TIM10, TIM12, TIM22 and TIM54, and imports integral inner membrane proteins without a matrix-targeting signal.[144] In addition to the described import machinery to the outer membrane, inner membrane or matrix, MIA40 (mitochondrial intermembrane space import and assembly protein 40) is essential for proper import into the intermembrane space (IMS).[145] The oxidoreductase MIA40 mediates the IMS disulphide relay system, which results in the oxidative folding of precursor proteins, such as the small TIM proteins, catalysing their import.[145] Furthermore, it has been also shown for MIA40 to play an important role in TIM22 biogenesis and complex assembly.[146] As most mitochondrial proteins are nuclear-encoded, translocation of proteins is vital for all processes, including respiration, replication, transcription and translation.[143]

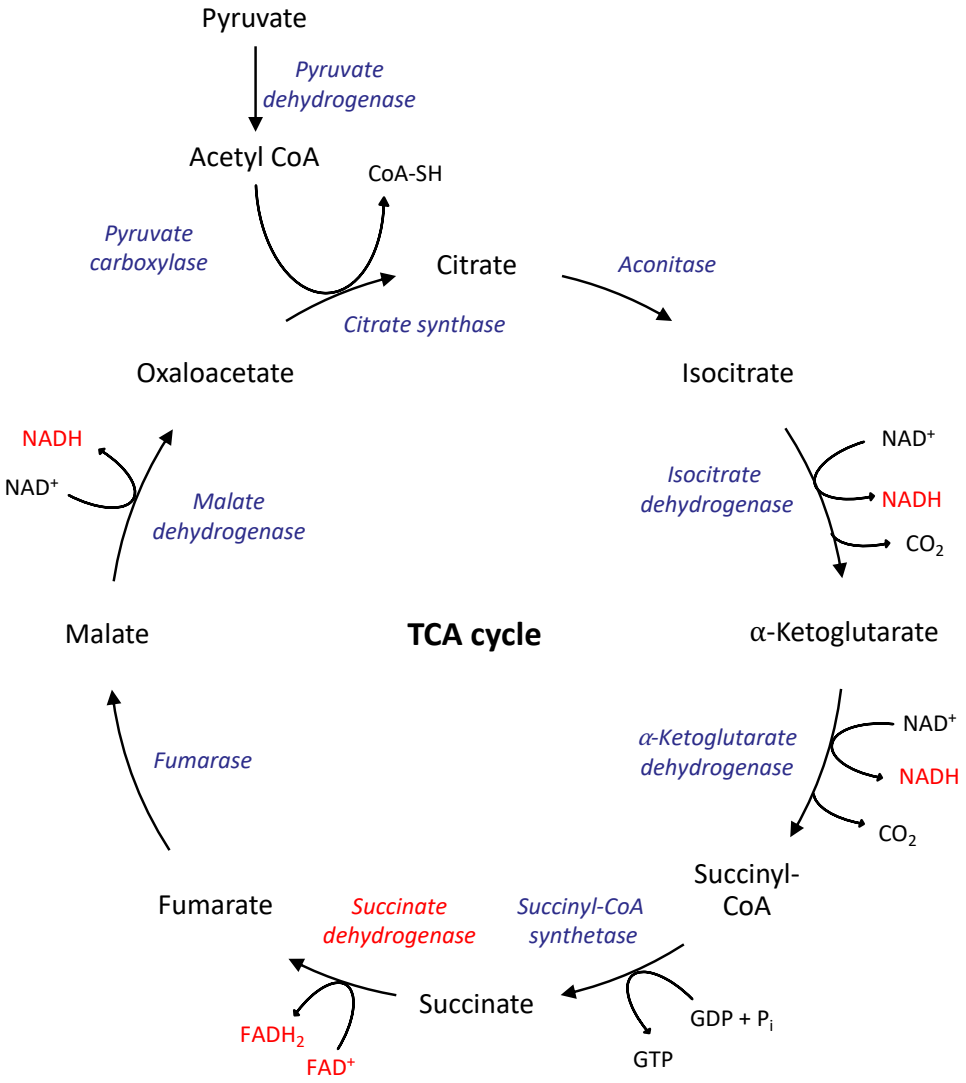

Figure 1.3 – TCA cycle. A simplified schematic of the TCA cycle, depicting in red the substrates and enzymes that are also involved in the electron transport chain. NADH (reduced nicotinamide adenine dinucleotide), NAD^+ (oxidised nicotinamide adenine dinucleotide), $FADH_2$ (reduced flavin adenine dinucleotide), FAD^+ (oxidised flavin adenine dinucleotide), CoA-SH (Coenzyme A). Figure based on Akram (2014), Kornberg (2000), and Nunes-Nesi *et al*. (2013).

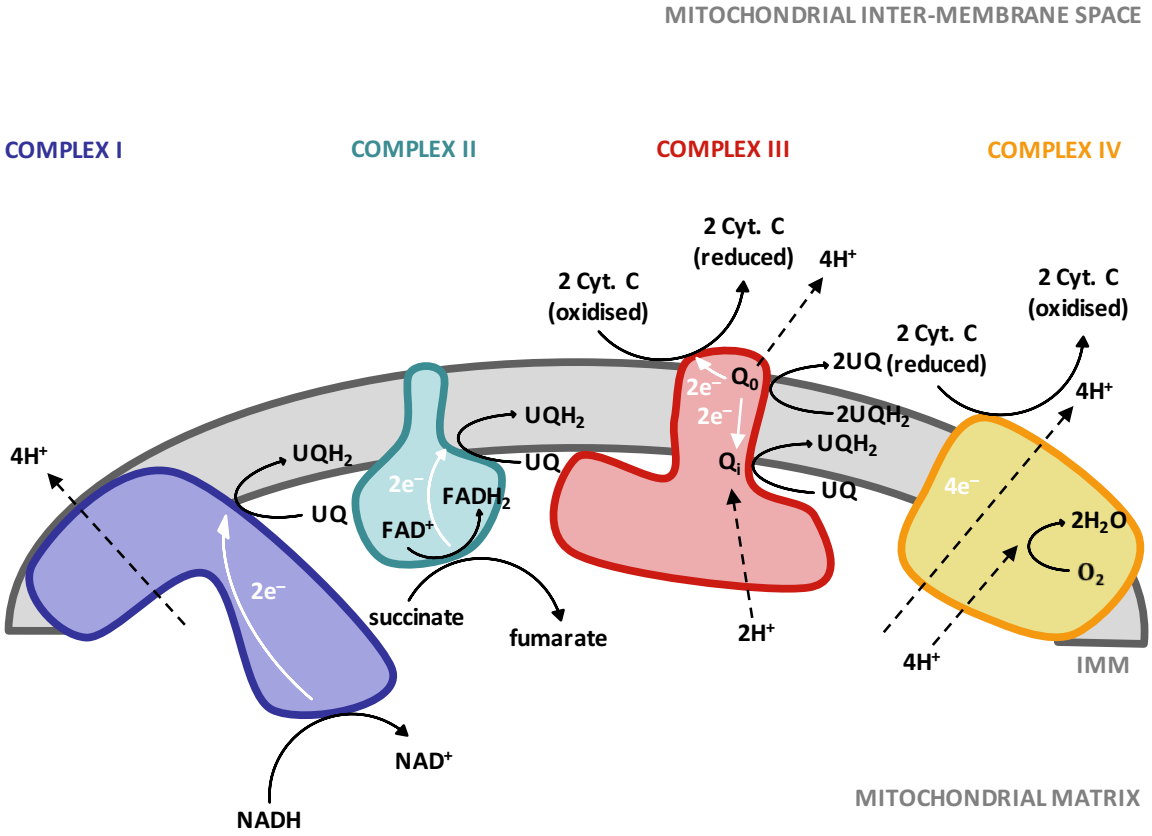

Figure 1.4 – The electron transport chain. A schematic depicting the redox reactions that occur in the four ETC complexes, the pathways of the electrons and protons being pumped into the mitochondrial inter-membrane space, creating the proton gradient that is later used by complex V to generate ATP. NADH (reduced nicotinamide adenine dinucleotide), NAD^+ (oxidised nicotinamide adenine dinucleotide), $FADH_2$ (reduced flavin adenine dinucleotide), FAD^+ (oxidised flavin adenine dinucleotide), UQ (ubiquinone), UQH_2 (ubiquinol), Cyt. C (cytochrome c), IMM (inner mitochondrial membrane). This figure is based on Lemarie *et al.* (2011) and Schultze *et al.* (2001).

1.2.3. Mitochondrial network morphology

Mitochondria are highly dynamic organelles that constantly undergo fusion and fission, which determines the morphology of the mitochondrial network.[147–150] The key protein regulating fission is DRP1 (dynamin-related protein 1),[151] whereas inner and outer mitochondrial membrane fusion is controlled mainly by MFN1, MFN2 (mitofusin-1/2) and OPA1 (optic atrophy 1).[152] The rate of oxidative phosphorylation can influence mitochondrial morphology, and vice versa. For instance, increased activity of the ETC can change the conformation of inner mitochondrial membrane cristae,[153] whereas reduction of mitochondrial complex activities can cause fragmentation of the mitochondrial network. Mitochondrial fragmentation has been observed in fibroblasts derived from patients with complexes I,[154] III[155] and IV[156] deficiencies. It has been also shown that loss of MFN2 function reduces mitochondrial membrane potential by inhibiting nuclear-encoded subunits of complexes I, II, III and V, thereby decreasing glucose, pyruvate and fatty acid oxidation.[157] Primary skin fibroblast harbouring *OPA1* mutations exhibit complex IV deficiency due to decreased levels of complex IV subunits.[158] Drug induced inhibition of complexes I, III, IV or V results in decreased OXPHOS and significant mitochondrial fragmentation.[159]

However, it is not always the case that only fragmented mitochondria coincide with respiration defects and fused mitochondria exhibit increased membrane potential and OXPHOS. Downregulation of DRP1 expression results in a decrease of mitochondrial membrane potential, respiration, mtDNA, proliferation and an increase in cellular ROS.[160] These cells also present with highly fused mitochondrial networks due to the downregulation of fission.[160] Downregulation of French Canadian Leigh Syndrome gene LRPPRC (leucine-rich pentatricopeptide repeat containing) results in complex IV deficiency, which in turn induced mitochondrial hyperfusion as a transient compensatory mechanism.[161] Mitochondrial hyperfusion can also occur as a pro-survival response when cells are exposed to stressors, such as starvation, inhibition of cytosolic protein synthesis, or oxidative stress.[149,161,162] Mitochondrial hyperfusion due to cytosolic protein synthesis inhibition usually results in cells exhibiting increased ATP production as a protective adaptation.[162] A study by Gomes *et al.* revealed that there is also a connection between mitochondrial morphology and macroautophagy.[163] Initiation of autophagy, during starvation, triggers mitochondrial elongation both *in vitro* and *in vivo* via DRP1 downregulation.[163,164] Subsequently, fused mitochondria maintain their

ATP production and are protected from autophagosomal degradation.[163] Thus, mitochondrial hyperfusion is a protective mechanism against apoptosis and mitophagy under stress.[165] Ultimately, there needs to be a balance between mitochondrial fission and fusion to ensure proper functioning of the organelle.[148]

1.2.4. Mitochondrial dysfunction in Parkinson's disease

Mitochondrial dysfunction has been often linked to Parkinson's disease[7,8,166–168] and other neurodegenerative disorders.[169,170] As previously mentioned, dopaminergic neurons of the substantia nigra pars compacta are selectively vulnerable to neurodegeneration in Parkinson's disease. A possible hypothesis is that vulnerable dopaminergic neurons are under exceptionally high energy demand due to their large unmyelinated axonal arbours.[171,172] Thus, any stressor affecting energy production would have a detrimental effect.

Many genetic-based PD models have been analysed for their effects on mitochondrial function. There is a link between PINK1 and Parkin as they interact to mediate mitophagy under stress and many studies have investigated their potentially defective role in mitochondrial quality control during Parkinson's disease.[8,173] When mitochondrial transmembrane potential drops, PINK1 accumulates on the outer membrane and recruits Parkin, an E3 ubiquitin ligase, which labels the defective mitochondria for mitophagy via ubiquitination.[173–176] PINK1 (PTEN-induced kinase 1) is a putative mitochondrial serine/threonine kinase and has a neuroprotective function. Downregulation of PINK1 in neuronal cultures results in decreased cell viability due to general mitochondrial dysfunction, increased oxidative stress and increased cellular susceptibility to mitochondrial-mediated apoptosis.[177–180] Observed mitochondrial phenotypes include fragmentation, depolarisation, reduced respiration, decreased complex IV activity, and increased mitophagy.[177–180] Whereas, a PINK1 knockout mouse model showed a selective decrease in mitochondrial respiration in the striatum, which later also spread to the cortex.[181] There have also been some studies describing an interaction between PINK1 and NDUFA10 (complex I subunit) in mouse and drosophila, which could also provide an explanation for the impaired OXPHOS phenotype. Morais *et al.* showed that the complex I mediated ubiquinone reduction was inhibited due to the lack of NDUFA10 phosphorylation in PINK1$^{-/-}$ mouse tissue.[182] Whereas, Pogson *et al.* showed that several PINK1 loss-of-function phenotypes were rescued by restoring

complex I activity in drosophila.[183] The functional link between PINK1 and Parkin has been further confirmed with drosophila models, in which Parkin overexpression is able to rescue phenotypes of a dPink1 knockout fly.[184] Whereas, a Parkin knockout mouse has decreased protein expression of complexes I and IV subunits, and of proteins that are neuroprotective against oxidative stress.[73] This could lead to impaired oxidative phosphorylation and fragmented and swollen mitochondrial cristae phenotypes.[73] Analysis of fibroblasts derived from human Parkin patients revealed a decrease of complex I activity and ATP production.[185] This leads to reduced mitochondrial potential, which is further exacerbated when fibroblasts were grown in media with galactose as the sole carbon source, making them dependent on OXPHOS for ATP production.[185] Furthermore, mitochondria present with a branching morphology defect in these patient cells.[185]

DJ-1 (protein deglycase DJ-1) is involved in the oxidative stress response, preventing cell death by eliminating hydrogen peroxide *in vitro*.[37,186] DJ-1 knockout cells show complex I assembly deficiency, loss of mitochondrial polarisation, mitochondrial fragmentation, upregulation of autophagy markers, and ultimately OXPHOS dysfunction.[187,188] It has been suggested that DJ-1 acts in parallel to the PINK1/Parkin pathway controlling mitochondrial function and mitophagy.[188] A mouse model harbouring a pathogenic *SNCA* A53T mutation also manifested with mtDNA damage, reduced complex IV activity, increased autophagy and mitochondrial degeneration, preceding the development of motor symptoms associated with PD.[189,190] Several studies have suggested that α-synuclein associates with the inner mitochondrial membrane where it can directly impair complex I activity and increase ROS production.[191–194] And this direct interaction may also be causing mitochondrial fragmentation by inhibiting fusion and upregulating fission.[195,196] LRRK2 has also been shown to interact with the outer mitochondrial membrane.[197] It directly interacts with DLP1 (dynamin-like protein 1), increasing expression of this mitochondrial fission protein and thereby inducing mitochondrial fragmentation.[198] Furthermore, a study by Iaccarino *et al*. indicated that mutant LRRK2 can activate mitochondrial-mediated apoptosis.[199]

It addition to genomic DNA mutations, mtDNA rearrangement and/or deletions have also been reported in PD patients.[200–203] Furthermore, several families have been identified with mutations in nuclear-encoded *POLG* (DNA polymerase gamma), which synthesises mitochondrial DNA and results in mtDNA deletions.[204] These patients

present with a progressive multisystem disorder, which also includes parkinsonism.[204] Cybrid (cytoplasmic hybrid) models of PD further confirm the link between mtDNA and PD pathophysiology.[205] In these models, control or PD patient donor mtDNAs are introduced into mtDNA-free genetically and environmentally identical cells.[205] PD patient cybrids develop increased oxidative stress, OXPHOS deficiency, reduced mitochondrial transport, and spontaneous Lewy body and neurite formation.[205] Several mtDNA-based models of PD have also been developed. For instance, mice expressing a mitochondrially targeted restriction enzyme (mt-PstI) to specifically damage mtDNA in dopaminergic neurons, not only had OXPHOS deficiency due to depletion of mtDNA, but also presented with SN neurodegeneration, decreased levels of striatal dopamine and a L-DOPA responsive motor phenotype.[206] Another mouse model with reduced mtDNA expression and ETC deficiency in midbrain dopaminergic neurons, due to specific knockout of TFAM, also had a progressive motor phenotype with inclusions and neurodegeneration.[207]

The centrality of mitochondria in PD pathogenesis is further emphasised by the identification of several environmental toxins, specifically affecting the mitochondria, that lead to PD-like phenotypes.[7,8] A commonly observed mitochondrial defect in post-mortem brains of PD patients is reduced activity and impaired assembly of mitochondrial complex I in the substantia nigra[208] and frontal cortex.[209] MPTP (1-methyl-4-phenyl-1,2,3,6-tetrahydropyridine), paraquat (1,1'-dimethyl-4,4'-bipyridinium) and rotenone disrupt the electron transport by inhibiting complex I of the ETC.[210–212] Historically, it was discovered that people exposed to the drug MPTP developed a severe form of PD.[8] Importantly, these PD phenotypes post-MPTP administration were reproduced in mouse, rat and primate models.[213–215] Upon crossing the blood brain barrier, MPTP metabolises into its toxic form MPP^+ (1-methyl-4-phenylpyridinium ion) and localises within the mitochondria of dopaminergic neurons via the dopamine active transporter (DAT).[8,216] Inside the mitochondria, MPP^+ blocks complex I electron transfer and inhibits the α-ketoglutarate dehydrogenase of the TCA cycle.[217] This leads to decreased ATP production, increased ROS generation, and activation of apoptotic pathways.[8,217] The herbicide paraquat is closely related to MPP^+, however its exposure results in lower complex I binding affinity, higher ROS generation, and it does not use DAT to enter dopaminergic neurons.[211] Its exact pathogenic mechanisms remain to be fully elucidated. Finally, the pesticide rotenone also disrupts

complex I activity, decreases ATP synthesis and increases ROS generation.[212] Importantly, rotenone rat models of PD exhibit key features of PD, which include selective degeneration of dopaminergic neurons, loss of the nigrostriatal pathway, bradykinesia, forelimb tremors and inclusions similar to Lewy bodies.[218–222]

Mitochondrial dysfunction seems to be at the centre of potential mechanisms that lead to both sporadic and familial PD pathogenesis. Some of the PD-contributing mitochondrial factors include mutations in mtDNA, mutations in nuclear DNA that are linked to mitochondria, changes in mitochondrial morphology, dynamics, and trafficking, or electron transport chain and oxidative phosphorylation defects.[8,166]

1.3. Lipid droplets

1.3.1. Overview of lipid droplet biology

Lipid droplets (LDs) are not simply passive storage of lipid esters, but rather complex and dynamic cytoplasmic organelles. They originate from the endoplasmic reticulum (ER) and are composed of a lipid ester core surrounded by a phospholipid monolayer and structural proteins (perilipins).[223] LDs are highly heterogeneous organelles, differing in size, core composition and surrounding proteins. Even though one may mainly associate LDs with adipocytes, where they occupy most of the cytoplasm, they are ubiquitous in all cells to variable extents.[224] LDs store superfluous cholesterol and fatty acids (FAs) as neutral lipids, which mainly consist of sterol esters (SEs) and triacylglycerols (TAGs).[225] Depending on the metabolic requirements of the cells, lipids are either stored or mobilised, serving as an energy source and substrates for membrane synthesis.[225] When needed, LDs mobilise fatty acids (FAs), which can be used for mitochondrial β-oxidation to generate ATP. This is a third possible entry point into the electron transport chain (discussed in section 1.2.2). Additionally, FAs can be also used for protein post-translational modifications and act as signalling molecules. Apart from mitochondria, LDs interact with many other organelles, including ER (phospholipid biosynthesis)[226] and caveolae (lipolysis and FA transport in adipocytes).[227] LDs can also interact with each other and fuse via microtubule-dependent processes,[228,229] regulated by SNARE proteins.[230]

Lipid droplet biogenesis usually occurs *de novo* from the ER,[231–233] but it can also occur by fission from already existing LDs.[234] One of the proposed models for *de novo* LD formation involves neutral lipid synthesis, followed by lens formation and finally drop formation.[235,236] Neutral lipids are synthesised and spontaneously aggregate within the ER membrane bilayer.[235,236] In brief, a lens forms after the neutral lipid concentration surpasses a certain threshold, which leads to further neutral lipid accumulation, deforming the bilayer and ultimately leading to a nascent LD to bud into the cytoplasm.[235,236] LD growth can occur either through the previously mentioned fusion with other LDs, or by expansion through local TAG synthesis at the LD surface.[235,236]

Intracellular lipids can be mobilised either through lipophagy or by cytosolic lipases.[224] Firstly, release of FAs is regulated by the interaction among lipases and perilipins present at the LD surface, and lipase activators or inhibitors.[224] The main contributing lipases are the adipocyte triglyceride lipase (ATGL), which hydrolyses TAGs into diacylglycerols (DAGs) and FFAs, and the hormone-sensitive lipase (HSL) that subsequently hydrolyses DAGs into monoacylglycerols (MAGs) and FFAs.[237] Alternatively, LDs can be completely or partially sequestered by autophagosomes, in a process called lipophagy.[224] Atg7 regulates the conjugation of Atg5 and Atg12, which then act as an assembly scaffold for other components.[224] In addition, Atg7 also effects the conjugation of LC3-I to phosphatidylethanolamine (PE), resulting in the generation of LC3-II.[238] The determinants for autophagic initiation on the surface of a LD remain unknown, but poly-ubiquitination may play a role.[239] Inhibition of autophagy causes a significant increase in LDs in various cell types, including fibroblasts and primary neurons.[240–242] Autophagy usually decreases with age in most tissues, and may therefore contribute to the toxic intracellular accumulation of LDs, leading to cell death.[243] A study by Kaushik and Cuervo showed that chaperone-mediated autophagy (CMA) is activated under starvation conditions, selectively targeting perilipin 2 (PLIN2) and perilipin 3 (PLIN3),[244] which are ubiquitously expressed among tissues.[245] The degradation of PLIN2 and PLIN3 by CMA facilitates both types of lipolysis by allowing the binding of either ATGL (and co-activator CGI-58) or ATG proteins.[244] CMA inhibition also causes LD accumulation and a decrease of FA mobilisation.[244]

1.3.2. Lipid droplets and mitochondria

As briefly mentioned above, LDs interact with the mitochondrial outer membrane to facilitate delivery of FFAs, mobilised by lipolysis, for mitochondrial β-oxidation. Furthermore, ATGL-mediated lipolysis has been shown to upregulate SIRT1, thereby inducing the expression of genes involved in mitochondrial β-oxidation and biogenesis.[246,247] Physical contact between LDs and mitochondria both *in vitro* and *in vivo* has been confirmed in yeast by transmission electron microscopy and fluorescence imaging.[248] Perilipin 5 (PLIN5) is highly expressed in oxidative tissue and has been suggested to provide both a physical and metabolic link between LDs and mitochondria.[249] Wang *et al.* showed that PLIN5 is involved in recruiting mitochondria to the LD surface (through a C-terminal region) and plays a dual role of either inhibiting TAG hydrolysis or promoting FA mobilisation depending on the metabolic demands.[249]

During starvation, cells shift from glucose metabolism to mitochondrial FA oxidation. Transient and stable interactions between LDs and mitochondria increase, relying on the distribution of both LDs and mitochondria to the cell periphery.[250] This organelle dispersion is mediated by AMPK activated detyrosinated microtubules and stimulates mitochondrial β-oxidation.[250] A study by Rambold *et al.* provided new insights into FA trafficking to the mitochondria under nutrient starvation conditions. As mentioned above, FAs are mobilised either via autophagosomal engulfment and fusion with the lysosome or via lipolytic breakdown by cytosolic lipases. This study was able to image FAs localised within LDs under basal conditions and their relocation to the mitochondria under starvation.[251] In these starvation assays, FAs were mobilised primarily by cytosolic lipases, whereas LDs were continuously replenished with FAs by autophagy.[251] Hence, despite increased mobilisation there was still an increase in LD number and size over time in starved cells.[251] Furthermore, it was also shown that a homogenous distribution of FFAs through a fused mitochondrial network is necessary for their efficient metabolism.[251] In cells deficient in MFN1, mitochondrial fragmentation resulted in non-homogeneous distribution of LD-derived FFAs and significantly reduced mitochondrial respiration due to suboptimal β-oxidation.[251] Mitochondrial fusion defects also lead to excess FFAs accumulation in the cytoplasm, which can be toxic.[251] Cells mitigate by re-esterifying FFAs into inert TAGs and either store them as LDs or release them into the extracellular medium.[251] Thus, there was a significant increase in

LDs and in the efflux of FFAs out of the cells in MFN1 knockout cells with fusion defects.[251]

In addition to their role in FA mobilisation, trafficking and utilisation, LD-mitochondrial interactions are also important for LD biogenesis and stability.[252] For instance, PEMT (phosphatidylethanolamine N-methyltransferase), which methylates PE into PC (phosphatidylcholine), is found in mitochondria-associated ER membranes (MAM).[253] PEMT-driven PC synthesis is important for LD growth and LD stability by affecting the association of perilipin A with LDs.[253] Furthermore, proteins important for TAG and DAG synthesis (DGAT2 and MGAT2) are also found in MAMs that are associated with LDs.[254]

1.3.3. Lipid droplets in neurodegeneration

Dysregulation of lipid droplet metabolism has been associated with Lewy bodies and neurites in PD. A study by Cole *et al.* found that in cells with high FA concentrations, wild-type α-synuclein redistributes to the surface of LDs, protecting them from lypolysis.[255] Whereas PD mutant α-synuclein remains distributed in the cytosol and does not influence TG metabolism.[255] Furthermore, this study also suggested that the surface of LDs may be one of the initial sites of α-synuclein oligomer aggregation.[255] Parkin has been shown to regulate systemic lipid metabolism.[256] Parkin$^{-/-}$ mice failed to induce lipid transport proteins (such as CD36, Sr-B1, and FABP) when exposed to a high fat diet.[256] Furthermore, Parkin was shown to stabilise CD36 via its function as a ubiquitin-ligase.[256]

Mutations in *SPAST* (Spastin) cause an autosomal dominant form of hereditary spastic paraplegia (HSP), resulting in axonal degeneration of long neurons in particular.[257] Spastin is a microtubule-severing protein involved in a wide variety of cellular processes, which include membrane trafficking and remodelling, endosome tabulation, organelle biogenesis and protein folding.[257] A study has shown that overexpressing an isoform of Spastin (Spastin-M1) results in fewer LDs of increased size.[257] Whereas expression of a mutant Spastin results in LD aggregation caused by its inability to bind to and sever microtubules.[257] Downregulation of dSpastin expression in drosophila resulted in a decrease in LD number and TAGs.[257] Thus, it seems that Spastin plays a role in lipid metabolism and the resulting LD phenotypes may contribute to neurodegeneration in HSP.

It is possible that mitochondrial dysfunction and increased oxidative stress contribute to neurodegeneration through the mismanagement of lipid metabolism. A study by Liu *et al.* has shown that mitochondrial defects and increased ROS in both flies and mice result in glial LD accumulation, prior to the onset of neurodegeneration.[258] In *Drosophila*, ROS upregulates JNK (c-Jun-N-terminal Kinase) and SREBP (Sterol Regulatory Element Binding Protein), leading to LD accumulation.[258] It was possible to reduce LD accumulation, and thereby delay neurodegeneration onset, by lowering ROS, overexpressing lipases or knocking-down JNK and SREBP expression.[258] Thus, LD accumulation may be considered as an early indicator of neurodegeneration.

1.4. Cell cycle regulation

1.4.1. Overview of the cell cycle

The cell cycle consists of alternating periods of interphase and mitosis (M).[259] The interphase is further subdivided into gap phase G_1 (preparing for DNA synthesis), S phase (DNA synthesis/replication) and gap phase G_2 (preparing for mitosis).[259] When cells are not undergoing growth or proliferation, they enter the resting quiescent state of G_0.[259] During M phase, cells undergo cytokinesis.[259] Different regulatory proteins are necessary to control the correct progression of the cell cycle.[259] Cyclins are synthesised, recruited and degraded at specific time points during the cell cycle in order to regulate cyclin-dependent (serine/threonine) kinase (CDK) activation.[259] Inactivation of these complexes occurs either due to the degradation of cyclins or by cell cycle inhibitory proteins, which include members of the INK family and CIP/KIP family.[259] A schematic of the cell cycle with some of its main regulators is depicted in **Fig.1.5**.

Various CDKs have been identified to regulate transitions at different stages of the cell cycle: CDK2, CDK4, and CDK6 during G_1, CDK2 during S, and CDK1 during both G_2 and M phases.[259] CDK activity needs to be tightly regulated via post-translational modifications because their protein expression remains stable throughout the cell cycle and to ensure the precise timings of cell division.[259] CDKs are only fully activated after both the binding of a cyclin and the phosphorylation of a conserved threonine by CAK (CDK-activating kinase), which is composed of CDK7 and cyclin H.[260] Unlike CDKs, cyclin protein levels rise and fall during the cell cycle, which allows for necessary periodical and sequential formation of CDK/cyclin complexes.[261,262] Thus, the cell cycle is able to

progress in a unidirectional manner due to these mechanisms. There are three types of D cyclins (cyclin D1, D2 and D3), which bind to CDK4 or CDK6, forming complexes that are necessary for G_1 entry from the G_0 quiescent state.[263] The CDK2/cyclin E complex regulates the progression from G_1 into S phase,[264] while cyclin E is degraded and CDK2 forms a complex with cyclin A during S phase.[265,266] Cyclin A forms a complex with CDK1 in late G_2 and early M phase to enable entry into mitosis, which is subsequently also regulated by CDK1/cyclin B complexes.[267,268] Consecutively, activated CDK/cyclin complexes phosphorylate their downstream target proteins.[262,269] The main downstream targets of CDK4 and CDK6 are members of the pocket protein family, which consists of the retinoblastoma protein (pRb), retinoblastoma-like protein 1 (p107) and retinoblastoma-like protein 2 (p130).[270,271] These proteins bind to and inhibit E2F transcription factors, thereby hindering the cell cycle.[270,271] pRb is initially mono-phosphorylated by CDK4,6/cyclin D complexes, resulting in E2F release.[270,271] Next, E2F activates not only cyclin E that promotes cell cycle progression, but also genes involved in nucleotide biosynthesis and DNA replication.[270,271] Complete inactivation of pRb is achieved by subsequent CDK2/cyclin E-mediated phosphorylation, which results in further E2F release and the cell cycle progressing into the S phase.[270,271] Next, cyclin A activates CDK2 to progress through the S/G_2 transition and subsequently CDK1 to initiate mitosis.[265]

CDK/cyclin complexes can be inhibited by CDK inhibitors (CDKI), encompassing the INK and CIP/KIP families. The INK family (including p15, p16, p18 and p19) binds to CDK4/6, blocking their interaction with D cyclins.[259] Whereas, the CIP/KIP family (p21, p27 and p57) inhibits catalytic activity of CDK/cyclin A, E, D complexes.[259] For instance, p21 binds to CDK2/cyclin A, CDK2/cyclin E, CDK4/cyclin D1, D2 complexes, thereby inhibiting pRb phosphorylation and E2F release.[272,273] The CDKI p21 can be activated through either p53-dependent or p53-independent pathways, causing cell cycle inhibition in response to various stimuli.[274] For example, DNA damage or increased oxidative stress results in p53 activity upregulation and the increase of p21 expression, which in turn inhibits cell cycle progression.[275] Under basal conditions, MDM2 (murine double minute 2 protein) inhibits p53 by functioning as an E3 ubiquitin ligase and targeting it for proteasomal degradation, and by preventing its binding to DNA.[276,277] However, MDM2 is also a transcriptional target of p53, so these two proteins function in a negative feedback loop.[276,277] Phosphorylation activates p53 by preventing its

association with MDM2.[276,277] It can then activate its transcriptional target, p21, that functions as a CDKI and can inhibit both CDK2 (G_1/S transition) and CDK1 (G_2/M transition) complexes.[274] p53 can also upregulate apoptotic regulators, such as Bax and PUMA, leading to programmed cell death.[278]

Both p21 and p27 shuttle between the cytoplasm and nucleus with their function being dependent on phosphorylation status and location.[259] Similarly to p21, p27 is also a tumour suppressor and inhibits cell cycle progression.[259,279,280] The levels of p27 expression change throughout the cell cycle and it controls cycle progression at the G_1 phase and beyond.[281,282] Firstly, p27 inhibits CDK2/cyclin E, A complexes by blocking CDK2-mediated hydrolysis of ATP, preventing substrate association, and inhibiting the CAK-mediated phosphorylation of CDK2.[279] Thus, the complex is unable to phosphorylate pRb and drive the cell cycle forward. Secondly, p27 also has an effect on CDK4,6/cyclin D complexes, which is dependent on cell type and growth stage.[279,282] Phosphorylation of p27 makes the CDK4,6/cyclin D complex active, whereas unphosphorylated p27 blocks the CDK4/6 ATP and substrate active sites, disabling pRb phosphorylation and G_1/S transition.[279]

Lastly, it has been also shown that p27 can bind to and inhibit CDK1/cyclin B complexes, inhibiting cell cycle progression.[283] The cell becomes committed to carry out DNA replication after passing this restriction point and entering S phase.[284] Phosphorylated p27 is ubiquitinated by SCF^{Skp2}, which targets it for proteasomal degradation.[285] Apart from its cell cycle regulatory role, p27 also affects differentiation[286] and migration.[287,288] These restriction points are crucial to ensure that the cell cycle only proceeds if the DNA is free from damage and chromosomes are correctly aligned.[289] It is vital for the cell cycle to have such intricate regulatory mechanism in order to maintain proper unidirectional cell division.

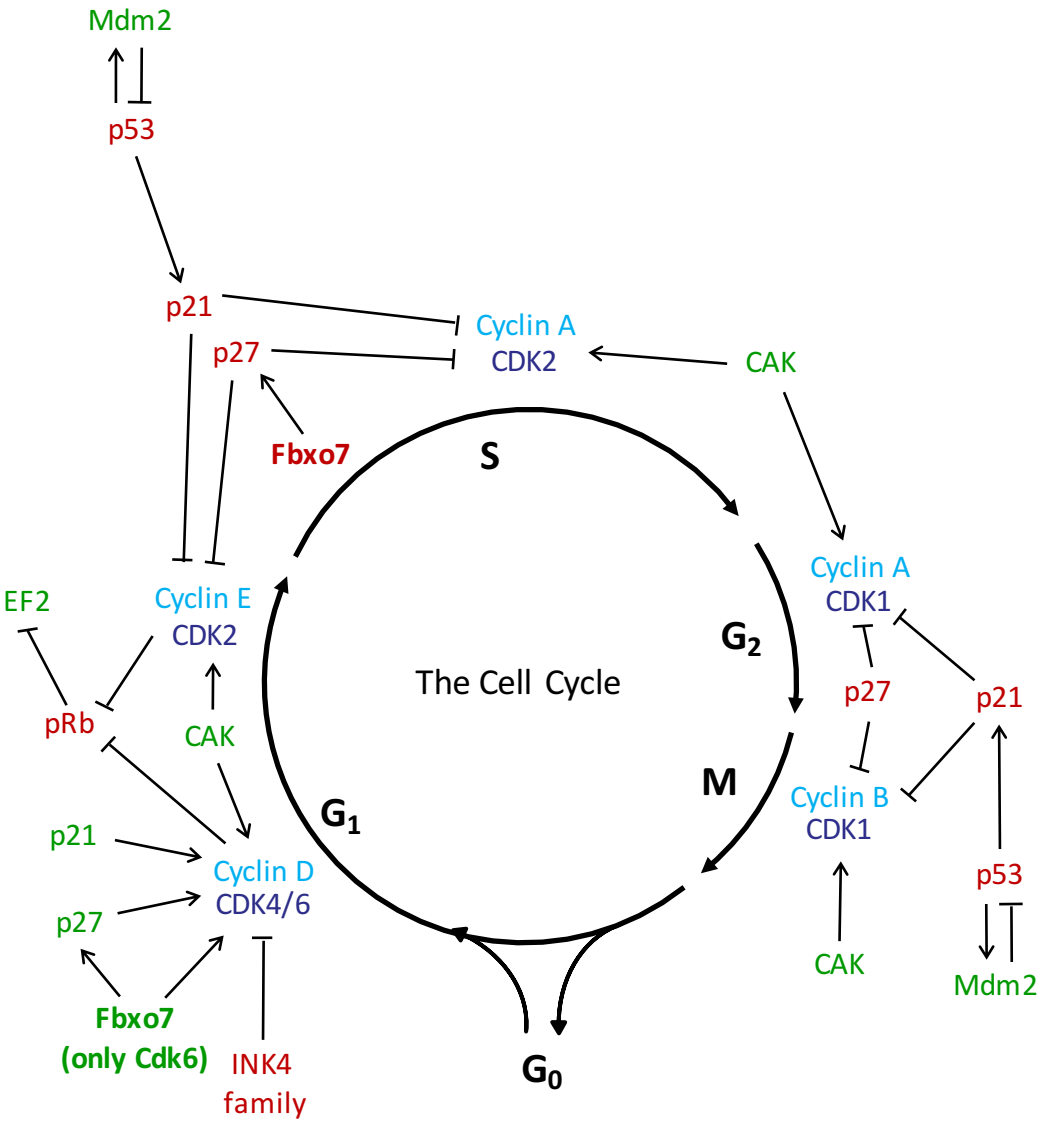

Figure 1.5 – Mammalian cell cycle. A schematic depicting the main players in regulating the cell cycle at the four different stages: G_1, S, G_2 and M. CDKs (purple) and Cyclins (light blue) form complexes that can be activated by kinases (CAK) or assembly factors (FBXO7, p21 and p27), all depicted in green. Or they can be inhibited by the INK4 family or CIP/KIP family (p21 and p27), all depicted in red. This figure is based on Vermeulen *et al.* (2003).

1.4.2. Cell cycle and Parkinson's disease

One of the proposed molecular mechanisms implicated in neuronal cell death in Parkinson's disease and other neurodegenerative disorders is the loss of cell cycle control.[10,290–292] Even though neurons are post-mitotic and terminally differentiated, it has been suggested that certain cell-cycle pathways become aberrantly reactivated during neurodegeneration, preceding neuronal death.[10,290–292]

For instance, Jordan-Sciutto *et al.* observed that phosphorylated pRb, which triggers cell cycle progression, was significantly upregulated in the post-mortem SNpc of PD patients.[293] Hoglinger *et al.* confirmed that the pRb-E2F pathway mediates cell death in PD by showing that there is an upregulation of E2F-1 in the cytoplasm of DA neurons in the post-mortem patient SNpc.[292] Furthermore, experiments in primary rat midbrain cultures showed that post-MPP+ exposure, cyclin D1 (G_1 phase), cyclin E (S phase), cyclin A (G_2 phase) and cyclin B (M phase) became upregulated and significantly more cells became positive for phosphorylated pRb and E2F-1.[292] Importantly, E2F-$1^{-/-}$ mice were protected against this MPP+/MPTP-induced toxicity.[292] Overall, this study suggests that there may be aberrant activation of the pRb-E2F-1 pathway and S phase cell cycle progression in PD.[292]

Furthermore, Staropoli *et al.* showed that Parkin is a component of an SCF-like ubiquitin ligase complex (Parkin-Cul1-hSel-10) that targets phosphorylated cyclin E for degradation.[294] Accordingly, Parkin deficiency results in the accumulation of cyclin E and the upregulation of apoptotic markers in primary neuronal cultures and in the SNpc of a Parkin-associated autosomal recessive PD patient.[294] The accumulation of cyclin E in neurons may either be a part of the apoptotic regulation or a cell cycle re-entry attempt by promoting S phase entry.[294,295] Another study conducted by Esteras *et al.* investigated peripheral cells from sporadic PD patients.[296] Their immortalised lymphocytes had higher CDK6/cyclin D3 complex activity and increased phosphorylation of pRb, leading to G_1/S checkpoint dysregulation and increased proliferation.[296]

Whereas, immortalised *Pink1*$^{-/-}$ MEFs had defective progression of the cell cycle with more cells present in the G_2M and fewer cells in the G_1 phase.[297] It seems that the MEFs went into mitotic arrest, not being able to undergo cytokinesis, to re-enter G_1 or

upregulate cyclin D1 when necessary.[297] It was further shown that this *Pink1* deficiency induced cell cycle dysfunction was linked to DRP1-mediated aberrant fission of mitochondria, which is vital for proper mitosis.[297]

1.4.3. Proliferation and differentiation

The balance between cell proliferation and differentiation is crucial for the correct development of numerous neuronal cell types.[298] Studies have shown that the cell cycle can directly influence early lineage commitment and terminal cell fate.[299,300] It has been also established that neural progenitors undergo overall cell cycle lengthening immediately prior neuronal differentiation due to an extended G_1 phase.[301] Elongation of the G_1 phase is a common phenomenon associated with differentiating cells, although contradictory evidence in murine embryonic stem cells showed that G_1 elongation is actually compatible with their pluripotent state.[302] Regardless, many G_1 cell cycle regulators have been implicated in this proliferative to neurogenic switch. For instance, during development, cyclin D2 plays a role in activating a critical proliferation stage prior to differentiation in the subventricular zone and cerebellum, without which microencephaly occurs.[303] Cyclin D2 is also essential for adult neurogenesis in the denate gyrus of the hippocampus and the olfactory bulb.[304]

Another important example is p27, which has both a cell-cycle-dependent and a cell-cycle-independent role in neurogenesis. Even though there are no changes in cell cycle length and G_1 phase as a result of losing p27 function, it does influence neuronal development during mid- to late-stage neurogenesis by regulating progenitor proliferation in the subventricular zone and hippocampus.[305,306] Interestingly, p27 also promotes neuronal differentiation and migration in the cerebral cortex independently to its role in cell cycle regulation.[307] It has been shown that p27 promotes neuronal differentiation by stabilising Neurogenin-2 protein and promoting neuronal migration by blocking RhoA signalling.[307] Considering the important role of FBXO7 in the G_1 phase of the cell cycle through its interaction with CDK6/cyclin D complexes and p27 (which will be discussed in the subsequent section),[308,309] it would be interesting to investigate its role further in neurogenesis and differentiation pathways.

1.5. FBXO7

1.5.1. FBXO7 structure and function

FBXO7 is a member of the F-box protein (FBP) family, which are the substrate-recruiting subunits of SKP1-Cullin1-FBP (SCF)-type E3 ubiquitin ligases. FBPs are defined by a 40-50 amino acid F-box domain (which binds to SKP1)[310,311] and are sub-classified based on the presence of leucine-rich repeats (FBXL), WD40 repeats (FBXW) or other binding motifs (FBXO).[312] FBXO7 also contains an N-terminal ubiquitin-like (Ubl) domain,[309] a C-terminal unstructured proline-rich region (PRR) that can bind substrates,[309] and a core globular FP (FBXO7/PI31) domain that is shared with the proteasome inhibitor protein of 31 kDa (PI31).[313] The *FBXO7* gene consists of nine exons from which three complete protein coding transcripts are formed.[312] Isoform 1 has the longest transcript, which encodes a 522 amino acid protein that is the most commonly expressed form of FBXO7 both *in vivo* and *in vitro*.[312] Isoform 2 only consists of exons 3-9 with alternative 5' exons (1b and 2b), thereby lacking the Ubl domain, and is 443 amino acids in length.[312] Even though isoform 3 contains exons 2-9 and begins with exon 1b (like isoform 2), it has an alternative protein translation start point, making it the shortest in length.[312]

The canonical function of FBXO7 is as a substrate-recruiting subunit of SCF-type E3 ubiquitin ligases. SCF-mediated ubiquitination can result in modification (mono-ubiquitination), protein degradation via the 26S proteasome (poly-ubiquitination linked via lysine 48 of ubiquitin (K48)) or the activation of the endosomal or autophagy/lysosomal pathways (poly-ubiquitination via K63 linkages).[312,314,315] In its canonical function, SCF^{FBXO7} ubiquitinates, and thereby regulates, various substrates. The most established substrates include hepatoma up-regulated protein (HURP),[316] inhibitor of apoptosis protein 1 (cIAP1)[317] and TNF receptor-associated factor 2 (TRAF2).[318] SCF^{FBXO7} ubiquitination of cIAP1 and TRAF2 does not result in their degradation, but in the inhibition of NF-κB activity, which is a signalling pathway linked to neurodegeneration and PD.[318] However this has not yet been shown to occur in any models based on *FBXO7* pathogenic mutations. Furthermore, a recent protein array screen conducted in our lab identified and validated GSK3β and TOM20 as two new substrates of FBXO7 (discussed further in subsequent sections).

FBXO7 also has a variety of other atypical, SCF-independent, functions. As a regulator of the cell cycle, FBXO7 aids the formation of CDK6/cyclin D1, D3 complexes by acting as an assembly scaffold.[308,309] FBXO7 stabilises their expression and promotes cell cycle progression.[308,309] It may also have a protective function by preventing the degradation of the complexes or by enhancing their import into the nucleus. Thus, the lack of FBXO7 can directly affect CDK6/cyclin D1, D3 complex formation and expression, which may result in the cells not progressing through the G_1 phase of the cell cycle.[308] FBXO7 also directly binds to p27, alone and in complex with CDK6/cyclin D, stabilising its expression. p27 functions as a cell cycle inhibitor of S/G_2/M phase CDK complexes (CDK2, CDK1) but paradoxically also as an assembly factor for the G_1 CDK4 and CDK6.[308,309] Thus, FBXO7 can either promote cell cycle entry by stimulating CDK6 activity or inhibit its progression by stabilising p27, and this seems highly cell type specific.[308,309] High affinity to PI31 through their shared FP domains, and the resulting stabilisation of PI31, suggests that FBXO7 also has a role in regulating its activity.[313] However, due to conflicting results from previous studies, the role of PI31 still remains unclear and requires further investigation. For instance, in contrast to its described function *in vitro*, PI31 does not seem to inhibit proteasome activity *in vivo*, but rather promotes it and also regulates immunoproteasome maturation.[312] While another analysis of PI31 function in mammalian cells did not report any effect on cellular proteasome content or function as a result of PI31 overexpression or knockdown.[319] FBXO7 also directly interacts with PINK1 and Parkin to mediate Parkin-mediated mitophagy under stress.[320] (**Figure 1.6**)

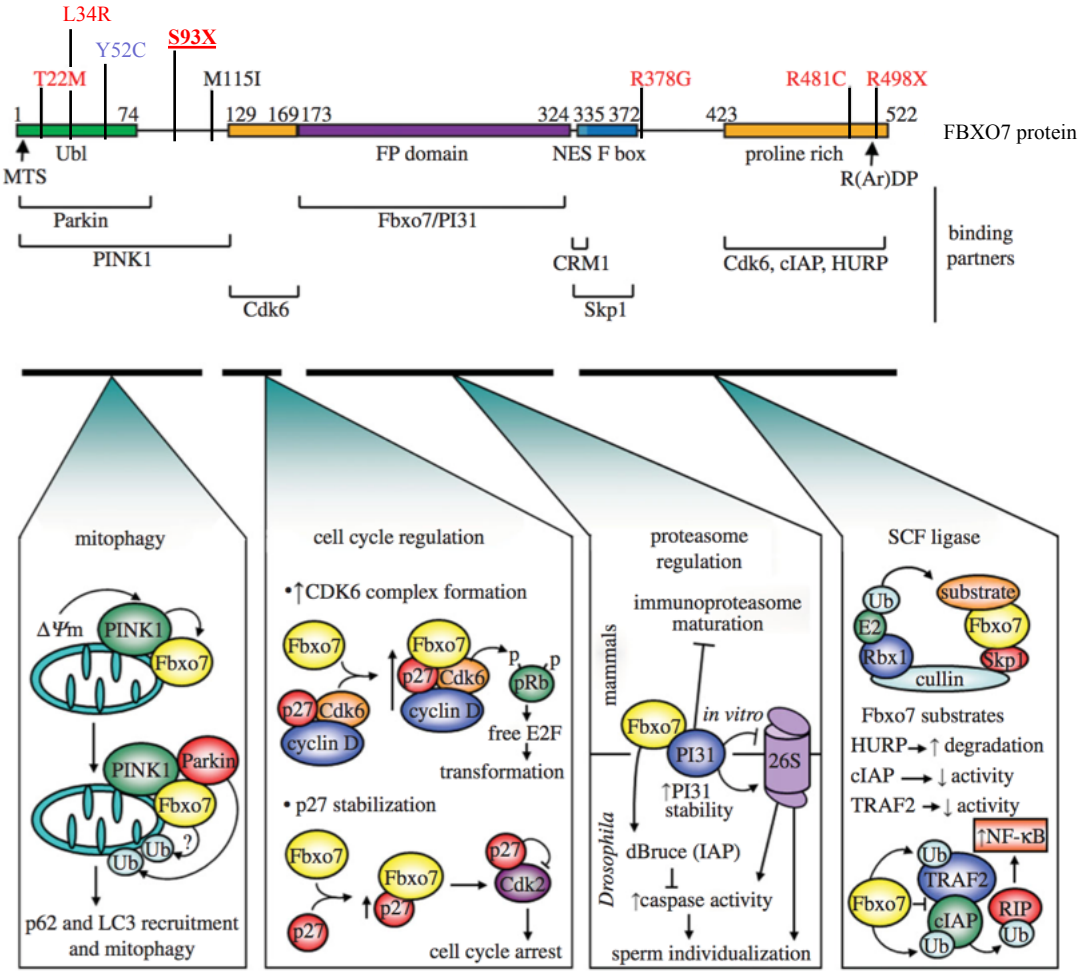

Figure 1.6 – FBXO7 structure and function. The protein structure of FBXO7 isoform 1 with annotated domains, binding partners and PD-associated mutations in red (with the mutation studied in Chapter 3 in bold and underlined in red, PD-protective mutation in purple, and SNP in black. Ubl (ubiquitin-like domain) depicted in green, FP (FBXO7/PI31 interacting domain) depicted in purple, proline rich region depicted in yellow, F-box domain depicted in blue, R(Ar)DP motif, NES (nuclear export signal), MTS (mitochondrial targeting signal). Canonical (SCF ligase) and non-canonical (mitophagy, cell cycle regulation, and proteasome regulation) functions of FBXO7. This figure is modified from Nelson *et al.* (2013).

1.5.2. FBXO7 and Parkinson's disease

FBXO7 mutations were first associated with Parkinson's disease by Shojaee *et al.* in 2008 via a genome-wide linkage analysis of families with a history of juvenile parkinsonism, and independently confirmed by Di Fonzo *et al*. in 2009. Mutations in *FBXO7* result in a juvenile form of parkinsonism,[41,46] also called parkinsonian pyramidal syndrome (PPS), which was originally described by Davison in 1954.[321] These patients usually present with a severe, rapidly-progressing levodopa-responsive parkinsonism that includes bradykinesia, resting tremor, rigidity, and postural instability.[40,317] Furthermore, they usually have additional pyramidal signs such as impaired fine movements, spasticity and the Babinski sign.[40,317] Atypical symptoms of cognitive decline, cortical atrophy, dystonia, dysphagia and dysarthria have also been reported.[41,46,322] There appears to be a wide heterogeneity of *FBXO7*-associated PD as patients with the L34R mutation seem to present with a more typical later-onset PD progression.[323] PD-associated mutations within *FBXO7* span the entire gene and different domains.[322] Within the Ubl domain, the L34R[323] missense mutation and the compound mutation comprised of a T22M[41] missense mutation together with an internal splice site mutation (IVS7 + 1G/T) have been described. The R378G[46] missense mutation lies adjacent to the F-box domain. Whereas the missense R481C[324] and the nonsense R498X[41,325] mutations are located within the PRR. In contrast, the Y52C polymorphism, within the Ubl domain, was actually found to be a PD protective factor.[326]

Protein aggregation and related UPS dysfunction have long been implicated in PD and other neurodegenerative disorders. Ubiquitin was discovered as a component of protein aggregates in neurodegeneration already in 1988.[327,328] FBXO7 has been also localised to α-synuclein Lewy bodies, suggesting that it may be involved in their formation.[42] Aggregated α-synuclein can also have a negative effect on proteasome function by inhibiting the 26S subunit.[329] Vingill *et al.* showed that FBXO7 interacts with and ubiquitinates the proteasomal subunit PSMA2 with K63-linked polyubiquitin chains, regulating functional proteasome assembly.[330] Thus, FBXO7 knockdown or knockout results in decreased proteasomal activity in these models.[330] Furthermore, post-mortem analysis of the substantia nigra of PD patients revealed a reduction in proteasome activity and its subunits.[331] Lastly, Wang *et al.* showed that rotenone is able to disrupt the activity of the 26S proteasome holoenzyme.[332]

The interplay of three PD related genes in the regulation of mitophagy further emphasises the importance of mitochondrial dynamics in PD pathogenesis.[320] During mitophagy, a form of macro-autophagy that identifies and removes damaged depolarized mitochondria, PINK1 senses when mitochondrial membrane potential ($\Delta\psi m$) is lost, accumulates on its outer membrane and recruits the E3 ligase Parkin for polyubiquitination of target proteins leading to eventual engulfment by autophagosomes.[320] FBXO7 is necessary for the recruitment of Parkin (directly interacting via the Ubl domain) and mitophagy becomes dysfunctional in cells with FBXO7 knockdown or in the presence of pathogenic *FBXO7* mutations.[320,333] Interestingly, it has also been shown that WT Fbxo7 is able to rescue a DA neurodegeneration phenotype in Parkin deficient drosophila, while PD-associated Fbxo7 mutants had no significant effect.[334] A study by Delgado-Camprubi *et al.* showed that lack of FBXO7 results in mitochondrial metabolism impairment via PARP (poly ADP-ribose polymerase) upregulation due to increased cytosolic ROS.[335] These FBXO7 deficient cells have reduced levels of NAD+, impaired ETC complex I activity, decreased membrane potential and lower ATP levels.[335] Lastly, Teixeira *et al.* identified TOM20 (translocase of outer mitochondrial membrane 20) as a ubiquitination target of FBXO7, which seems to have a stabilising non-proteolytic effect.[336] Taken together, these studies place FBXO7 at the centre of PD pathology.

Until now, a very limited number of FBXO7-based animal models have been created. A zFbxo7 knockdown zebrafish model presented with two important PD hallmarks; loss of DA neurons and DA-dependent bradykinesia.[337] *In situ* hybridisation revealed a significant decreased in diencephalic TH-expressing neurons, which correspond to the human SN or VTA DA neurons.[337] Importantly, the severity of these phenotypes was dependent on the level of zFbxo7 deficiency and the locomotor disturbances significantly improved after apomorphine (DA agonist) administration.[337] Vingill *et al.* generated a complete *Fbxo7* knockout mice, which presented with proteasome activity reduction, locomotor phenotypes and premature death.[330] When *Fbxo7* was disrupted conditionally either in forebrain or dopaminergic neurons, the mice developed early-onset dyscoordination and late-onset motor defects respectively.[330] The early-onset dyscoordination seems to recapitulate pyramidal tract signs seen in FBXO7 patients.[330] Whereas, chronic DA deficiency accompanies the late-onset progressive motor defects.[330]

Within the scope of this PhD project, I aimed to utilise a variety of *in vitro* and *in vivo* PD models to characterise the functional role of FBXO7. As described above, FBXO7 lies at an intersection of crucial PD pathways: proteasomal function, through its role as a ubiquitin ligase and its interaction with PI31, and mitochondrial function, by mediating mitophagy under stress with PINK1 and Parkin. I hoped to gain more insight into these mechanisms by generating and characterising novel FBXO7-associated models of PD. In the FBXO7 null patient fibroblasts, I focused mainly on studying mitochondrial phenotypes and the more established effects of FBXO7 on proliferation and the cell cycle (Chapter 3). Subsequently, my aim was to see whether any of these phenotypes would translate into MEFs from a *Fbxo7* null mouse (Chapter 3) and FBXO7 knockdown/ knockout SH-SY5Y cells that are still widely used in this research area (Chapter 4). I wanted to determine which cell lines were better at looking into which phenotypes, and which models perhaps should not be used for the study of FBXO7 functionality. Lastly, I also sought to characterise an aging conditional *Fbxo7* knockout mouse model (Chapter 5) to study the protein in an *in vivo* context and look for novel substrates that may underpin its pathogenic phenotypes.

CHAPTER 2

MATERIALS AND METHODS

2.1. Molecular genetics

2.1.1. DNA constructs

Name	Vector	Insert	Source
Vec	pcDNA3.1	-	Invitrogen, V79029
Vec FLAG		FLAG	Heike Laman, Dept. of Pathology, University of Cambridge
Vec T7		T7	
Vec HA		HA	
FBXO7		FBXO7 (1-522)	Heike Laman, Dept. of Pathology, Cambridge Described in Laman *et al.*, 2005[309]
ΔF-box		FBXO7 (1-522ΔF-box) (F-box domain aa 335–367 deletion)	
FLAG FBXO7		FLAG-FBXO7 (1-522)	Heike Laman, Dept. of Pathology, Cambridge
FLAG ΔF-box		FLAG-FBXO7 (1-522ΔF-box)	
FLAG Fbxo7-R378G		FLAG-FBXO7-R378G (1-522)	
FLAG FBXO7-R498X		FLAG-FBXO7-R498X (1-498)	
FLAG FBXO7-T22M		FLAG-FBXO7-T22M (1-522)	
FLAG FBXO7-R481C		FLAG-FBXO7-R481C (1-522)	
FLAG FBXO7-V253E		FLAG-FBXO7-V253E (1-522)	
T7-FBXO7		T7-FBXO7 (1-522)	
T7-ΔF-box		T7-FBXO7 (1-522ΔFbox)	
FBXO7 CRISPR sg2 resistant		FBXO7 (1-522) with silent mutations at CRISPR site	Described in section 2.1.3.
RPL23		RPL23	Heike Laman, Dept. of Pathology
FLAG RPL23		FLAG-RPL23	
RPL23 HA		HA-RPL23	
Vec IRES-GFP	pMSCV	-	From R. Dickins (Clontech) and S. Lowe (Cold

Vec IRES-mCherry		-	Spring Harbor Laboratories, New York)
Vec Puro-IRES-GFP		-	Addgene, 21654
Vec Puro-IRES-mCherry		-	Heike Laman, Dept. of Pathology, Cambridge
FBXO7 IRES-GFP		FBXO7 (1-522)	
ΔF-box IRES-GFP		FBXO7 (1-522ΔF-box)	
FBXO7 IRES-mCherry		FBXO7 (1-522)	
ΔF-box IRES-mCherry		FBXO7 (1-522ΔF-box)	
FBXO7 Puro-IRES-GFP		Fbxo7 (1-522)	
ΔF-box Puro-IRES-GFP		Fbxo7 (1-522ΔF-box)	
Vector sh	LMP-IRES-GFP	-	From R. Dickins (Clontech) and S. Lowe (Cold Spring Harbor Laboratories, New York)
FBXO7 sh1		FBXO7 miR30 shRNA1 5'-CGCCCAGTCTGGTGTTTGGAAT (HP_3087)	Heike Laman, Dept. of Pathology, Cambridge Described in detail in Meziane *et al.*, 2011[308]
FBXO7 sh2		FBXO7 miR30 shRNA2 5'-CGCTGAGTCAATTCAAGATAAT (HP_434828)	
VSV-G		Viral envelope packaging vector (human cell lines)	From R. Dickins (Clontech) and S. Lowe (Cold Spring Harbor Laboratories, New York)
Psi Ψ		Viral envelope packaging vector (murine cell lines)	
pLOX-Ttag-IRESTK	pLOX	SV40 Large T, HSV1-TK	Massimo Zeviani, MRC Mitochondrial Biology Unit, University of Cambridge
pMD2.G	pMD2.G	VSV-G envelope expressing plasmid	
psPAX2	psPAX2	Lentiviral packaging plasmid	

Table 2.1 – *List of constructs used*

2.1.2. PCR and molecular cloning

DNA fragments were amplified using primers that would incorporate restriction endonuclease recognition sites, allowing for unidirectional cloning. VENT DNA Polymerase and ThermoPol reaction buffer from NEB (M0254) were used, as described in **Table 2.2**.

PCR RECIPE (per reaction)		PCR CONDITIONS		
Component	**Final concentration**	**Temperature (°C)**	**Time**	**Cycles**
10x ThermoPol buffer	1x	95	5 mins	1
dNTPs	0.4 mM	95	1min	35
Forward primer	1 µM	50-68*	1min	
Reverse primer	1 µM			
VENT DNA polymerase	1 U	72	1min	
DMSO#	10%	72	7mins	1
DNA template	50-60ng			
ddH2O	q.s. to 50µL			

Table 2.2 – *General PCR conditions for cloning.*

#DMSO only added if the annealing temperature was above 60

*Annealing temperature dependent on primer pair sequence

The PCR products were separated by electrophoresis on a 1XTAE agarose gel (0.8-1.2% agarose depending on the size of the product). Then, they were gel extracted and purified (QIAquick Gel Extraction Kit, Qiagen, 28704). Purified PCR products were subsequently digested using the appropriate restriction enzymes, gel purified again and ligated. Fragments were usually ligated at volume ratios of 1:1, 3:1, or 7:1 (insert:vector), or 1:1:1 or 2:2:1 (insert 1:insert 2:vector) for 3-way ligations, using T4 DNA ligase and reaction buffer (NEB, M020S). Ligation reactions were performed at room temperate for 45 minutes. The entire ligation reaction was added to 50µL chemically competent DH5α cells (Subcloning Efficiency™ DH5α™ Competent Cells, Invitrogen, 18265017). The transformation was incubated on ice for 45 minutes, followed by 40 seconds at 42-45°C. Cells were selected on LB agar plates, containing either ampicillin (100µg/mL) or kanamycin (50µg/mL), and grown overnight at 37°C. Single colonies were then cultured overnight in 3mL of 2xTY (Trypton/Yeast Extract) media, containing an antibiotic for selection, and DNA was extracted using the QIAprep Spin Miniprep Kit (Qiagen, 27104). A starter culture was usually required for kanamycin resistant bacteria, prior to culturing overnight. The cloned plasmids were verified using

test digests for the presence of the insert and fully sequenced to ensure no mutations were introduced during PCR amplification and cloning.

2.1.3. Generating CRISPR lines (sgRNA cloning and viral transductions)

The sgRNA cloning for the CRIPSR cell lines was conducted by Mr. Liam Lee. The best predicted sgRNA sequences were established based on their potency score (Doench *et al.,* 2014[338] and available through sgRNA Designer www.broadinstitute.org/rnai/public/analysis-tools/sgrna-design) and off-target score (CRISPR Design from Zhang Lab MIT and available through CRISPR.MIT.edu). Off-target scores great than 50 are considered acceptable for use with minimal off-target effects. For both, the higher the score, the better. Subsequently, the sgRNAs were synthesised through Sigma Aldrich (standard desalt oligos), and annealed and phosphorylated with T4 PNK (T4 Polynucleotide Kinase, NEB M0201S). The resulting phosphorylated DNA fragments were ligated into *BsmB*I cleaved p-Lentiguide_puro (Addgene 52963), which was CIP treated after restriction enzyme digest. The ligation reactions were then transformed in RecA deficient strain (NEB Stable) via standard heat shock reaction and cloned at 30°C. The plasmids were isolated with QIAprep Spin Miniprep Kit (Qiagen, 27104). Subsequently, the 2nd-gen lentivirus packaging system from the Trono Lab (psPax2 and MD2.G) was used to prepare lentiviral particles for all sgRNAs. In more detail, 1µg sgRNA lentiviral plasmid, 1µg psPax2 and 0.5µg MD2.G were incubated with TransIT-293 transfection reagent (Mirus, MIR 2704) in Opti-MEM (Life Technologies, 31985062) for 15 minutes at room temperature. Then, it was added onto 1x10^{6} 293FT cells (ThermoFisher Scientific, R70007) seeded in a well of a 6-well plate in 1mL of DMEM (Gibco, 41965039). Media was collected and stored in -80°C 72 hours post-transfection until ready to use. LentiCas9-blast (Addgene, 52962) was packaged into lentiviral particles in the same manner, except on a larger scale in T175 flasks. To generate CRIPSR lines, SH-SY5Y cells were first transduced with lentiCas9-blast virus. 24 hours post-transduction, cells were trypsinised and replated into blasticidin (10 µg/mL) media, which was replaced after 2 days and cells were maintained in blasticidin media for a total of 5 days. After blasticidin selection, the SH-SY5Y-Cas9 cell line was transduced with sgRNA lentiviruses and mainlined in puromycin (2 µg/mL) media for 10 days. Afterwards, the cells were maintained in regular cell culture media (with neither balsticidin nor puromycin).

2.1.4. Site directed mutagenesis (CRISPR-resistant plasmids)

Site directed mutagenesis was used to generate CRISPR-resistant plasmids, which enabled FBXO7 complementation in CRISPR FBXO7 knockout cell lines. This required a two-step PCR cloning protocol, which introduced silent mutations within the Cas9 recognition sequence. In the first step, fragments either side of the CRISPR site were amplified separately (using *FBXO7 Eco*RI forward with CRISPR site mutant reverse, and CRISPR site mutant forward with *FBXO7 Xho*I reverse primer pairs). The primers were composed of a longer homologous region and a shorter homologous overhang containing the series of silent point mutations within the CRISPR sequence. In the second step, these two PCR products annealed together during 10 cycles of primer-free PCR, after which primers were added for a further 30 cycles to amplify the whole sequence (using *FBXO7 Eco*RI forward with *FBXO7 Xho*I reverse primer pair). The CRISPR site was mutated from bp483-505 GATAATGCGCATATGGCAGAGGG into GACAACGCACACATGGCTGAAGGT so that it would be no longer recognised by sgRNA2 and allow for FBXO7 expression. All CRISPR-resistant constructs were verified by sequencing. A list of primers used are listed in **Table 2.7**.

2.1.5. Genotyping PCR (including DNA extraction from mouse tissue)

Genomic DNA was extracted from ear or tail clips by incubating them in a Chelex solution composed of 10% Chelex 100 Resin (Bio-rad, 1422822), 0.1% Tween 20 (Sigma, P9416), and 0.1 mg/mL Proteinase K (Sigma, P8044), for 45 minutes at 50°C, followed by 30 minutes at 95°C (to inactive the Proteinase K). The debris was pelleted by centrifugation (13,000RPM for 1 minute), and the supernatant was used in PCR reactions. The Cre allele was amplified in a single product PCR, whereas the ΔF-box, 'floxed' FBXO7 and Rosa26YFP alleles were genotyped in multiplexed PCR containing a common 5' primer and two different 3' primers yielding two products, one within the WT sequence and the other within the transgenic sequences. REDTaq® ReadyMix™ PCR Reaction Mix (Sigma, R2523) was used for all genotyping PCR. PCR products were separated on a 1.2% 1xTAE agarose gel. A list of all genotyping primers can be found in **Table 2.7**.

PCR RECIPE (per reaction)		PCR CONDITIONS		
Component	**Final**	**Temperature**	**Time**	**Cycle**
2x RedTaq RM	1x	92	5 mins	1
Forward primer	0.4 µM	92	30secs	35
Reverse primer	0.2 µM	62	30secs	
ΔF-box/Floxed FBXO7 Reverse primer	0.2 µM	72	30secs	
DNA	1 µL	72	3mins	1
ddH2O	q.s. to 20µL			

Table 2.3 – *Example genotyping PCR conditions for ΔFbxo7/Floxed Fbxo7 alleles*

For the Rosa26-YFP PCR, the forward, mutant forward and reverse primers were used at a final concentration of 0.25 µM and the PCR conditions were as follows: 1 cycle of 94°C (3 minutes); 35 cycles of 94°C (30 seconds), 58°C (1 minute), 72°C (1 minute); and 1 cycle of 72°C (2 minutes).

For the Cre PCR, the forward and reverse primers were used at a final concentration of 0.25 µM and the PCR conditions were as follows: 1 cycle of 92°C (5 minutes); 35 cycles of 92°C (30 seconds), 58°C (30 seconds), 72°C (30 seconds); and 1 cycle of 72°C (3 minutes).

2.1.6. Sequencing

All sequencing was conducted at the DNA Sequencing Facility of the Department of Biochemistry, University of Cambridge. Results were analysed using SnapGene® Viewer and BLAST® (NCBI, NIH) software.

2.1.7. DNA extraction and qPCR

DNA was extracted from an 80% confluent T75 flask of primary fibroblasts using the Wizard Genomic DNA Purification Kit (Promega, A1120), following the manufacturer's instructions. Extracted DNA was resuspended in 50µL of rehydration solution, and the concentration was measured with a NanoDrop™ Spectrophotometer (ThermoFisher Scientific). The DNA was diluted to 5ng/µL and 20ng was used per reaction. Each qPCR was set up in triplicate using TaqMan™ Gene Expression Master Mix (ThermoFIsher Scientific, 4369016) and Primers and Probes Mix (all from ThermoFisher Scientific, see **Table 2.5** for details) and quantified on the 7900HT Fast Real-Time PCR System (ABI Prism). Expression of the genes of interest was normalised to APP, RNaseP or GAPDH

levels (depending on the experimental set-up), and ΔΔCT values were expressed relative to control cell lines.

qPCR RECIPE (per reaction)		qPCR CONDITIONS		
Component	**Volume (µL)**	**Temperature**	**Time**	**Cycle**
TaqMan2x Master Mix	10	50	2mins	1
Primer and Probe Mix	1	95	10mins	1
DNA/RNA	4	95	15secs	40
ddH2O	5	60	1min	

Table 2.4 – *qPCR conditions*

Gene	ThermoFisher Scientific cat
7S	Hs02596861_s1
MT-RNR1 (12S)	Hs02596859_g1
MT-RNR2 (16S)	Hs02596860_s1
APP	Hs0239796_cn
MT-ATP6	Hs02596862_g1
MT-CO1	Hs02596864_g1
MT-CYB	Hs02596867_s1
GAPDH	Hs2758991_g1
MT-ND1	Hs02596873_s1
RNaseP	4401631

Table 2.5 – *List of primers used for qPCR and qRT-PCR*

2.1.8. RNA extraction, cDNA synthesis and qRT-PCR

RNA was extracted from an 80% confluent T75 flask of primary fibroblasts using TRIzol reagent (Invitrogen, 15596018). Cells were first washed in PBS and 2mL of TRIzol was added to the flask and incubated at room temperature for 5 minutes. Cell suspensions were split into two tubes. 200µL chloroform (Sigma, 15593031) was added to each 1mL of cell suspension, vortexed for 10 seconds, incubated at room temperature for 5 minutes, and centrifuged at 11000 RCF for 15 minutes at 4°C. The aqueous phase was transferred into a new tube and RNA was precipitated with 500µL 100% isopropanol for 20 minutes at room temperature. Then it was centrifuged at 11000 RCF for 10 minutes at 4°C. The supernatant was discarded, and the pellet was washed with 1mL of 75% ethanol and centrifuged at 11000 RCF for 5 minutes at 4°C. The supernatant was discarded, and the pellet air dried for 5-15 minutes. Finally, the pellet was resuspended in 12µL of nuclease free water, and the RNA concentration was measured with a NanoDrop™ Spectrophotometer (ThermoFisher Scientific).

4μg of RNA (in 8μL of nuclease free water) was treated with DNase using Turbo DNA-free kit (Invitrogen™, Ambion™, AM1907), following manufacturer's instructions. cDNA was synthesized using Omniscript Reverse Transcriptase Kit (Qiagen, 20511), following the manufacturer's instructions. 7.5μL of DNase-treated RNA was mixed with 15μL of Omniscript master mix. Following cDNA synthesis, 35μL of nuclease free water was added to each reaction and 4μL of diluted DNA was used for qPCR (described in **section 2.1.7.**).

Omniscript Master Mix (per reaction)	
Component	**Volume (μL)**
10x RTase buffer	2
dNTPs (5mM each)	2
random hexamer (50μM)	0.2
oligo dT	0.2
RNase inhibitor	0.25
Omniscript RTase	1
RNase free water	9.35

Table 2.6 – *cDNA synthesis*

2.1.9. shRNA constructs

The mir-30 based shRNA FBXO7 constructs are not natural human miRNA and were designed via RNAi Codex from Cold Spring Harbour Laboratories (http://cancan.cshl.edu/cgi-bin/Codex/Codex.cgi). Based on their algorithm, the chosen constructs do not have homology to other genes in the human genome and thus should not have off-target effects. Subsequently, the FBXO7 constructs were cloned into an empty mir30-based vectors (supplied from Scott Lowe's lab).

2.1.10. Primers

Primer	Sequence (5'-3')	
FBXO7 *EcoR*I forward	CG*GAATTC*TT**ATG**AGGCTGCGGGTG CGGCTTCTG	To generate CRISPR resistant plasmid (section 2.1.4)
FBXO7 *Xho*I reverse	CCG*CTCGAG***TCA**CATGAATGACAGC CGGCCATC	
CRISPR site mutant forward	GACAACGCACACATGGCTGAAGGTA CAGGTTTCTATCCCTCAGAA	
CRISPR site mutant reverse	TACCTTCAGCCATGTGTGCGTTGTC TTGAATTGACTCAGCTTCAA	
FBXO7 genotyping forward	CAGGATCAGGGAACGCCTGT	To genotype mice (section 2.1.5)
FBXO7 genotyping reverse	TGCAGGGTGAATAGCACTTCC	
Dat Cre forward	ATCCGAAAAGAAAACGTTGA	
Dat Cre reverse	ATCCAGGTTACGGATATAGT	
Floxed reverse	GAACTGATGGCGAGCTCAG	
Delta reverse	CACCGCCTACTGCGACTATAG	
Rosa26 YFP reverse	AAAGTCGCTCTGAGTTGTTAT	
Rosa26 YFP forward	GGAGCGGGAGAAATGGATATG	
Rosa26 YFP mutant forward	AAGACCGCGAAGAGTTTGTC	

Table 2.7 – *List of primers used*

*Notes: restriction sites are italicised and underlined, start (ATG) and stop (TCA) codons are in bold, and introduced silent mutations are in red.

2.2. Cell culture and assays

2.2.1. Cell lines used

Name	Type	Species	Standard Medium	Source
SH-SY5Y	Neuroblastoma, mixed	Human	DMEM, 10% FBS, Penicillin and Streptomycin	American Type Culture Collection (ATCC)
HEK293T	Embryonic kidney, adherent	Human		
U2OS	Osteosarcoma, adherent	Human		
Eco-phoenix	HEK-293 based virus packaging cell line, adherent	Human		
MEF	Primary mouse embryonic fibroblasts, adherent	Mouse		Heike Laman, Department of Pathology, University of Cambridge
P19	Teratocarcinoma, adherent	Mouse	αMEM, 10% FBS, L-glutamine, Penicillin and Streptomycin	Anna Philpott, Department of Oncology, University of Cambridge
Human fibroblasts	Patient derived primary fibroblasts	Human	DMEM with GlutaMAX-I, 20% FBS, Penicillin and Streptomycin	Jan-Willem Taanman, Institute of Neurology, University College London
	Patient derived immortalised fibroblasts	Human	DMEM with GlutaMAX-I, 10% FBS, Penicillin and Streptomycin	This study

Table 2.8 – *List of cell lines used*

2.2.2. Standard cell culture conditions

SH-SY5Y, HEK293T, U2OS, Eco-phoenix and MEF cells lines were maintained in Dulbecco's Modified Eagle Medium (DMEM) containing 4.5 g/L glucose (Gibco, 41965039) and supplemented with 10% heat-inactivated foetal bovine serum (HI-FBS) (Gibco, 10500064), 100 U/ml Penicillin and 100 µg/ml Streptomycin (Gibco 15140122).

For some experiments, SH-SY5Y cells were cultured in DMEM media containing no glucose (Life Technologies, 11966025) and supplemented with 4.5 g/L galactose (Sigma, G5388) in addition to HI-FBS and antibiotics.

P19 cells were maintained in αMEM containing nucleosides (Invitrogen, 22571-020) and supplemented with 10% HI-FBS, 100 U/ml Penicillin, 100 µg/ml Streptomycin, and 2mM L-glutamine (PAA, M11004).

Patient fibroblasts were maintained in DMEM containing 4.5 g/L glucose and GlutaMAX-I™ (Gibco, 31966-021) and supplemented with either 20% (for primary) or 10% (for immortalised) HI-FBS, 100 U/ml Penicillin and 100 µg/ml Streptomycin.

All cell lines were cultured at 37°C in a humidified 5% CO_2 incubator.

2.2.3. Transient transfections

Cell lines were transfected with 3 µL polyethylenimine (PEI; Polysciences 23966-2) for every 1µg of DNA. PEI and DNA transfection complexes were incubated in serum-free Opti-MEM media (Life Technologies, 31985062) for 15-30 minutes at room temperature. Then, the solution was added drop-wise to 60-80% confluent cells and further incubated for 24-48 hours.

2.2.4. Retroviral and lentiviral transduction

Eco-phoenix (HEK-293 based viral packaging) cells were transfected with 3µg of the appropriate short hairpin expression vector and 2µg of packaging vector (VSV-G for human cell lines or Psi for mouse cell lines). SH-SY5Y, HEK293T or U2OS cells were transfected with a short hairpin cloned into MSCV/LTRmiR30-IRES-GFP or MSCV/LTRmiR30-IRES-mCherry vectors targeting human mRNA. P19 cells were transfected with a short hairpin cloned into MSCV/LTRmiR30-IRES-GFP targeting mouse mRNA. 24 hours post-transfection, DMEM media was replaced with fresh media of the target cells to be infected. Following another 24 hours, the cell culture media containing retroviruses were filtered through a 0.45µM filter and supplemented with 4µg/mL of polybrene (Sigma, H9268) to neutralise the charge repulsion and facilitate viral uptake. This mixture was added dropwise to recipient cells and tissue culture dishes were centrifuged at 2000 RPM for 30 minutes. Infections were repeated the

following day. 48 hours post infection, cells were selected in puromycin (1-2 μg/mL depending on cell line) (Sigma, P9620) and analysed for GFP or mCherry expression by microscopy and flow cytometry. Eco-phoenix cells were periodically cultured in 300 μg/mL of hygromycin B (Lifetech, 10687010) to continue selection for the gag-pol expression vector.

2.2.5. Generating clonal lines

Clonal SH-SY5Y cell lines were generated by limited dilution cloning. Cell cultures were diluted to 1 cell per 450μL (so 1 cell per 3 wells) and seeded onto a 96 well plate. Media was added and replaced regularly. Well were continuously monitored over a period of 2 weeks and those with multiple cells were eliminated and those with single clones were picked and grown further. Clonal lines were then verified by immunoblotting.

2.2.6. Proliferation and viability assay

Cells were seeded in triplicate at a density of $2x10^5$ or $2.5x10^5$ cells/well in a 6-well plate. Cell number, viability, mean cell volumes and peak diameter histograms were noted every 2-4 days using a CASY Cell Counter (Scharfe System), an electric field cell counting system. Cell viability was determined by assaying cell plasma integrity with electric current exclusion. Cells were then re-seeded at their seeding density and this procedure was repeated over the course of 1-3 weeks. During the analyses, counted cell number was normalised to seeded cell number, converted to a $\log_2$ scale and plotted as cumulative population doublings against time.

2.2.7. Cell cycle assay (propidium iodide staining)

For cell cycle analysis by quantification of DNA content, $3\text{-}5x10^5$ fibroblasts were trypsinised, washed in PBS, and fixed in cold 85% ethanol by adding it dropwise to the cell pellet while vortexing. Cells were stored in ethanol for at least 24 hours at 4°C before staining with PI. Then, they were washed in PBS and resuspended in 0.5-1mL (depending on cell amount) PI staining solution, containing 50 μg/mL PI (Sigma, P4864) and 50 μg/mL RNase A (ThermoFisher Scientific, EN0531). Cells were incubated in PI staining solution in the dark for 20 minutes at 37°C and then analysed by flow cytometry on a Cytek DxP8 instrument at a rate of 100-200 events per second and using the BluFL2 laser.

2.2.8. Apoptosis assay (annexin V staining)

3-5x10^5 fibroblasts were stained using AnnexinV-647 (Invitrogen, A13199), according to the manufacturer's instructions. Cells were analysed by flow cytometry on a Cytek DxP8 instrument, using the RedFL1 laser. In some experiments, cells were co-stained with 2.5μg/mL PI to distinguish early apoptotic from late apoptotic cells.

2.2.9. P19 cell line differentiation

P19 cells were seeded at 1x10^6 cells onto a 100x15mm non-adhesive bacterial petri dish in αMEM supplemented with 5% HI-FBS, 100 U/ml Penicillin, 100 μg/ml Streptomycin and 0.5 μM all-trans retinoic acid (RA; Sigma R-2625). On day 2, media was replaced (with same RA concentration), and aggregates were returned to the bacterial petri dish. On day 4, media (without RA) was replaced and aggregates were placed in a tissue culture-grade petri dish. Media (without RA) was refreshed on days 6 and 8. By day 9, axonal projections were visible, and cells cultures were imaged by light microscopy and harvested for immunoblotting.

2.2.10. Primary fibroblast immortalisation

Primary human fibroblasts were immortalised using pLOX-Treg, psPAX2 (packaging), and pMD2.G (envelope) plasmids. Lentiviral vectors were produced in HEK293T cells. HEK293T cells were seeded at 2.5-3x10^6 cells per 10cm plate. On day 2, fresh media with chloroquine disulphate salt (25μM) was added to the cells 2 hours prior to transfection. One 10cm dish was transfected dropwise with complexes that consisted of 10μg pLOX-Treg, 6.55μg psPAX2, 3.5μg pMD2.G, serum-free Opti-MEM media and a 3:1 PEI-to-DNA ratio (incubated at room temperature for 30 minutes). 8-12 hours post-transfection, media was replaced with fresh DMEM. On day 4, media containing the lentivirus was collected, centrifuged at 3000RPM for 5 minutes at room temperature and filtered through a 0.45μM syringe filter. 5-8μg/mL of polybrene was added to the viral supernatant and put on the primary human fibroblasts. Media was changed 24 hours after the viral supernatant was added to the cells. Immortalisation occurred within 3 weeks of lentiviral transduction.

2.2.11. Flow cytometry of cell lines after transfection or transduction

Following transient transfection or viral transduction, the percentage of cells expressing the fluorescent constructs was determined by flow cytometry (Cyan ADP Analyser or Cytek DxP8). Voltages were set using negative and positive control cells. Cells were gated for live, single cells (using forward and side scatter, and pulse width and area respectively) and then for either GFP or mCherry expression. Data was analysed using either FlowJo(R) or Summit 4.3 software.

2.2.12. Human fibroblasts ethics statement

Ethical approval for the culturing and biochemical research of the dermal fibroblasts was obtained from the Royal Free Hospital and Medical School Research Ethics Committee (REC 07/H0720/161).

2.3. Molecular biology

2.3.1. Cell lysis (protein extraction)

Depending on the experiment, cells were lysed in RIPA, NET-N, ELB, KCL, TG or hypotonic lysis buffer, supplemented with 1x protease inhibitor cocktail (Sigma, P8340), 10mM NaF (Sigma, S7920), 1mM Na_3VO_4 (Sigma, S6508), 1mM PMSF (Sigma, 329-98-6) for 30 minutes on ice. In some experiments, the lysis buffer was also supplemented with 25mM NEM (ThermoFisher Scientific, 23030). Debris was pelleted by centrifugation at 4°C, 13000 RPM, for 20 minutes. Protein concentration was determined using BCA protein assay kit (ThermoFisher Scientific, 23225).

2.3.2. Immunoblotting

Protein samples were mixed in a 1:1 ratio with 2x Laemmli buffer and denatured by incubating at 95°C for 5 minutes. Samples that were used to detect protein expression of mitochondrial complexes were incubated in Laemmli for 30 minutes at room temperature. Protein lysates were then separated using Tris-Glycine SDS polyacrylamide gel electrophoresis (SDS-PAGE). Proteins were transferred from acrylamide gels onto polyvinylidene fluoride (PVDF) membranes (Millipore, IPVH00010) via a Trans-Blot® SD Semi-Dry Transfer Cell (Biorad). Membranes were

blocked for 1 hour at room temperature with 5% dried skimmed milk/PBS-Tween 20 (0.05%) and subsequently probed with primary antibody overnight at 4°C in 5% milk/PBS-T. After washing membranes with PBS-T, they were incubated with either donkey anti-rabbit or goat anti-mouse HRP-conjugated secondary antibody for 1 hour at room temperature. Protein levels were detected with ECL™ Wester Blotting Detection Reagent (GE Healthcare, RPN2209) or Immobilon Western Chemiluminescent HRP Substrate (Merck Millipore, WBKLS0500), and exposed onto X-ray film (Konica Minolta). ImageJ software was used for image analysis and quantification of the scanned X-ray films.

2.3.3. Co-immunoprecipitation

Cells were transfected with at least 3μg of FLAG-tagged, HA-tagged or untagged mammalian expression vector per 10cm dish. Cell were lysed 48 hours post-transfection in 500-1000μL of KLC, NET-N, or RIPA buffer (as described in section **2.3.1**). Following lysis, 50μL of the supernatant was taken for total lysate, while the remainder was incubated with beads for immunoprecipitation (IP). For an anti-FLAG or anti-HA IP, 20μL of 50% bead slurry of anti-FLAG M2 Affinity Gel (Sigma, A2220) or anti-HA Affinity Gel (Sigma, A2095) was pre-washed and incubated with the lysate for 2-4 hours, rotating at 4°C.

For co-immunoprecipitation with a specific antibody, the lysate was pre-cleared with 20μL of pre-washed Protein A/G Plus Agarose (Santa Cruz, sc-2003) for 30-60 minutes, rotating at 4°C. Afterwards, the beads were discarded and 20μL of new pre-washed A/G beads were added together with 1-2μg of the antibody or relevant IgG control. Then they were incubated for 2 hours, rotating at 4°C. Lastly, the beads were washed 4 times in 1mL of lysis buffer, resuspended in 20-40μL of 2x Laemmli buffer, and incubated at 95°C for 5 minutes. Samples were stored at -20°C if not immediately used.

2.4. Functional assays

2.4.1. Lipid droplet staining

SH-SY5Y cells were seeded at a density of 2 x 10^5 cells/well in a 6 well plate and cultured on glass coverslips coated with poly-L-lysine (0.1% (w/v) in H_2O, Sigma, P8920). Cells were fixed with 4% PBS buffered paraformaldehyde (Fisher, FOR008) for 10 minutes. Oil-Red-O stock solution contained 0.5g of ORO powder (Sigma, O0625) dissolved in 100 ml 100% isopropanol. An Oil-Red-O (ORO) working solution of 3 parts ORO stock solution to 2 parts distilled water was prepared just prior to staining. The ORO working solution was filtered with a 0.2µM syringe filter and applied on the fixed cells for 5 minutes at 37°C with gentle rocking. The coverslips were rinsed with 60% isopropanol and distilled H_2O until excess stain was removed. They were mounted with Mowiol® (Sigma, 81381) mounting media (containing 0.025mg/mL DAPI) onto glass slides and imaged using a confocal microscope (Zeiss 710), obtaining both phase contrast and red fluorescence images. Lipid droplets were quantified using the analyse-particles function on ImageJ software.

2.4.2. Free fatty acid assay

A Free Fatty Acid Assay Kit (Abcam, ab65341) was used to quantify the amount of long-chain free fatty acids in cells. 1x10^6 cells were harvested by trypsinisation and washed with ice cold PBS. They were then homogenised in 1% Triton X-100 (VWR, 9002-93-1) in pure chloroform (Sigma, 15593031) by pipetting and incubated on ice for 30 minutes. Samples were centrifuged at maximum speed for 10 minutes. The lower organic phase was collected, air dried for 30-60 minutes at 50°C in a heat-block, vacuum dried for a further 30 minutes and the dried lipid pellet was resuspended by vortexing in Fatty Acid Assay Buffer. All reagents provided with the kit were equilibrated to room temperature prior to use. All palmitic acid standards (0-10nmol/well) and experimental samples were run in duplicate. ACS (Acyl-CoA Synthetase) reagent was added to all standard and sample wells, and this mixture was incubated at 37°C for 30 minutes. Then the reaction mix (consisting of assay buffer, FA probe, enzyme mix and enhancer) was added to each well and incubated in the dark at 37°C for 30 minutes. Colorimetric output was measured (OD at 570nm) on a plate reader (BioTek, Synergy HT). Absorbance values of samples were normalized to the palmitic acid standard curve.

2.4.3. Mitochondrial respiration (Seahorse)

Oxygen consumption rate (OCR) was measured in primary fibroblasts with a XF24 extracellular flux analyser (Seahorse Biosciences, Billerica, MA, USA). A day prior to analysis (approximately 16 hours), 4-5 $x10^4$ cells were seeded in a XF 24-well cell culture microplate and incubated at 37°C with 5% CO_2. The sensor cartridge for the XF24 analyser was hydrated at 37°C for 4–12 hours before starting measurements. Cell media was replaced with pre-warmed bicarbonate-free DMEM (pH 7.2-7.4) and incubated in a non-CO_2 37°C incubator for an hour prior to the assay. After baseline OCR measurements were recorded, OCR was measured sequentially after 3 injections (final concentrations per well: 1μM oligomycin, 0.5-2.0μM CCCP, and 0.5μM of antimycinA with 0.5μM rotenone). OCR measurements were normalised to cell number, quantified by CyQUANT™ Cell Proliferation Assay Kit (ThermoFisher Scientific, C7026), and represented as pmol of O_2 per minute.

2.4.4. Biochemical analysis of mitochondrial complexes

A cell pellet of 2-3 x 10^6 primary fibroblasts was resuspended in 400μL of MRC Buffer A, containing 250mM sucrose, 20mM MOPS KOH (pH 7.4). Then 400μL of 0.2mg/ml digitonin was added, incubated on ice for 5 mins and centrifuged at 5000g for 3 minutes at 4°C. The supernatant (containing the cytosolic fraction) was discarded and the pellet was resuspended in 600μL of MCR Buffer B, containing 250mM sucrose, 20mM MOPS KOH (pH 7.4), 1mM EDTA-N_{a4}, and incubated on ice for 5 minutes and centrifuged at 10000 G for 3 minutes at 4°C. The supernatant was discarded and the digitonised pellets were either used immediately or frozen at -80°C for up to 3 months prior to analysis.

On the day of analysis, the digitonised mitochondrial pellets were snap-frozen and thawed at 37°C three times before being directly used in the enzymatic measurements. Enzyme activities of respiratory chain complexes CI, CII, CIII and CIV, and citrate synthase (CS) were measured spectrophotometrically. Briefly, CI activity was measured by recording the oxidation of NADH as the decrease in the absorbance over time at 340nm, as described in Bugiani *et al.* (2004)[339]. Samples were incubated at 30°C in a 1mM EDTA pH 7.4 solution containing 20mM KP buffer pH 8, 0.2mM NADH, 1mM sodium azide and 0.1% BSA.[339] The reaction was initiated with 50μM CoQ_1 and inhibited with 5μM rotenone.[339] CII activity was measured, by recording the absorbance at 600nm

upon reduction of DCPIP (an artificial electron acceptor) following an injection of 16mM succinate (IIa: SDH activity) and 50μM CoQ_1 (complex IIb), as described in Ragan *et al*. (1989)[340]. Prior to the reaction, samples were preincubated with 50mM KP buffer pH 7, 1.5mM KCN and 0.1mM DCPIP.[340] CIII activity was measured by recording the absorbance of cytochrome c reduction over time at 550nm, as described by Zheng *et al.* (1990)[341]. Samples were incubated with 50nM KP buffer pH 7.4, 2mM NaN_3, 1mg/mL BSA (in EDTA 10mM pH 7.4), 50mM cytochrome *c* (C7752, Sigma), and 50mM reduced decylubiquinone (DBH_2, D7911, Sigma).[341] CIV was measured, by following cytochrome c oxidation over time in 90-95% reduced cytochrome *c* (1.3mg/mL, C7752, Sigma) on 50mM KP buffer pH 7, as described in Warthon (1967)[342]. All enzymatic activities were normalized to protein levels (DC assay kit, Bio-Red) and in some cases, citrate synthase activity. CS activity measurements were based on the strategy described in Srere (1969)[343]. The reaction that CS catalyses between acetyl-CoA and oxaloacetate was combined with the generation of TNB (5-thio-2-nitrbenzoic acid) from DTNB, and the absorbance of the formed product was measured at 412 nm.[343]

2.4.5. MitoSOX staining for mitochondrial oxidative stress

3 x 10^5 cells per well were seeded in a 6 well plate. Cells were trypisinsed and stained in suspension for 10 minutes at 37°C in a 96 well plate in 100μL of 5μM MitoSOX (Life Technologies, M36008) in HBSS (Invitrogen, 24020-091) media, supplemented with calcium and magnesium (140mg/L $CaCl_2$, 100mg/L $MgCl_2$-$6H_2O$ and 100mg/L $MgSO_4$-$7H_2O$). Following staining, cells were washed three times with fresh HBSS media, resuspended in PBS and individually analysed on the Cytek DxP8 (Ex/Em 510/580nm). Cells treated with 100μM H_2O_2 (ThermoFisher Scientific, HYD005) for 45 minutes were used as a positive control for the staining. There were three technical replicates for every condition and sample. Compensation was required for co-staining MitoSOX with eGFP or mCherry (although in some cases, it was not possible to fully compensate the additional fluorescent marker).

2.4.6. MitoTracker staining (flow cytometry)

2-3 x 10^5 cells were seeded per well of a 6 well plate. The following day, cells were stained with either 250nM of MitoTracker Deep Red (ThermoFisher Scientific, M22426) or 200nM of MitoTracker Green FM (ThermoFisher Scientific, M7514) for 30 minutes at

37°C. MitoTracker Deep Red is a far-red fluorescent dye that stains polarised mitochondria, whereas MitoTracker Green stains all mitochondria regardless of membrane potential. Then, cells were trypsinised into single-cell suspension in PBS, passed through a 40μm cell strainer and analysed by flow cytometry.

2.4.7. MitoTracker staining (imaging)

2-3 x 10^5 cells were seeded on poly-L-ornithine (Sigma, P4538) and laminin (Sigma, L2020) coated glass coverslips 24 hours prior to staining. Cells were stained with 250nM-500mM of MitoTracker Deep Red (ThermoFisher Scientific, M22426) for 30-45 minutes, washed twice with fresh media and twice with PBS. Cells were fixed in 4% PBS buffered PFA for 10 minutes, washed three times with PBS and mounted with Mowiol mounting media (containing 0.025mg/mL DAPI) onto glass slides. The slides were imaged using a confocal microscope (Zeiss 710).

2.4.8. DCFDA staining for cellular oxidative stress

2-3 x 10^5 cells were seeded per well of a 6 well plate. 24 hours after seeding, cells were stained with 10μM DCFDA (2',7'-Dichlorofluorescin diacetate, Sigma, D6883) in HBSS media at 37°C for 30 minutes. DCFDA is a cell-permeable non-fluorescent probe that is de-esterified intracellularly and becomes fluorescent upon oxidation. Cells were then washed twice with fresh HBSS and twice with PBS. Cells were trypsinised into single-cell suspension in PBS and analysed with flow cytometry.

2.5. Electrophysiology

2.5.1. Brain slice preparation

The brain was extracted from Zp3-Cre *Fbxo7* knockout mice (15-16 days post-natal) into ice-cold oxygenated (95% O_2 and 5% CO_2) slicing solution containing 100mM sucrose, 52.5mM NaCl, 2.5mM KCl, 1.25mM NaH_2PO_4, 26mM $NaHCO_3$, 25mM glucose, 5mM $MgCl_2$, 1mM $CaCl_2$, and 0.1mM kynurenic acid. 280 μm thick horizontal mid-brain slices were prepared using a vibrating microslicer (Ci 700smz-2, Campden Instruments) at a cutting speed of 0.08 mm/s and frequency of 80 Hz. Prior to recording, slices recovered for at least one hour in oxygenated (95% O_2 and 5% CO_2) ACSF (artificial cerebral spinal fluid)

Ringer solution containing 119mM NaCl, 2.5mM KCl, 1.25mM NaH_2PO_4, 26mM $NaHCO_3$, 10mM Glucose, 1mM $MgCl_2$, and 2mM $CaCl_2$.

2.5.2. Patch-clamp recordings

Patch pipettes were pulled from borosilicate glass (Harvard Apparatus PG150T-7.5) to a final resistance of 2-3 MΩ using a micropipette puller (Sutter Instruments P-87). The patch pipette tip was filled with filtered internal solution containing 120mM K-gluconate, 10mM KCl, 2.8mM NaCl, 20mM Hepes, 3mM $MgCl_2$, 2mM MgATP, 0.3mM NaGTP, and 0.6mM EGTA, pH 7.2 (osmolarity: 280 mOsm). Slices were transferred into a recording chamber on an upright microscope stage (Olympus BX51WI), heated to 30°C, and continuously bathed the same oxygenated ACSF Ringer solution as during recovery (but with decreased $MgCl_2$ to 0.1mM). The patch pipette was controlled by a motorised micromanipulator (Sutter Instruments MP 285) Whole-cell recordings were made from visually identified dopaminergic neurons in the substantia nigra pars compacta (SNpc) confirmed by the presence of regular spontaneous firing and/or a hyperpolarization-activated inward current (I_h) in response to a voltage stimulation. A seal of at least 1 GΩ was made before breaking in the cell membrane. 50µM of picrotoxin was added to the ACSF Ringer solution when blocking of inhibition was necessary. Recordings were performed in voltage-clamp and current-clamp mode using a patch-clamp EPC9 amplifier (HEKA) and a CED Micro 1401 data acquisition unit. Spike2 (Cambridge Electronic Design LTD) software was used for data acquisition and analysis.

2.6. Statistics

Significance of data was analysed either using a 2-way ANOVA or a Student's T-test. Values of $p<0.05$ were considered statistically significant. The 2-way ANOVA was used when more than two groups needed to be compared.

2.7. Antibodies

Antigen	Species	Dilution	Source
FBXO7	Rabbit	1:1000	Lab made
FLAG	Mouse	1:5000	Sigma, F3165
HA	Rabbit	1:1000	CST, 3724S
T7	Mouse	1:5000	Novogen, 69522-3
Actin	Rabbit	1:5000	Sigma, A2066
GAPDH	Rabbit	1:5000	Sigma, G9545
RPL23	Rabbit	1:500	ATLAS Antibodies, HPA003373
RPL23	Rabbit	1:500	Universal Biologicals, A-305-009 A
CDK6	Rabbit	1:500	Santa Cruz Biotechnology, sc-177
Cyclin D2	Rabbit	1:500	Santa Cruz Biotechnology sc-181
Cyclin D3	Mouse	1:500	Santa Cruz Biotechnology, sc-182
TOM20	Rabbit	1:1000	Abcam, ab186734
Mouse IgG-HRP	Goat	1:10000	Santa Cruz Biotechnology, sc-2055
Rabbit IgG-HRP	Donkey	1:10000	Santa Cruz Biotechnology, sc-2313
-	Mouse IgG	-	Santa Cruz Biotechnology, sc-2025
-	Rabbit IgG	-	Santa Cruz Biotechnology, sc-2027

Table 2.9 – *List of antibodies used*

2.8. Buffers and solutions

Buffer	Components
PBS	20 mM sodium phosphate buffer pH 7.4 with 150 mM NaCl
PBS-T	PBS with 0.05% Tween 20
1xTAE	40mM Tris pH 7.6, 20 mM acetic acid, 1mM EDTA
RIPA	50 mM Tris-HCl, 150mM NaCl, 1% NP-40, 0.5% sodium deoxycholate, 0.1% SDS, adjusted to pH 7.5
2x Laemmli	120 mM Tris pH 6.8, 4 % SDS, 20 % Glycerol, 0.02 % Bromophenol Blue, 10 % β-mercaptoethanol
KCL	50 mM Tris-HCl pH 7.5, 225 mM KCl, 1% NP-40
AnnexinV binding buffer	10 mM HEPES pH 7.4, 140 mM NaCl, 2.5 mM KCl
Chelex solution	10 % chelex 100 resin (Bio-Rad), 0.1 % Tween 20, 0.1 mg/mL Proteinase K
NET-N	10 mM Tris pH 7.5, 1 mM EDTA, 0.2 % NP-40, 150 mM NaCl
Hypotonic lysis buffer	10 mM Tris, 10 mM NaCl, 2 mM EDTA, 0.5 % Triton X-100
ELB	50 mM HEPES pH7.5, 160 mM NaCl, 5 mM EDTA, 0.1 % NP-40
PI staining solution	1x PBS, 2mM $MgCl_2$, 50 µg/mL propidium iodide, 50 µg/mL RNase A
TG lysis buffer	40mM Tris pH 7.5, 150mM NaCl, 2mM EDTA, 2% Triton-X-100, 20% Glycerol, 3mM $MgCl_2$
MRC buffer A	250mM sucrose, 20mM MOPS KOH (pH 7.4)
MRC buffer B	250mM sucrose, 20mM MOPS KOH (pH 7.4), 1mM EDTA-N_{a4}

Table 2.10 – *List of buffers and solutions used*

CHAPTER 3

CHARACTERISATION OF PATIENT FIBROBLASTS AND MOUSE EMBRYONIC FIBROBLASTS LACKING FBXO7 EXPRESSION

3 – Introduction

It has been shown that rare homozygous mutations in *FBXO7* cause autosomal recessive, early-onset form of Parkinson's disease (PD), Parkinsonian-Pyramidal syndrome (PPS).[40,41,323,344,345] PPS is defined as inherited early-onset progressive parkinsonism with pyramidal tract signs.[346] However, the mechanisms by which *FBXO7* contributes to the disease have not yet been fully elucidated. An 11-year-old male patient presents with infantile onset of motor neuropathy, ponto-cerebellar hypoplasia, anaemia, and peripheral nerve damage. Furthermore, a muscle biopsy revealed that he has mitochondrial complex IV deficiency. Whole exome sequencing showed a nonsense homozygous S93X *FBXO7* mutation. The patient's attending physician, Dr. Shamima Rahman (UCL Institute of Child Health, Great Ormond Street Hospital), provided us with fibroblasts (passages 7 and 8) and two control fibroblast lines (passages 12 and 14) for characterisation. Control 1 came from a 12-year-old male whereas control 2 came from a 6-year-old male, both of whom were biopsied due to a mistaken diagnosis with a mitochondrial disorder.

FBXO7 plays an important role in mitochondrial biology. Previous research in the lab showed that *FBXO7* directly interacts with two other autosomal recessive Parkinson's disease genes, *PINK1* and *Parkin*, to mediate mitophagy under stress conditions.[320] Co-immunoprecipitation assays were used to show a direct protein-protein interaction between the N-terminal ubiquitin-like (Ubl) domain of FBXO7 and Parkin, and the amino terminus of FBXO7 and PINK1.[320] In this study, cells with decreased FBXO7 expression showed a defect in mitophagy, Mitofusin 1 ubiquitination and Parkin translocation to the mitochondria.[320] This mechanism was further supported by Zhou et al., who showed that PD-linked *FBXO7* mutations increase deleterious FBXO7 protein aggregation in mitochondria and inhibit mitophagy.[333] Another study reported that FBXO7 deficiency

results in PARP (poly ADP-ribose polymerase) activation, leading to impaired mitochondrial metabolism.[335] FBXO7 knockdown SH-SY5Y cells and patient fibroblasts with a pathogenic R378G mutation presented with complex I impairment that resulted in reduced mitochondrial respiration and increased cytosolic reactive oxygen species, leading to PARP activation.[335] Furthermore, the lab has recently identified TOM20, a mitochondrial translocase, as a substrate of FBXO7.[336] Even though SCF^{FBXO7} (SKP1-CUL1-FBXO7 E3 ubiquitin-protein ligase complex) has been shown to ubiquitinate TOM20, it seems that FBXO7 may stabilise its protein expression through a ubiquitination-independent pathway.[336] Finally, a previously conducted *FBXO7* gene expression microarray analysis in the lab revealed an increased oxidative phosphorylation signature when FBXO7 was overexpressed in murine fibroblasts (microarray described by Laman *et al.* in 2005 but OXPHOS signature was unpublished[309]). Thus, various experimental evidence suggests a neuroprotective role for FBXO7 in mitochondria, albeit via different mechanisms.

In this chapter, I first want to establish whether there is a mitochondrial defect in cells with a FBXO7 deficiency due to this novel mutation. I also want to compare findings in the primary patient fibroblasts with primary embryonic fibroblasts from a systemic *Fbxo7* knockout mouse model that the lab has generated (explained in more detail in chapter section 5.1). This mouse has a runted phenotype, shows pre-weaning lethality at 2.5 weeks of age and does not express FBXO7 like the patient. Thus, I want to examine whether or not these MEFs could be used as a model for the patient phenotypes and therefore utilised to investigate the biology of FBXO7-mediated PD/PPS.

3 – Results

3.1 – Cell cycle phenotypes of primary patient fibroblasts

Exome sequencing conducted by our collaborators, Drs. Shamima Rahman and Jan-Willem Taanman from the UCL Institute of Child Health, revealed that the patient harbours a homozygous point mutation resulting in a truncation at aa 93 (S93X). I first tested the effects of this mutation on FBXO7 expression by immunoblotting cell lysates from the patient and two control fibroblast lines. As can be seen in **Fig3.1A**, no FBXO7 expression was detected in patient fibroblasts. A noticeable phenotype of the patient fibroblasts was a slower doubling time, under standard cell culture conditions,

compared to the two controls. To quantify whether this observation was due to a slower rate of proliferation and/or increased cell death, I conducted a cell proliferation assay in which cells were seeded at equal densities and cell counts were recorded every 2-4 days. During the first proliferation assay, cells were cultured in media supplemented with 10% FBS. **Fig3.1B** shows patient fibroblasts had a negative population doubling curve, suggesting cell death exceeded cell proliferation. As growth under these culture conditions would result in a net loss of cells over time, I increased the FBS concentration to 20% which resulted in increased cell numbers. Under these conditions, patient cells proliferated 43.5% slower than the control fibroblasts at day 7, when the assay was terminated (**Fig3.1C**). In order to expand patient fibroblasts for further experiments, all primary fibroblasts were maintained in media supplemented with 20% FBS. The slower proliferation rate of the patient fibroblasts may be due to, among other things, a cell cycle defect, an upregulation of cell death, low energy production, mitochondrial dysfunction, or a combination of the above.

A decrease in cell viability might also contribute to the reduced population doubling times of the patient fibroblasts. To quantify cell death, I stained equal numbers of cells with Annexin V and propidium iodide (PI), and analysed them by flow cytometry. Annexin V detects the externalisation of phosphatidylserine on the membrane of apoptotic cells, whereas PI stains late apoptotic or necrotic cells when their membranes become compromised. Therefore, live cells are double negatives, early apoptotic cells are Annexin V positive but PI negative, and late apoptotic/necrotic cells are double positives. **Fig3.2** depicts representative flow cytometry plots of Annexin V/PI staining and the gating strategy used. **Fig3.3** shows that patient fibroblasts have significantly 3.8x more apoptotic cells compared to controls, encompassing 10.1x more early-apoptotic cells and 1.5x more late-apoptotic cells. Thus, it is possible to conclude that increased apoptosis contributes to the patient fibroblasts undergoing fewer population doublings than the controls.

To check whether cells are properly progressing through the cell cycle, I quantified DNA content and protein expression of cell cycle regulators in patient fibroblasts. PI staining in fixed cells enables the measurement of DNA content using flow cytometry. DNA content is measured as 2N diploid or 4N tetraploid, allowing to categorise cells in G_0/G_1 (2N) and G_2/M (4N) phases, with S phase being in between 2N and 4N, and cells with less than 2N as undergoing cell death. **Fig3.4** depicts representative PI flow cytometry

plots and the gating strategy used. **Fig3.5** shows that patient fibroblasts have 9.6% more cells with 2N content of DNA in the G_0/G_1 phases and 4% fewer cells with 4N content in the G_2/M phases. This suggests that fewer cells progress through the G_0/G_1 phases of the cell cycle in the patient fibroblasts line. The significant increase of cells in G_0/G_1 and decrease of cells in G_2/M phases of the cell cycle is consistent with slower cell proliferation, contributing to the observed reduction in cell number seen in the proliferation assays. Previously, it has been shown that FBXO7 acts as a scaffold for CDK6/cyclin D1 and CDK6/cyclin D3 complexes, stabilising their protein expression and promoting cell cycle progression in immortalised fibroblasts.[308,309] Thus, the lack of FBXO7 in the patient cells may directly affect CDK6/cyclin D1 complex formation, which may be the reason for patient fibroblasts having increased numbers of cells in G_0/G_1 phases of the cell cycle and a slower proliferative rate. To test this, I immunoblotted cell lysates from patient and control fibroblasts for these G_1 phase cyclins and CDK6. **Fig3.6A** shows that patient fibroblasts express 87% less CDK6 compared to both control lines, suggesting that decreased CDK6 may be responsible for their reduced proliferative rate. With regard to D-type cyclins, patient fibroblasts have 77% less cyclin D1 (CCND1) and showed no differences in cyclin D2, cyclin D3 or p21 expression (**Fig3.6B**). It has been previously shown that fibroblasts predominantly express and utilise cyclin D1 for proliferation, and that upon deletion of cyclin D1, cyclin D2 expression levels can be increased.[347–349] However, it appears that upregulation of cyclin D2 upon CDK6 downregulation was not a compensatory mechanism utilised in these cells. Thus, patient fibroblasts express less CDK6 and its activator, cyclin D1, which can hinder proliferation. In the future, it would be also interesting to investigate whether patient fibroblasts are undergoing senescence earlier than the controls, which might also explain their lack of proliferation.

Overall, these results show that patient fibroblasts proliferate slower possibly due to increased apoptosis and fewer cells progressing through the G_0/G_1 phase of the cell cycle, which was likely to be due to the lower levels of CDK6 in these cells. These results concur with FBXO7 having an important role in regulating the cell cycle in patient fibroblasts.

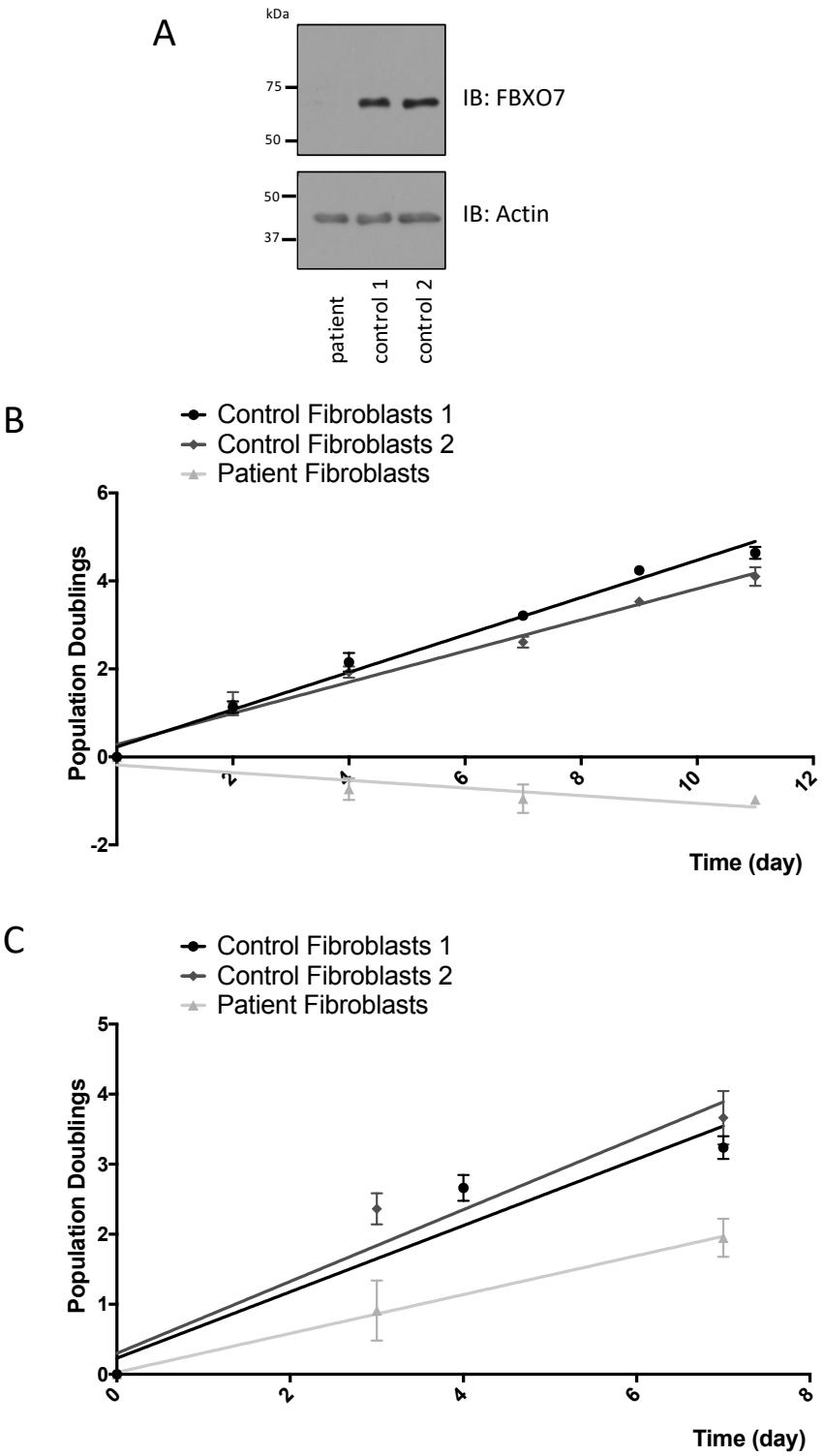

Figure 3.1 – FBXO7 expression and proliferation assays. (A) Representative immunoblot showing that patient fibroblasts do not express FBXO7 (n=4). (B) Patient fibroblasts proliferate slower (at day 11) compared to two control fibroblast lines (grown in DMEM supplemented with 10% FBS). Cells were re-seeded in duplicate at 2.5 x 10^5 cells per well every 3-4 days and the population doubling rate was determined (n=1). (C) Improved growth rate of patient fibroblasts when grown in DMEM supplemented with 20% FBS, but still 43.5% (at day 7) slower compared to control fibroblasts (n=1). Data points represent the mean, error bars represent ±SD.

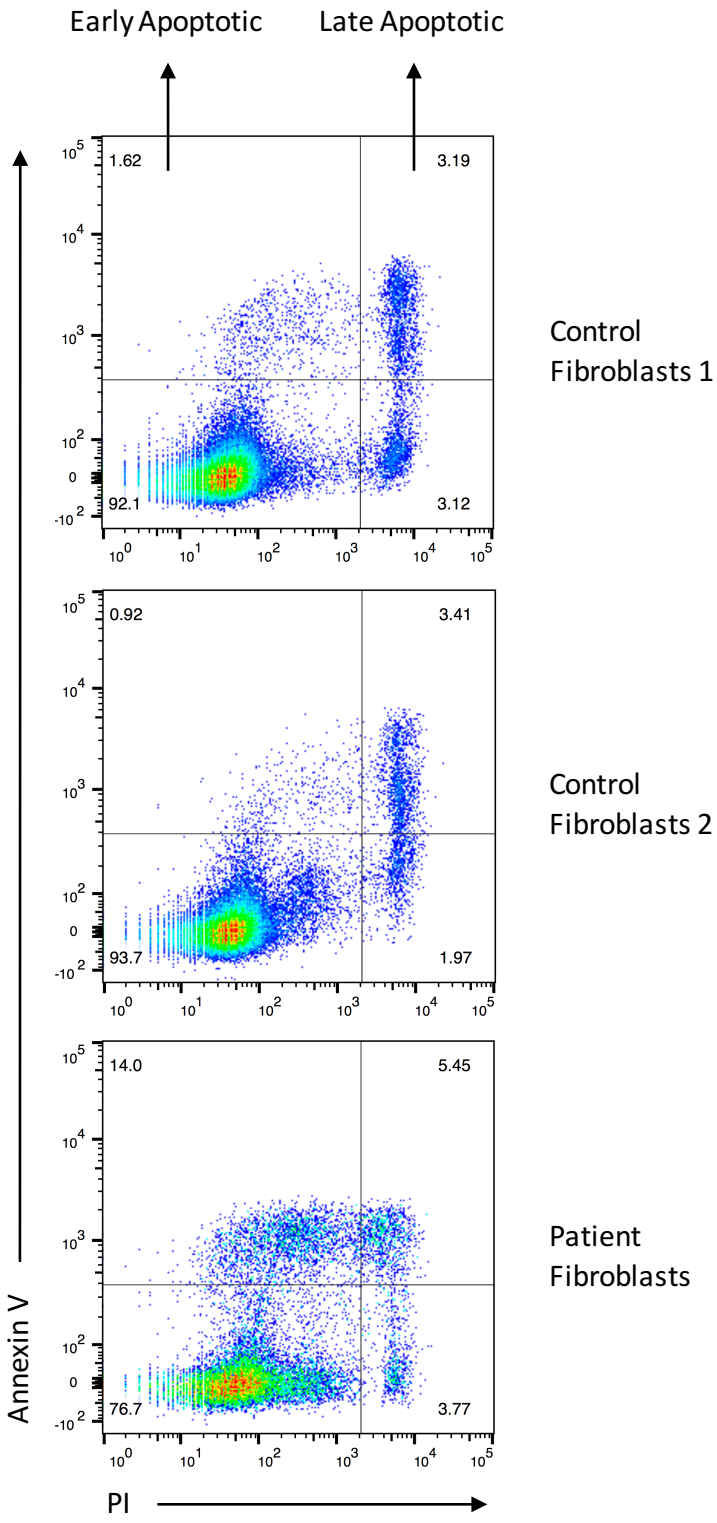

Figure 3.2 – Apoptosis assay (gating strategy). Representative plots of cells co-stained with Annexin V and PI, and analysed by flow cytometry. Early apoptotic cells are Annexin V positive, but PI negative. Late apoptotic cells are Annexin V and PI double positives.

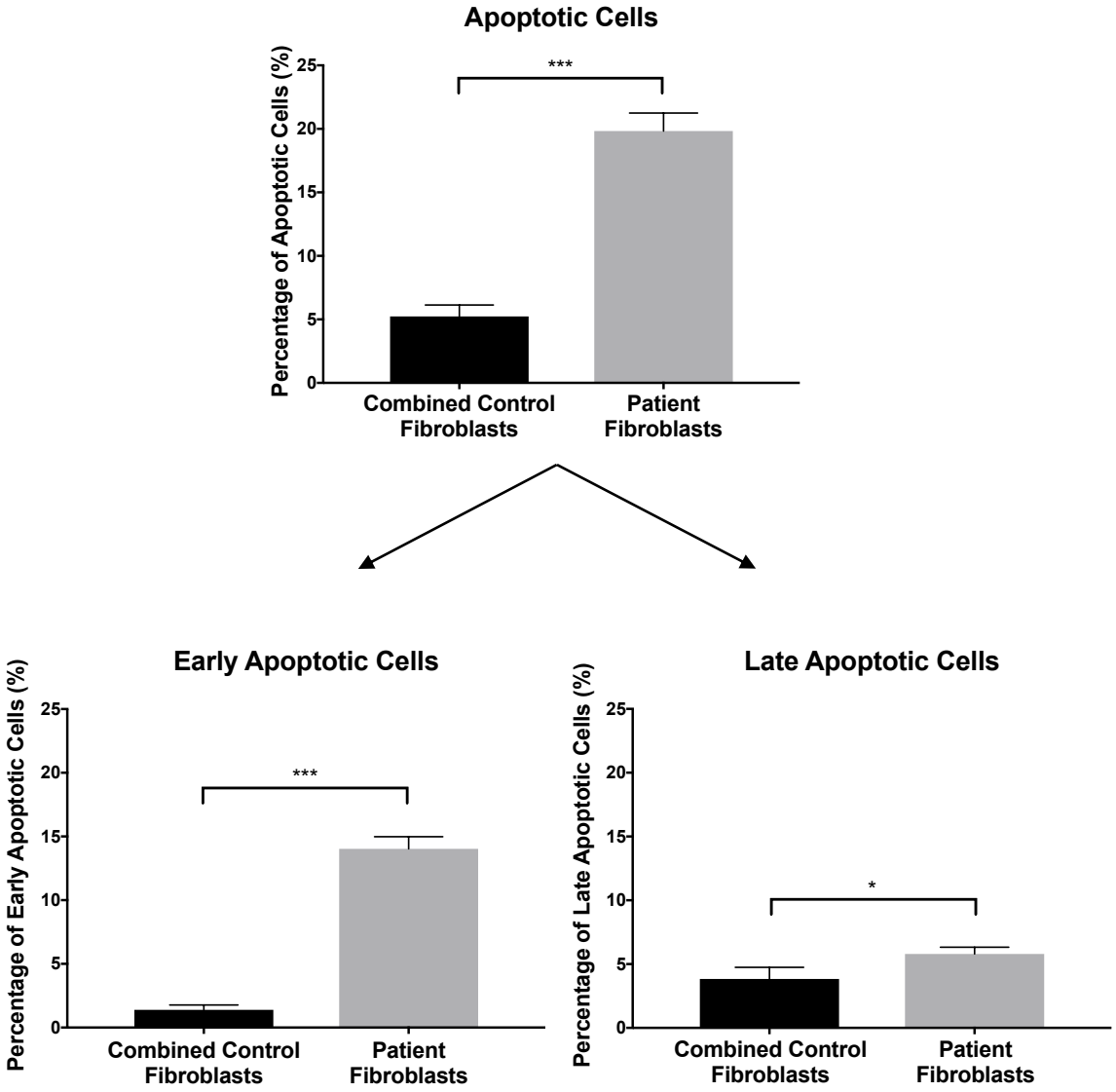

Figure 3.3 – Apoptosis assay. Patient fibroblasts have 3.8x more apoptotic cells compared to control cell lines, which includes 10.1x more early apoptotic cells and 1.5x more late apoptotic cells. The experiment differentiating between early and late apoptotic cells was observed twice (n=2), whereas the overall increased apoptotic phenotype was observed three times (n=3). Data points represent the mean and error bars represent ±SD. *p<0.05, ***p<0.001

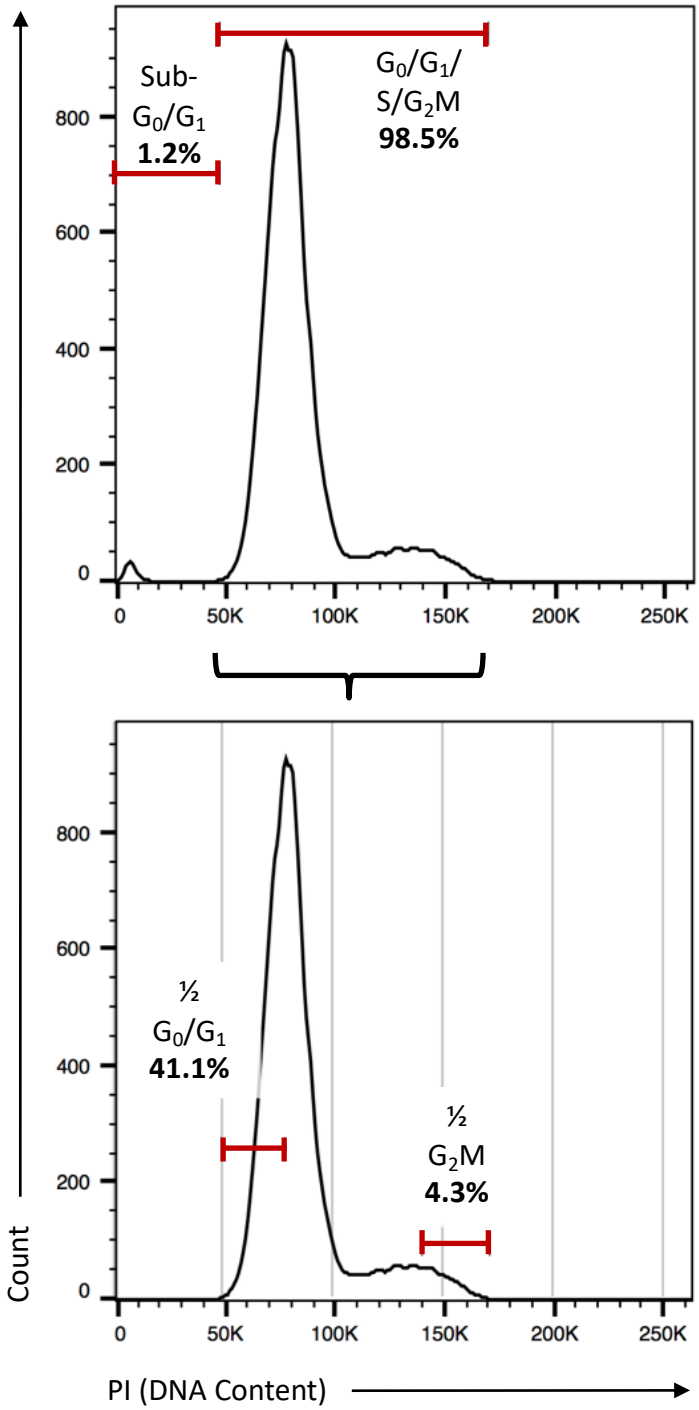

Figure 3.4 – DNA content analysis (gating strategy). Representative plots of cells stained with PI and analysed by flow cytometry. PI staining in fixed cells enables the differentiation of cells in G_0/G_1, S and G_2M phases of the cell cycle. DNA content is measured as 2N diploid or 4N tetraploid, allowing to categorise cells in G_0/G_1 (2N) and G_2M (4N) phases, with S phase being in between 2N and 4N. The gating strategy (red) involved quantifying half of the population (from the edge to the middle of the peak) and then doubling the obtained percentage.

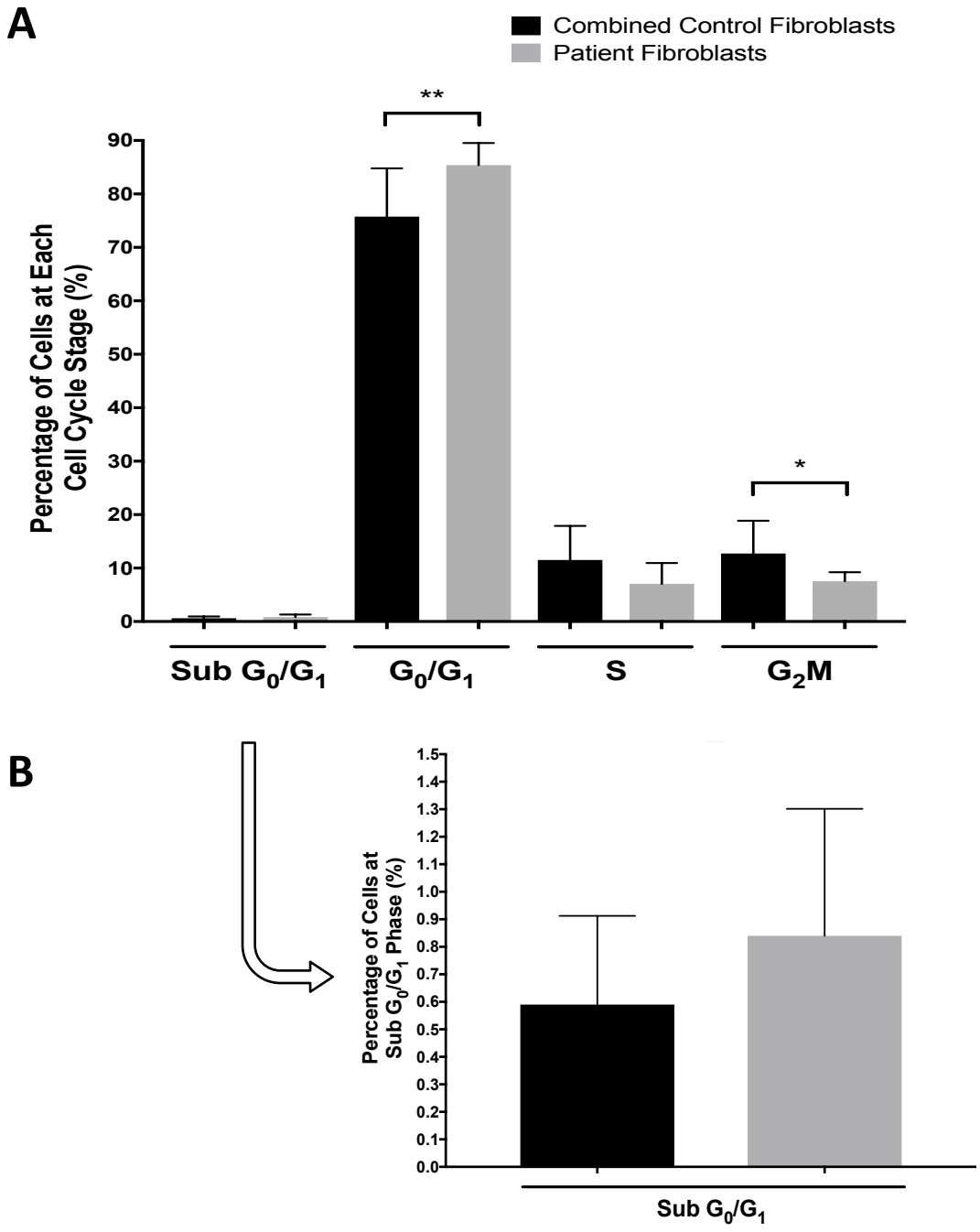

Figure 3.5 – DNA content assay. (A) Patient fibroblasts have 9.6% more cells in G_0/G_1 phase and 4% fewer cells in G_2M phase. (B) Zoomed-in section of the graph showing the percentage of cells in the Sub-G_0/G_1 phase of the cell cycle. (n=3) Data points represent the mean and error bars represent ±SD. *p<0.05, **p<0.01

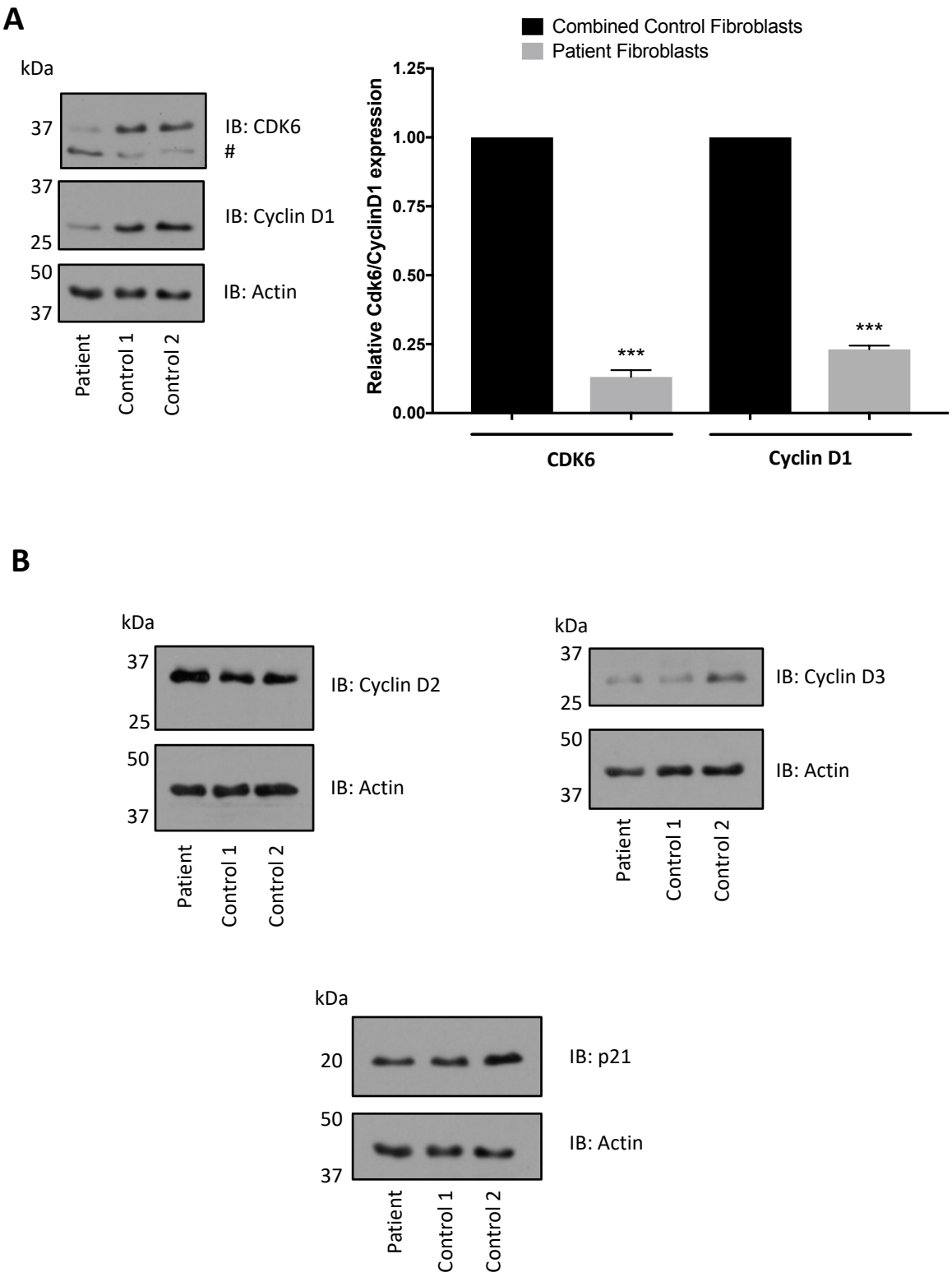

Figure 3.6 – Protein expression of cell cycle regulators. (A) Representative immunoblot showing that patient fibroblasts express 86.9% less CDK6 and 76.9% less cyclin D1. Expression levels were normalised to actin as the loading control and calculated relative to the fibroblast control cell lines (n=2). (B) There were no differences in the expression of cyclin D2, cyclin D3 or p21 (n=1). Data points represent the mean and error bars represent ±SD. # denotes a non-specific band or degradation product. *** $p<0.001$

3.2 – Mitochondrial dysfunction in primary patient fibroblasts

Our collaborators indicated that muscle tissue from this patient showed a mitochondrial complex IV deficiency. In addition, a previous study reported complex I deficiency in both SH-SY5Y FBXO7 KO cells and patient fibroblasts harbouring a R378G pathogenic mutation.[335] As each cell type and tissue has different energy demands and thus a specific oxidative phosphorylation capacity and mitochondrial characteristics,[350] I assayed mitochondrial function in these primary fibroblasts.

To begin assessing mitochondrial function, I evaluated respiration using the Agilent Seahorse XF Cell Mito Stress Test, which directly measures the oxygen consumption rate (OCR) of intact cells using endogenous substrates. Sequential injections of a complex V inhibitor, an uncoupling agent and complex I and complex III inhibitors onto the cells enables measurements of basal respiration, ATP production, maximal respiration, spare capacity, proton leak and non-mitochondrial respiration (**Fig3.7**). In brief, basal respiration relates to the energetic demand of the cell under baseline conditions, encompassing both oxygen consumption to meet ATP demand and that resulting from the proton leak. Thus, when oligomycin inhibits complex V (ATP synthase), the OCR is decreased by the amount that was being used to drive ATP production. The proton leak is the remaining basal respiration that is not coupled to ATP production. CCCP uncouples oxygen consumption from ATP production by making the mitochondrial inner membrane completely permeable to protons. It increases oxygen uptake, stimulating the respiratory chain to operate at maximum capacity and thus increasing the OCR. The spare respiratory capacity is the difference between the basal respiration and the maximum capacity and is an indicator of how well a cell can respond to an increased energy demand. Lastly, rotenone inhibits complex I and antimycin A inhibits complex III, thus preventing all mitochondria-dependent respiration and decreasing the OCR to the minimum. This results in the measurement of non-mitochondrial respiration, which is then subtracted from all previous measurements so that only the OCR that is dependent on mitochondria is analysed.

I conducted this analysis on 5 x 10^4 patient fibroblasts compared to both control fibroblast lines. **Fig3.8** shows a representative graph of the OCR per 1000 cells over time. I observed that when compared to two control lines averaged together, the patient fibroblasts have significantly lower basal respiration (65% reduction), ATP production

(70.3% reduction), maximal respiration (56.6% reduction) and spare capacity (46.7% reduction). There was no significant difference in the proton leak. In summary, patient cells show lower overall oxygen consumption as well as less respiration dedicated to ATP production, which is also significantly reduced. Therefore, this experiment indicates that the mitochondria in patient fibroblasts have a defect in the mitochondrial oxidative phosphorylation (OXPHOS) system, which is not functioning as efficiently as in the controls.

Subsequently, I checked whether a decrease in total mitochondrial mass in the patient fibroblasts could provide a reason for their reduced respiration. Thus, I immunoblotted for steady-state levels of citrate synthase (CS) that is routinely used as a marker of mitochondrial mass. CS is an enzyme that catalyses the first reaction of the TCA cycle. It is localised within the mitochondrial matrix and is encoded by nuclear DNA. **Fig3.9** shows that patient fibroblasts express 55.7% less citrate synthase compared to controls, indicating that they may have fewer mitochondria or impaired TCA cycle progression, both of which would contribute to a reduction in mitochondrial respiration. Importantly, due to this significant difference in CS expression between patient and control fibroblasts, I decided it was not reliable to use CS activity as a value to normalize mitochondrial samples in further mitochondrial respiratory chain complex activity experiments. Similar to CS, TOM20 is also encoded by nuclear DNA and used as a mitochondrial marker for quantification. However, as previously mentioned, TOM20 is also a substrate of FBXO7, which stabilises its protein expression.[336] This relationship is confirmed as patient fibroblasts lacking FBXO7 have a 50% reduction of TOM20 expression (**Fig3.9**), which is also a similar level of reduction as for CS. As TOM20 is involved in the import of nuclear-encoded mitochondrial proteins, its decreased levels may result in OXPHOS impairment and reduced replication, transcription and translation of mitochondrial DNA in general. However, these pathways will be differentially affected, for instance, due to varying protein half-lives.

Due to patient cells exhibiting more apoptosis in culture, I also immunoblotted for VDAC1 (voltage-dependent anion-selective channel 1), a nuclear encoded protein that forms an ion channel in the outer cell and mitochondrial membranes. In mitochondria, it enables ATP diffusion out of the organelle, maintaining cell metabolism and cell death.[351,352] Over-expression or dysregulation of VDAC1 can lead to apoptosis, and it is used as a marker of mitophagy.[353] One interpretation is that as there is no change in

VDAC1 levels, there is probably no significant difference in mitophagy levels in the patient fibroblasts. However, as the other two mitochondrial markers (CS and TOM20) are reduced, the unchanged levels of VDAC1 may also suggest that it is actually twice as high as it should be relative to mitochondrial mass. And this may be indicative of mitophagy upregulation. To establish whether the absolute or relative VDAC1 levels should be considered requires further experiments, such as immunoblotting for LC3B (MAP1LC3B, microtubule associated protein 1 light chain 3 beta) and p62 levels.

Next, I immunoblotted for mitochondrial complex proteins to see if a decrease in their expression could explain the less efficient mitochondria of the patient. Patient and control samples were independently assayed twice for the expression of various proteins from the electron transport chain (ETC). Patient fibroblasts expressed 33% less of ATP5A (complex V subunit) and 86.1% less of SDHB (complex II subunit), whereas UQCRC2 (complex III subunit), MT-CO1 (complex IV subunit) and MT-CO2 (complex IV subunit) expressions were unchanged compared to the controls (**Fig3.9**). It was not possible to obtain a signal in patient or control samples for neither NDUFS3 nor NDUFB8 (complex I subunits). The decreased protein expression of complex II and V subunits suggests that complex formation may be compromised, and they may not be functioning at their regular capacity. Complex II functions in a parallel ETC pathway to complex I, which does not involve proton transport and therefore contributes less energy to the overall respiration process. Thus, it seems that the lower expression of a complex V subunit may have more impact as it is responsible for ATP synthesis from the proton gradient generated by complexes I, III and IV, and this can have a substantial effect on overall mitochondrial respiration. Each mitochondrial complex is composed of multiple subunits, and the fact that there was no difference in expression of complexes III and IV in this immunoblot does not eliminate the possibility that expression of other subunits may have been affected.

As I discovered that patient fibroblasts had reduced mitochondrial respiration and lower expression of mitochondrial respiratory chain (MRC) complex subunits II and V, I subsequently measured the specific activities of MRC complexes I-IV to see whether their deficiency could be contributing to the observed phenotypes. This assay relies on spectrophotometric measures of the reaction kinetics of NADH dehydrogenase (complex I), succinate dehydrogenase (complex II), DBH_2:cytochrome c oxidoreductase (complex III), and cytochrome c oxidase (complex IV). **Fig3.10** shows two independent repeats of

specific activity measurements normalised to total mitochondrial protein levels, with each measurement conducted in duplicate. The specific activity of complex I was decreased by 70.7% on average across two independent experiments, which was measured by recording the oxidation of NADH as the decrease in the absorbance over time. This reaction was initiated with CoQ_1 and inhibited with rotenone. The specific activity measurements of complex II were inconsistent between the two repeats, possibly due to the very low levels of SDHB protein expression. Complex II was measured by recording the absorbance upon reduction of DCPIP (an artificial electron acceptor) following an injection of succinate (IIa: SDH activity) and subsequent addition of CoQ_1 to the reaction (complex IIb). The specific activity of complex III was decreased by 75.3%, which was measured by recording the absorbance of cytochrome c reduction over time. Lastly, the specific activity of complex IV was also reduced by 72.3%. This was measured by adding 90-95% reduced cytochrome c to the reaction and following its oxidation over time. Thus, the specific activities of complexes I, III and IV were lower in the patient fibroblasts in both biological replicates, and in agreement with the reduced respiration capacity seen in the Seahorse assay. The fact that there was a decrease in activity of complexes III and IV, despite there being no difference in protein expression of one of their subunits, implies that either other subunits were affected or that there might rather be a defect in their assembly to form fully functional complexes.

As *FBXO7* mutant patient fibroblasts show significantly lower activities in ETC complexes with subunits encoded by mitochondrial DNA (complexes I, III and IV), I hypothesised that mitochondrial DNA replication and/or expression of these genes could be affected as a result of reduced import of mtDNA regulatory factors. To test this possibility, I quantified mitochondrial DNA copy number, which was normalised to genomic DNA. qPCR analysis (**Fig3.11A**) of three mtDNA genomic regions corresponding to the coding sequences of MT-ND1, MT-CO1 and MT-RNR2, were compared to the amount of two nuclear encoded genes, APP and RNaseP. MT-ND1 (ND1, NADH-ubiquinone oxidoreductase chain 1) is a subunit of respiratory complex I, and MT-CO1 (CO1, cytochrome c oxidase I) is the main subunit of respiratory complex IV. MT-RNR2 (16S ribosomal RNA) is a mitochondrial homologue of the eukaryotic nuclear 28S ribosomal RNA. The copy number of these mitochondrially-encoded genes was compared to either genomic APP (amyloid precursor protein), an integral membrane protein, or RNaseP (Ribonuclease P), a ribozyme. Subsequently, ratios were calculated

relative to control 1 fibroblast values. For all three mitochondrial genes tested (MT-ND1, MT-CO1, and MT-RNR2), there was a 2.0-, 2.2- and 2.1-fold increase respectively compared to either of the genomic DNA sequences. Taken together, the patient fibroblasts have at least two-fold more mtDNA than the control fibroblasts. A previous study has shown that there is a positive and significant correlation between mtDNA copy number and mitochondrial mass as quantified by CS activity, and with respiratory capacity as quantified by complex IV activity.[354] Thus, this data may suggest that the patient fibroblasts have an increase in mitochondrial mass compared to the control cells, but it will need to be verified by other methods. Due to the disparity between the two-fold increase in mtDNA levels and the reduced respiration levels, I next looked at the amount of polarised mitochondria. Based on increased mtDNA, it may be possible to hypothesise an increase in mitochondrial load. However, the decreased respiration would rather suggest a potential decrease in the amount of polarised mitochondria and/or an abnormal mitochondrial network. Flow cytometry analysis of MitoTracker Deep Red staining revealed that patient fibroblasts have more mitochondria that maintain a membrane potential. **Fig3.11B** shows a 1.9x increase of mitochondrial load in the patient fibroblasts compared to controls. One explanation for these data is that there might be an increase of mitochondria in an attempt to compensate for their decreased respiration level and complex activities. However, despite this increase, patient cells still have mitochondrial respiration defects, suggesting that the mitochondria are not functioning properly.

I next investigated whether despite having twice the amount of mtDNA, deficiencies in mitochondrial gene expression might account for the observed defects in respiration. To test this, I used qRT-PCR to look at mRNA levels of mitochondrial ribosomal genes and genes encoding mitochondrial ETC complexes (**Fig3.12**). The qRT-PCR values were normalised to GAPDH, and calculated relative to control 1 fibroblasts. I analysed the transcripts in two ways, either by looking at their absolute amount (number of transcripts per cell) or their relative amount compared to the amount of mtDNA present. When looking at absolute mRNA levels (**Fig3.12A**), patient fibroblasts showed no difference in the absolute mRNA levels of the mitochondrially-encoded complex subunits MT-ND1 (complex I), MT-CYB (complex III), MT-CO1 (complex IV), or MT-ATP6 (complex V). Complex II is the only complex that is entirely composed of nuclear encoded subunits, and was therefore not included in the qPCR analysis. Although these

complexes were unchanged, significantly decreased levels of mRNA transcripts were observed for MT-RNR1 (35% reduced), MT-RNR2 (36.2% reduced) and 7S RNA (56.2% reduced). MT-RNR1 (12S RNA) and MT-RNR2 (16S RNA) are mitochondrially-encoded components of the small and large subunits of the mitochondrial ribosome respectively. 7S RNA is a poly-adenylated transcript which terminates near the 5' end of the nascent D-loop strand and has been proposed to be involved in the synthesis of 7S DNA (D-loop strand).[355] It has also been used as a measure of transcription levels from the light strand promoter (LSP).[355] Such a significant decrease in ribosomal transcripts would be expected to affect the function of the mito-ribosome, and therefore impact translation of mitochondrially-encoded transcripts including those of the ETC complex subunits.

When the data quantifying the amount of mRNA was normalized relative to the increase in mtDNA seen in the patient fibroblasts, the differences in mRNA expression levels became more pronounced. When calculated this way, the decrease in transcript levels of MT-CO1 (complex IV) became statistically significant (**Fig3.12B**) and supported the finding of decreased complex IV activity in muscle tissue from the patient and in the patient fibroblasts. Taken together, patient fibroblasts showed increased mtDNA copy number, yet lower levels of MT-RNR1 (12S RNA) and MT-RNR2 (16S RNA) ribosomal mRNA transcripts and similar levels of mRNAs encoding structural subunits, indicating a deficiency in mitochondrial transcription. Moreover, MT-RNR1 and MT-RNR2 are necessary for the translation of mitochondrially-encoded subunits of complexes I, III, and IV. And this may explain why I observed significant deficiencies of complexes I, III and IV, but not of complex II whose subunits are nuclear encoded. However, I also observed reduced SDHB protein levels (**Fig3.9**) and subtle decreases in complex II activity (**Fig3.10b**), which might be attributed to impaired protein import due to decreased TOM20 levels.

My results suggest that mitochondrial transcription is impaired when FBXO7 is mutated. Previous screens in the lab for proteins that interact with FBXO7 discovered TEFM (transcription elongation factor of mitochondria) as a FBXO7 target. TEFM is a co-factor that positively regulates mitochondrial genome transcription by interacting with mitochondrial RNA polymerase (POLRMT).[356] Previous studies have shown that inactivation of TEFM results in downregulation of H- and L-strand promoter-distal mitochondrial transcripts, leading to respiratory defects.[97] I therefore tested whether there were changes in TEFM levels in the patient fibroblasts. Immunoblotting of cell

lysates shows that there is 44.8% reduction of TEFM protein in the patient fibroblasts (**Fig3.13**). The decreased expression of TEFM in patient fibroblasts suggests a positive regulatory relationship between FBXO7 and TEFM. This interaction may explain the reduced transcription of mitochondrial DNA observed in the patient's cells lacking both FBXO7 and TEFM.

The experiments undertaken here characterise a number of phenotypes in this patient's cells which may be attributed to the loss of FBXO7 expression. These include a reduced doubling time of the cells in culture due to a slower proliferative rate and increased apoptosis. Mechanistically, this is due to lower CDK6 expression and likely its activity, which results in more cells being in the G_0/G_1 phase of the cell cycle. The observed mitochondrial respiration defects may also contribute to the slower proliferative rate of the patient fibroblasts. Patient fibroblasts exhibit lower basal respiration, ATP production, maximal respiration and spare capacity, associated with complex I, III and IV deficiencies. They also have approximately twice the amount of mtDNA, yet lower levels of two ribosomal RNA transcripts. This suggests a deficiency in relative expression of mitochondrial RNAs, possibly related to decreased TEFM expression. This may also affect mitochondrial protein expression, accounting for the complex I, III and IV specific-activity defects. Apart from lower rRNA expression, these cells also have significantly lower levels of the mitochondrial CO1 transcript, which could further contribute to decreased complex IV levels. These results suggest that FBXO7 impacts mitochondria in many ways, including playing a role in mitochondrial DNA expression. Moreover, the observed increase in mtDNA copy number and polarised mitochondrial load suggests multiple downstream compensatory effects for the overall reduced respiration rate in these cells. Direct interactions with mitochondrial proteins like TOM20 and TEFM imply global effects on mitochondrial gene expression and protein import will be among the most upstream effects of FBXO7 on mitochondrial biology.

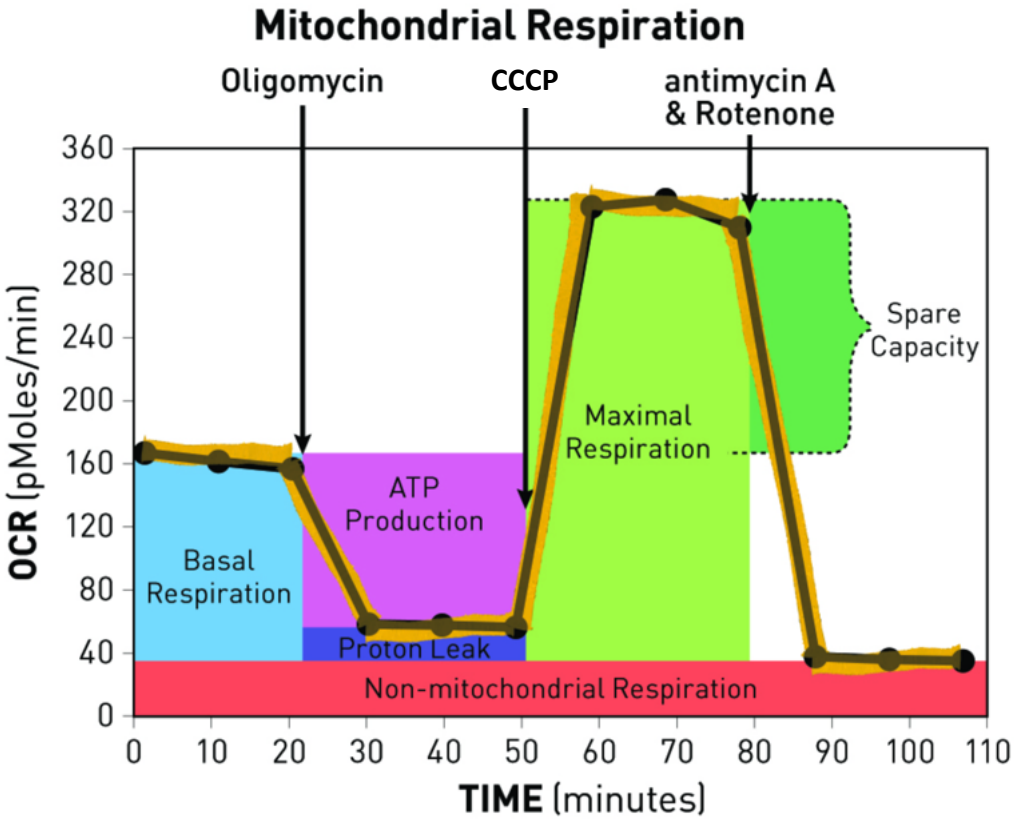

Figure 3.7 – Schematic representation of the oxygen consumption rate (OCR) measured by the Agilent Seahorse XF. It depicts how basal respiration, ATP production, maximal respiration, spare capacity and proton leak are calculated from the OCR time course measurements. Figure adapted from Agilent Seahorse XF Cell Mito Stress Test Kit User Guide.

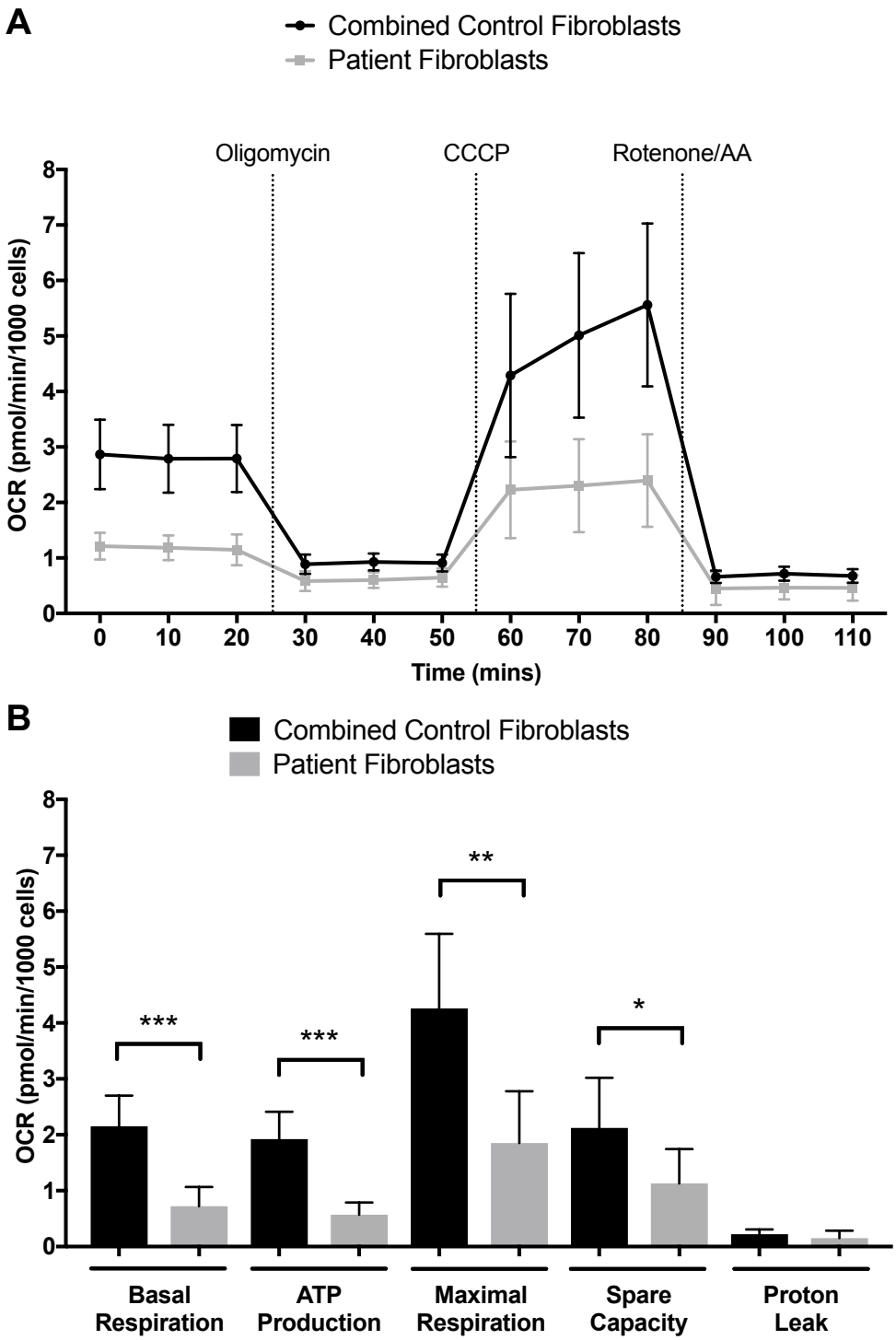

Figure 3.8 – Mitochondrial oxygen consumption rate. (A) OCR following 3 injections of Oligomycin, CCCP and Rotenone/Antimycin A. Representative plot showing that patient fibroblasts (8 technical replicates(have lower mitochondrial respiration compared to combined control fibroblasts (each measured from 6 technical replicates). The amount of cells was quantified post-measurement, which was used to normalise values per 1000 cells. (B) Basal respiration (down 65%), ATP production (down 70.3%), maximal respiration (down 56.6%), spare capacity (down 46.7%) and proton leak (no significant difference) were calculated as shown in the previous figure. These phenotypes were repeated in another biological replicate (n=2). Data points represent the mean and error bars represent ±SD. *p<0.05, **p<0.01, ***p<0.001

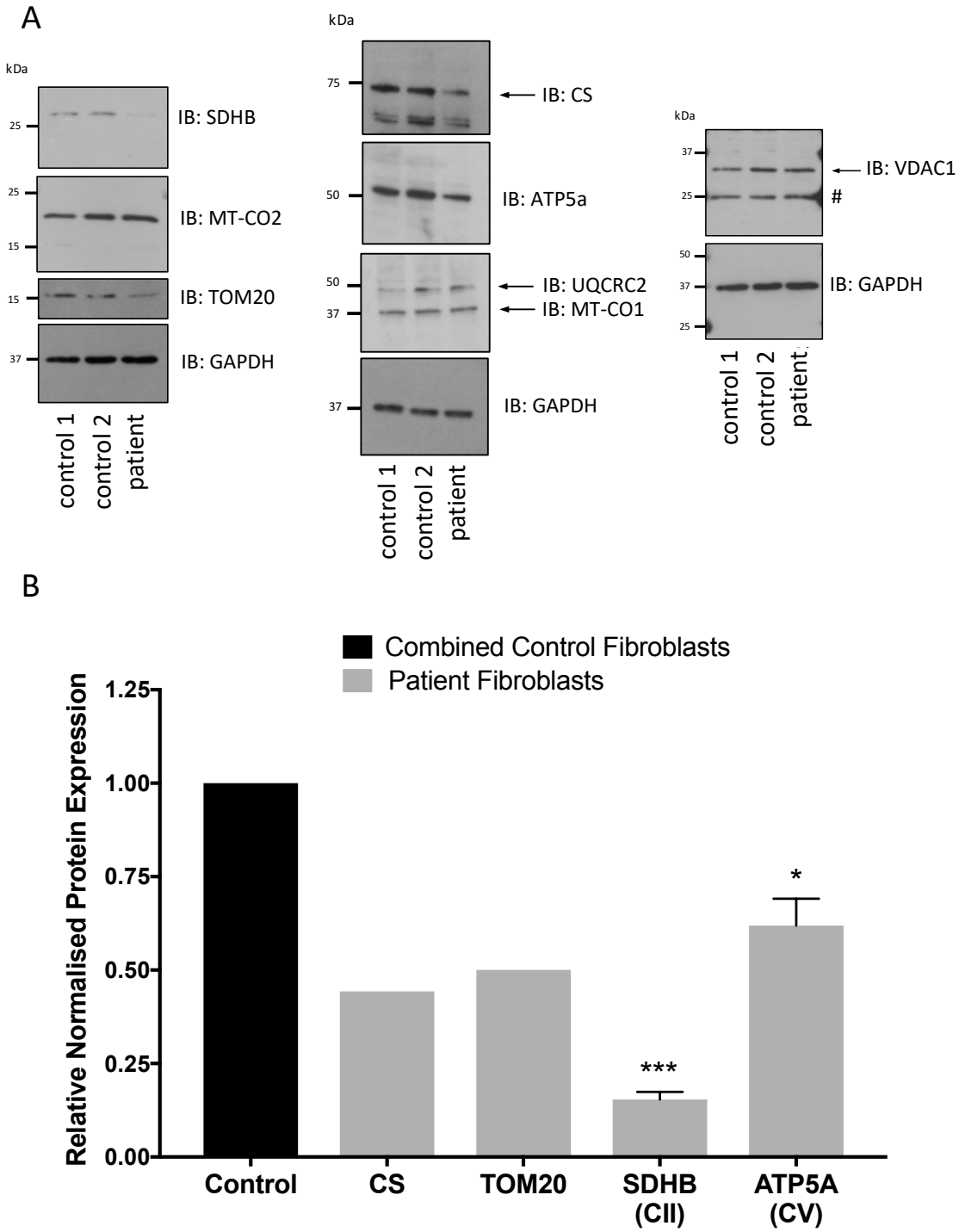

Figure 3.9 – Protein expression of mitochondrial markers and MRC complex subunits. (A) Immunoblots showing lower expression of SDHB, TOM20, CS, and ATP5A in the patient fibroblasts. There was no significant difference in the expression of MT-CO2, UQCRC2, MT-CO1 and VDAC1 between patient and controls. (B) Expression levels were normalised to GAPDH and calculated relative to the combined controls. There was lower expression of CS (down 55.7%, n=1), ATP5A (down 33%, n=2), SDHB (down 86.1%, n=2), and TOM20 (down 50%, n=1) in the patient fibroblasts. Error bars represent ±SD. # represents a non-specific band. *p<0.05, ***p<0.001

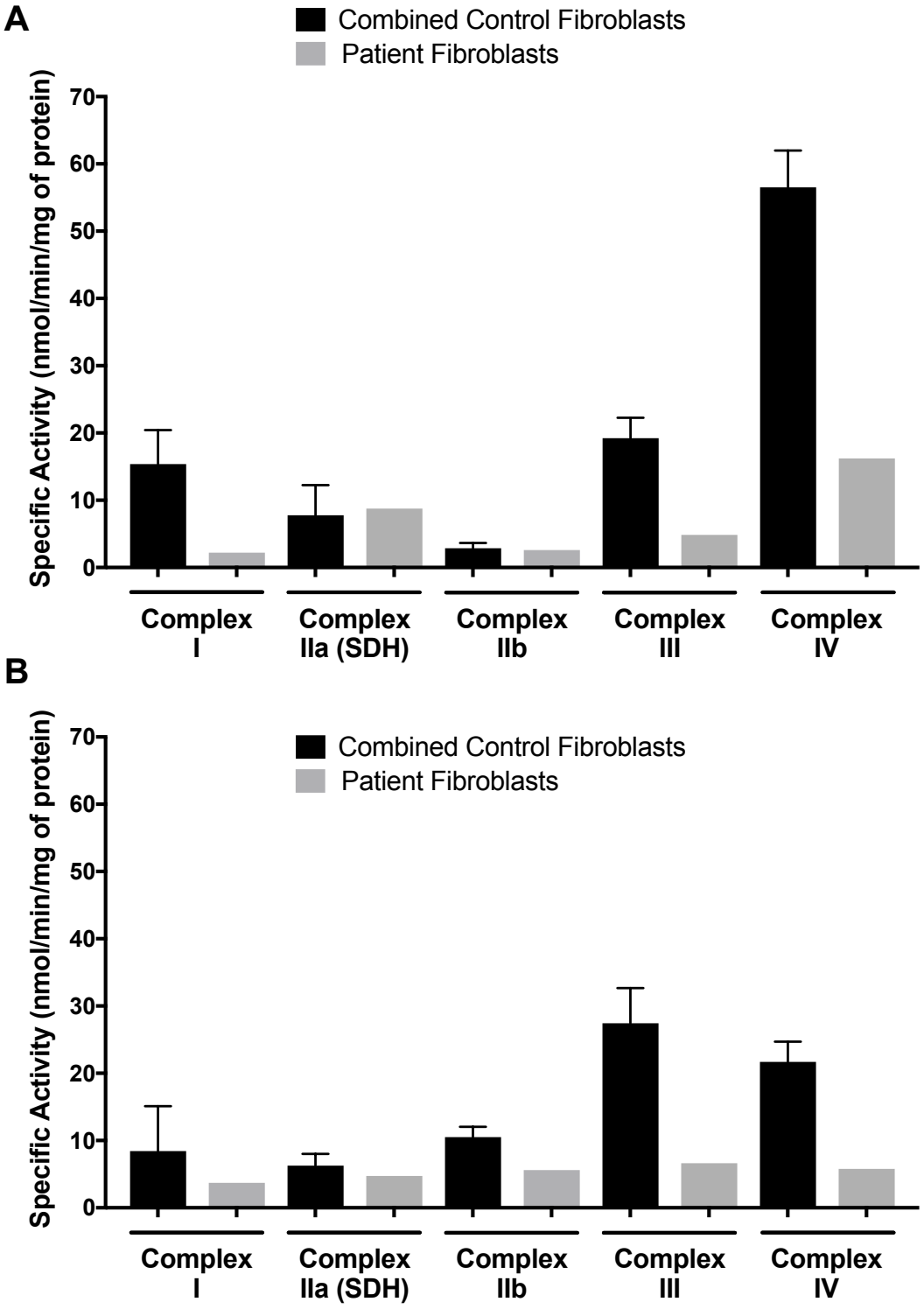

Figure 3.10 – Mitochondrial enzymatic activity of complexes I–IV normalised to protein concentration. (A) MRC specific activities (nmol/min/mg of protein) in isolated mitochondria from patient and control fibroblasts. Patient fibroblasts exhibit lower specific activity of complex I (down by 85.6%), complex III (down by 74.8%), and complex IV (down by 71.3%). (B) A biological repeat of the assay, confirming lower activities of complex I (down by 55.8%), III (down by 75.8%), and IV (down by 73.3%) in the patient fibroblasts. Data points represent the mean and error bars represent ±SD.

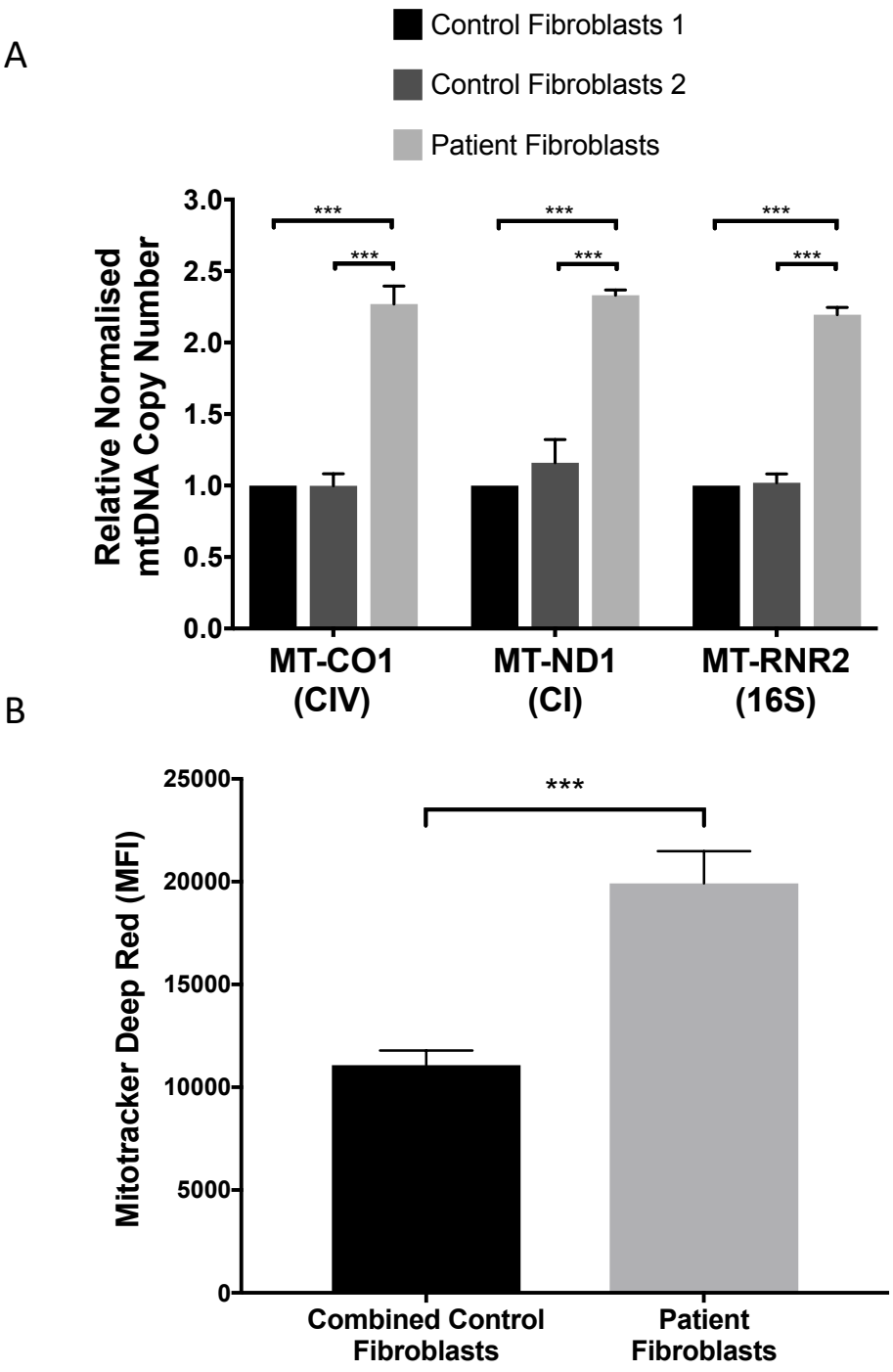

Figure 3.11 – mtDNA copy number and polarised mitochondrial load. (A) DNA expression analysis of mitochondrial genes quantified by qPCR, normalised to the amount of APP or RNaseP gene transcripts, and expressed as fold variation to Control 1. Patient fibroblasts have 2.1x more mtDNA (B) Amount of polarised mitochondria, stained with MitoTracker Deep Red and quantified by flow cytometry. Patient fibroblasts have 1.9x more polarised mitochondria. (n=2) Data points represent the mean and error bars represent ±SD. ***p<0.001

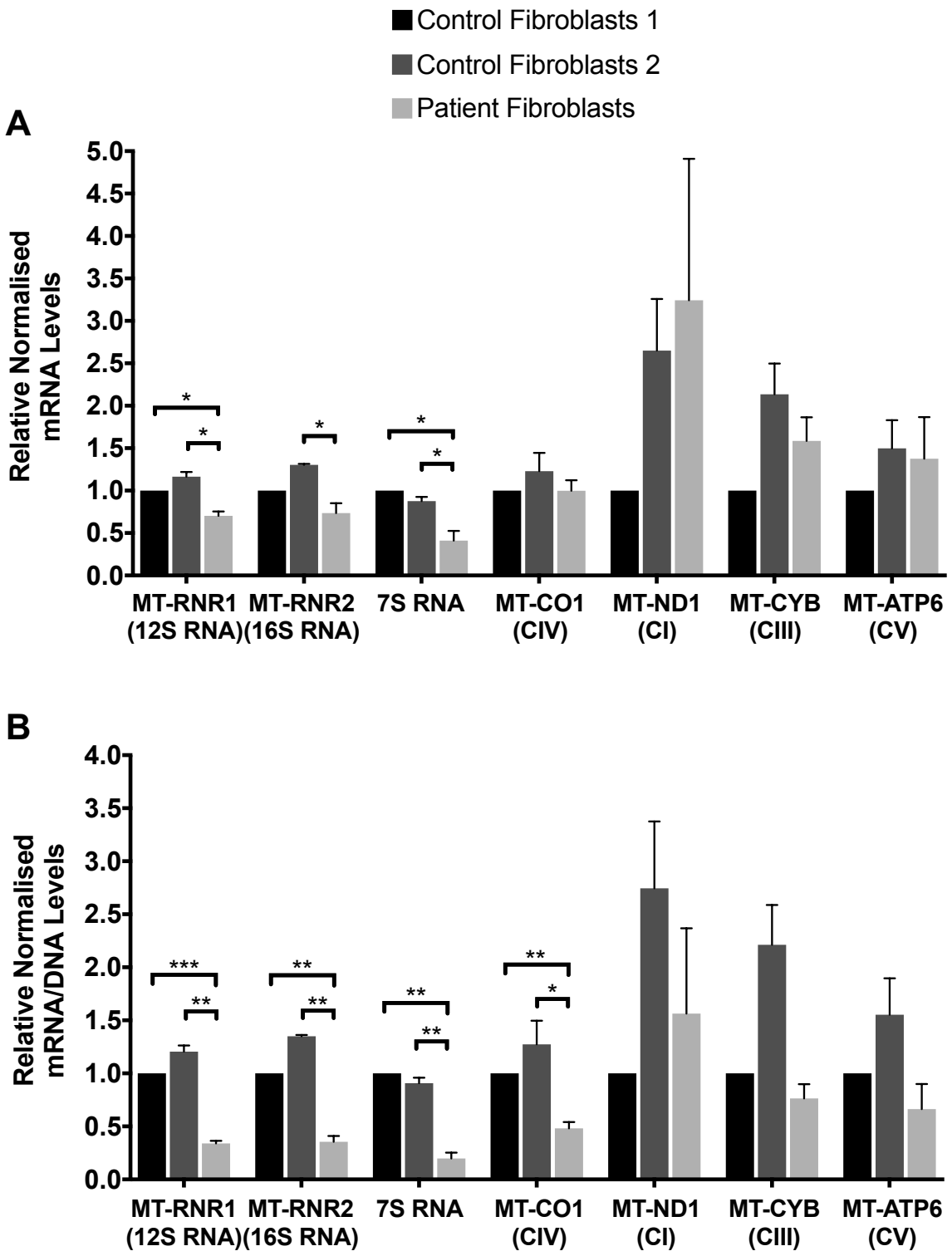

Figure 3.12 – mRNA levels of mitochondrial genes. (A) Gene transcripts, reverse-transcribed into cDNA, were quantified by qRT-PCR, normalised to GAPDH gene transcripts and expressed as fold variation to Control 1. Patient fibroblasts have lower absolute amounts of MT-RNR1 (down 35%), MT-RNR2 (down 36.2%) and 7S RNA (down 56.2%) transcripts. (n=2) (B) Gene transcript expression relative to mtDNA amount (from Fig 3.8A), shows that patient fibroblasts have lower relative amounts of MT-RNR1, MT-RNR2, 7S RNA and MT-CO1 transcripts. (n=2) Data points represent the mean and error bars represent ±SD. *p<0.05, **p<0.01, ***p<0.001

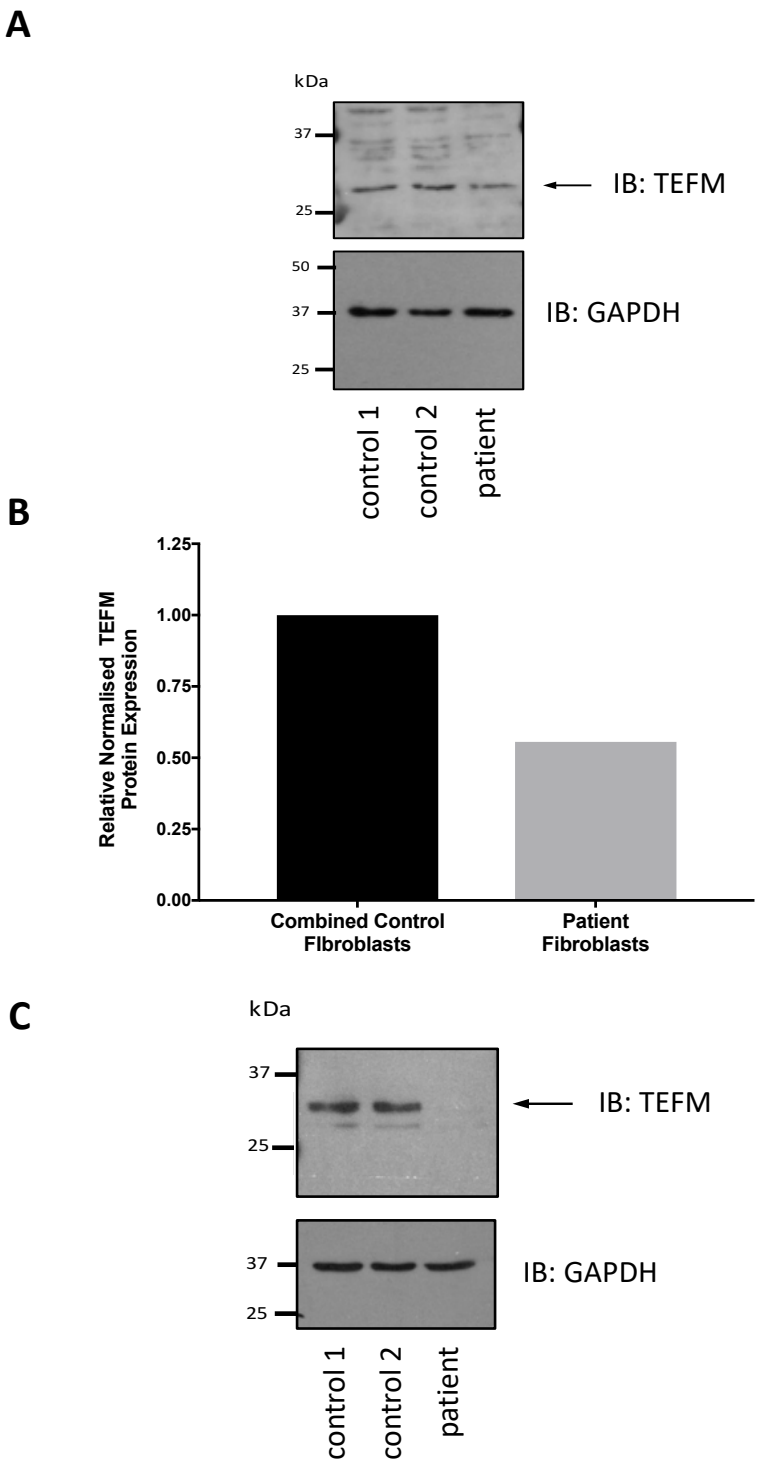

Figure 3.13 – TEFM expression. (A) Immunoblots showing lower expression of TEFM in primary patient fibroblasts. (B) Quantification of TEFM expression normalised to actin reveals a 44.8% reduction in TEFM levels in the patient. (C) A repeat shows an even higher reduction of TEFM levels in the patient (too low to be able to quantify).

3.3 – Immortalisation of patient fibroblasts and FBXO7 complementation

To directly link cellular phenotypes to the *FBXO7* mutation, I sought to complement the loss of FBXO7 expression in the primary patient fibroblasts. I attempted both retroviral transduction and transient transfections of *FBXO7*. Most of the cells died post-infection with retroviruses, whereas flow cytometry analysis of transient transfections using PEI showed a 0.6% transfection rate for the vector control and a 0.3% transfection rate for the *FBXO7* plasmid. Moreover, **Fig3.14A** shows there was no FBXO7 protein expression detectable in the patient fibroblasts post-transfection, most likely due to the very low transfection efficiency.

Due to their growth defect and the inability to complement FBXO7 in primary cells, I decided to immortalise all the fibroblast lines with a lentiviral infection of the SV40 large T antigen that inactivates tumour suppressor genes. At 2-3 weeks post-infection, there was a noticeable change in patient and control fibroblast morphology and the immortalised cells outgrew non-immortalised cells in culture. As shown in **Fig3.14B**, patient fibroblasts still do not express FBXO7 following immortalisation. Two independent *FBXO7* transfections of the immortalised patient fibroblasts resulted in FBXO7 expression (**Fig3.14B**), despite there only being a 1% transfection rate (as quantified through flow cytometry analysis).

In order to achieve a higher percentage of FBXO7 positive cells during complementation, immortalised patient fibroblasts were infected, rather than transfected, with GFP labelled *FBXO7* or empty vector plasmids. An infection rate of 6.9-9.0% was achieved as assayed by flow cytometry. I then examined the effects of immortalisation on apoptosis and mitochondrial phenotypes of the patient fibroblasts. Following immortalisation, the percentage of apoptotic cells in the patient fibroblast culture decreased from 20% to 7.8%, whereas there was a slight increase of apoptotic cells from 5% to 8.5% in the control fibroblast cultures (**Fig3.15A**). As expected, these data indicate that immortalisation with SV40T antigen suppressed the apoptotic phenotype of the patient cells. It was therefore not possible to test whether theses phenotypes in FBXO7 deficient cells could be rescued by FBXO7 complementation.

Similarly, the process of immortalisation also altered mitochondrial phenotypes seen in the primary patient fibroblasts. For example, whereas primary patient fibroblasts had a higher mitochondrial load, there was no longer a significant difference in the polarised mitochondrial load between immortalised patient and control fibroblasts when stained with MitoTracker Deep Red (**Fig3.15B**). However, a pilot experiment with MitoTracker Green, which labels all mitochondria regardless of membrane potential, showed an increase in total mitochondrial load in the immortalised patient lines compared to control cells (**Fig3.15D**). This implies that in immortalised patient fibroblasts, the amount of damaged unpolarised mitochondria may be increased. Thus, the absence of FBXO7 in immortalised patient lines might cause an accumulation of damaged mitochondria, possibly due to impaired mitophagy.

Despite these differences in the results of mitochondrial mass upon immortalisation, increasing FBXO7 expression levels did impact upon mitochondria in these cells. When immortalised patient cells were transduced with *FBXO7*, there was a 12.5% trending increase in polarised mitochondria upon the introduction of FBXO7 compared to a vector control into patient cells (**Fig3.15C**). This would suggest that FBXO7 increases the amount of mitochondria if its expression is increased, but that is the opposite of what was observed in primary patient fibroblasts (**Fig3.11B**). Apoptosis and polarised mitochondrial phenotypes were altered by immortalisation and thus, these phenotypes were not suitable for complementation studies. It would still be interesting to test the effects of complementation on TOM20/TEFM levels, mtDNA copy number and mitochondrial respiration, as some phenotypes may be unaffected by immortalisation. It would also be interesting to know if these phenotypes are present in cells with the other FBXO7 pathogenic mutations as well.

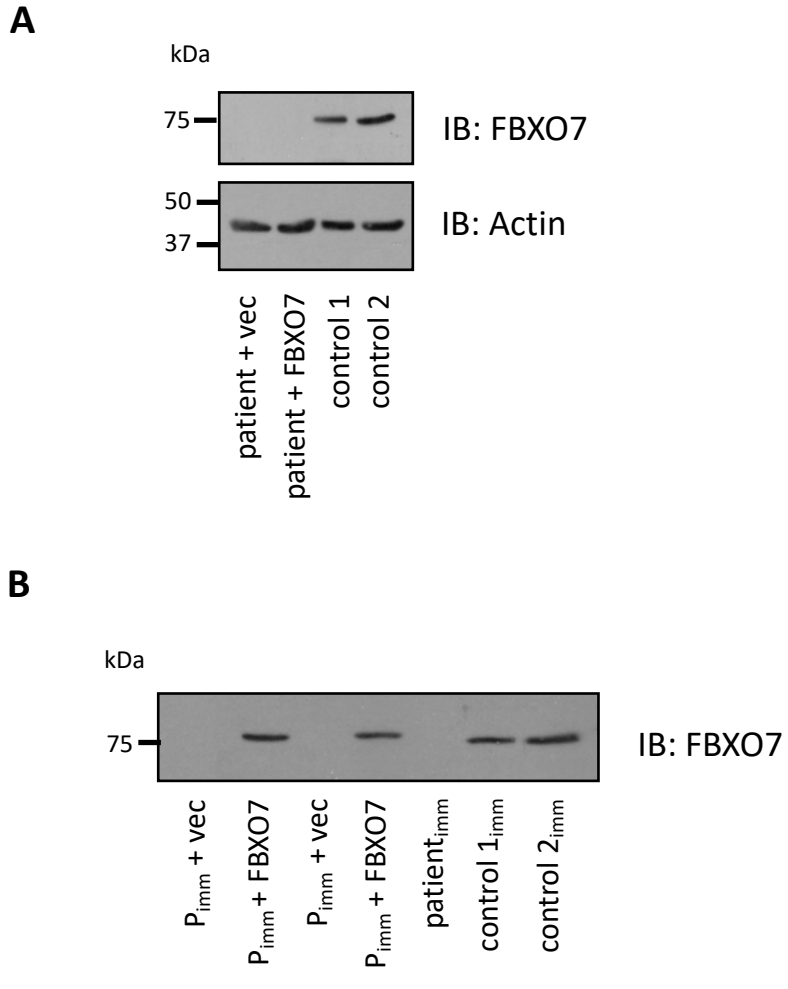

Figure 3.14 – FBXO7 complementation in primary and immortalised patient fibroblasts. (A) Infection of primary patient fibroblasts with empty vector (vec) and *FBXO7* plasmids. An infection rate of 0.3-0.6% was achieved when analysed with flow cytometry. There was no FBXO7 protein expression in lane 2. (B) Two independent transient transfections of immortalised patient fibroblasts (P_{imm}) with empty vector and *FBXO7*. A average transfection rate of 1% was achieved when analysed with flow cytometry and an equal number of cells were lysed. There is FBXO7 protein expression in the transfected patient lines (lanes 2 and 4).

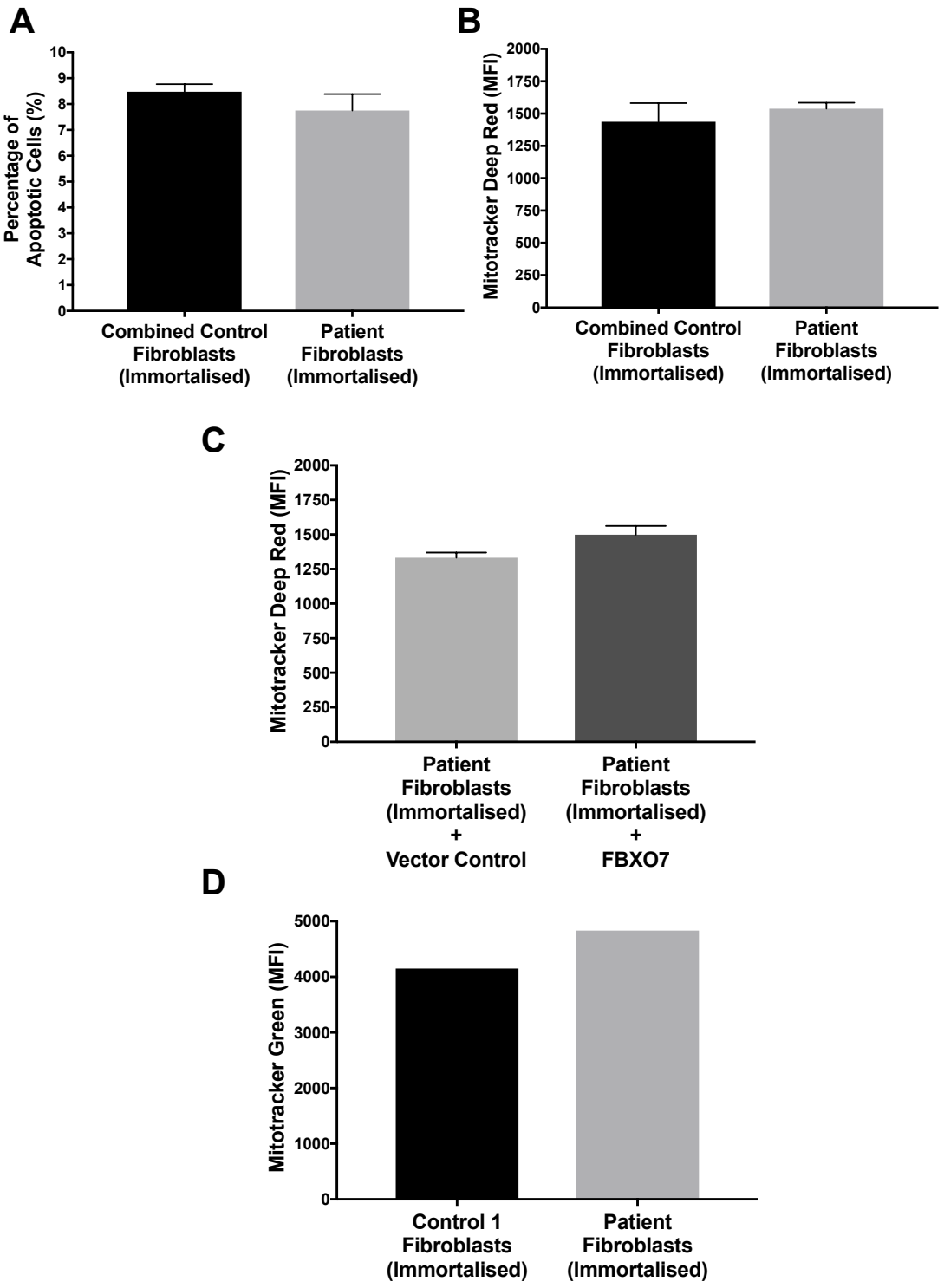

Figure 3.15 – Characterisation of apoptosis and mitochondrial load in immortalised patient fibroblasts complemented with FBXO7. (A) Immortalised fibroblasts were stained with Annexin V and analysed with flow cytometry, showing no significant difference. (B) MitoTracker Deep Red staining of immortalised patient and control fibroblasts, showing no significant difference. (C) MitoTracker deep red staining of patient fibroblasts post-infection with vector control and *FBXO7* plasmids, showing a 12.5% increase in MFI with *FBXO7* overexpression. An infection rate of 6.9-9.0% was achieved. (D) Pilot MitoTracker Green staining of immortalised patient and control 1 fibroblasts. Data points represent the mean and error bars represent ±SD. (n=1)

3.4 – Fbxo7 KO mouse embryonic fibroblasts as a model for the patient

The lab previously developed a germline *Fbxo7 Zp3*-Cre KO ($Zp3^{Cre}$*Fbxo7*$^{-/-}$) mouse, which has a severe runty phenotype and fails to survive after 2.5 weeks post-natal. I investigated mouse embryonic fibroblasts (MEFs) from this mouse to see whether they present similar phenotypes to those seen in the patient fibroblasts.

An equal number of primary MEFs from WT, Het and KO littermates were lysed and immunoblotted to confirm the lack of FBXO7 expression and to check for differences in protein levels of CDK6 and cyclin D1 (CCND1). **Fig3.16** shows that KO MEFs do not express FBXO7. In contrast to protein expression in the patient fibroblasts, the KO MEFs had increased CDK6 levels by 24.5%, but decreased amounts of the kinase activator, cyclin D1, by 20.6%. However, the overall net effect would be expected to be a decrease in CDK6 activity due to cyclin D1 being its rate-limiting activator. A proliferation assay revealed that similar to the patient fibroblasts, FBXO7 KO MEFs also proliferate 16.9% slower compared to WT MEFs (**Fig3.17**). However, the proliferation defect was more pronounced in the patient with cells lacking FBXO7 proliferating 43.5% slower than the controls. I next investigated whether an increase in apoptosis may also be a contributing factor to the slower proliferation rate. When primary MEFs were stained for apoptotic cells with Annexin V and PI, KO MEFs had a 3.1-fold increase in apoptotic cells than WT MEFs (**Fig3.18**). This included 6-times more early-apoptotic cells and 2.1-times more late-apoptotic cells. These proliferative and apoptotic data are similar to those observed in the patient fibroblasts.

Next, I investigated mitochondrial respiration using the Agilent Seahorse XF Cell Mito Stress Test. **Fig3.19** shows a representative graph of the WT and KO MEFs Oxygen Consumption Rate (OCR) over time. The assay showed that KO MEFs have lower basal respiration (35.5% reduction) and ATP production (47.8% reduction) compared to WT MEFs. Whereas, the difference in maximal respiration was 24.4% lower on average, a trend that resembles observations in the patient fibroblasts. There were no trending differences in spare capacity or proton leak. Overall, the differences between WT and KO MEFs were not as large as between patient and control fibroblasts, but these data argue that a similar mitochondrial respiratory chain defects exists.

Overall, these results suggest that the primary MEFs from the Zp3^{Cre}*Fbxo7*$^{-/-}$ mouse are a promising disease model for the patient primary fibroblasts. In both cases, the patient fibroblasts and KO MEFs presented with a decrease in proliferation, an increase of apoptotic cells (early apoptotic cells in particular) and a decrease in basal respiration and ATP production. These similarities indicate conservation of FBXO7 involvement in pathways regulating proliferation, apoptosis and mitochondrial respiration in both human and mouse. Therefore, it seems that this would be a good model to further investigate the pathogenic mechanisms that are involved in the patient.

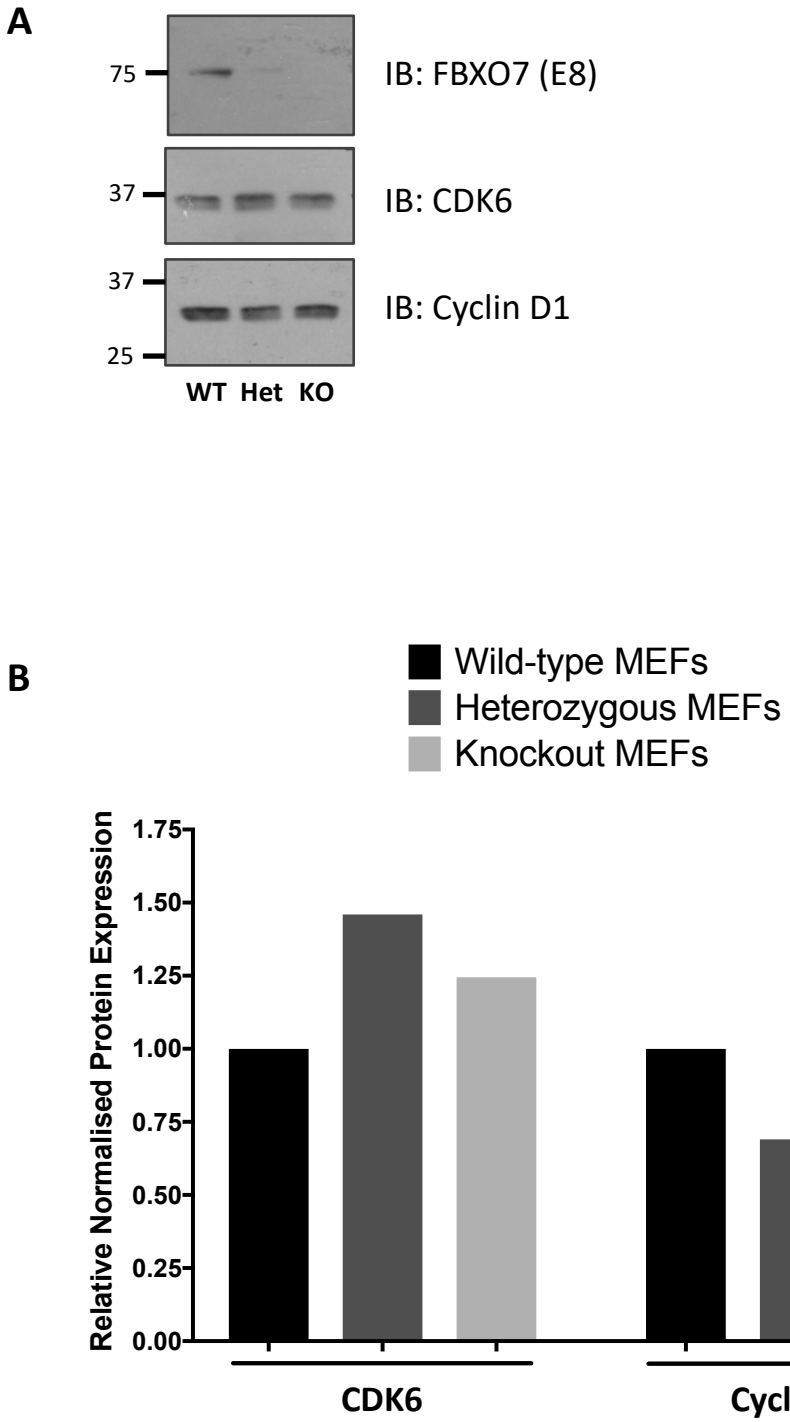

Figure 3.16 – FBXO7, CDK6 and cyclin D1 protein expression in *Fbxo7* KO MEFs. (A) Immunoblots of *Zp3*-Cre knockout MEFs lysates showing no FBXO7 expression. (B) Quantification of relative normalised CDK6 and cyclin D1 protein expression to WT MEFs showing that FBXO7 KO MEFs expression more CDK6 and a similar amount of cyclin D1 (n=1). As equal number of cells were lysed, equal loading is assumed for the quantification. Data points represent the mean.

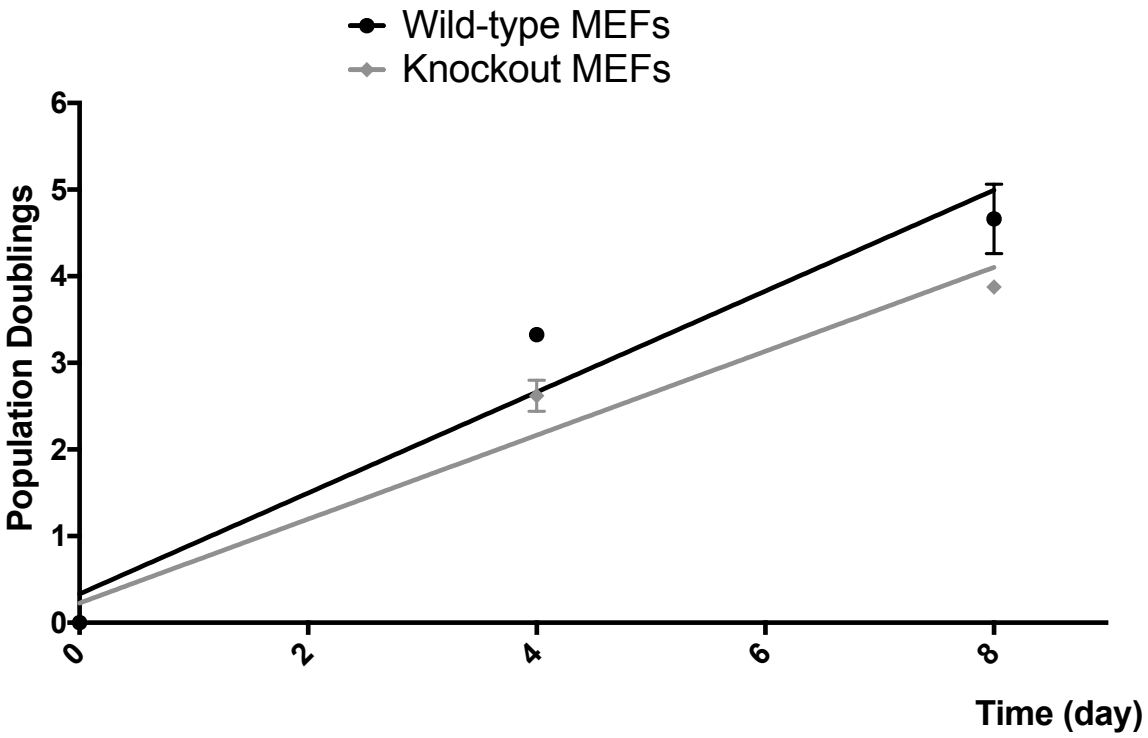

Figure 3.17 – FBXO7 KO MEFs proliferation assay. FBXO7 KO MEFs proliferate 16.9% slower compared to WT MEFs. Cells were re-seeded in duplicate at $2.5x10^5$ cells per well every 3-4 days and the population doubling rate was determined. (n=1) Data points represent the mean, error bars represent ±SD.

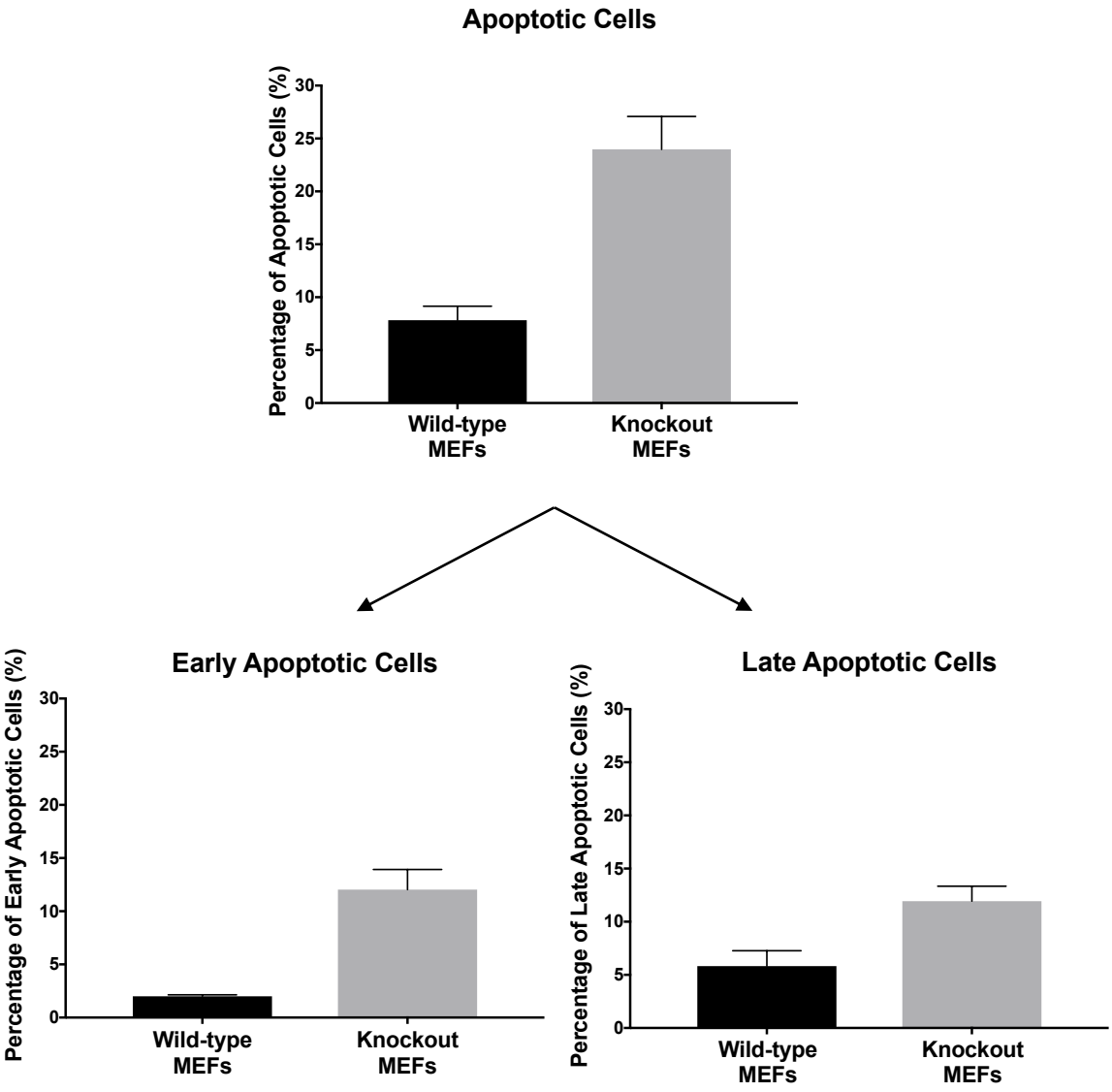

Figure 3.18 – FBXO7 KO MEFs apoptosis assay. Cells were co-stained with Annexin V and PI, and analysed by flow cytometry. Early apoptotic cells were Annexin V positive, but PI negative. Late apoptotic cells were both Annexin V and PI positive. *Zp3* knockout MEFs have 3.1x more apoptotic cells compared to WT MEFs, which includes 6x more early apoptotic cells and 2.1x more late apoptotic cells. (n=1) Data points represent the mean and error bars represent ±SD.

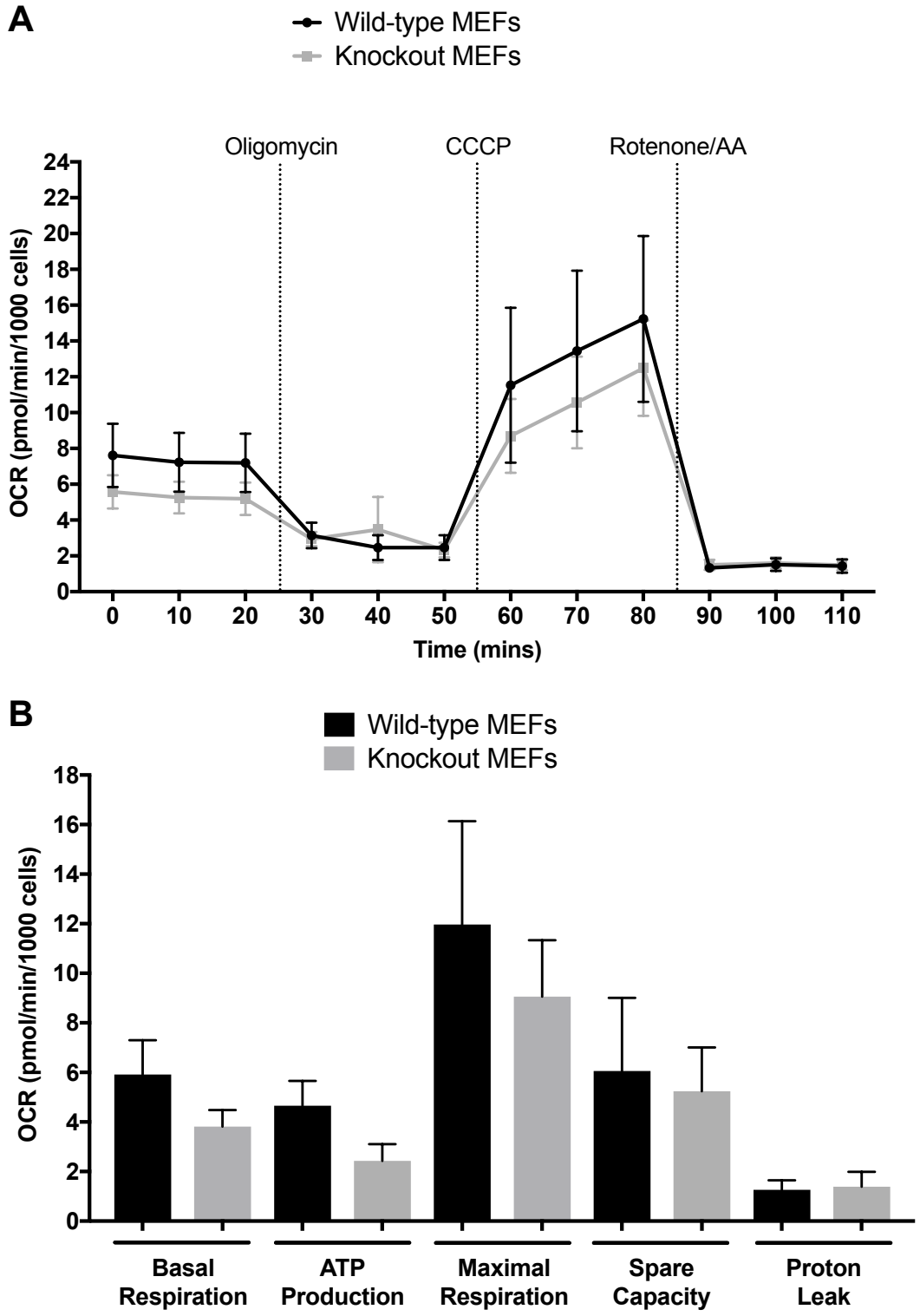

Figure 3.19 – FBXO7 KO MEFs mitochondrial oxygen consumption rate. (A) Oxygen consumption curves per 1000 cells, following 3 injections of Oligomycin, CCCP and Rotenone/Antimycin A. An OCR plot shows that KO MEFs (measured from 6 technical replicates) have lower mitochondrial respiration compared to WT MEFs (measured from 4 technical replicates. (n=1) (B) KO MEFs had lower basal respiration (down 35.5%) and ATP production (down 47.8%), whereas there were no significant differences in maximal respiration, spare capacity and proton leak. (n=1) Data points represent the mean and error bars represent ±SD.

3 – Discussion

The aim of this chapter was to characterise *FBXO7* KO patient fibroblasts and see how their phenotypes compare to MEFs from our *Fbxo7* KO mouse model. There has always been a lack of accurate models for the study of neurodegeneration. The main advantages of using skin fibroblasts derived from a patient for studying Parkinson's disease are that they express most PARK genes, reflect polygenic risk factors and cumulative phenotypes of the patient, and that they are relatively easy to obtain and maintain.[357] Also, unlike tumour-derived cell lines, fibroblasts are not affected by the Warburg effect and continue producing energy through mitochondrial oxidative phosphorylation and not primarily through high-rate glycolysis.[357] This is especially important when investigating mitochondrial phenotypes. However, like any model, they also exhibit some disadvantages which need to be considered. For instance, slow growth and higher adherence with increased passages, difficulty in matching patient cells with controls which can affect result reproducibility, and that their signalling and gene expression profile can differ from neurons.[357] Overall, this chapter shows that primary MEFs from the $Zp3^{Cre}$*Fbxo7*$^{-/-}$ mouse are a promising model to explain some of the abnormalities found in the patient fibroblasts lacking FBXO7 expression, as many of the phenotypes are conserved.

Firstly, both patient fibroblasts and KO MEFs proliferate slower and have an increase in apoptosis compared to their respective controls. Based on these results, one can postulate that cell death is a major factor contributing to slower proliferation due to the clear increase in apoptosis in both patient fibroblasts and KO MEFs. PI staining of DNA content in the patient fibroblasts showed an increase of cells in G_0/G_1 phase, a decrease of cells in G_2M phase, and an insignificant decrease of cells in S phase. This suggests that cells are not progressing through the G_0/G_1 phase of the cell cycle in the same capacity as the controls, possibly due to a decrease in CDK6 and cyclin D1 protein expression. A second band of lower molecular weight was apparent in the CDK6 immunoblot of the patient fibroblasts, which could be either be a non-specific band or a degradation product of CDK6. If that were to be the case, then it would suggest that CDK6 is more readily degraded in the patient compared to the controls. It would be interesting to look at actual kinase levels, or levels of Rb S780 phosphorylation, to confirm that the lack of CDK6/cyclin D1 activity is directly causing decreased cell proliferation. The decrease in CDK6/cyclin D1 complex formation and stability can be a direct result of the lack of

FBXO7 in these cells. Alternatively, these results may also suggest that patient fibroblasts are resting in G_0 rather than cycling in G_1 and due to the inability to cycle, they may end up being apoptotic. It would have been also interesting immunoblot for a cyclin that is increased at end of the G_1 phase, such as cyclin E, but it was not possible to detect it in fibroblasts using the available antibodies. It was also not possible to obtain a signal for p27, which would have been valuable as FBXO7 also directly interacts with p27 to either inhibit cell cycle progression or further enhance CDK6/cyclin D1 complex assembly, depending on the context or cell line.[308]

In KO MEFs lysates, even though the levels of CDK6 were higher, the lower levels of cyclin D1 potentially recapitulated the net effect of reduced CDK6 activity due to cyclin D1 being the rate-limiting CDK6 activator. In terms of the increased apoptosis phenotype, there were significantly more early-apoptotic cells compared to late-apoptotic cells in both patient fibroblasts and KO MEFs. Over time, patient fibroblasts became noticeable more adherent compared to both control fibroblast lines and had to undergo progressively longer trypsinisation, which could have also caused the higher early-apoptosis artefact. However, as trypsinisation was kept constant and as the same phenotype was present in the MEFs, which did not become more adherent, it seems that this was not simply an artefact.

Finally, it is important to remember that slower proliferation rate can not only be caused by a cell cycle defect or an upregulation of cell death, but also due to low energy production, mitochondrial dysfunction, genotypic differences, or the way the skin biopsies were made. Thus, a combination of these factors may all be contributing to the decrease in proliferation of patient fibroblasts, which is why a more tractable model would be useful.

Secondly, mitochondrial respiration experiments showed that both patient fibroblasts and KO MEFs have decreased basal respiration, ATP-linked respiration and maximal respiratory capacity, suggesting mitochondrial impairment in both human and mouse FBXO7 deficient cells. Mitochondrial dysfunction could also be a contributing factor to the decreased proliferation phenotype due to lack of energy production. Repeating the proliferation assay with cells growing in galactose media would further confirm this hypothesis. These respiration defects could be caused by decreased activity of mitochondrial complexes I, III and IV, which can directly affect the oxygen consumption

rate. It would have been interesting to measure mitochondrial respiratory complex activities in MEFs to check if they are reduced as well and consistent with the observed decreased oxygen consumption. In the patient fibroblast assays, the high standard deviation of the controls for complex I in the second biological repeat and inconsistencies in complex II activities necessitates another repeat to confirm the trends. It seems that the complex II measurements did not work very well in the first repeat as the specific activity of complex IIb should be higher than complex IIa (SDH).

Subsequent immunoblots of patient fibroblast lysates for mitochondrial markers and MRC subunits of each of the complexes showed a decrease in expression of CS, TOM20, SDHB (complex IIa) and ATP5A (complex V). Lower CS could result in impaired TCA cycle progression which would contribute to the reduction of mitochondrial respiration. Whereas, lower ATP5A expression could indicate lower ATP synthase levels, which in turn would produce decreased ATP synthesis in line with the observed ATP-linked respiratory component. There was also a reduction in SDHB protein levels, which does completely coincide with the functional results and should be further confirmed and investigated. In this case, the effect on complex II might be attributed to a potential protein import impairment, due to decreased TOM20 levels, which could affect all complexes.

Without further experiments, it is quite difficult to explain the reason behind decreased complex activities based on protein levels of a limited number of subunits. For instance, the protein expression of two complex IV and one complex III subunits is unchanged despite their activities being decreased, whereas the expression of a complex II subunit is decreased even though its activity seems to unaffected. However, these complexes are formed from many subunits, and it is only necessary to have a downregulation of a structural protein or an assembly factor for the entire complex to be affected. Thus, it would be important to look at more subunits and also whether they correctly assemble into functioning complexes. Blue-native SDS PAGE would show whether mitochondrial complexes are being formed properly or whether an assembly defect may be responsible for their decreased activities. This would reveal the levels of fully assembled complexes, which will probably correlate better with their activities.

Based on decreased CS and TOM20 protein expression and decreased respiration, the amount of polarised mitochondria in these cells was expected to be decreased as well. However, MitoTracker Deep Red staining revealed an increase of polarised mitochondria, which could be due to a compensatory mechanism employed by the cells. It would be informative to also stain these cells with MitoTracker green, which labels all mitochondria regardless of membrane potential. Together with the MitoTracker Deep Red staining, this would reveal the ratio of damaged and healthy mitochondria and possibly suggest whether the problem lies with increased biogenesis or also with the accumulation of damaged mitochondria.

Furthermore, qPCR and qRT-PCR analysis showed that patient fibroblasts have twice as much mtDkNA, implying increased mtDNA replication. Nevertheless, these same cells have a significant downregulation of MT-RNR1 (12S RNA), MT-RNR2 (16S RNA) and 7S RNA transcripts, as well as mRNAs, when normalised to mtDNA levels. This is suggestive of a defect in mitochondrial transcription possibly due to a decrease in TEFM. As the most downregulated transcripts are the mitochondrial MT-RNR1 (12S rRNA) and MT-RNR2 (16S rRNA), essential components of the mitochondrial ribosome, one would expect to have reduced mitochondrial translation in the FBXO7 mutated cell lines. All these effects at the different levels of mtDNA expression could account for the observed reduction in complexes I, III and IV enzymatic activity and respiratory capacity. Therefore, important future experiments should include investigating *in vivo* mitochondrial translation and mitoribosome protein levels. The fact that the disappearance of FBXO7 has such an impact on TOM20 levels implies that the mitochondrial import machinery is very much affected, and this can be directly related to the reduced TFEM levels, which in turn could very well explain the observed reduced mitochondrial transcription.

This chapter proposes a potential mechanism through which the lack of FBXO7 may be contributing to decreased proliferation and increased cell death in primary patient fibroblasts. Firstly, lower expression of CDK6 and cyclin D1 may be causing an increased proportion of cells in G_0/G_1 and a decrease of cells in G_2M, thus limiting cell cycle progression. Furthermore, FBXO7 can no longer act as a scaffold for CDK6/cyclin D1, which inhibits proliferation. Secondly, increased apoptosis also results in a reduced proliferation, and mitochondrial dysfunction can contribute to both decreased proliferation and increase apoptosis phenotypes. A decrease in mitochondrial

respiration seems to be potentially caused by a decrease in CI, CIII and CIV activities, and a decrease in CS and ATP5A protein expression. Furthermore, there also appears to be a defect in the expression of mitochondrial RNAs, despite there being an increase in mtDNA. This could be as a result of decreased TOM20 and TEFM expression, both of which are substrates of FBXO7 and are downregulated in cells lacking FBXO7 expression. Thus, a preliminary model shown in **Fig3.20** suggests that *FBXO7* plays an important in cell cycle regulation and mitochondrial function in primary patient fibroblasts carrying a S93X mutation.

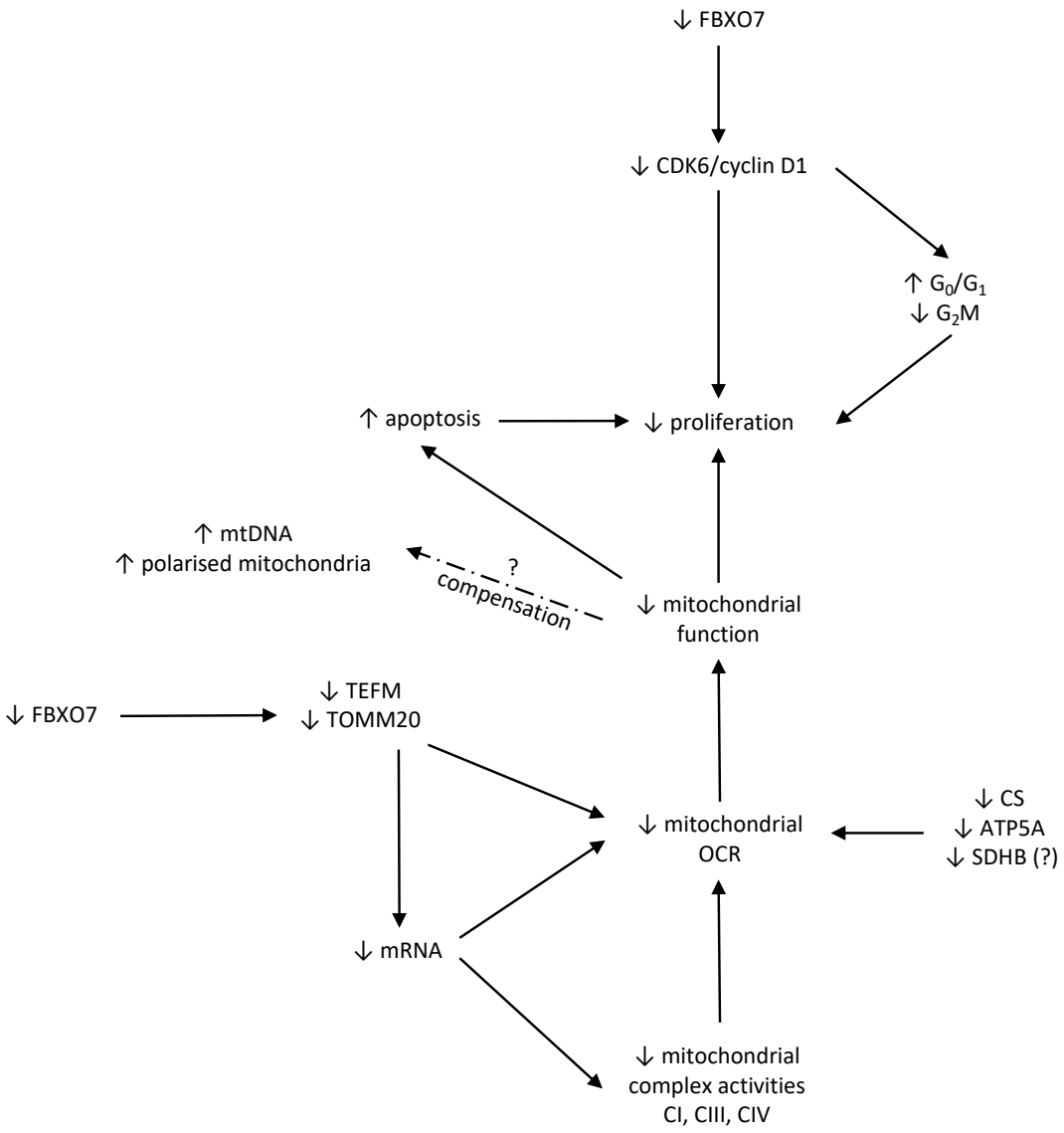

Figure 3.20 – Potential schematic of phenotypes seen in primary patient fibroblasts. Some important phenotypes include lower expression of CDK6 and cyclin D1 may be causing an increased proportion of cells in G_O/G_1 and a decrease of cells in G_2M, thus limiting cell cycle progression. Furthermore, FBXO7 can no longer act as a scaffold for CDK6/cyclin D1, which can also inhibits proliferation. Increased apoptosis can also results slower proliferation. Mitochondrial dysfunction can contribute to both decreased proliferation and increase apoptosis phenotypes. A decrease in mitochondrial respiration seems to be potentially caused by a decrease in CI, CIII and CIV activities, and a decrease in citrate synthase and ATP5A protein expression. There also appears to be a defect in the expression of mitochondrial RNAs, despite there being an increase in mtDNA. This could be as a result of decreased TOMM20 and TEFM expression, both of which are substrates of FBXO7 and are downregulated in cells lacking FBXO7 expression.

CHAPTER 4

CHARACTERISATION OF SH-SY5Y *FBXO7* KNOCKDOWN AND KNOCKOUT CELL LINES

4 – Introduction

The overall aim of this research is to characterise the functional role of FBXO7 in various *in vitro* and *in vivo* models of Parkinson's disease. Canonically, FBXO7 functions as a substrate-recruiting subunit of the Skp1-Cullin1-FBP(SCF)-type E3 ubiquitin ligase. SCF-complex-mediated ubiquitination can result in protein modification, protein degradation via the 26S proteasome, or the activation of the endosomal or autophagy/lysosomal pathways. FBXO7 also has a variety of other atypical functions, such as cell cycle regulation, proteasome regulation, and mitophagy.[312]

The focus of this chapter is on *in vitro* SH-SY5Y based cell lines. I chose the human neuroblastoma SH-SY5Y cell line as the neuronal model because it is widely used as a cell line model for *in vitro* Parkinson's disease research.[359] I wanted to test whether some of the observed phenotypes in FBXO7 deficient patient fibroblasts and MEFs (Chapter 3) could be recapitulated in a neuronal-based model. SH-SY5Y cells are easier to obtain, maintain, genetically manipulate, and are phenotypically closer to dopaminergic neurons that become affected in PD. It may also be easier to complement back FBXO7 into these cell lines. I generated both *FBXO7* shRNA transient knockdown SH-SY5Y cell lines and FBXO7 CRISPR knockout SH-SY5Y cell lines for characterisation.

Based on the observed differences in fibroblasts post-immortalisation, I expect that certain phenotypes may also not be recapitulated in these tumour-derived cells lines. However, FBXO7 can have distinctive, sometimes opposing, effects in different cell lines and it is therefore important to investigate its function in various models. It is also possible that different models may be more suitable for the study of certain phenotypes. Given prior observations, I started with investigating the effect of FBXO7 knockdown or

knockout on proliferation rate, cell death and mitochondrial biology. Additionally, due to the dynamic interaction between mitochondria and lipid droplets, I also investigated lipid metabolism in these cells.

4 – Results

4.1 – Cell cycle and viability of FBXO7 shRNA knockdown cells

FBXO7 plays an important function in cell cycle regulation by stabilising p27 and aiding CDK6/cyclin D1, D3 complex formation. I showed in chapter 3 that patient fibroblasts and MEFs lacking FBXO7 expression had reduced proliferation rates compared to their controls. In contrast, an increased proliferative rate upon reduced FBXO7 expression has been previously observed in B cell lines and was attributed to reduced levels of p27, a cell cycle inhibitor.[308] Thus, as its role can be cell-type specific, I investigated the effect of reducing FBXO7 expression on the proliferation of a neuronal cell line. A reduction of FBXO7 expression was achieved by infecting cells with retroviruses expressing FBXO7 miR-30 based short-hairpin RNA (within a Puro-IRES-GFP/mCherry vector). Flow cytometry analysis of a representative viral transduction showed that 78-93% of SH-SY5Y cells expressed GFP or mCherry post-selection in puromycin (**Fig4.1**). Immunoblotting for FBXO7 expression showed that it was reduced by 60.4% in the GFP SH-SY5Y FBXO7 knockdown line and by 85% in the mCherry SH-SY5Y FBXO7 knockdown line when normalised to actin levels (**Fig4.1**).

To assess whether cells had any cell cycle defects, I measured their proliferative rate while they were cultured in either glucose or galactose as the carbon source. Growth in galactose forces cells to rely solely on oxidative phosphorylation (OXPHOS) for energy production and may therefore reveal underlying mitochondrial dysfunction.[360,361] Cells were seeded at equal densities and viable cell counts were recorded every 2-3 days with a CASY Cell Counter. The increase in cell number was normalised to seeded cell number and converted to a $\log_2$ scale and plotted as cumulative population doublings against time. **Fig4.2A** shows that no significant differences in population doublings were observed between the control and FBXO7 knockdown cell lines in neither glucose nor galactose media.

It has been previously shown that certain mitochondrial defects become apparent when cells are grown under conditions requiring OXPHOS, which would cause a reduction in cell viability.[360] **Fig4.2B** shows the combined cell viability over the course of three proliferation assays. Even though there are no significant differences, there is a trend that the survival of FBXO7 knockdown cells was lower in galactose media, compared to vector control cells grown in glucose/galactose and FBXO7 knockdown cells grown in glucose. When going from glucose to galactose media, there was a 6.4% reduction in average cell viability in the absence of FBXO7, compared to a 2.2% reduction in the vector control cell lines. Overall FBXO7 knockdown cell lines show a trending reduction in cell viability under galactose conditions compared to the control lines. Furthermore, cell lines with reduced FBXO7 expression seem to have a proportionally larger decrease in cell viability when switched from glucose to galactose media. This trend may suggest a potential mitochondrial defect, however there may be some adaptation or compensation which prevents the defect increasing towards significance.

To investigate whether increased apoptosis could be contributing to decreased cell viability under galactose conditions, I stained cell lines with Annexin V and Propidium Iodide (PI) and analysed them using flow cytometry. As previously mentioned, early apoptotic cells are Annexin V positive, but PI negative; whereas late apoptotic/necrotic cells are Annexin V and PI double positives. The role of mitochondria in apoptosis versus necrosis is still debated, however currently it seems that apoptosis relies on mitochondria as an integral part of the execution pathway, whereas necroptosis is not mitochondria-dependent.[362] **Fig4.3** depicts the relative percentage of early apoptotic or late apoptotic/necrotic cells in the FBXO7 KD lines compared to the vector control line. I found no significant differences in the number of apoptotic cells when FBXO7 KD cells were grown in glucose or galactose media. There was no significant difference in the number of late apoptotic/necrotic cells between the two growth conditions. PI can stain cells dying by both apoptotic and necrotic pathways, however a further assay would be necessary to distinguish between late-apoptotic and necrotic cells. These data indicate that the overall levels of apoptotic and necrotic cell death are not significantly different. Therefore, the observed changes in decreased viability are not due to an increase in apoptotic cells, but rather due to other pathways.

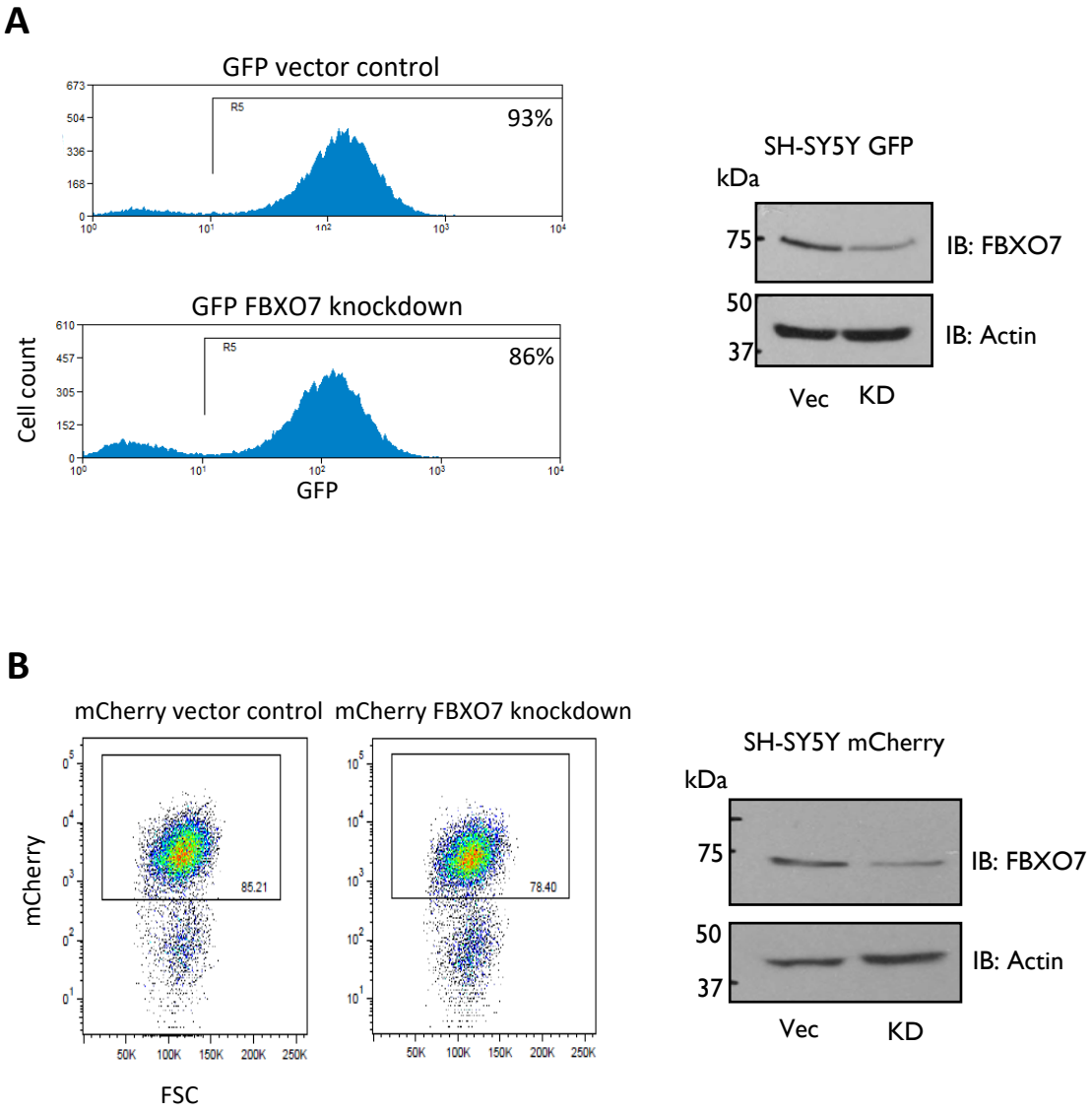

Figure 4.1 – Generation of FBXO7 shRNA knockdown SH-SY5Y cell lines. (A) Flow cytometry analysis shows that infection efficiency was 93% and 86% for SH-SY5Y-GFP control (Vec) and knockdown (KD) cell lines respectively. Immunoblotting for FBXO7 normalised to Actin shows a 60.4% reduction in expression. (B) Flow cytometry analysis shows that infection efficiency was 85% and 78% for SHSY-5Y-mCherry control and knockdown cell lines respectively. Immunoblotting for FBXO7 normalised to Actin shows a 85% reduction in expression.

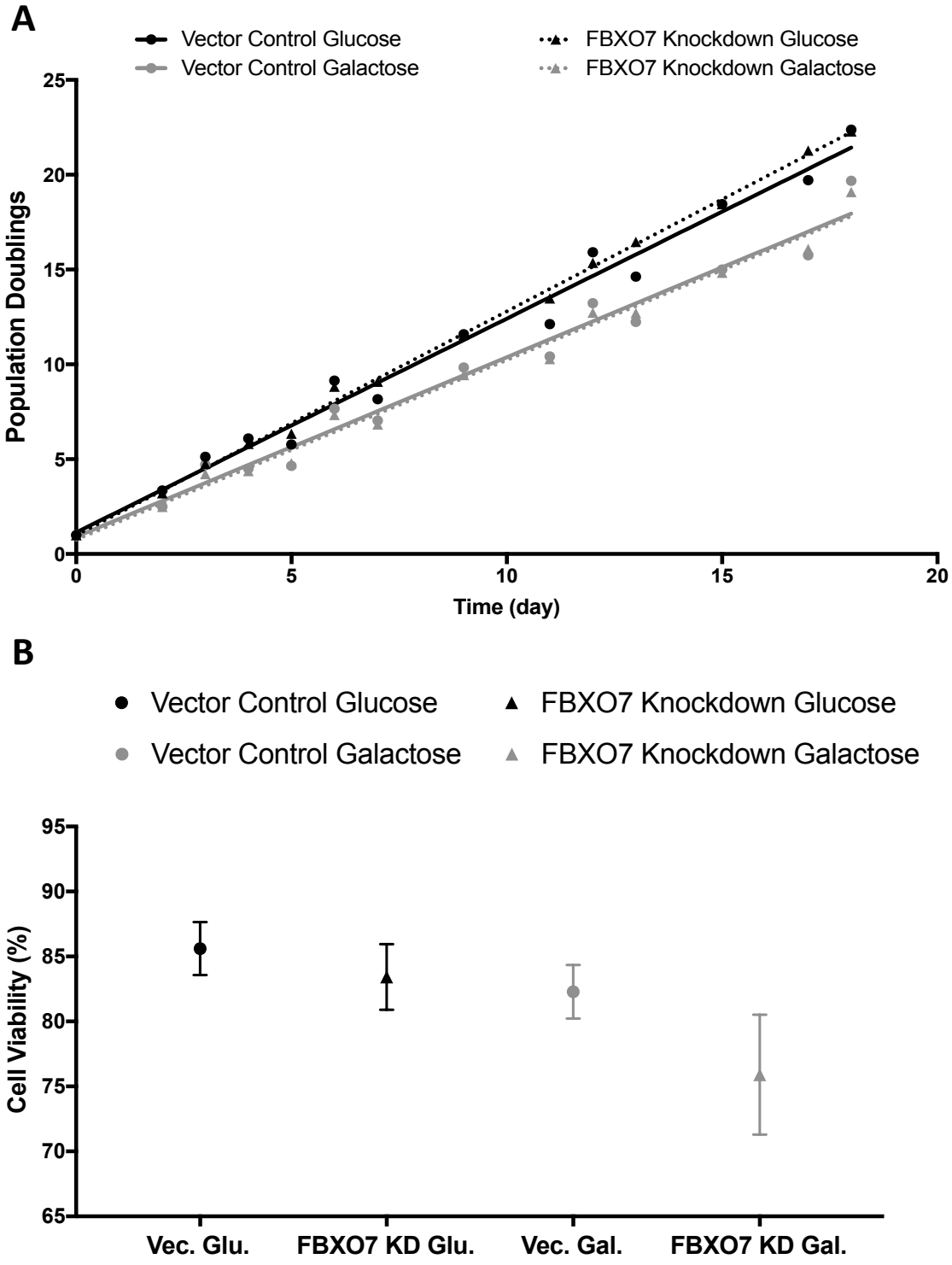

Figure 4.2 – Proliferation and viability assays of FBXO7 shRNA knockdown SH-SY5Y cell lines. (A) SH-SY5Y-GFP vector control (Vec) and SH-SY5Y-GFP shRNA FBXO7 (KD) cell lines grown in glucose or galactose supplemented DMEM. The population doubling rate was determined by re-seeding cell lines in triplicate at $2x10^5$ cells per well every 2-3 days. (B) Combined cell viability means (measured by the CASY Cell Counter) of SH-SY5Y-GFP vector control (Vec) and FBXO7 knockdown (KD) grown in glucose or galactose supplemented DMEM. Data points represent the mean, error bars represent ±SD. There were no significant differences in proliferation rate or viability. (n=3)

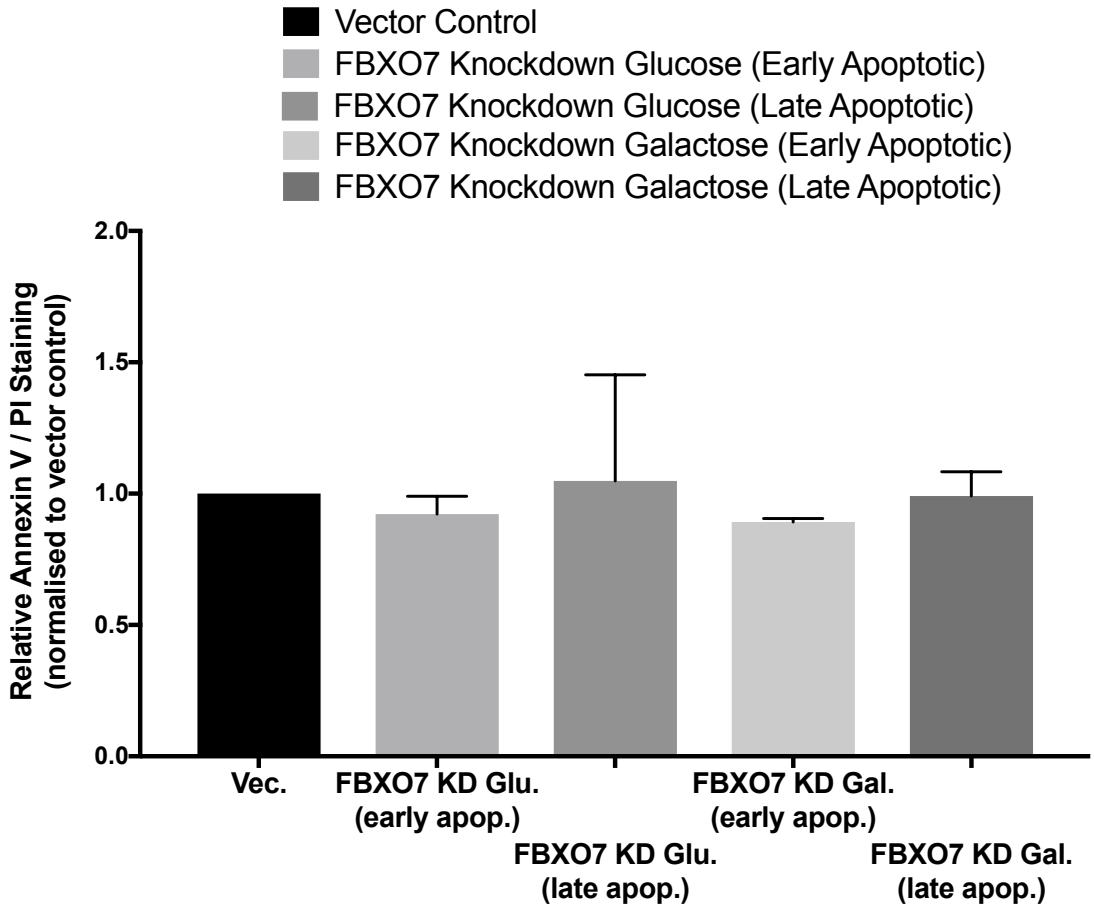

Figure 4.3 – Apoptosis of FBXO7 shRNA knockdown SHSY-5Y cell lines. Cells were co-stained with Annexin V and PI, and analysed by flow cytometry. Early apoptotic cells were Annexin V positive, but PI negative. Late apoptotic cells were Annexin V and PI double positives. Quantification of early and late apoptotic cells relative to the vector control cell line showing no significant differences (n=1). Error bars represent ±SD.

4.2 – FBXO7 shRNA knockdown cells have fewer polarised mitochondria

The results from the experiments shown in **Fig4.2** indicate a subtle trend in decreased cell viability when FBXO7 deficient cells are grown in galactose, being entirely dependent on mitochondrial mediated OXPHOS for energy production. Thus, I next assayed the cellular ability to regulate mitochondrial load to cope with the energy production shift. MitoTracker Deep Red staining and flow cytometry analysis of polarised mitochondria (**Fig4.4**) showed a significant increase of mitochondria in cells grown in galactose media. In media containing glucose, cells with FBXO7 knockdown had significantly 13.8% fewer polarised mitochondria compared to control lines. However, upon shifting to media with galactose for three weeks, the control cell line increased mitochondria 2.2-fold, whereas FBXO7 deficient cells increased mitochondria 2.5-fold. Thus, even though their initial mitochondrial load was significantly lower than that of the control, FBXO7 deficient cells still had more mitochondria in response to increased demands for oxidative phosphorylation. The significantly reduced mitochondrial load under basal conditions could indicate that FBXO7 functions to promote mitochondrial biogenesis. However, the fact that reduced FBXO7 levels did not impact on the cell's ability to increase their mitochondrial load when grown in galactose suggests that either mitochondrial biogenesis is unaffected or that there may be several redundant pathways involved. Another possibility is that the reduction of polarised mitochondria may also be a consequence of defective mitophagy, in which the role of FBXO7 has already been established, albeit under stress and not basal conditions.[320] Defective mitophagy may lead to less polarised mitochondria due to impaired inhibition of fusion,[320] spreading damaged mitochondrial components to healthy mitochondrial.[363]

4.3 – FBXO7 shRNA knockdown cell lines accumulate lipid droplets

There is a dynamic interaction between lipid droplets and the outer membrane of mitochondria to facilitate free fatty acid (FFA) delivery for mitochondrial β-oxidation.[224,364] Therefore, mitochondrial dysfunction can directly lead to lipid droplet accumulation.[224,364] As my results indicate a possible defect in mitochondrial OXPHOS in FBXO7 knockdown cell lines, I assayed lipid droplet accumulation as an indirect measure of mitochondrial health. Oil Red O (ORO) staining and confocal imaging was used to quantify the number of lipid droplets in control and FBXO7 deficient cell lines. **Fig4.5A** shows representative microscopy images showing a trend of more ORO lipid

droplet staining in cells with reduced FBXO7 levels. On average, there were 2.9x more lipid droplets per cell in the FBXO7 knockdown cell line when compared to the vector control (**Fig4.5B**). This preliminary data suggests that knockdown of FBXO7 results in intracellular lipid droplet accumulation, possibly due to less efficient mitochondrial β-oxidation of fatty acids, and thereby indicative of poor mitochondrial health.[224] The accumulation of lipid droplets could alternatively, or additionally, be attributed to a lipophagy defect due to the knockdown of FBXO7. It is tempting to consider a role of FBXO7 in regulating lipophagy as previous studies in the lab have shown that FBXO7 interacts with Parkin to induce mitophagy,[320] another form of selective macro-autophagy that follows a similar pathway.

In sum, the proliferative and cell viability phenotypes of FBXO7 knockdown SH-SY5Y cell lines were not robust. Although trending results were initially observed in some experiments, subsequent biological repeats showed loss of the phenotypes. This data suggest that the proliferation and viability phenotypes are transient and may be compensated for by redundant mechanisms while cells are maintained in culture. Interestingly, cells with reduced FBXO7 have significantly fewer polarised mitochondria under basal conditions and they have a trending increase in lipid droplets, which may indicate mitochondrial dysfunction. Thus, FBXO7 may play a role in certain mitochondrial and/or lipid biology pathways, though these cell lines may not be the best model to investigate these phenotypes further.

4.4 – Fbxo7 shRNA knockdown has no effect on P19 differentiation

The balance between cell proliferation and differentiation is crucial for the correct development of numerous cell types, including the nervous system.[20] Studies have shown that the cell cycle can directly influence early lineage commitment and terminal cell fate.[21,22] It has been also established that neural progenitors undergo overall cell cycle lengthening immediately prior neuronal differentiation due to an extended G_1 phase.[23] Many G_1 cell cycle regulators have been implicated in this proliferative to neurogenic switch, such as Cyclin D2[25,26] and p27.[27,28,29] Considering the important role of FBXO7 in the G_1 phase of the cell cycle through its interaction with CDK6/cyclin D1, D3 complexes and p27, I investigated its role further in neuronal differentiation of P19 cells. The P19 mouse embryonal carcinoma-derived stem cell line is robust, easy to maintain and differentiates into cells with a neuronal phenotype upon retinoic acid

treatment. A stable reduction of FBXO7 expression was achieved by infecting cells with retroviruses expressing mouse *Fbxo7* miR-30 based short-hairpin RNA, IRES-GFP, and puromycin sequences. Flow cytometry analysis showed that 98% of P19 cells expressed GFP in both the control and knockdown cell lines (**Fig4.6A**) and that FBXO7 expression was reduced by 95% (**Fig4.6B**).

P19 differentiation with retinoic acid occurs over a period of nine days. It includes an initial stage of proliferation and aggregation into embryoid bodies in non-adhesive tissue culture dishes, and subsequent adherence in regular tissue culture dishes and neurite outgrowth. Both vector control and knockdown P19 cell lines were differentiated using retinoic acid treatment. Upon differentiation, there does not seem to be any apparent qualitative difference in the extent of differentiation between the cell lines (**Fig4.7**). To confirm that differentiation along a neuronal lineage was achieved and given the established role for FBXO7 in the proliferation and differentiation in several haematopoietic lineages, immublotting was used to investigate any effects of reduced FBXO7 on relevant regulators before and after differentiation (**Fig4.8**). Intriguingly, FBXO7 was almost entirely downregulated during differentiation in the P19 control cell line suggesting its absence is either required for, or secondary to, differentiation (**Fig4.8A**). A FBXO7 interacting partner, CDK6, was also reduced in both P19 vector control and FBXO7 knockdown cell lines during differentiation (**Fig4.8B**), similar to that seen in erythrocyte terminal differentiation.[308] This coincided with p27 upregulation upon differentiation (**Fig4.8C,D**), as this protein, along with p21 inhibits CDK/cyclin complexes and thereby hindering cell division. Furthermore, it has been also shown that p27, independently of its cell cycle function, promotes neural differentiation and migration.[305,307,365–367] βIII tubulin, a microtubule marker expressed exclusively in neurons, is also upregulated during differentiation confirming neuronal cell differentiation (**Fig4.8B**). As we observed more cell death in the FBXO7 knockdown cell cultures, cleaved caspase 3 levels were examined as an apoptotic marker, but they were upregulated to the same extent in both differentiated cell lines (**Fig4.8D**). Surprisingly, cyclin D2 levels were lower in differentiating P19 FBXO7 deficient cells (**Fig4.8C**). Apart from forming complexes with CDK4 or CDK6 and driving G_1/S cell cycle transition, cyclin D2 has been shown to be critical for adult neurogenesis.[304] This would suggest that due to the lack of cyclin D2 upregulation during differentiation, adult neurogenesis may be impaired in mice deficient for FBXO7 expression. However, this potential phenotype

would need to be investigated further. In order to gain a clearer picture of what is occurring in P19 control and FBXO7 knockdown cell lines over the course of their nine-day neuronal differentiation protocol, it might be interesting to set up a time-course differentiation experiment. This would involve harvesting cells on each day of the protocol for immunoblotting to see when FBXO7 and CDK6 expression is reduced and when βIII tubulin and p27 proteins are upregulated during differentiation. This time course will be conducted with a high and low concentration of retinoic acid to see whether FBXO7 knockdown affects differentiation potential under any of these conditions. I would also include immunoblots for other cell cycle regulators like cyclin E, cyclin A, cyclin D3, and CDK4 to gain a better overview of the kinetics of cell cycle withdrawal during differentiation. This would also be correlated with visual checks of cell morphology and neurite elaboration over the course of the experiment. Overall, at this stage, it does not seem that FBXO7 has a substantial effect on the differentiation of the P19 cell line.

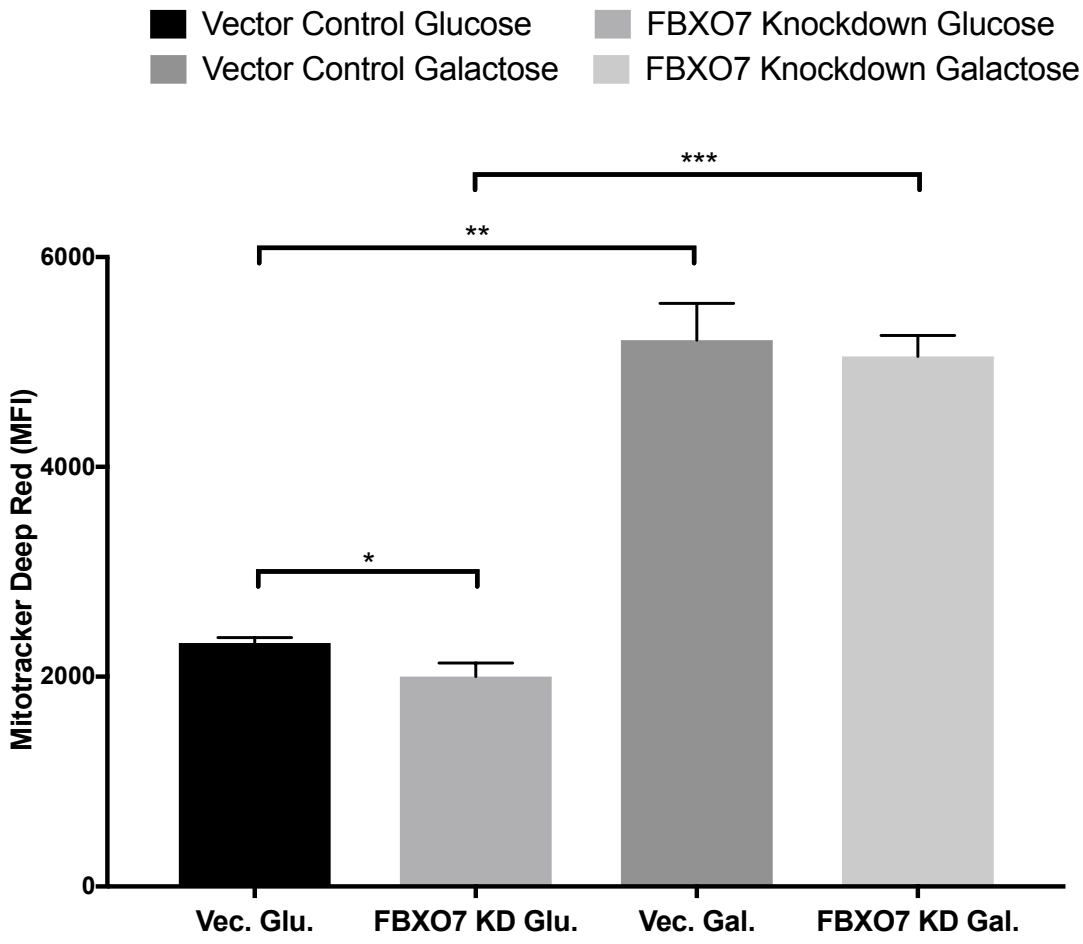

Figure 4.4 – Polarised mitochondrial load of FBXO7 shRNA knockdown SH-SY5Y cell lines. MitoTracker Deep Red staining and flow cytometry analysis of SH-SY5Y-GFP vector control (Vec) and FBXO7 knockdown (KD) cells grown in glucose or galactose supplemented DMEM. Under glucose conditions, KD cells had 13.8% fewer polarised mitochondrial compared to control lines. In the Vec and KD lines, mitochondria increased 2.24-fold and 2.54-fold respectively when grown in galactose compared to glucose media. Data points represent mean values and error bars represent ±SD. (n=3) *p<0.05, **p<0.01, ***p<0.001

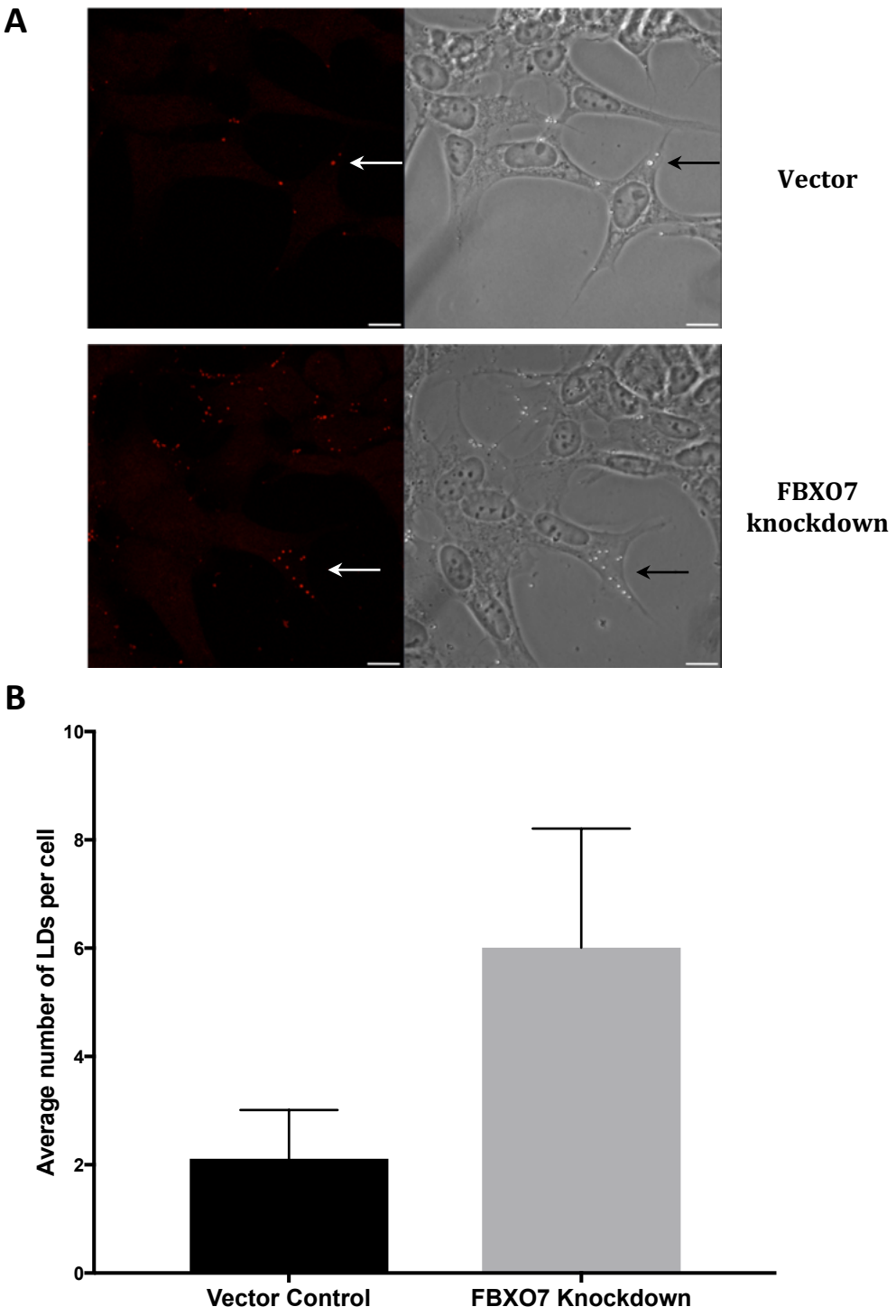

Figure 4.5 – Lipid droplet staining in FBXO7 shRNA knockdown SH-SY5Y cell lines. (A) Representative fluorescence (left panels) and phase contrast (right panels) images of Oil Red O lipid droplet staining in SH-SY5Y-mCherry vector control and FBXO7 knockdown cells. Scale bar represents 10µm. (B) Quantification shows the average number of lipid droplets per cell was 2.11 in SH-SY5Y-mCherry vector control cells (85 cells counted) and 6.01 in SH-SY5Y-mCherry FBXO7 knockdown cells (90 cells counted) (n=1). Data points represent the mean and error bars represent ±SD.

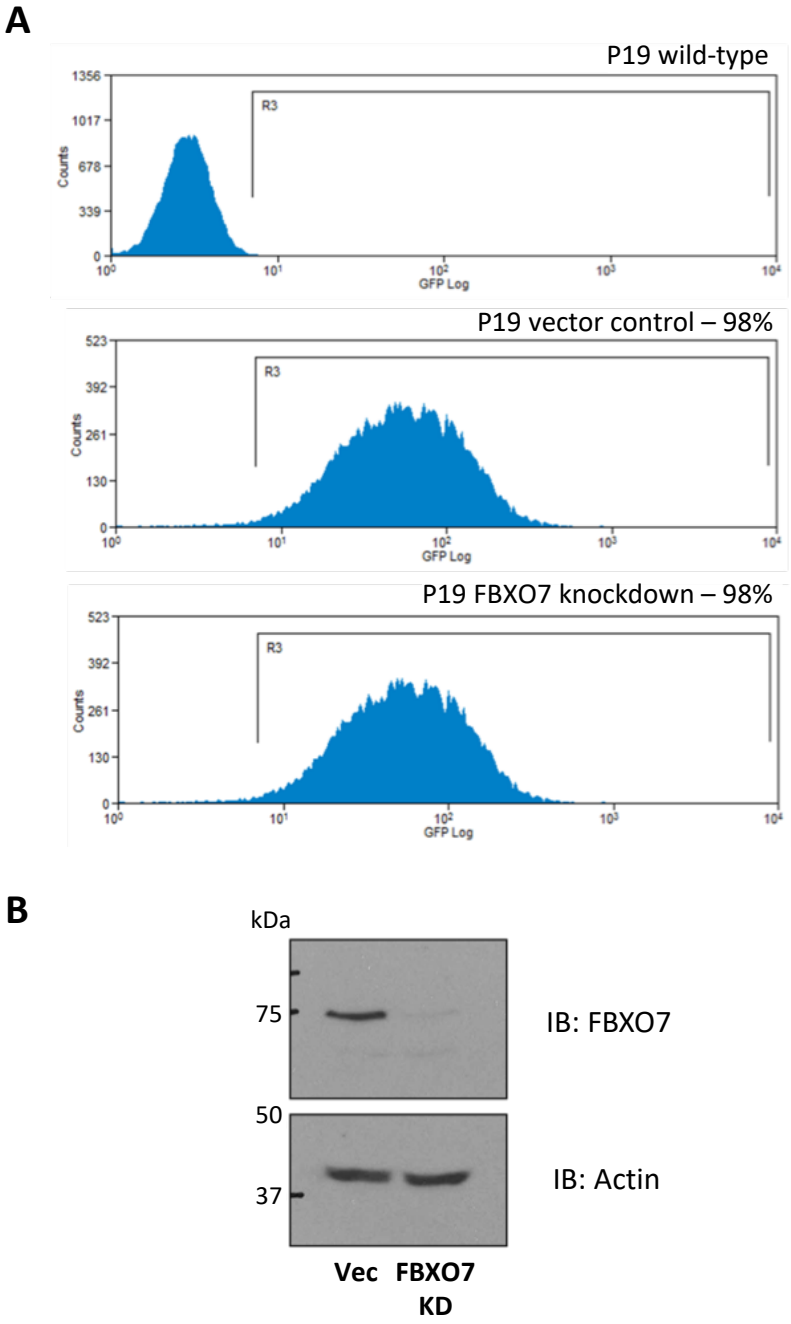

Figure 4.6 – Generation of P19 cell lines with reduced FBXO7 expression. (A) Flow cytometry analysis shows that infections efficiency was 98% in both P19 vector control (vec) and knockdown (KD) cell lines. (B) Immunoblotting for FBXO7 shows a 95% reduction in FBXO7 expression. Quantified normalised to actin levels as the loading control.

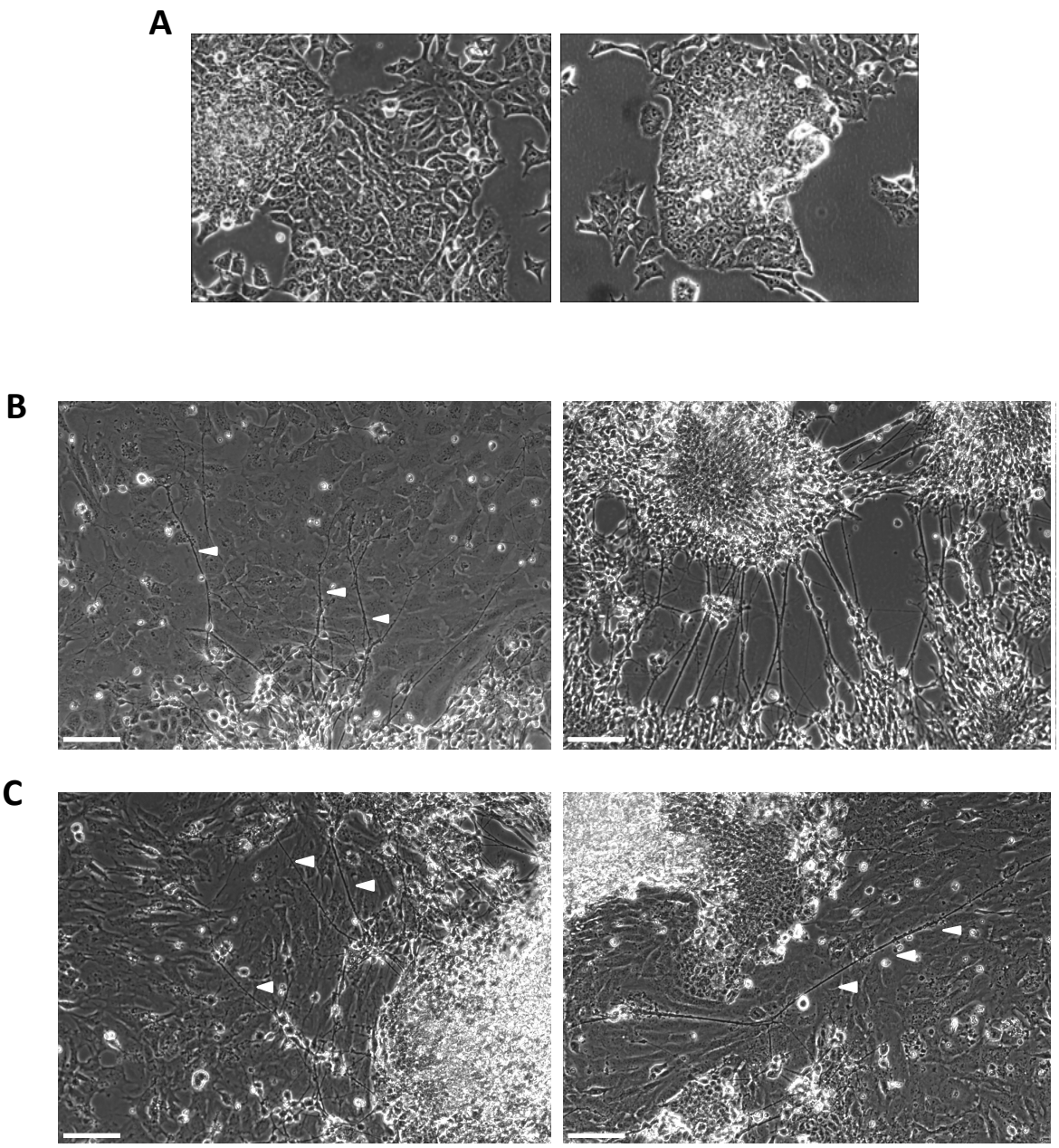

Figure 4.7 – Differentiation of *Fbxo7* knockdown P19 cells with retinoic acid. (A) Phase contrast images of wild-type undifferentiated P19 cells. (B) Phase contrast images of differentiated P19 vector control line. (C) Phase contrast images of differentiated P19 FBXO7 knockdown cells line. Scale bars represent 100µm. Arrows point to projections.

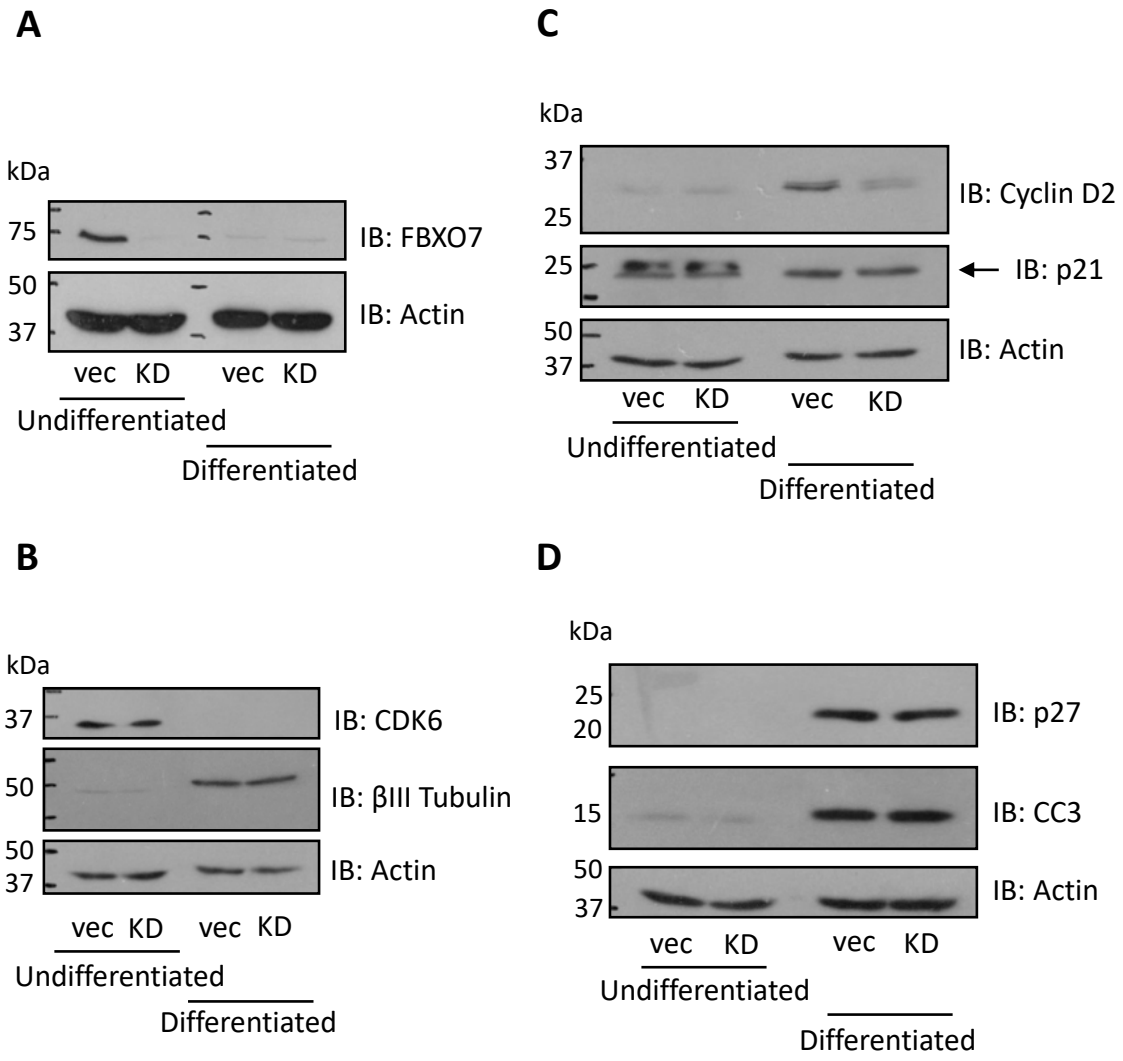

Figure 4.8 – Immunoblots of undifferentiated and differentiated control and FBXO7 knockdown P19 cell lines. Expression of FBXO7 (A), CDK6 and βIII Tubulin (B), cyclin D2 and p21 (C), and p27 and cleaved caspase 3 (CC3) (D) in undifferentiated and differentiated vector control (vec) and FBXO7 knockdown (KD) P19 cells.

4.5 – Proliferation and viability of FBXO7 CRISPR knockout cells

I engineered a complete *FBXO7* knockout SH-SY5Y cell line to prevent any effects that may be occurring due to residual FBXO7 expression in the knockdown lines and because the patient fibroblasts did not express any FBXO7 either. I generated an FBXO7 KO cell line using the Genome-scale CRIPSR Knock-Out (GeCKO) system. SH-SY5Y cells were infected with two lentiviral vectors, the lentiCas9-Blast with the SpCas9 cassette and the lentiGuide-Puro with the sgRNA sequences. Four single guide RNAs (sgRNA) targeting *FBXO7* exons 2 and 3 (**Fig4.9A**) and one non-targeting (NT) sgRNA as a control were designed and cloned into the lentiGuide-Puro plasmids by our collaborator Mr. Liam Lee in Dr. Suzanne Turner's laboratory (Department of Pathology, Addenbrooke's Hospital). The design, cloning and transduction of sgRNAs is described in more detail in Chapter 2, Section 2.1.3.

Once expressed in cells, the Cas9-sgRNA complex binds to the specific target sequence with a PAM motif (Protospacer Adjacent Motif) and the target DNA is cleaved by Cas9 forming a double-strand break. I selected infected cell lines with 3μg/mL puromycin and 10μg/mL blasticidin, and took cell lysates to immunoblot for FBXO7 expression. **Fig4.9B** showed no FBXO7 expression was detected in cell lines infected with sgRNA1, sgRNA2 and sgRNA4. SgRNA3 did not ablate FBXO7 expression possibly because it spans an exon boundary. I next created clonal cell lines by serial dilution of the sgRNA2 line which had the lowest off-target score out of the three sgRNAs that caused a loss of FBXO7 expression in their polyclonal populations. Immunoblots of clonal cell lysates show that clone 2.2 retained what is thought to be either a non-specific band or a truncated protein caused by a frameshift, so complete FBXO7 null clones 2.1 and 2.3 were carried forward (**Fig4.9C**).

I first investigated the proliferation rate and viability to check whether having a null allele would reveal any significant phenotypes not observed in the knockdown lines. As seen in **Fig4.10,** the two FBXO7 knockout clones proliferate faster in both glucose and galactose media compared to the non-targeting control line. I found FBXO7 KO clones 2.1 and 2.3 proliferate 30% and 15.6% faster in glucose and 13.7% and 9.6% faster in galactose than NT control cells. In order to establish the mechanism by which FBXO7 KO increases SH-SY5Y proliferation rate, I would next assay for a panel of cell cycle regulators, in the first instance checking for differences in p27 levels. Accordingly, PI

staining for total DNA content and EdU/BrdU staining for active DNA synthesis would give a comprehensive overview of cells at each stage of the cell cycle, allowing for clear separation of cells in G_1 from early S phase, and late S phase from G_2/M. We would be able to see whether FBXO7 KO cells are cycling faster, possibly due to alleviated p27 inhibition.

There were no differences in cell viability throughout the assay (**Fig4.11**), coinciding with the increased proliferation rate. These findings do not coincide with the trend observed in the knockdown cell line, implying that FBXO7 does not affect cell viability under basal conditions or when cells were reliant on OXPHOS. It might be also informative to include a polyclonal CRISPR line to confirm that these phenotypes are not as a result of clonal effects, or test FBXO7 loss in a transient or inducible manner.

4.6 – Mitochondrial load and morphology in FBXO7 CRISPR knockout cells

Mitochondria are very dynamic organelles, undergoing fusion and fission events continuously.[368] Their morphologies are fundamental to the functionality of the cell and can range from fragmented to hyperfused networks.[368] Therefore, to further test for the presence of a mitochondrial defect, I stained cells with MitoTracker Deep Red and analysed with flow cytometry to quantify polarised mitochondrial load and with confocal microscopy to image their network. Firstly, I looked at polarised mitochondrial load under basal glucose conditions (**Fig4.12**) and following growth in galactose (**Fig4.13**). MitoTracker Deep Red staining and flow cytometry analysis of polarised mitochondria showed that there was no significant difference between NT control and FBXO7 KO clone 2.3 when cells were grown in glucose-containing media (**Fig4.12**). Thus, the absence of FBXO7 does not result in any dysregulation of polarised mitochondrial load under basal conditions. Overall, these CRISPR lines did not respond to being cultured in galactose in the same way as the knockdown cells did in **Fig4.4,** where staining of mitochondria was increased 2.3- to 2.5-fold for control and FBXO7 deficient cells. In NT and FBXO7 null CRISPR cells, there was no increase of polarised mitochondria when cells were grown in galactose compared to glucose **(Fig4.13)**. This difference could once again be due to the different time scales of these experiments, with the shRNA MitoTracker staining conducted after 21 days of galactose exposure. **Fig4.13** shows that after 24-hour of growth in galactose, there were 19.7% more mitochondria in KO clone 2.3 compared to NT control, and this difference increased after longer

periods of growth in galactose-containing media. Both clones 2.1 and 2.3 had respectively 29.1% and 43% more mitochondria compared to the NT control after being grown in galactose media for 11 days. This data may suggest that FBXO7 functions to inhibit the increase of mitochondria upon the switch to a requirement for greater OXPHOS in these CRISPR lines.

I also used MitoTracker Deep Red to image the mitochondrial network in these cells. As seen in **Fig4.14**, the FBXO7 KO clone 2.3 appeared to have a more fragmented and punctate mitochondrial network under basal conditions, compared to the NT control. Previous studies have shown that a fused mitochondrial network can increase mitochondrial robustness, oxidative capacity and efficiency.[368] This results in connected mitochondria having higher protection against apoptotic stresses, an increase in ATP production and improved quality control.[368] Thus, the qualitative observations that mitochondria were not as elongated and connected as in the NT cell lines is indicative of possible mitochondrial dysfunction in cells lacking FBXO7 expression and that the loss of FBXO7 affects mitochondrial morphology. However, quantification of this phenotype would be necessary.

A

FBXO7 exon 2

TTCTAATACCCGATTTACAATTACATTGAACTACAAGGATCCCCTCACTGGAGATGAAGAGACCTTGGCTT
CATATGGGATTGTTTCTGGGGACTTGATATGTTTGATTCTTCAAGATGACATTCCAGCGCCTAATATACCTT
CATCCACAGATTCAGAGCATTCTTCACTCCAGAATAATGAGCAACCCTCTTTGGCCACCAGCTCCAATCA
GACTAGCATGCAGGATGAACAACCAAGTGATTCATTCCAAGGACAGGCAGCCCAGTCTGGTGTTTGGA
ATGACGACAGTATG

FBXO7 exon 3

TTAGGGCCTAGTCAAAATTTTGAAGCTGAGTCAATTCAAGATAATGCGCATATGGCAGAGGGCACAGGT
TTCTATCCCTCAGAACCCATGCTCTGTAGTGAATCGGTGGAAGGGCAAGTGCCACATTCATTAGAGACCT
TGTATCAATCAGCTGACTGTTCTGATGCCAATGATGCCTTGATAGTGTTGATACATCTTCTCATGTTGGAGT
CAGGTTACATACCTCAG

			potency score	off-target score
sgRNA #1	ACCGATTCACTACAGAGCAT	antisense	0.59	82
sgRNA #2	GATAATGCGCATATGGCAGA	sense	0.45	76
sgRNA #3	GGAATGACGACAGTATGTTA	sense	0.45	72
sgRNA #4	AGATAATGCGCATATGGCAG	sense	0.40	78

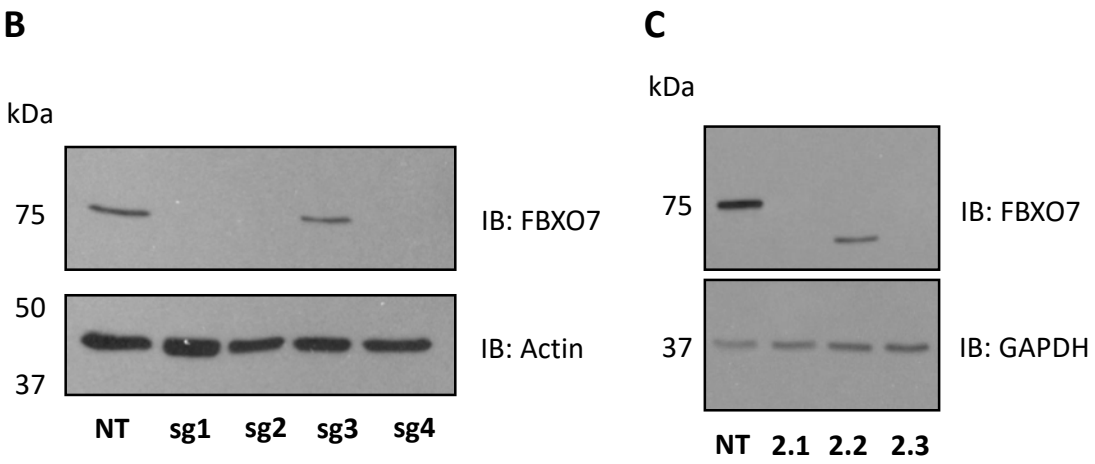

Figure 4.9 – Generation of CRISPR FBXO7 KO SH-SY5Y cell lines. (A) Sequences and characteristics of the 4 sgRNAs that were used and which FBXO7 sequence they target. The Protospacer Adjacent Motif (PAM) is underlines for each sgRNA. Potency score based on Doench *et al.,* 2014 (Nat. Biotech.), available through sgRNA Designer (http://www.broadinstitute.org/rnai/public/analysis-tools/sgrna-design). Off-target score based on CRISPR Design website from Zhang Lab MIT, available through CRISPR.MIT.edu. Off-target scores greater than 50 are considered acceptable for use with minimal off-target effect. For both scores, the higher the score, the better. (B) Immunoblots of SH-SY5Y lysates, treated with non targeting (NT) sgRNA and 4 different sgRNA targeting FBXO7, showing sgRNA1,2 and 3 achieved FBXO7 KO. (C) Immunoblots of SH-SY5Y lysates after generating clones from the sgRNA2 polyclonal population. Clone 2.2 may express the second isoform of FBXO7, whereas clones 2.1 and 2.3 do not express any FBXO7 compared to the NT control.

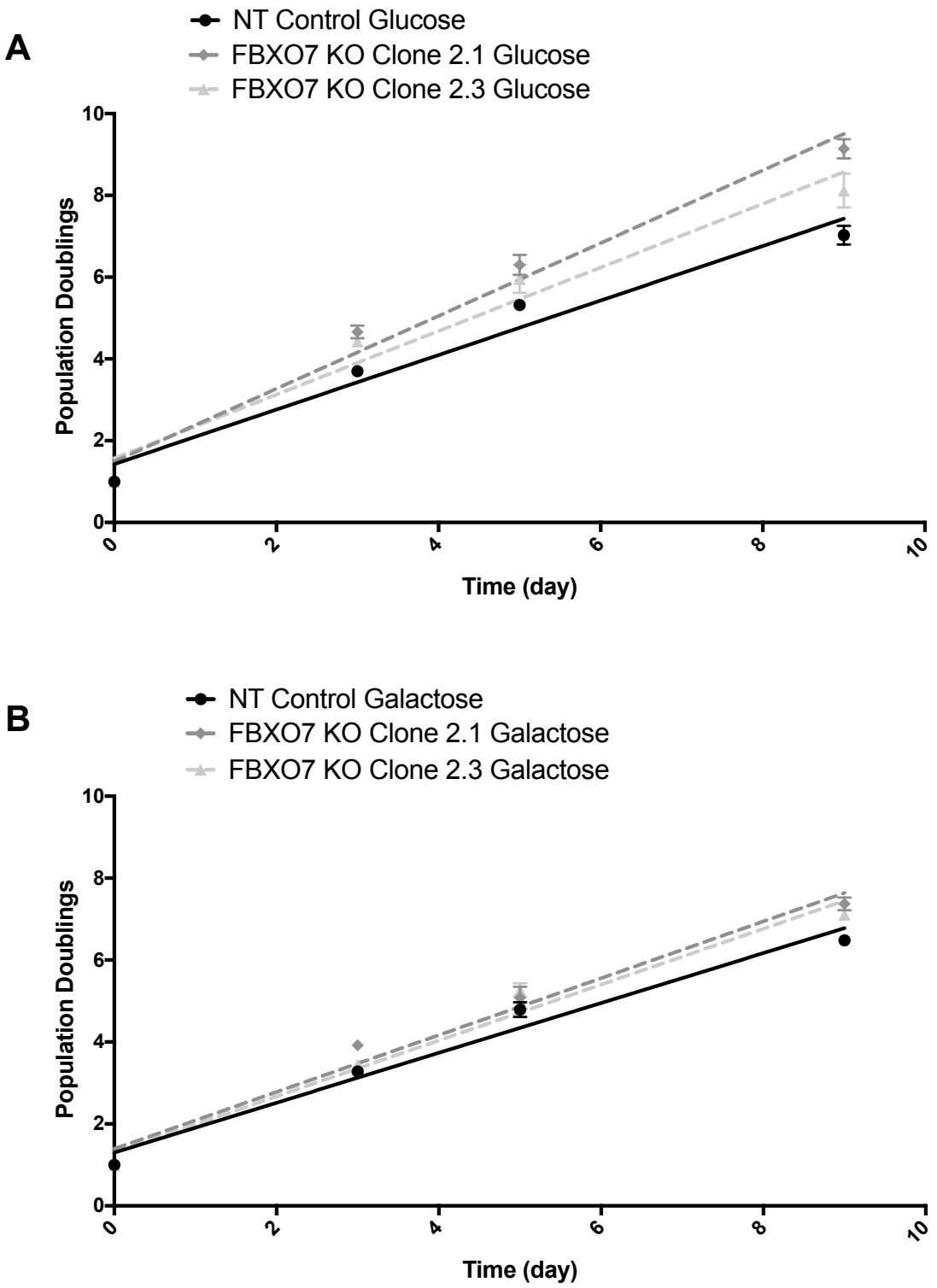

Figure 4.10 – Proliferation assays of CRISPR FBXO7 KO SH-SY5Y cell lines. (A) Clones 2.1 and 2.3 proliferate 1.3x and 1.2x faster compared to NT control when grown in DMEM supplemented with glucose. (B) Clones 2.1 and 2.3 proliferate 1.1x and 1.1x faster compared to NT control when grown in DMEM supplemented with galactose. The population doubling rate was determined by re-seeding cell lines in triplicate at $2x10^5$ cells per well every 2-3 days. (n=1) Data points represent the mean and error bars represent ±SD.

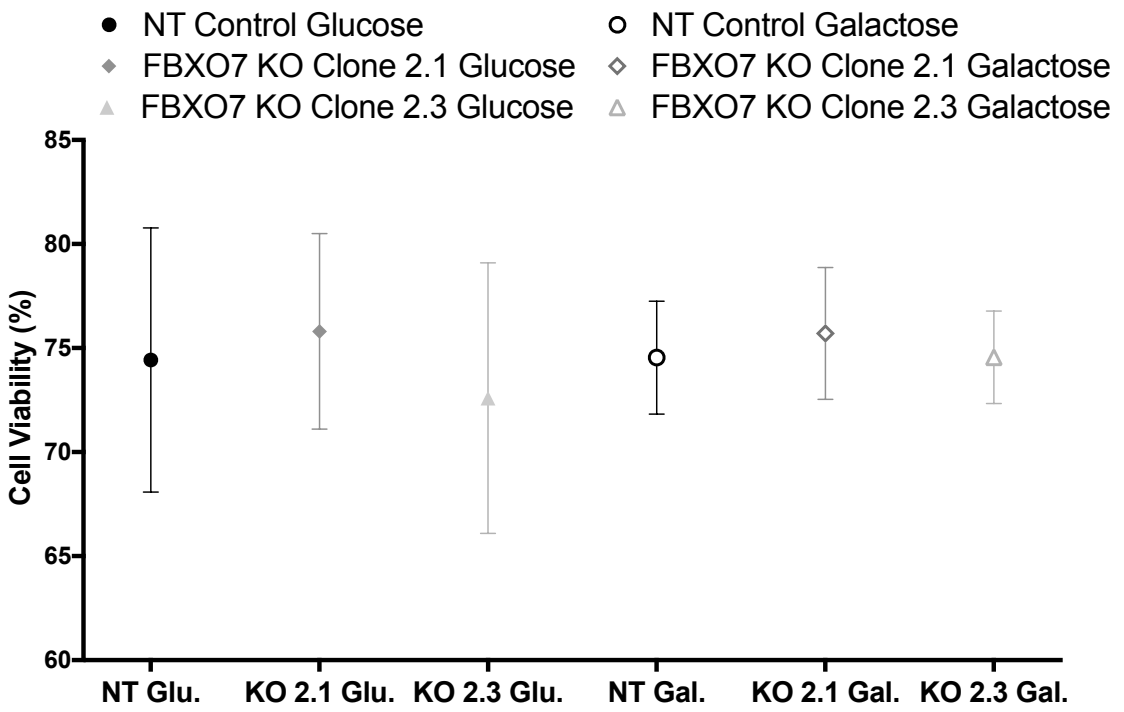

Figure 4.11 – Viability of CRISPR FBXO7 KO SH-SY5Y cell lines. Cell viability (measured by the CASY Cell Counter) of non- targeting control (NT) and FBXO7 KO clones grown in glucose or galactose supplemented DMEM. There were no significant differences among NT, clone 2.1 and clone 2.3 over the course of the proliferation assays when grown in both glucose or galactose media. (n=1) Data points represent the mean and error bars represent ±SD.

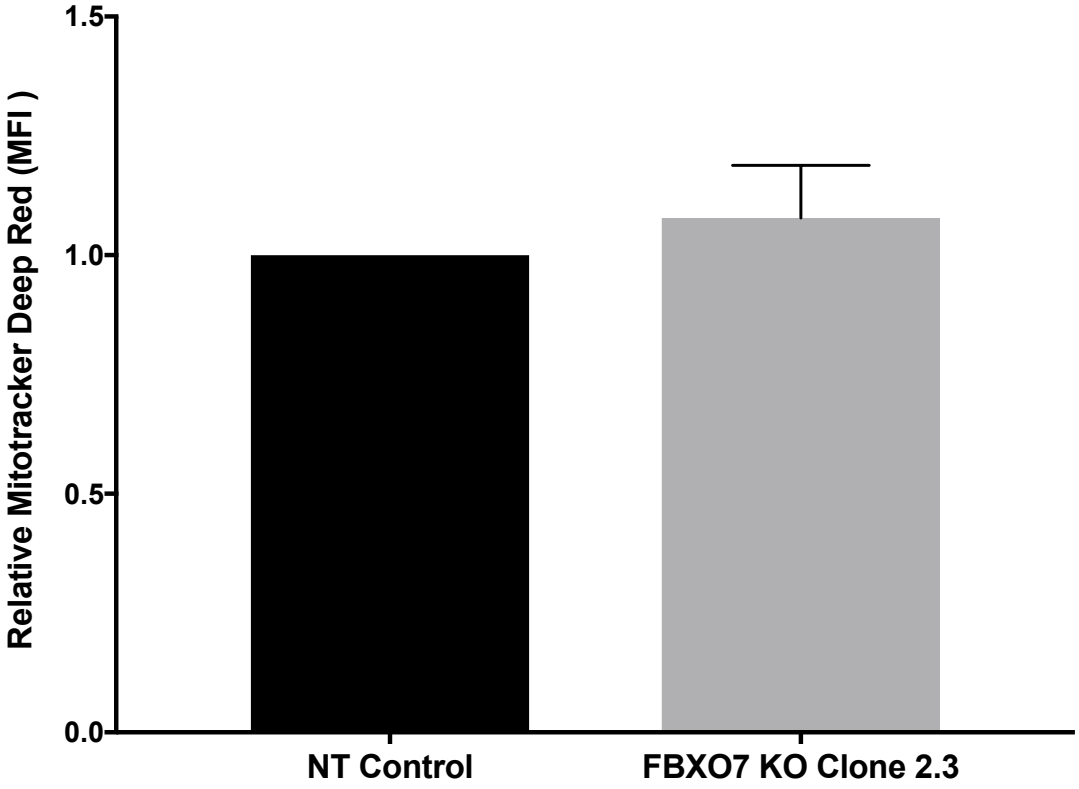

Figure 4.12 – Polarised mitochondrial load in CRISPR FBXO7 KO SH-SY5Y cell lines under basal conditions. Amount of polarised mitochondria, stained with MitoTracker Deep Red and quantified by flow cytometry. MFI of FBXO7 KO clone 2.3 analysed relative to NT control, showing no significant differences (n=5). Error bars represent ±SD.

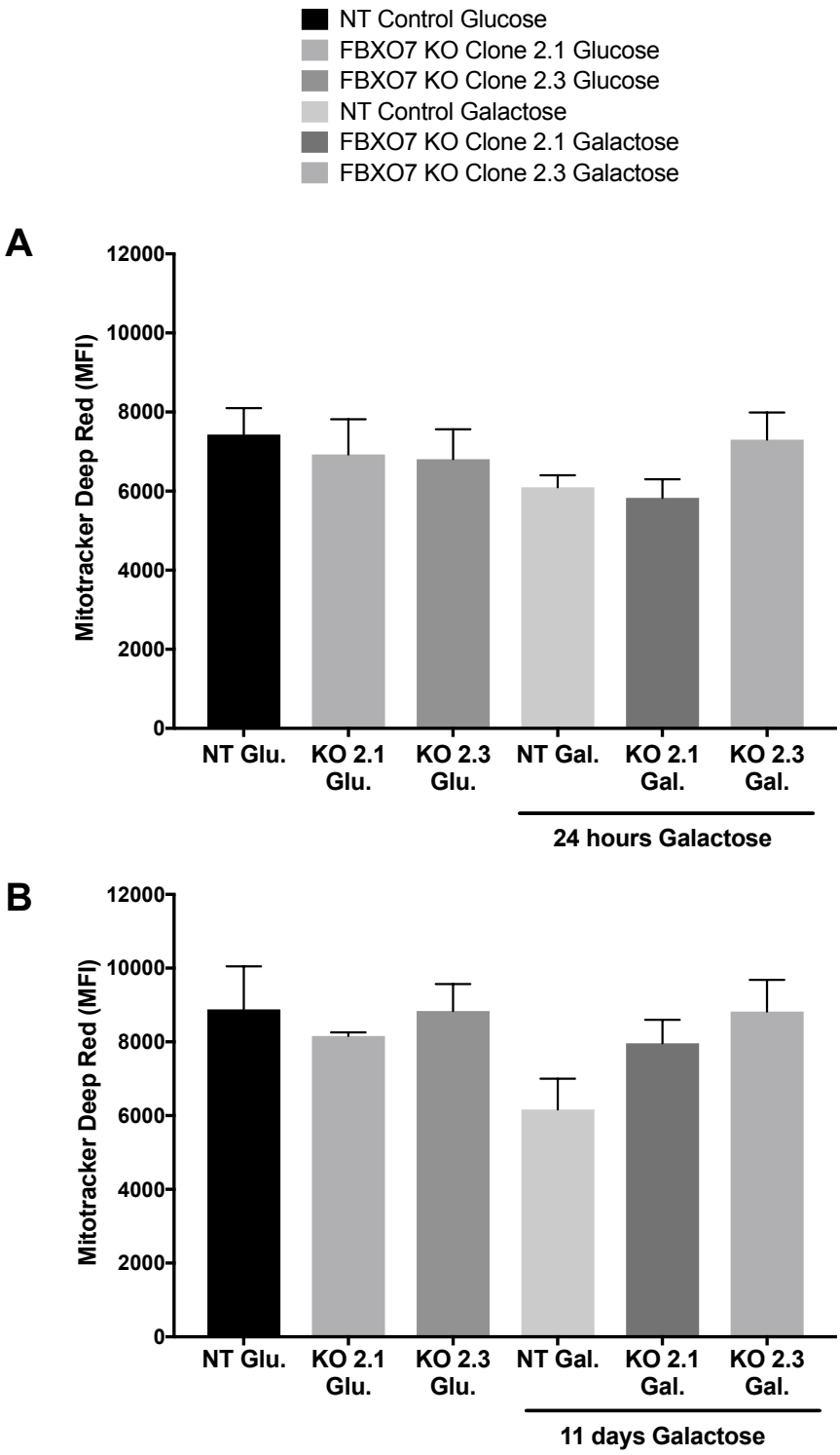

Figure 4.13 – Polarised mitochondrial load in CRISPR FBXO7 KO SH-SY5Y cell lines under galactose growth conditions. MitoTracker Deep Red staining and FACS analysis of cell lines grown in glucose, short-term galactose and long-term galactose exposure. (A) There were no significant differences when cells lines were grown in glucose media. After 24 hour growth in galactose media, there was a trending increase in polarised mitochondria in clone 2.3 but not clone 2.1. (B) No significant differences were confirmed when cells lines were grown in glucose media. After growing in galactose media for 11 days, there was a trending increase in polarised mitochondria in both clone 2.1 and 2.3. (n=1) Data points represent the mean and error bars represent ±SD.

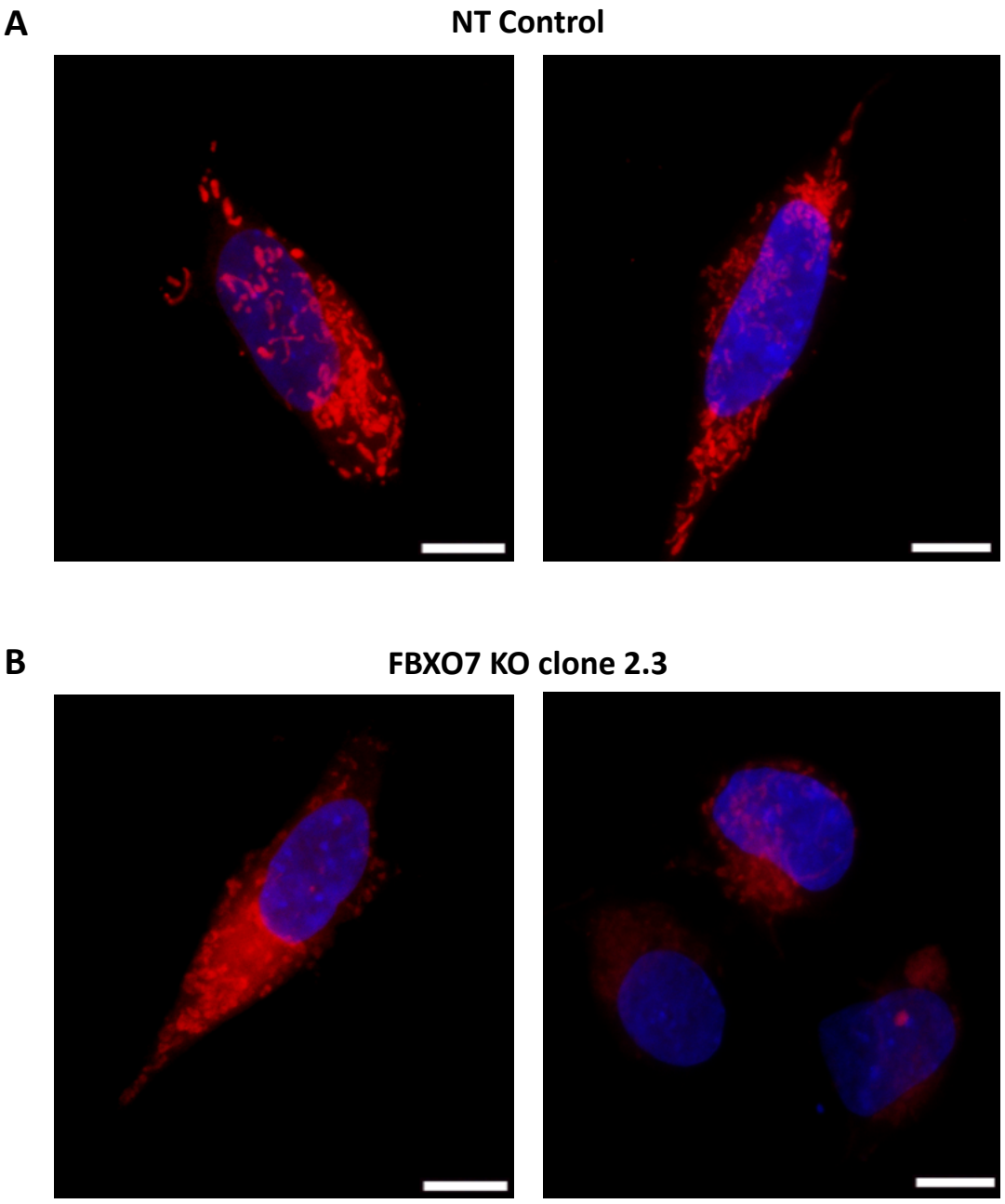

Figure 4.14 – MitoTracker Deep Red imaging of polarised mitochondrial network in CRISPR FBXO7 KO SH-SY5Y cells. (A) Representative images of mitochondrial network in NT control cells (analysed 40 cells, 13 fields of view). (B) Representative images of FBXO7 KO clone 2.3 cells (analysed 34 cells, 12 fields of view), showing a more fragmented and punctate mitochondrial network (not quantified). Scale bar represents 10µm.

4.7 – Lipid droplet phenotype of FBXO7 CRISPR knockout cells

Due to the previously mentioned dynamic interaction between lipid droplets and mitochondria and the observed trend of LD accumulation in the FBXO7 knockdown cell lines, which can also be an indication of mitochondrial dysfunction, I explored the potential for a lipid droplet phenotype in FBXO7 CRISPR KO cells. I first quantified FFA levels in these cell lines to test whether they may be upregulated in FBXO7 KO clone 2.3 cells due to the observed change of the mitochondrial network morphology and potential mitochondrial dysfunction. Long-chain FFA were quantified using a colorimetric Free Fatty Acid Assay Kit and normalised to a palmitic acid standard curve. **Fig4.15** shows that the FBXO7 KO clone 2.3 had significantly 16.7% more FFA compared to the NT control. This suggests that there might be more LDs and/or larger LD surface area per cell in FBXO7 KO clone 2.3 cells. However, ORO staining under basal glucose conditions showed that FBXO7 KO clone 2.3 had 55.1% fewer LDs per cell and 56.1% less LD surface area per cell, relative to the NT control cells (**Fig4.16**).

Subsequently, an additional starvation condition was added to the ORO assay, which consisted of a 24-hour incubation period in HBSS media. Under starvation, cells shift from glucose metabolism to mitochondrial fatty acid oxidation and can be used to investigate whether LDs were being utilised properly and whether mitochondrial fusion occurs, which is necessary for the proper distribution and oxidation of FAs. Due to the fragmented mitochondria that were observed in FBXO7 KO clone 2.3 cells, it was hypothesised that FA oxidation could be defective. Based on a study by Rambold *et al*., it is expected for the number of LDs to increase over time in a wild-type setting under starvation due to LDs being constantly replenished with FAs via autophagy.[251] **Fig4.17** shows that when grown in glucose media, the NT control cells had 3.4x more LDs, which were 4.6x larger in area, compared to FBXO7 KO clone 2.3 cells. The NT control line had a trending decrease in the number of LDs (49.7% reduction) and in their surface area (55% reduction) per cell. Whereas, the FBXO7 KO clone 2.3 line had an increase in the number of LDs (3.2x more) and in their surface area (5.4x larger) per cell. Representative confocal images of the cells stained with ORO that were quantified in **Fig4.17** can be seen in **Fig4.18**.

The discrepancy among the FFA assay, lipid droplet experiments and mitochondrial fragmentation may be due to the adaptation and/or compensatory mechanisms. However, this would need to be further tested in other cell lines, perhaps with inducible loss of FBXO7 expression. In addition, to check whether continued fatty acid biosynthesis is responsible for the accumulation of lipids, we can treat cells with inhibitors. If this does not impact LD accumulation, it would suggest that it is as a result of LDs not being utilised efficiently by the mitochondria (reduced oxidation) or through a direct defect in lipolysis (either via cytosolic lipases or by lipophagy). Taken together, these data suggest that FBXO7 may play a role in lipid droplet metabolism, but this hypothesis would need to be confirmed in a better cell model for these types of assays.

4.8 – CRISPR FBXO7 knockout leads to increased mitochondrial and cytosolic oxidative stress

I next measured mitochondrial oxidative stress as another indicator of mitochondrial health in these cells. I used MitoSOX Red Mitochondrial Superoxide Indicator to stain cells and analyse them by flow cytometry. The MitoSOX Red reagent selectively targets mitochondria and becomes fluorescent upon oxidation by superoxides, but not other reactive oxygen species (ROS) or reactive nitrogen species (RNS). **Fig4.19A** shows that FBXO7 KO clone 2.3 had 6% more MitoSOX MFI relative to the NT control under basal conditions. The cells were also treated with low (100μM) and high (1mM) concentrations of H_2O_2, which resulted in the FBXO7 KO clone 2.3 having 19.1% and 25.5% more MitoSOX MFI compared to NT control lines under the same conditions. When the data was analysed in terms of the relative percentage of MitoSOX positive cells in culture, FBXO7 KO clone 2.3 had a 41.7% and 46.7% relative increase in MitoSOX positive cells under low and high H_2O_2 respectively (**Fig4.19B**). Under basal conditions, the increase of MitoSOX positive cells in the KO was increased by 27.9% but it was not statistically significant. This experiment suggests that the lack of FBXO7 results in the cells exhibiting more mitochondrial oxidative stress under basal conditions, which is further increased under hydrogen peroxide stress.

I also tested whether this increase in oxidative stress is a more global cellular phenotype. Thus, I measured intracellular oxidative stress by staining cells with DCFDA (2', 7'-Dichlorofluorescin diacetate), a cell-permeable non-fluorescent probe that is de-esterified intracellularly and becomes fluorescent upon oxidation, and flow cytometry

analysis. **Fig4.20** shows that the DCFDA MFI, representing intracellular stress, was 8.3% higher in FBXO7 KO clone 2.3 compared to the NT control. Thus, the absence of FBXO7 expression results in an increase of both intracellular and mitochondria-specific oxidative stress. Overall, these experiments suggest that FBXO7 may negatively regulate, either directly or indirectly, oxidative stress levels, playing a protective role. It is also possible that the increased oxidative stress is caused by defective mitophagy,[369] which is mediated by FBXO7, PINK1 and Parkin.[320]

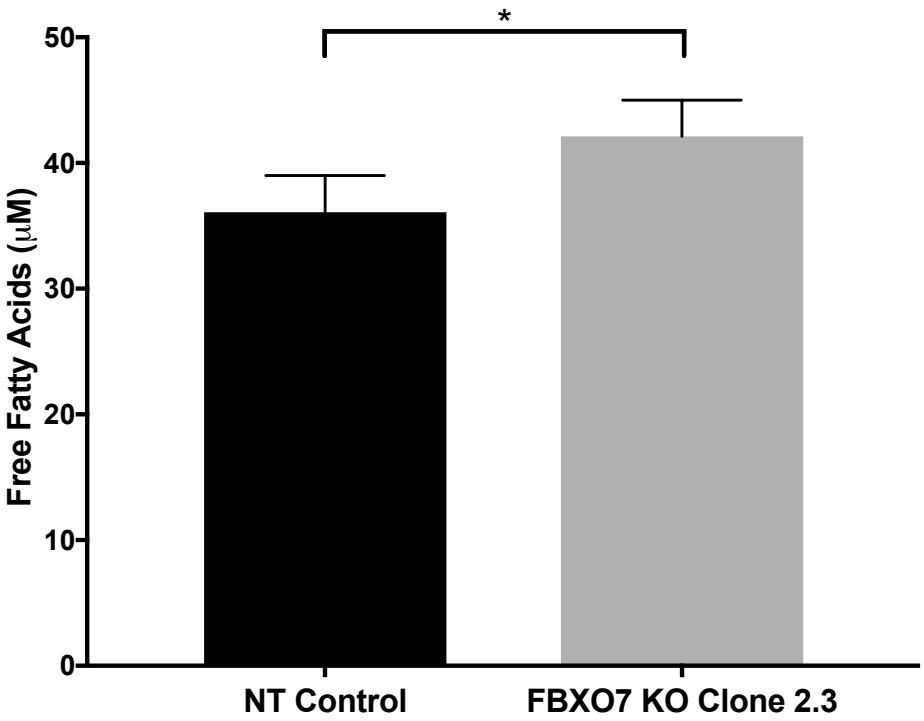

Figure 4.15 – Free fatty acid quantification in CRISPR FBXO7 KO SH-SY5Y cells. The FBXO7 KO clone 2.3 had significantly 16.7% more FFA compared to the NT control. The amount of long-chain FFAs quantified by staining with Free Fatty Assay Kit resulting in a colorimetric output. Absorbance values were normalised to a palmitic acid standard curve. Data points represent the mean and error bars represent ±SD. (n=2) *p<0.05

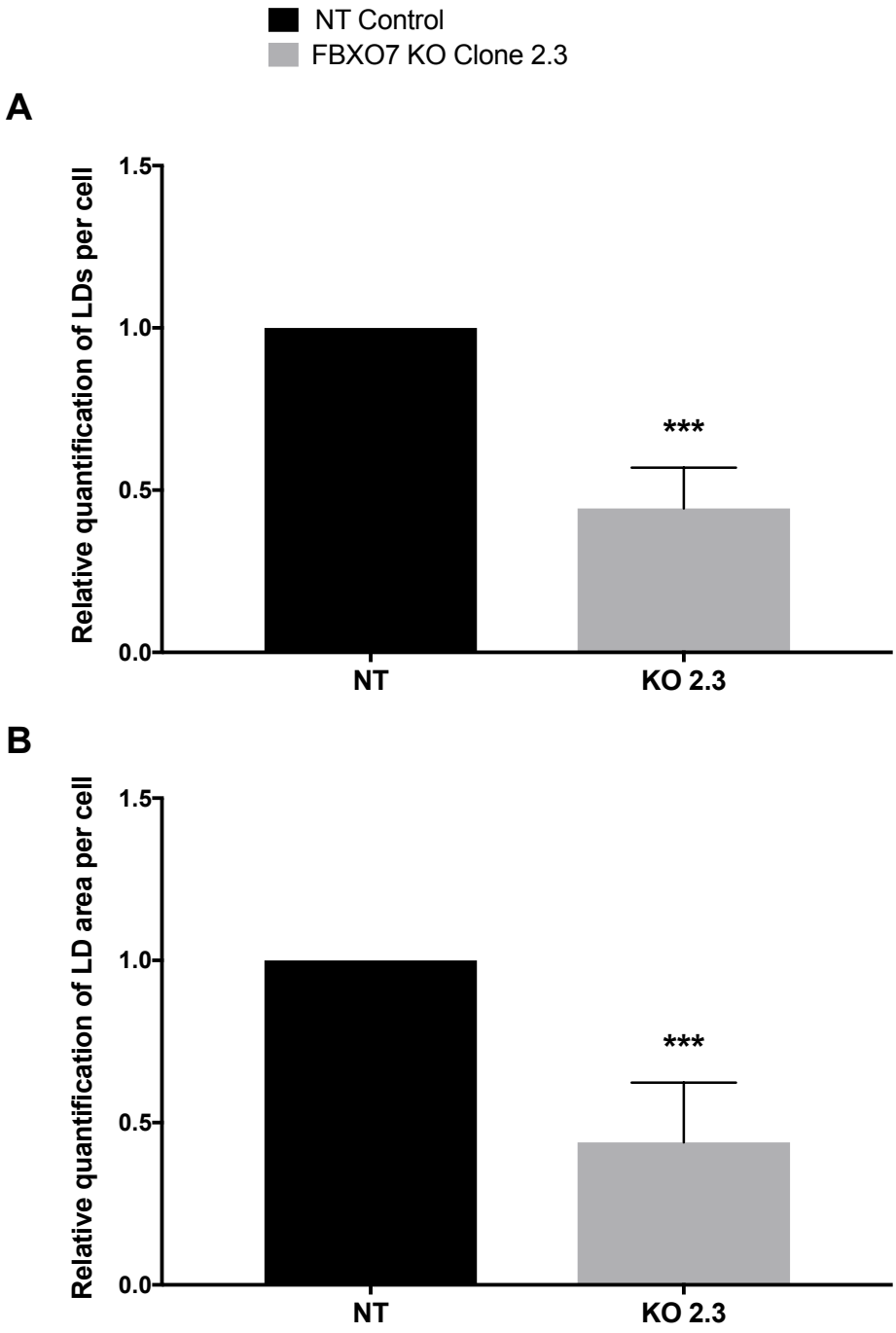

Figure 4.16 – Basal lipid droplet staining in CRISPR FBXO7 KO SH-SY5Y cells. Quantification of ORO staining under basal glucose conditions showing the number of LDs and LD area per cell, relative to the NT control cells. (A) FBXO7 KO clone 2.3 cells have 55.1% fewer LDs per cell relative to NT control cells. (B) FBXO7 KO clone 2.3 cells have 56.1% smaller LD area per cell relative to NT control cells. Data points represent the mean and error bars represent ±SD. A total of 347 cells were counted for the NT condition and 276 cells for the KO 2.3 condition (n=4). ***p<0.001

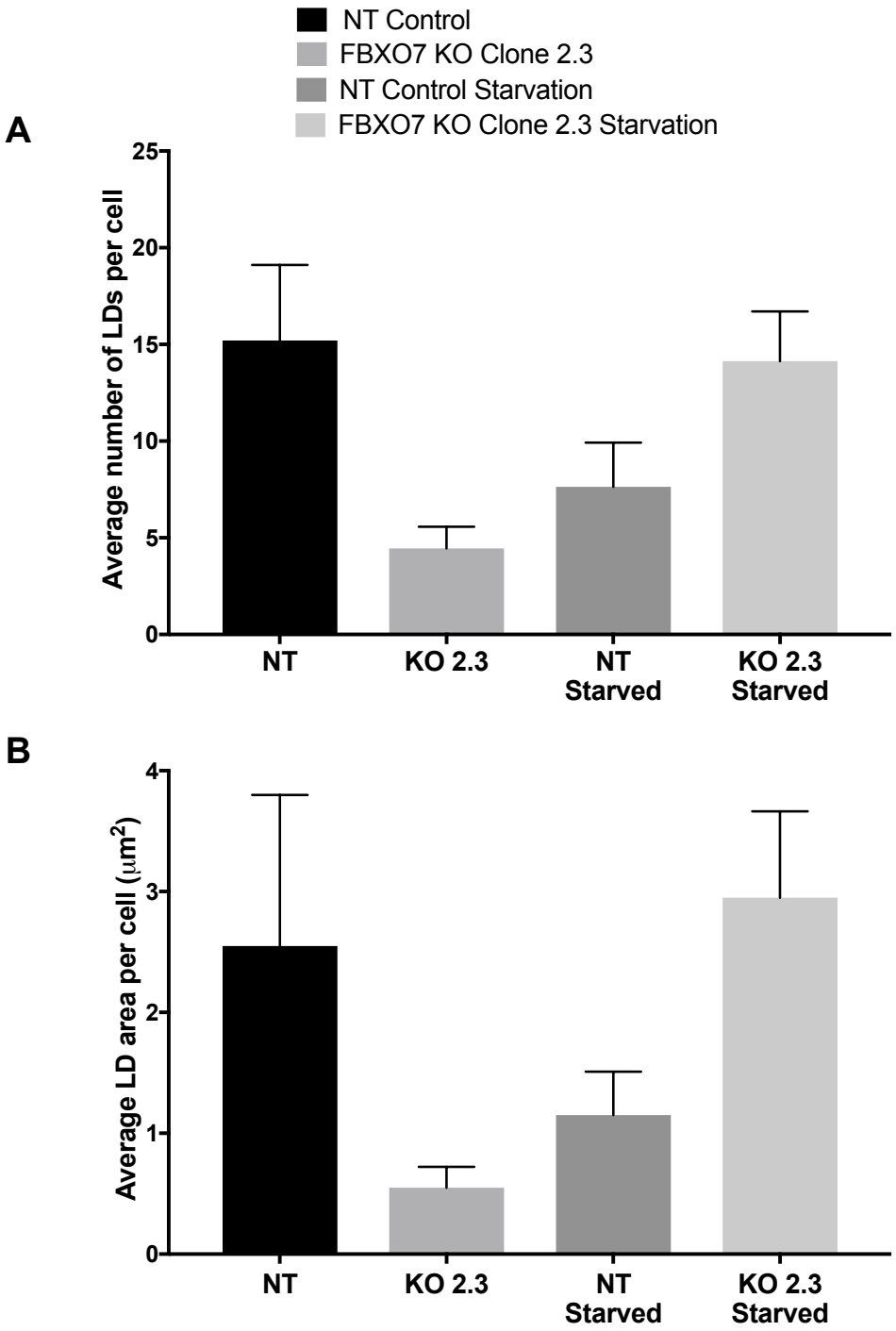

Figure 4.17 – Lipid droplet staining in CRISPR FBXO7 KO SH-SY5Y cells under starvation. Quantification of ORO staining shows the average number of lipid droplets per cell was 15.2 in NT control cells (115 cells counted) and 4.5 in FBXO7 KO clone 2.3 cells (74 cells counted) under basal glucose conditions. The average surface area of lipid droplets per cell was 2.6 μm^2 in NT control cells and 0.6 μm^2 in FBXO7 KO clone 2.3 cells under basal glucose conditions. Upon 24-hour starvation in HBSS media, the average number of lipid droplets per cell decreased to 7.6 and their average surface area per cells decreased to 1.2 μm^2 in NT control cells (74 cells counted). Whereas, the average number of lipid droplets per cell increased to 14.1 and their average surface area per cells increased to 2.3 μm^2 FBXO7 KO clone 2.3 cells (125 cells counted). Data points represent the mean and error bars represent ±SD.

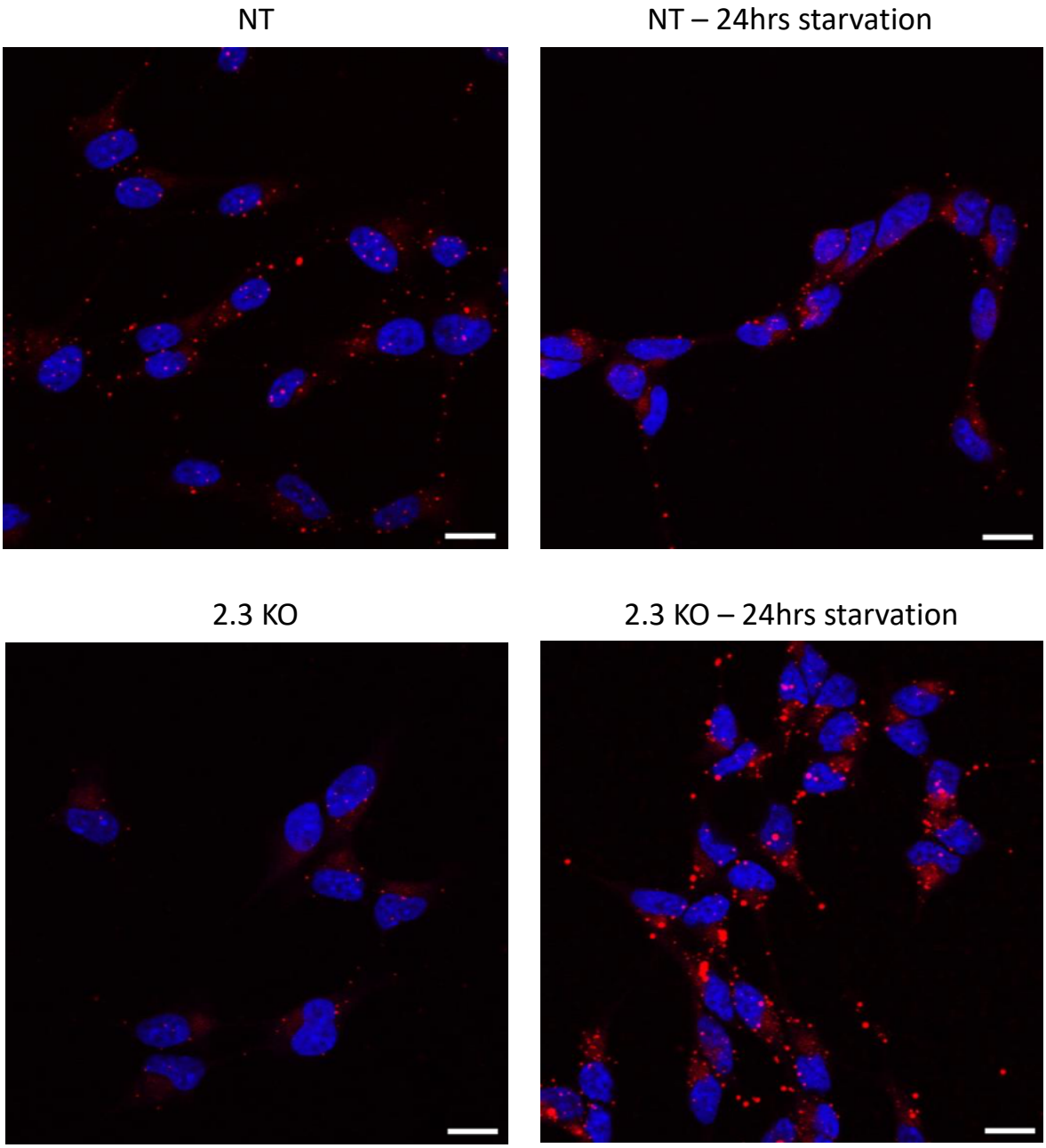

Figure 4.18 – Lipid droplet imaging in CRISPR FBXO7 KO SH-SY5Y cells. Representative fluorescence images of Oil Red O lipid droplet staining in CRISPR FBXO7 KO clone 2.3 and NT cells used for the quantification in Fig4.17. Images show fewer lipid droplet in FBXO7 KO cells compared to NT control cells under basal conditions and an upregulation of lipid droplets in the FBXO7 KO cells after 24-hour starvation in HBSS media. Scale bar represents 10µm.

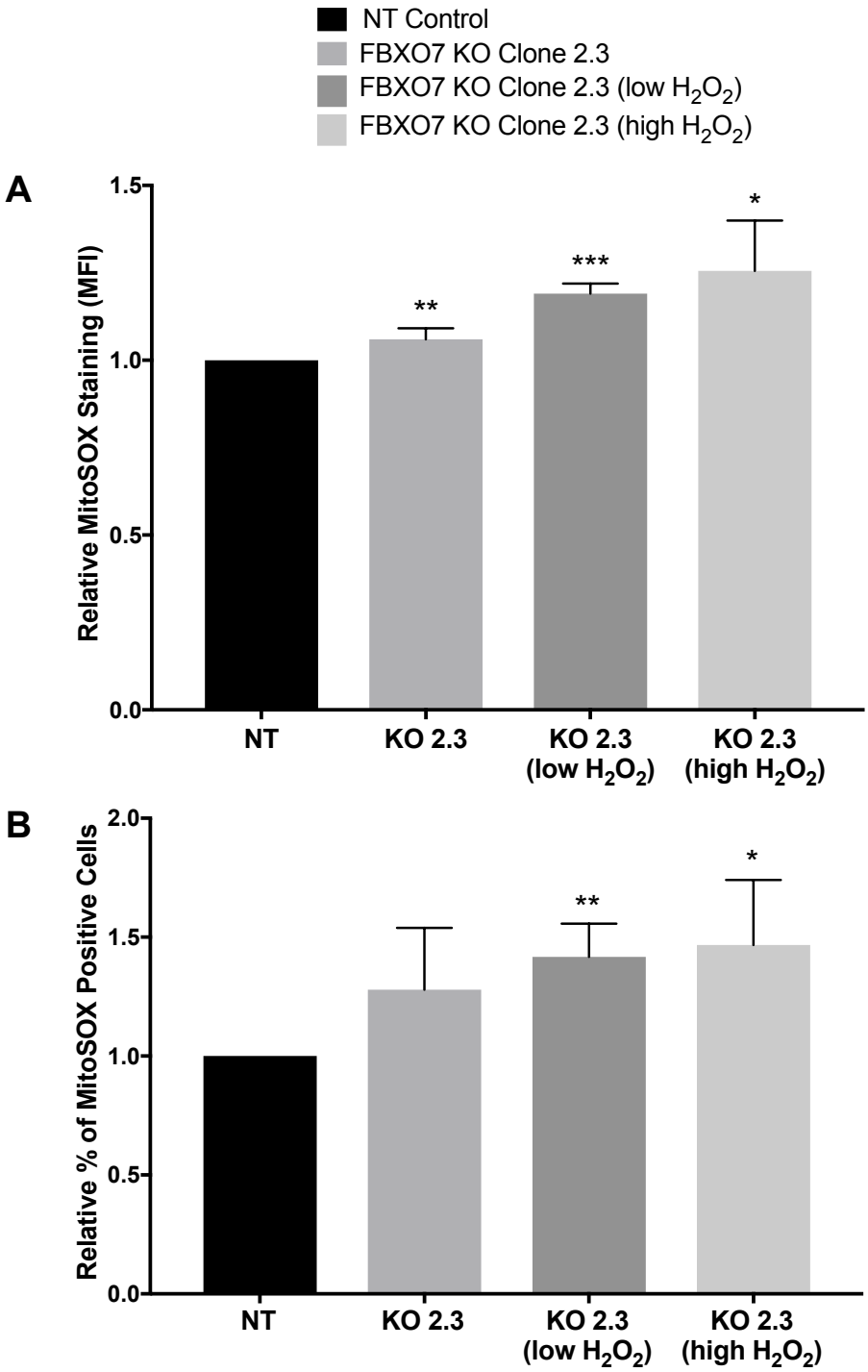

Figure 4.19 – Mitochondrial oxidative stress in CRISPR FBXO7 KO SH-SY5Y cells. MitoSOX staining following by quantification with flow cytometry. MitoSOX Mean Fluorescent Intensity (MFI) and percentage of MitoSOX positive cells were quantified relatively to NT control levels. (A) There is a significant 6% increase of MitoSOX MFI in FBXO7 KO clone 2.3 under basal conditions and an increase of 19.1% and 25.5% under low and high hydrogen peroxide stress respectively compared to NT control. (B) There is a significant 41.7% and 46.7% increase in the percentage of MitoSOX positive cells in FBXO7 KO clone 2.3 under low and high hydrogen peroxide stress respectively, but not under basal conditions, compared to the NT control. (n=3) Error bars represent ±SD. *p<0.05, **p<0.01, ***p<0.001

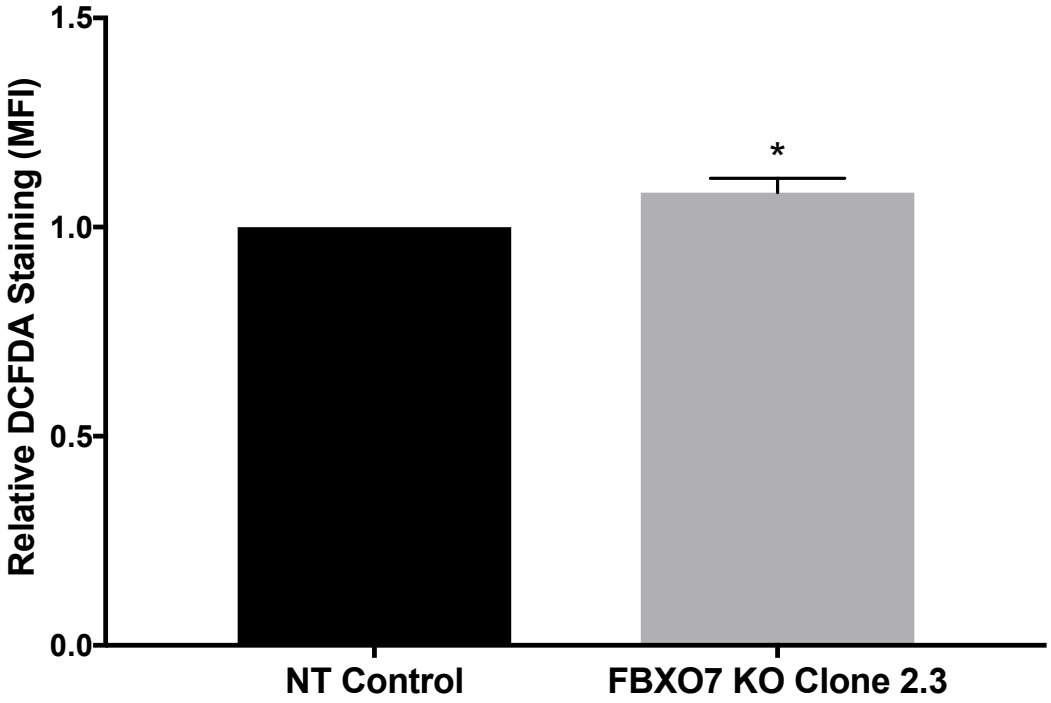

Figure 4.20 – Intracellular oxidative stress in CRISPR FBXO7 KO SH-SY5Y cells. Cells were stained with 10µM DCFDA (2',7'-Dichlorofluorescin diacetate) in HBSS media and analysed with flow cytometry. DCFDA MFI was quantified relative to NT control. FBXO7 KO clone 2.3 had 8.3% more cellular oxidative stress compared to NT control. Error bars represent ±SD. (n=3) *p<0.05

4.9 – Complementation of CRISPR FBXO7 knockout cells

Complementation of FBXO7 back into FBXO7-null cells is important to be able to link the observed phenotypes directly to FBXO7 expression. I first attempted complementation by transient transfection of FBXO7 into the CRISPR KO cells. However, due to the constitutive expression of Cas9 endonuclease in these cells, only low levels of FBXO7 were expressed via transient transfections of FBXO7 expression plasmids. As can be seen in **Fig4.21A**, human FBXO7 (hFBXO7) is expressed very weakly at 48 and 72 hours post-transfection, compared to the expression levels of FBXO7 in the NT controls. Subsequently, I transfected mouse FBXO7 (mFBXO7) to see whether its expression might be higher reasoning that the divergence in sequence might make it less susceptible to cleavage. **Fig4.21B** shows that there is some expression of mFBXO7 48 and 72 hours post-transfection, however it is still low compared to endogenous levels of the NT cells. Thus, due to the sgRNA-Cas9 complex interference with the expression of transfected FBXO7, I created a CRISPR-resistant version of the *hFBXO7* construct. This involved generating silent mutations (depicted in red in **Fig4.22A,** *FBXO7* exon 3) within the guide RNA recognition sequence so that it would no longer be recognised by the sgRNA-Cas9 complex yet retain a wild-type coding capacity. Using this CRISPR-resistant *hFBXO7* plasmid, I was able to re-establish FBXO7 expression in the FBXO7 KO clone 2.3 cells to levels comparable to endogenous FBXO7 in the NT cell line (**Fig4.22B**).

I then tested whether the expression of FBXO7 could rescue the effects of loss of FBXO7 on levels of mitochondrial oxidative stress (as seen in **Fig4.19**). To do this, I transfected cells with the CRISPR-resistant FBXO7 plasmid, and stained cells with MitoSOX 24 hours later. I analysed the MitoSOX MFI of the transfected populations, which were APC-positive, and the untransfected populations, which were APC-negative. The negative and single controls, and representative FACS plots from each cell line are depicted in **Fig4.23**. The first complementation attempt showed an increase in mitochondrial oxidative stress in the FBXO7 KO clone 2.3, which reduced to NT control levels following the addition of FBXO7 (**Fig4.24A**). These trends support the hypothesis that the absence of FBXO7 in the KO cells caused an increase in mitochondrial oxidative stress in these cells. However, when I analysed the untransfected population, the same pattern of MitoSOX MFI was apparent. **Fig4.24B** shows that there was more mitochondrial oxidative stress in the FBXO7 KO cells compared to the NT control. Thus, it seems that this pattern of MitoSOX staining intensity was not directly dependent on FBXO7

complementation. This was further confirmed when this assay was repeated, and there were no significant differences among any of the cell lines (**Fig4.25A**) despite the complemented cell line still expressing FBXO7 (**Fig4.25B**). Due to these cell lines being in culture longer, it is also possible that compensatory mechanisms may have developed which would have resulted in the change of the phenotype in the final repeat of the assay. Furthermore, it may also be that 24 hours may not have been long enough to suppress the levels of oxidative stress in the mitochondria and that a longer timescale may be necessary to reverse this phenotype. Overall, even though I was not able to show a causal effect of FBXO7 on mitochondrial oxidative stress with this experimental design, it does not exclude the hypothesis completely. A future experiment should include a longer timescale, which could be achieved by complementing back WT FBXO7 into these cells using CRISPR and homology directed repair. Alternatively, as my experiments suggest that most effects of FBXO7 seem to be temporary, perhaps a cell model with an inducible system would be better.

In summary, the characterisation of SH-SY5Y CRISPR FBXO7 KO cell lines showed an anti-proliferative trend in this cell type. Furthermore, the lack of FBXO7 expression results in a fragmented mitochondrial network and an increase in both intracellular and mitochondrial oxidative stress suggesting FBXO7 plays an important role in regulating mitochondrial biology. However, there were also inconsistencies in the lipid droplet phenotype and in MitoSOX assays, as transient expression of FBXO7 into the KO line failed to rescue the mitochondrial oxidative stress phenotype. This was possibly due to compensatory mechanisms (as seen with other FBXO7 knockdown phenotypes), the duration of keeping these lines in culture, clonal effects, or other reasons elaborated above. Despite these obstacles, one is still able to take away valuable information as certain experiments are suggestive of FBXO7-deficiency leading to proliferation, lipid droplet and/or mitochondrial phenotypes.

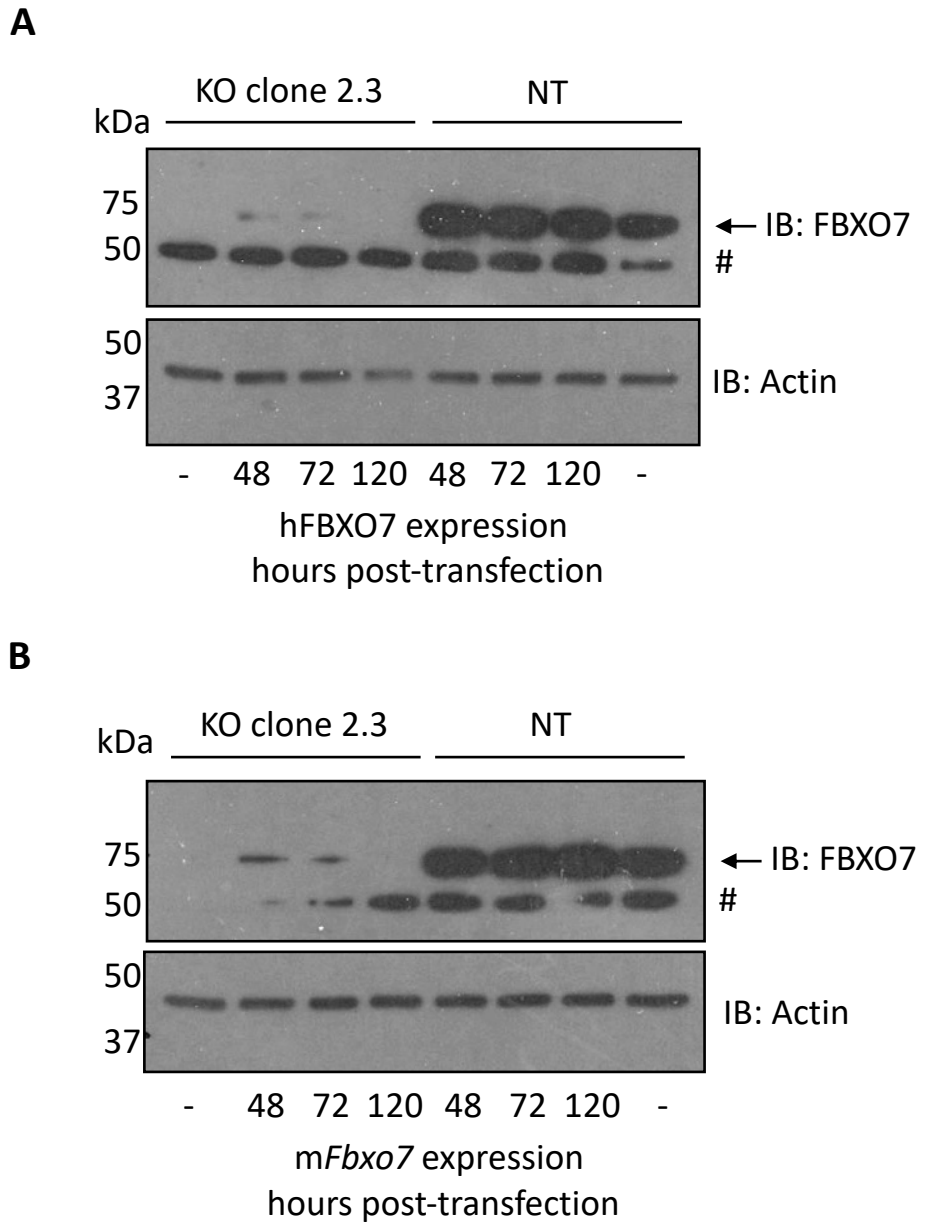

Figure 4.21 – Complementing back FBXO7 into CRISPR lines with h*FBXO7* and m*Fbxo7* transient transfections. (A) Immunoblots showing FBXO7 expression levels at 48, 72 and 120hours post-transfection of human *FBXO7* (*hFBXO7*) into CRISPR FBXO7 KO clone 2.3 and NT control. (B) Immunoblots showing FBXO7 expression levels at 48, 72 and 120 hours post-transfection of mouse *Fbxo7* (*mFbxo7*) into CRISPR FBXO7 KO clone 2.3 and NT control. # indicates a non-specific band

A

FBXO7 exon 2

TTCTAATACCCGATTTACAATTACATTGAACTACAAGGATCCCCTCACTGGAGATGAAGAGACCTTGGCTT
CATATGGGATTGTTTCTGGGGACTTGATATGTTTGATTCTTCAAGATGACATTCCAGCGCCTAATATACCTT
CATCCACAGATTCAGAGCATTCTTCACTCCAGAATAATGAGCAACCCTCTTTGGCCACCAGCTCCAATCA
GACTAGCATGCAGGATGAACAACCAAGTGATTCATTCCAAGGACAGGCAGCCCAGTCTGGTGTTTGGA
ATGACGACAGTATG

FBXO7 exon 3

TTAGGGCCTAGTCAAAATTTTGAAGCTGAGTCAATTCAAGACAACGCACACATGGCTGAAGGTACAGGT
TTCTATCCCTCAGAACCCATGCTCTGTAGTGAATCGGTGGAAGGGCAAGTGCCACATTCATTAGAGACCT
TGTATCAATCAGCTGACTGTTCTGATGCCAATGATGCCTTGATAGTGTTGATACATCTTCTCATGTTGGAGT
CAGGTTACATACCTCAG

			potency score	off-target score
sgRNA #1	ACCGATTCACTACAGAGCAT	antisense	0.59	82
sgRNA #2	GATAATGCGCATATGGCAGA	sense	0.45	76
sgRNA #3	GGAATGACGACAGTATGTTA	sense	0.45	72
sgRNA #4	AGATAATGCGCATATGGCAG	sense	0.40	78

B

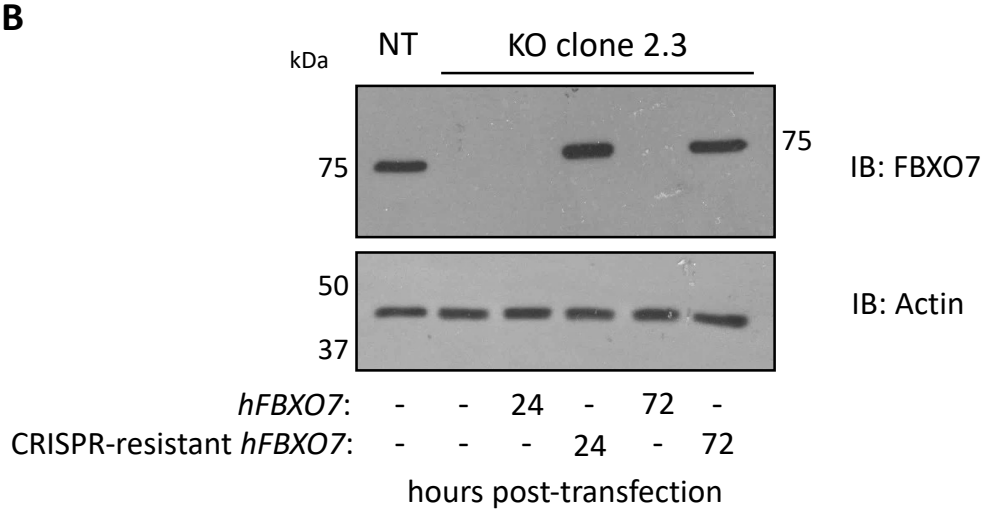

Figure 4.22 – Generating hFBXO7 CRISPR-resistant plasmid to complement back FBXO7. (A) Sequences showing the silent mutations introduced (in red) into the FBXO7 DNA sequence so that it would no longer be recognised by sgRNA2. (B) Immunoblots of SH-SY5Y lysates comparing FBXO7 expression 24 and 72 hours following *hFBXO7* and CRISPR-resistant *hFBXO7* transfections. CRISPR-resistant *hFBXO7* is able to be expressed in FBXO7 KO clone 2.3 cells.

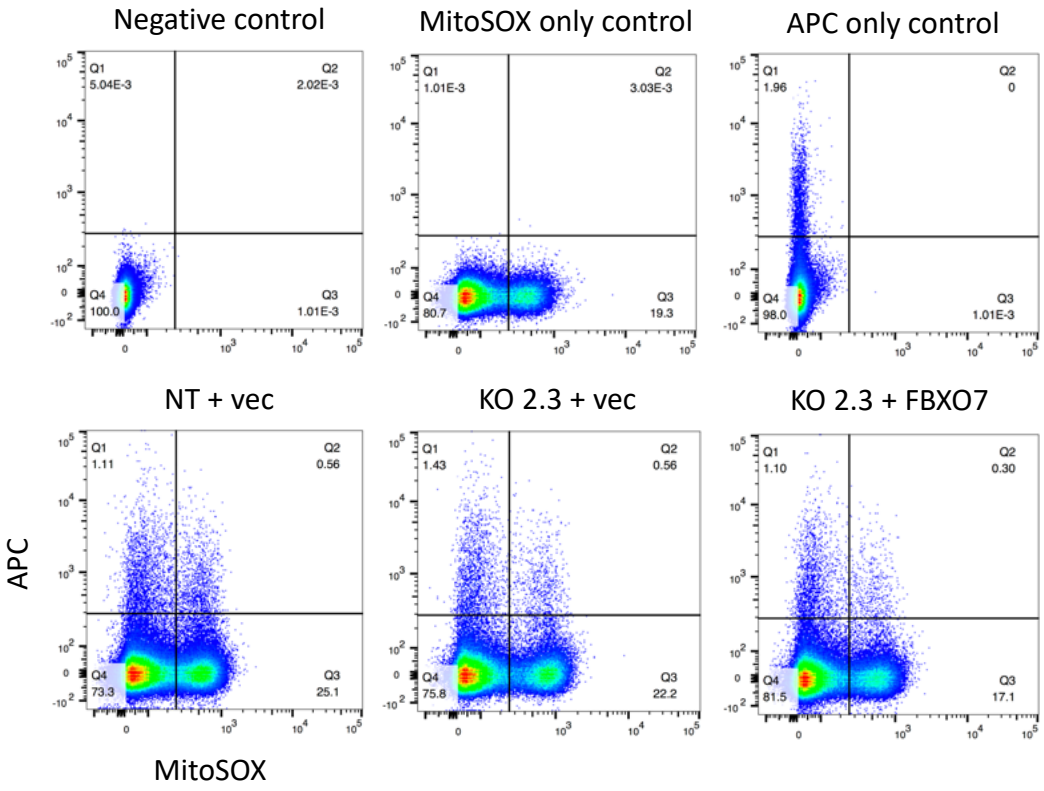

Figure 4.23 – FACS gating strategy for mitoSOX complementation assay. FACS plots showing negative and single-staining controls (top row). FACS plots showing representative staining of NT cells transfected with vector control, FBXO7 KO clone 2.3 cells transfected with vector control (vec) and FBXO7 KO clone 2.3 cells transfected with CRISPR-resistant *hFBXO7* plasmid (bottom row). All transfected cells are APC positive.

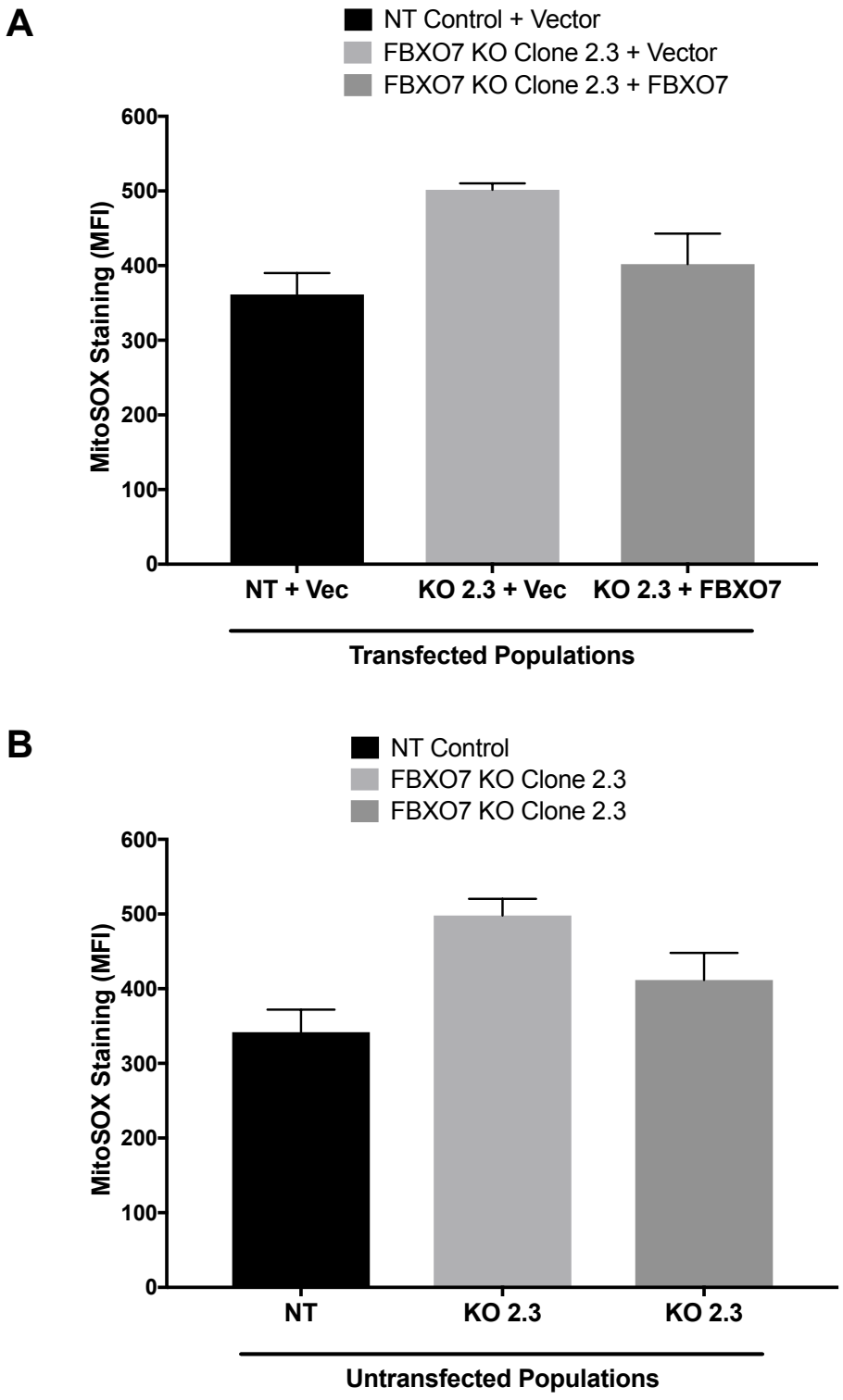

Figure 4.24 – Mitochondrial oxidative stress in complemented CRISPR FBXO7 KO SHSY-5Y cell lines. MitoSOX staining followed by quantification with flow cytometry. (A) When gated on APC positive (transfected) cells, there was an upregulation in MitoSOX MFI in the KO cell line, which decreased to wild-type levels following the re-introduction of FBXO7 into the cell line. (B) The same pattern is apparent in the APC negative (untransfected) cells. Data points represent the mean and error bars represent ±SD (n=1).

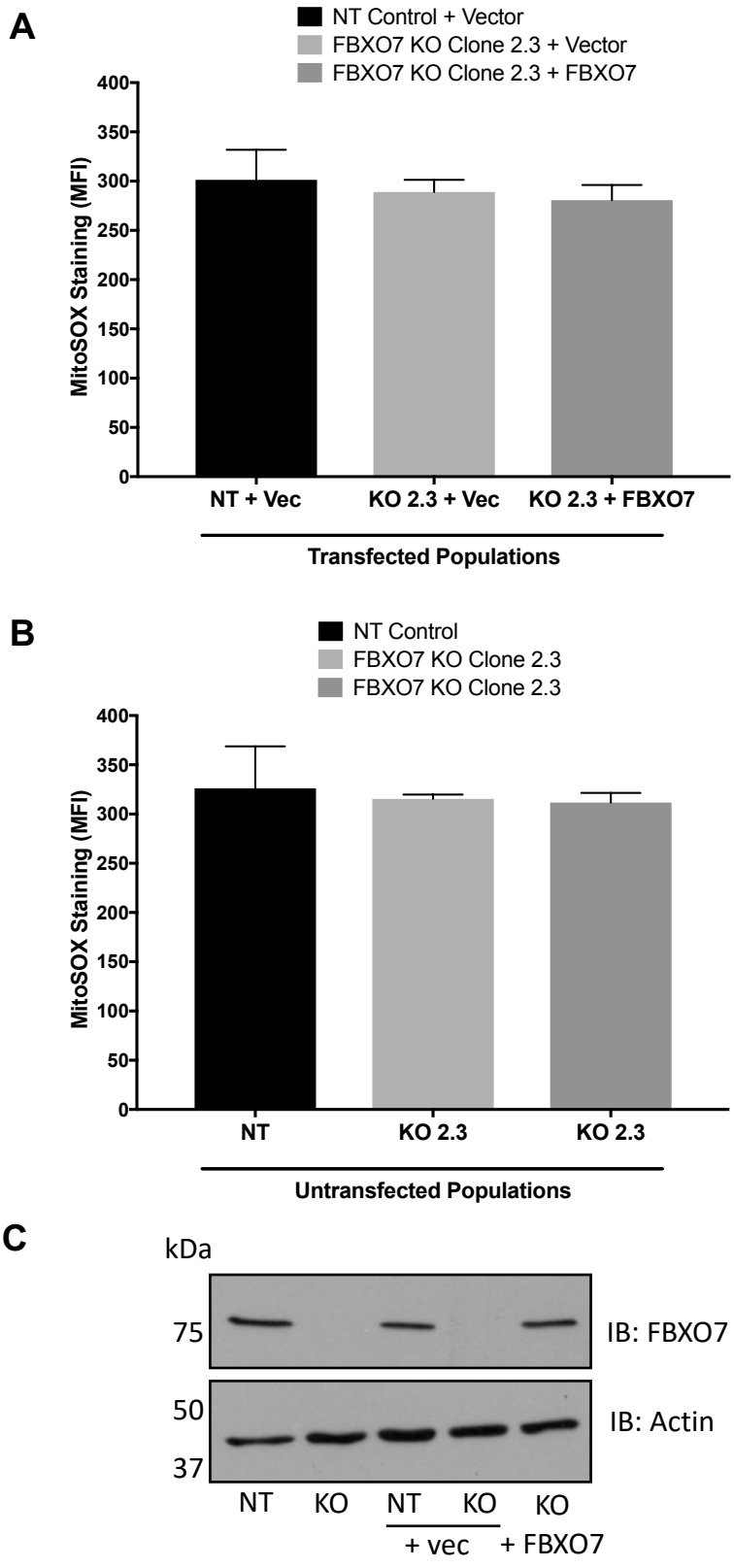

Figure 4.25 – Mitochondrial oxidative stress in complemented CRISPR FBXO7 KO SH-SY5Y cell lines repeat. (A) MitoSOX staining followed by quantification with flow cytometry. The repeat showed no difference in MitoSOX MFI in any of the conditions in neither the transfected nor untransfected cell populations. Data points represent the mean and error bars represent ±SD. (n=1). (B) Immunoblots confirming FBXO7 expression in the complemented FBXO7 KO cell line.

4 – Discussion

The experiments I have undertaken were to understand what consequence losing FBXO7 expression has on neuronal cells. As FBXO7 has pleiotropic effects in different cell types, a broad characterisation of its roles within cell proliferation, cell viability and other properties was necessary. I have also investigated the effect of FBXO7 loss on mitochondrial function and lipid droplets, as potential mechanisms underlying neurodegeneration in PD. Overall, my results show that these SH-SY5Y cell lines are not the best models for investigating FBXO7 biology as many phenotypes were either transient or highly variable and thus inconclusive. We were nevertheless able to extract some indications about FBXO7 pathways that could be further investigated in other type of models.

Previous research has shown that FBXO7 can have both a proliferative and anti-proliferative effect, depending on the cell line. For instance, FBXO7 reduction increases the proliferation rate of haematopoietic pro-B (Ba/F3) cells, decreases p27 expression, shortens their G_1 phase, and increases S phase cyclin levels and CDK2 activity. [308] This also had the effect of altering the maturation of B cells, as assessed by cell surface markers.[308] FBXO7 also has an anti-proliferative effect on peripheral activated T cells, however paradoxically, it also promotes proliferation of thymocytes within the thymus.[370] The lack of FBXO7 expression in patient fibroblasts and MEFs lead to slower proliferation. Whereas, in the case of SH-SY5Y CRISPR KO cells, FBXO7 has a trending anti-proliferative effect, as reducing its expression results in an increase in proliferation. However, there were no significant differences in proliferation rate in the FBXO7 shRNA KD cells, possibly due to residual expression of FBXO7 in these lines. I also showed that there was a trending decrease in viability in FBXO7 KD cells when grown in galactose media, however this was not reproduced in the CRISPR KO cells. The lack of an apoptotic phenotype in both immortalised fibroblasts and tumour-derived SH-SY5Y cells suggests that they may not be the best models to study the effects of FBXO7 on apoptosis, and possibly also proliferation, due to their aberrant cancerous changes.

There is also an important link between cell cycle and differentiation.[298] Research has shown that lengthening of the cell cycle, via G_1 phase extension, occurs prior to differentiation.[301] Furthermore, various cell cycle regulators such as cyclin D2 and p27 have been implicated in neurogenesis.[303–307] My tests for FBXO7 on its ability to affect

neuronal differentiation in P19 cells showed no apparent difference between control and FBXO7 KD cells in their level of differentiation, as visualized by light microscopy of altered morphology and the appearance of neurites. Immunoblotting of lysates for differentiated cells showed that the population was behaving in a fairly uniform manner, at least with regard to the down-regulation of proteins, like FBXO7 and CDK6. Thus, FBXO7 has an anti-proliferative effect in SH-SHY5Y cells and doesn't affect the ability of P19 cells to differentiate. Although a proliferation assay in P19 cells was not conducted, the fact that FBXO7 is downregulated during P19 differentiation perhaps suggests it is pro-proliferative in these cells, and therefore inhibitory to differentiation, which necessitates its decreased protein expression. This hypothesis would need to be investigated further to be confirmed.

Due to its role mediating mitophagy,[320,333] mitochondrial metabolism,[335] and ubiquitination of TOM20,[336] I also investigated the effect of FBXO7 KD and KO on several mitochondrial properties in SH-SY5Y cells. The FBXO7 KD cell line had significantly fewer polarised mitochondria under basal conditions, which were then increased to the same extent as in the control line when grown in galactose media. However, the significantly reduced polarised mitochondrial load under basal conditions suggests that it is still possible for FBXO7 to have a role in promoting mitochondria biogenesis and that there may be redundant pathways that are involved in their upregulation under stress. A similar assay was conducted in the FBXO7 KO lines, which showed no significant differences in polarised mitochondrial load under basal conditions and there was also no increase of mitochondrial upon galactose media incubation. The only trending difference recorded was when comparing polarised mitochondria levels in the NT and the KO clones when cultured in galactose for 11 days. Compared to the NT cells, the amount of polarised mitochondria was increased after long-term galactose exposure. This data suggests that FBXO7 may function to inhibit the increase in polarised mitochondria upon the switch to a requirement for greater OXPHOS. Furthermore, the qualitative observations that mitochondria were not as elongated and connected as in the NT cell lines is indicative of possible mitochondrial dysfunction in cells lacking FBXO7 expression and that the loss of FBXO7 affects mitochondrial morphology. In addition, the FBXO7 KO cells did possess a significant increase mitochondrial and cellular oxidative stress, which is also indicative of some form of mitochondrial dysfunction.

As there is an active and dynamic interaction between lipid droplets and the outer membrane of mitochondria, to facilitate FFA delivery for mitochondrial β-oxidation, it is possible to use the amount of lipid accumulation as an indirect measure of mitochondrial health.[36,37] My results showed there were almost three times as many LDs in the FBXO7 KD cells compared to the control lines under basal conditions, which is suggestive of mitochondrial and/or lipid metabolism dysfunction. This trending phenotype appeared to be confirmed with the FFA quantification assay in the CRISPR FBXO7 KO cells, showing a significant increase of FFA in these cells. In contrast, the LD assay in the CRISPR lines showed a reversal of the phenotype with the NT cells harbouring more LDs compared to the knockout cells. The discrepancy between the lipid droplet quantification experiments may be due to when the cells were assayed following the KO of the FBXO7 allele and/or compensatory mechanisms.

Overall, this broad set of experiments in both FBXO7 KD and KO SH-SY5Y cells showed that they are not good models for the conducted assays as much of the data was inconclusive. The variability could have also arisen due to different sources of SH-SY5Y parental cells from which the models were generated, clonal effects of the CRISPR FBXO7 KO lines, and compensatory mechanisms. FBXO7 seems to be a protein involved in the cell stress response and cells are able to adapt around its function, especially in the context of the knockdown cells. Thus, it seems that FBXO7 functionality *in vitro* should be further investigated rather in primary patient fibroblast and mouse embryonic fibroblast lines. It would also be interesting to repeat the assays described in Chapters 3 and 4 in patient-derived iPSCs differentiated into dopaminergic neurons, which may also provide a more physiologically relevant neuronal environment.

CHAPTER 5

CHARACTERISATION OF *FBXO7* KNOCKOUT MOUSE MODELS

5 – Introduction

Mutations have been identified throughout the *FBXO7* gene to cause a severe recessive early-onset form of parkinsonism. As with most neurodegenerative diseases, the PD field lacks animal models that present with most symptoms, mirroring those observed in patients. Having already characterised various cellular models (Chapter 3 and Chapter 4), we continued to investigate the role of FBXO7 in a more physiological setting by generating systemic (*Zp3*-Cre KO) and conditional (*Dat*-Cre KO) *Fbxo7* knockout mouse models.

Briefly, EUCOMM targeted allele mouse ES cells were injected into blastocysts, creating the LacZ mice on a C57BL/6J background. The loxP sites were located on either side of *Fbxo7* exon 4, so when LacZ mice were crossed with the ActB:FLPe strain, mice with a 'floxed' *Fbxo7* allele were generated (**Fig5.1A**). Subsequently, these mice were crossed with strains expressing Cre from either *Zp3* (Zona Pellucida Glycoprotein 3) or *Dat* (Dopamine Active Transporter) promoters to excise exon 4 of *Fbxo7* and generate FBXO7 null cells. *Fbxo7 Zp3*-Cre KO ($Zp3^{Cre}Fbxo7^{-/-}$) mice, with a systemic deletion of *Fbxo7* exon 4, have a runty phenotype (**Fig5.1B,C**) and pre-weaning lethality. They also present with a small thymus and anaemia, but a full histological work up did not reveal any apparent deficiencies in their major organs. The aim of creating *Fbxo7* KO mice was to investigate the role FBXO7 in DA neurons, which also required the possibility of aging. Thus, conditional *Fbxo7 Dat*-Cre KO ($Dat^{Cre}Fbxo7^{-/fl}$) mice with a deletion of *Fbxo7* exon 4 only in dopamine (DA) neurons expressing *Dat* were also generated and characterised.

The experiments characterising the two mouse models were undertaken as part of a collaborative project between our lab and that of Prof. Roger Barker (John van Geest Centre for Brain Repair, University of Cambridge), with Drs. Suzanne Randle and Simon Stott also working on this project.

5 – Results

5.1 – Zp3^{Cre}Fbxo7$^{-/-}$ mice show no changes in electrophysiology or dopaminergic neuron cell number

We first investigated the expression pattern of *Fbxo7* mRNA and FBXO7 protein in the mouse brain. Dr. Simon Stott undertook experiments confirming that *Fbxo7* is expressed in the WT adult mouse brain. *In situ* hybridisation showed that *Fbxo7* mRNA is expressed throughout the adult mouse brain, with the strongest signal obtained in the white matter, midbrain and brain stem. Whereas immunoblotting of dissected brain regions, conducted by Dr. Suzanne Randle, showed FBXO7 protein expression was detected in the prefrontal cortex, ventromedial nucleus, olfactory bulb (OB), striatum, cerebellum and medulla/pons, with the OB having the highest levels. These data collectively demonstrate widespread expression of *Fbxo7* and FBXO7 in the wild-type adult mouse brain.

Previous PD mouse models have shown that certain phenotypes, such as altered firing patterns, occur at the level of single DA neurons prior to the onset of overt motor symptoms.[371,372] Due to PD having a long asymptomatic phase, it is important to study these types of early functional adaptations. Thus, I started my characterisation of the Zp3^{Cre}*Fbxo7*$^{-/-}$ mice by assaying their firing rates and responses using electrophysiology in the lab of Dr. Susan Jones (Department of Physiology, Development and Neuroscience, University of Cambridge). As DA neurons are selectively vulnerable in PD, I characterised the electrophysiological properties of DA neurons in the substantia nigra pars compacta (SNpc) in the absence of FBXO7 expression. As previously mentioned, an initial characterisation of Zp3^{Cre}*Fbxo7*$^{-/-}$ mice showed that they exhibit a runty phenotype and by day 18 they are only 45% of the body mass of their WT (Zp3^{Cre}*Fbxo7*$^{+/+}$) and Het (Zp3^{Cre}*Fbxo7*$^{+/-}$) littermates (**Fig5.1B-C**). Due to this failure to thrive, null and control mice were culled pre-weaning and brains were promptly harvested for electrophysiology experiments. I performed whole-cell patch clamp recordings from Zp3^{Cre}*Fbxo7*$^{-/-}$ brain sections. SNpc DA neurons were located by their proximity to the easily identifiable medial temporal (MT) nucleus of the accessory optic tract. Once a cell had been identified, two standard characteristics of DA neurons, spontaneous pacemaker activity and a hyperpolarisation-activated cation current with a sag component, further verified its identity.[373,374] **Fig5.2** depicts an example of the initial

characteristics of an SNpc-DA neuron from a P16 $Zp3^{Cre}$*Fbxo7*$^{-/-}$ brain slice. Spontaneous firing was recorded in cell-attached mode, prior to breaking the 3 GΩ seal on the membrane (**Fig5.2B**). Pulses were regular, firing at 1-2 per second, which is within the standard range of 1-5 pulses per second in wild-type DA neurons.[373,374]

Once the membrane was broken, recordings were conducted in whole-cell mode, but still under voltage clamp conditions. Therefore, it was possible to apply a series of hyper-polarisations and record the cation current sag (I_{SAG}) responses (**Fig5.2C**). The I_{SAG}'s increased with each hyperpolarisation as expected.[373,374] After switching to the current clamp setting, it was possible to measure other characteristics of these neurons. The resting membrane potential of this FBXO7 null dopaminergic cell was -46 mV. After a small 30 pA current was injected to aid firing, the cell responded with increased firing frequency (**Fig5.3A**). The cells also had regular increasing downward deflections with each hyperpolarisation (**Fig5.3B**). It was necessary to inject -144 pA to reduce the membrane potential to -70 mV for step current injections. As expected, there was more firing when the step current pulses were increased from 5 pA steps (range: 5 - 25 pA) (**Fig5.3C top**) to 50 pA steps (range: 50 – 250 pA) (**Fig5.3D top**).

To investigate the reaction of these cells to a $GABA_AR$ antagonist, picrotoxin was added to the perfusion artificial cerebral spinal fluid (ACSF) solution. Due to a blocking of inhibition, one would expect to see increased frequency or burst firing, but no noticeable difference was observed during the regular firing condition (**Fig5.3E**). This suggests that the spontaneous firing rate is not controlled by tonic inhibition. However, when the step current protocols were repeated under picrotoxin treatment, there was a slight increase in firing (**Fig5.3C-D bottom**) and only an injection of -20 pA was necessary for the membrane potential to reach -70 mV. The lack of tonic inhibition of spontaneous firing and its presence during excitation-driven firing could be due to the equilibrium potential of chloride ions (Cl^-) being very close to the holding potential. This could result in no net movement of Cl^- with the opening/closing of $GABA_A$ chloride channels, and thereby no pricrotoxin effect under tonic conditions. Subsequently, the cell was depolarised prior to step current injections, which results in a larger difference between its holding potential and the equilibrium potential of Cl^-. This allows for Cl^- to flow into the cell after the opening of the $GABA_A$ chloride channels, resulting in increased excitation when the channels are blocked with picrotoxin. As all the other characteristics were within normal range, it is uncertain at this stage whether this abnormality is a phenotype or

rather a patch-clamping artefact, and it would need to be investigated further by comparing it to control WT DA cells from the same mouse strain. Thus, overall it seems that these DA neurons were firing within the regular range, and there were no significant changes towards hypo- or hyperexcitability.

As the loss of DA neurons is one of the main hallmarks of PD, we next investigated whether lack of FBXO7 expression affected the number of DA neurons in the SNpc. Tyrosine hydroxylase (TH) is a key enzyme in the DA biosynthetic pathway that converts L-tyrosine to L-3,4-dihydroxyphelylalanine (L-DOPA), a dopamine precursor, and it is used as a marker of DA neurons. Preliminary TH immunofluorescence of P21 *Fbxo7 Zp3*-Cre KO perfused brain sections, showed that the overall TH MFI of the SNpc in the KO section was 81% of the Het section (**Fig5.4**). However, when this was repeated by Dr. Simon Stott in a larger sample (n=4) with DAB staining that allowed for more accurate optical density-based quantification, the difference between KO and Het samples was not significant (data not shown). Thus, the absence of *Fbxo7* expression does not affect the number of TH+ neurons in the SNpc, suggesting that *Fbxo7* may not be necessary for DA neuronal development at this stage. In conclusion, at least up until three weeks of age, there was neither an electrophysiological defect of DA neurons, nor a decrease in TH+ cell number in mice with a systemic loss of *Fbxo7* expression.

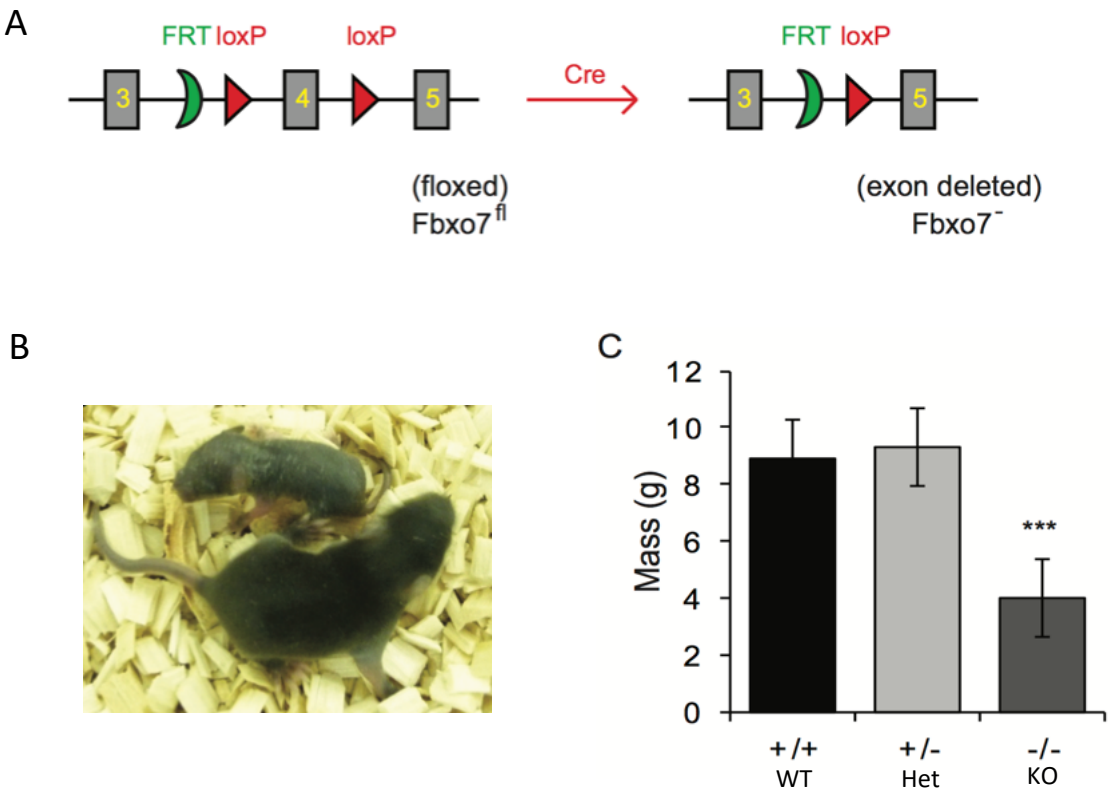

Figure 5.1 – Generating *Fbxo7* KO mouse models. (A) A schematic of the transgene used to generate complete null *Zp3*-Cre and conditional *Dat*-Cre *Fbxo7* knockout mouse models. Mice with 'floxed' *Fbxo7* allele were crossed with mice expressing Cre either from the Zp3 promoter (generating a systemic deletion of *Fbxo7* exon 4) or from a *Dat* promoter (generating a deletion of *Fbxo7* exon 4 only in dopaminergic neurons). (B) WT and runty Zp3 KO littermates (p8). (C) $Zp3^{Cre}Fbxo7^{-/-}$ have a significantly reduced weight compared to WT and Het littermates (p18) Data points represent the mean, error bars represent ±SD. *** p<0.001 **(Figure modified from one produced by S. Randle)**

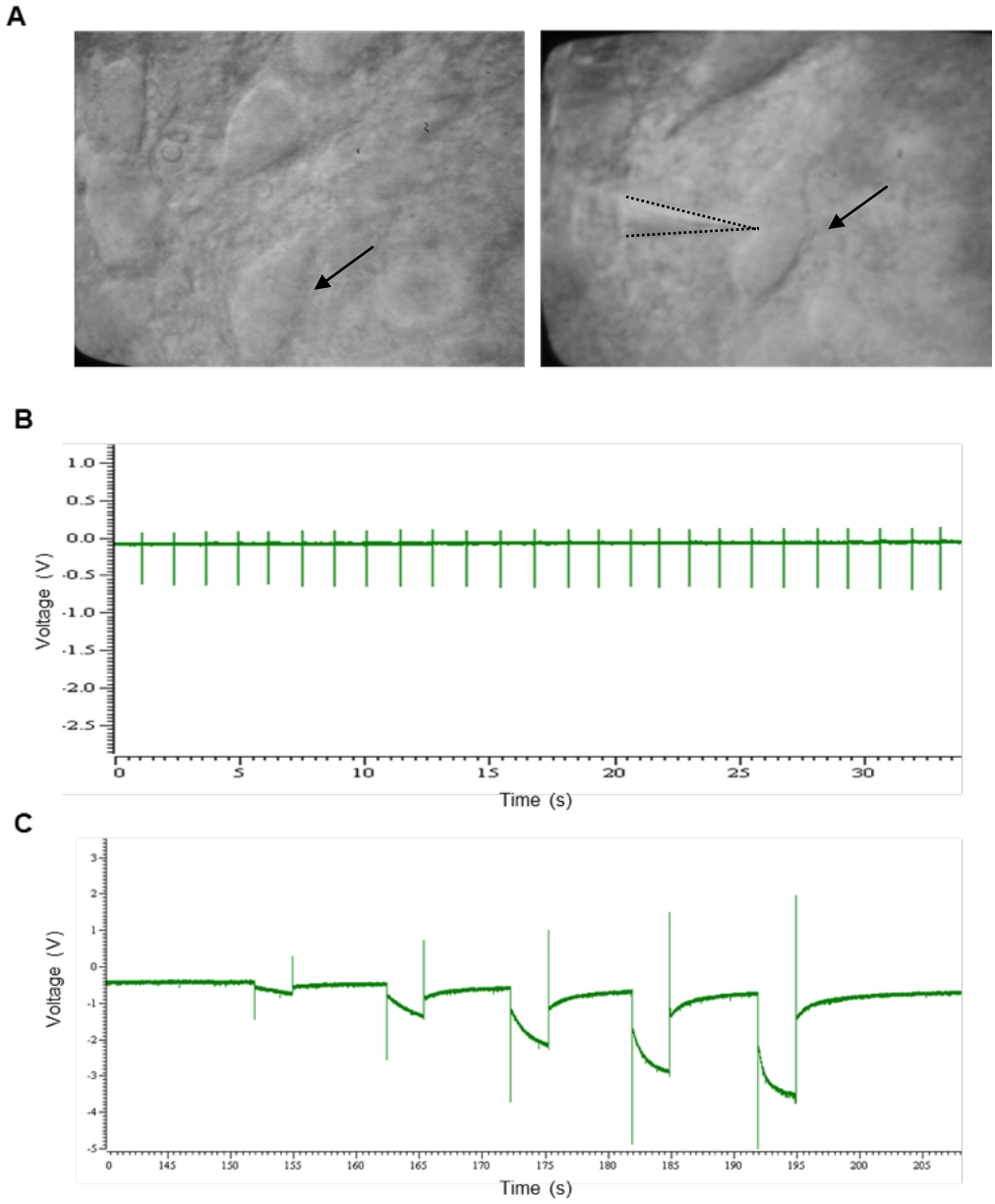

Figure 5.2 – Identification of dopaminergic neurons in the substantia nigra pars compacta. (A) Zp3^{Cre}*Fbxo7*$^{-/-}$ SNpc dopaminergic neuron before (left) and during patch clamp (right). Arrows point to the patched cell and dashed lines follow the outline of the micropipette. The presence of regular spontaneous firing (B) in cell-attached mode and/or a hyperpolarisation-activated cation current (I_h) with a sag component (C) in whole-cell mode further confirming that the patch clamped neurons were dopaminergic. For (B) 1V = 100 pA and for (C) 1V = 200 pA. Measurements from six DA neurons were recorded.

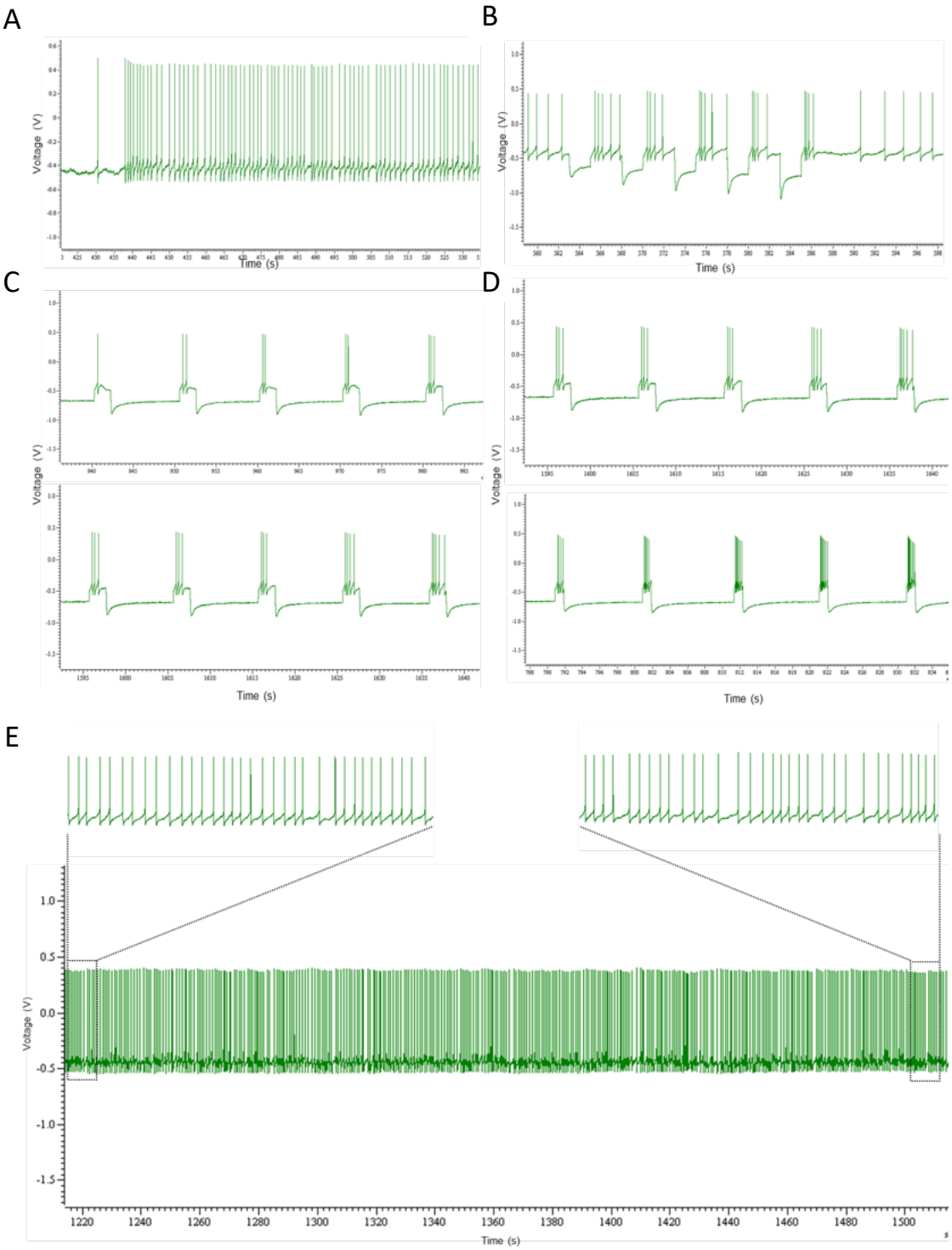

Figure 5.3 – Electrophysiological characterization of dopaminergic neurons in the substantia nigra pars compacta of Zp3^{Cre}*Fbxo7*$^{-/-}$ mouse (p16) (A) Firing pattern following a 30 pA steady-state current injection, (B) VSAG responses to hyperpolarising current injections, note downward deflection followed by slow upward sag, (C) responses after 5 pA, 10 pA, 15 pA, 20 pA, 25 pA step current injections before (top panel) and after 50µM picrotoxin (lower panel), (D) responses after 50 pA, 100 pA, 150 pA, 200 pA, 250 pA step current injections before (top panel) and after 50µM picrotoxin (lower panel), (E) unchanging firing pattern before and after picrotoxin administration. (n=1, in technical triplicate) Recordings were performed in 6 dopaminergic neurons from the same mouse.

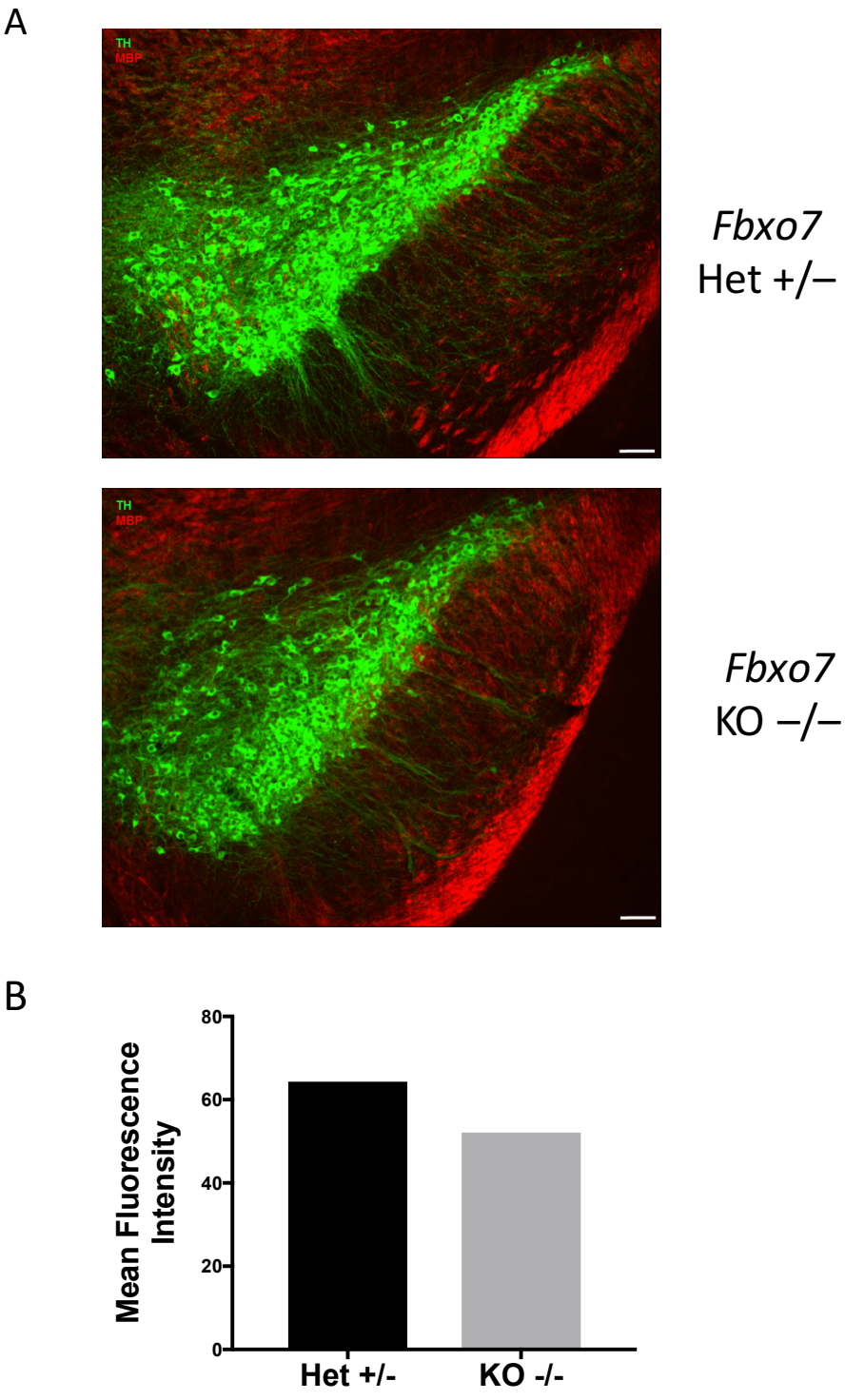

Figure 5.4 – TH immunostaining in Zp3^{Cre}*Fbxo7* brain sections. (A) TH immunofluorescence (green) of the substantia nigra pars compacta from Het (Zp3^{Cre}*Fbxo7*$^{+/–}$) and KO (Zp3^{Cre}*Fbxo7*$^{–/–}$) brain sections, showing no significant differences. Scale bar represents 100 µm. (B) Quantification of TH staining mean fluorescence intensity of the images in (A). (n=1)

5.2 – RPL23 identified as a FBXO7 ubiquitination substrate

As it was not possible to age the systemic KO mice beyond 3 weeks, we generated a conditional KO mouse that lacks FBXO7 expression only in DA neurons. In this Dat^{Cre}*Fbxo7*$^{-/fl}$ mouse model, a phenotype was observed at 6 weeks. TH-immunostaining of midbrain sections conducted by Dr. Simon Stott in **Fig5.5** showed that the TH innervation of the striatum and nucleus accumbens in the KO brain was 69.6%±1.9 and 58.3%±3.1 respectively than that of the WT brain at 6 weeks. At 12 weeks, the TH+ fibre density was further reduced in the striatum and nucleus accumbens to 55.6%±1.7 and 59.1%±2.9 (**Fig5.5**). Despite this significant reduction of TH+ fibres, there was no significant difference in the number of TH+ DA neurons in the SNpc at 6 or 12 weeks (**Fig5.5A,B**). Furthermore, there was a significant decrease in TH+ cell diameter in the SNpc (88.9%±3.1 of control), but not in the VTA (**Fig5.6C**). Interestingly, the decrease in neurite density and reduction in cell body size at 12 weeks, was followed by a significant reduction in the number of TH+ DA neurons in the SNpc at 20 weeks (81.3%±1.0 of control) as seen in **Fig5.5B**. Overall, these results indicate a delayed TH+ cell death phenotype in the ventral midbrain of the conditional Dat^{Cre}*Fbxo7*$^{-/fl}$ mice. It suggests that FBXO7 may be needed for proper DA neuronal development and/or maintenance.

In order to investigate potential mechanisms underlying the observed cell death phenotype, we looked at cellular pathways regulated by FBXO7 that may be involved. From a previously conducted protoarray screen for FBXO7 substrates in the lab, ribosomal proteins were identified as one of the most abundant classes of proteins to interact with FBXO7.[336] Furthermore, two ribosomal proteins that interacted with FBXO7 in this screen, RPL11 and RPL23, were found to be highly expressed in DA neurons, according to the Allen Brain Atlas (available from http://mouse.brain-map.org/experiment/show/74819237). RPL11 (60S ribosomal protein L11) and RPL23 (60S ribosomal protein L23) are both components of the 60S ribosomal subunit and act as sensors of cellular stress.[375,376] Thus, the lab utilised LC-MS/MS analysis with label free quantification of peptide fragments to examine changes in the expression of ribosomal proteins in the ventral midbrain of Dat^{Cre}*Fbxo7*$^{-/fl}$ mice at 5 weeks. This experiment showed that among 23 ribosomal proteins detected in the ventral midbrain using this method, only RPL23 expression was elevated in the conditional knockout mouse (data not shown). Direct immunofluorescence staining for RPL23 in tissue

sections of the midbrain confirmed an increase in RPL23 expression in the SNpc of the Dat^{Cre}*Fbxo7*$^{-/fl}$ mouse at 12 weeks (**Fig5.6D**). This data indicates that there may be a regulatory relationship between FBXO7 and RPL23, which could then potentially link to the observed cell death phenotype. Elevated RPL23 expression also suggests that there is an increase in cellular stress in the midbrain lacking FBXO7 expression.

To test whether FBXO7 regulates RPL23 expression levels through ubiquitination or if their inverse expression pattern is merely correlative, I examined whether RPL23 levels would change with FBXO7 or ΔF-box overexpression in HEK293T cells. In the first experiment (**Fig5.7A-B**), I co-transfected RPL23, either WT or ΔF-box *FBXO7* alleles, into HEK293T cells. The ΔF-box FBXO7 mutant lacks the F-box domain and is therefore unable to bind SKP1, making the SCF ligase inactive. Thus, if one sees ubiquitin smears with FBXO7 but not with the ΔF-box FBXO7 mutant, then it suggests that SCF^{FBXO7} plays a role in the ubiquitination. Cells were harvested and immunoblotting of cell lysates showed that levels of exogenous RPL23 were reduced by 33.9% when FBXO7, but not the ΔF-box mutant, was co-expressed. Moreover, **Fig5.7C-D** shows that endogenous RPL23 levels were reduced by 46.2% upon FBXO7 over-expression and unchanged upon ΔF-box overexpression. The inverse relationship in protein expression between RPL23 and FBXO7 and its dependence on the SKP1-recruiting domain within FBXO7 implies that ubiquitination of RPL23 by SCF^{FBXO7} may play a role in the decreased expression of RPL23.

Thus, I next tested whether RPL23 and FBXO7 interact in cells using co-immunoprecipitation assays. I co-transfected HEK293T cells with FLAG-RPL23 and either WT or ΔF-box mutant FBXO7, and immunoprecipitated RPL23 from cell lysates with FLAG beads. Immunoblots for RPL23 showed that FLAG-RPL23 interacted with FBXO7 but not ΔF-box mutant (**Fig5.8A**). Due to the inverse correlation in protein expression levels between FBXO7 and RPL23, I tested whether FBXO7 expression promotes the ubiquitination of RPL23. I conducted a ubiquitination assay. I transfected HEK293T cells with HA tagged ubiquitin (Ub-HA), untagged alleles of either WT or ΔF-box mutant FBXO7, and FLAG tagged RPL23 (FLAG-RPL23). Cell lysates were immunoprecipitated with FLAG beads which were then immunoblotted for HA-tagged ubiquitin or with an antibody that specifically detects K48 linked ubiquitin chains, a linkage type which promotes proteasomal degradation. **Fig5.8B** shows there was high

molecular weight ubiquitin laddering detected in samples with FBXO7 overexpression, which was significantly reduced in samples where the mutant ΔF-box FBXO7 was expressed. Furthermore, there was a high molecular weight band for K48 ubiquitin linkages. In parallel, the total lysate was immunoblotted for FBXO7, FLAG and GAPDH as controls (**Fig5.8C**). Taken together, these data indicate that FBXO7 is able to increase RPL23 K48 linked ubiquitination, which promotes its proteasomal degradation. Therefore, these data suggest that FBXO7 promotes the proteolytic degradation of RPL23.

Taken together, the conditional Dat^{Cre}*Fbxo7*$^{-/fl}$ mouse exhibits several phenotypes similar to those seen in PD. These include decreased TH innervation of the striatum, a motor coordination defect and delayed loss of TH cells in the SNpc at 20 weeks. This implies that FBXO7 is important for the proper development or maintenance of DA neurons in the striatum and SNpc. Furthermore, the identification of RPL23 as a new ubiquitination substrate of FBXO7 raises the possibility that RPL23 over-expression, which is known to activate the stress-responsive RPL23-MDM2-p53 pathway,[375,376] may contribute to the observed cell death in this mouse model. In support of this hypothesis, qRT-PCR's conducted by Dr. Suzanne Randle showed that p53-responsive genes regulating apoptosis (Aspp1, Bak, Bax and Puma) were specifically and significantly upregulated in the ventral midbrain of the Dat^{Cre}*Fbxo7*$^{-/fl}$ mice (data not shown). Together these results suggest a model where the absence of FBXO7 causes an accumulation of RPL23, which activates a p53 pro-apoptotic pathway, leading to cell death in PD/PPS.

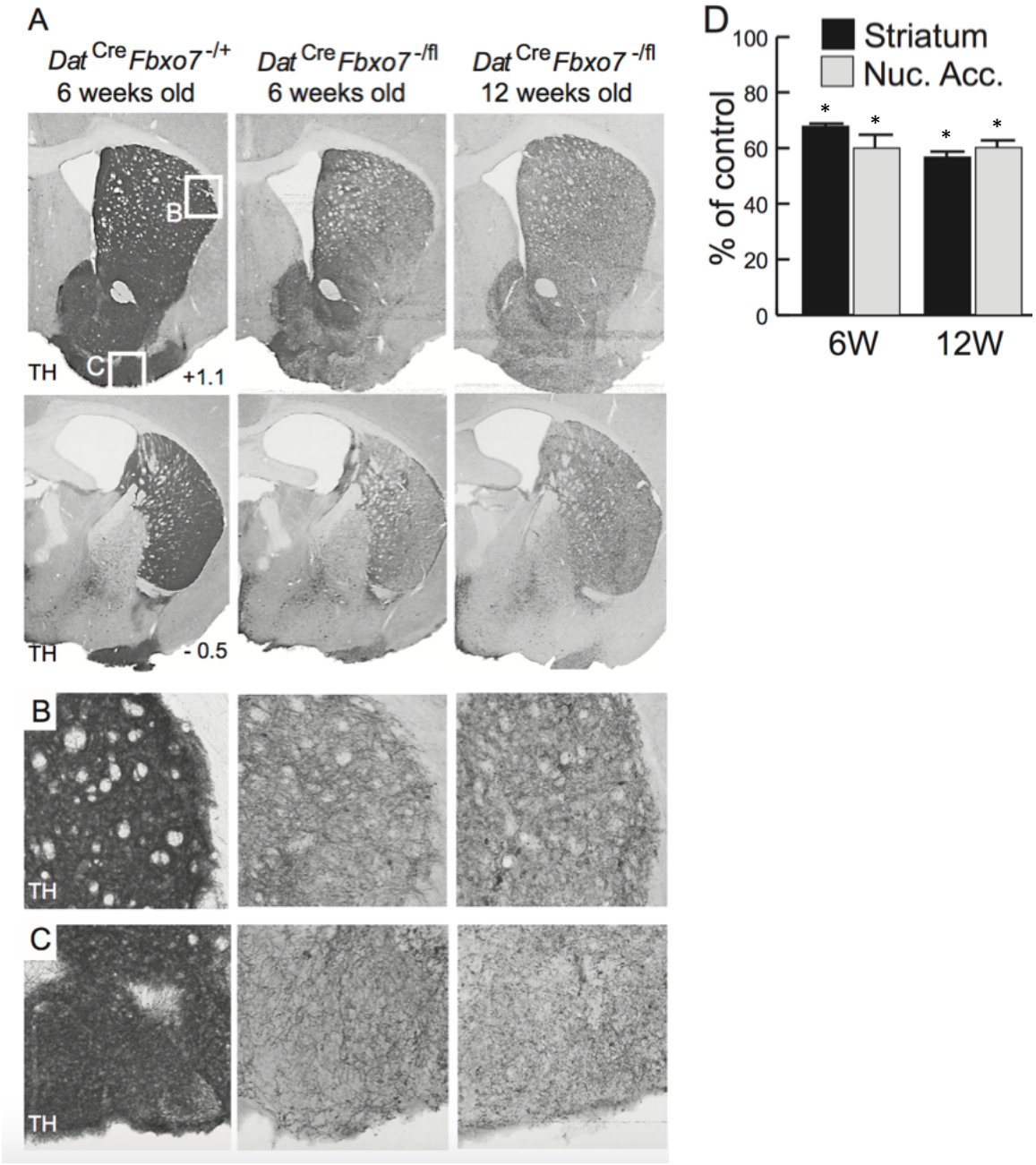

Figure 5.5 – Less TH innervation of the striatum in Dat^{Cre}*Fbxo7*$^{-/fl}$ mouse brain sections. (A) TH-immunostained sections of the striatum and nucleus accumbens at 6 and 12 weeks of Dat^{Cre}*Fbxo7*$^{-/fl}$ mice, compared to control mice. (B) Magnified region depicting TH+ fibres in the striatum. (C) Magnified region depicting TH+ fibres in the olfactory tubercle. (D) Quantification of TH+ fibre density, as a percentage of control, at 6 and 12 weeks in the striatum and nucleus accumbens. * p<0.05 **(Figure modified from one produced by S. Stott)**

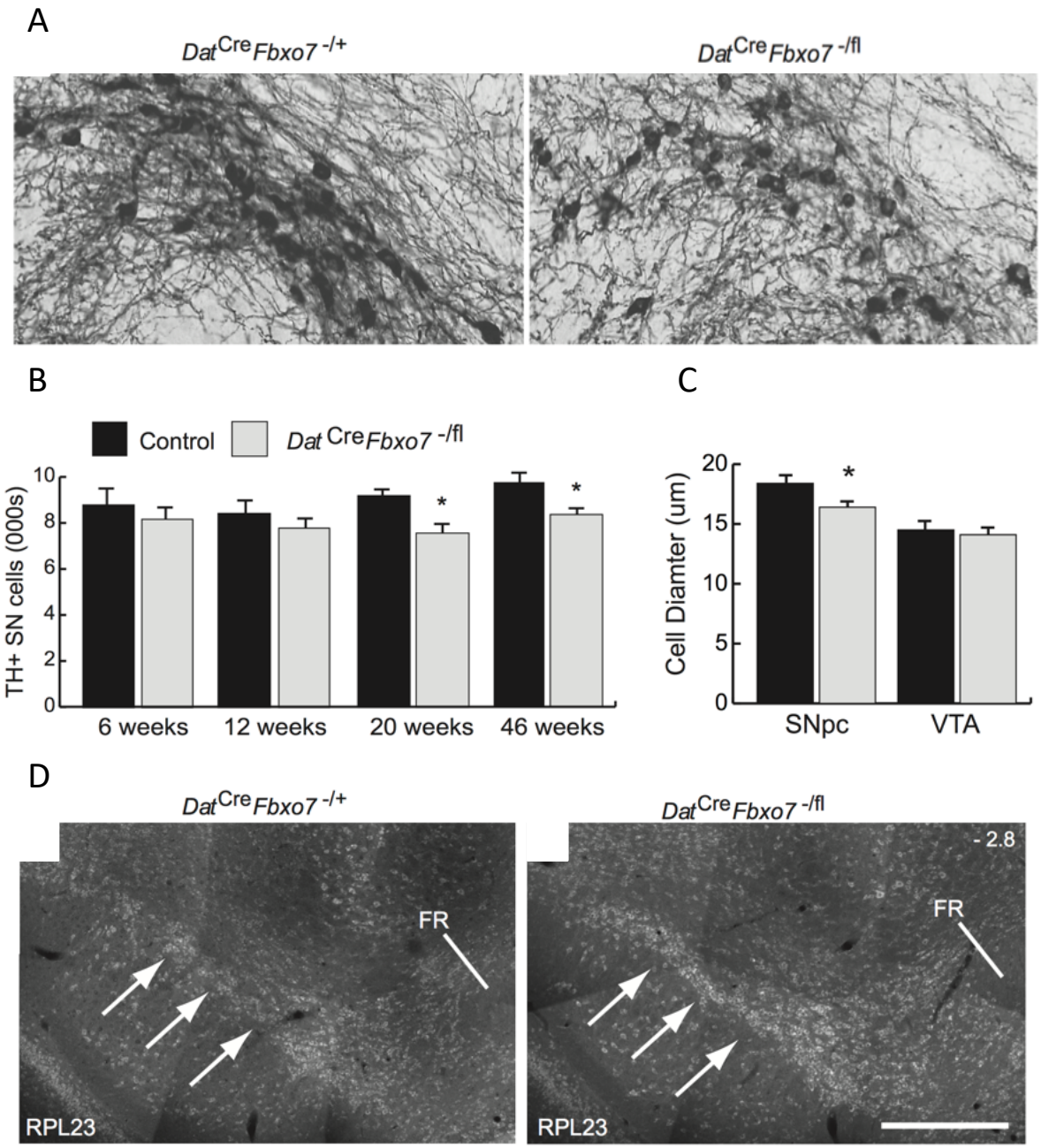

Figure 5.6 – Fewer neurites, smaller TH+ cells and increased levels of RPL23 in Dat^{Cre}*Fbxo7*$^{-/fl}$ mouse. (A) TH-immunostained sections of the SNpc at 12 weeks of control (left) and Dat^{Cre}*Fbxo7*$^{-/fl}$ mice (right) showing fewer neurites and smaller TH+ cell bodies in the KO mice. (B) Quantification of the number of TH+ cells in the SNpc at different time points, showing a significant decrease in the number of cells from 20 weeks onwards. (C) Quantification of the diameter of TH+ cell bodies, showing a significant decrease in the SNpc but not the VTA cells of KO mice. (D) RPL23 immunofluorescence of the substantia nigra pars compacta (arrows) of control (left) and KO (right) Dat^{Cre}*Fbxo7*$^{-/fl}$ mice (12 weeks) showing upregulation of RPL23 expression in the KO mice. FR, fasciculus retroflexus. Scale bars represents 200µm. * p<0.05 **(Figure modified from one produced by S. Stott)**

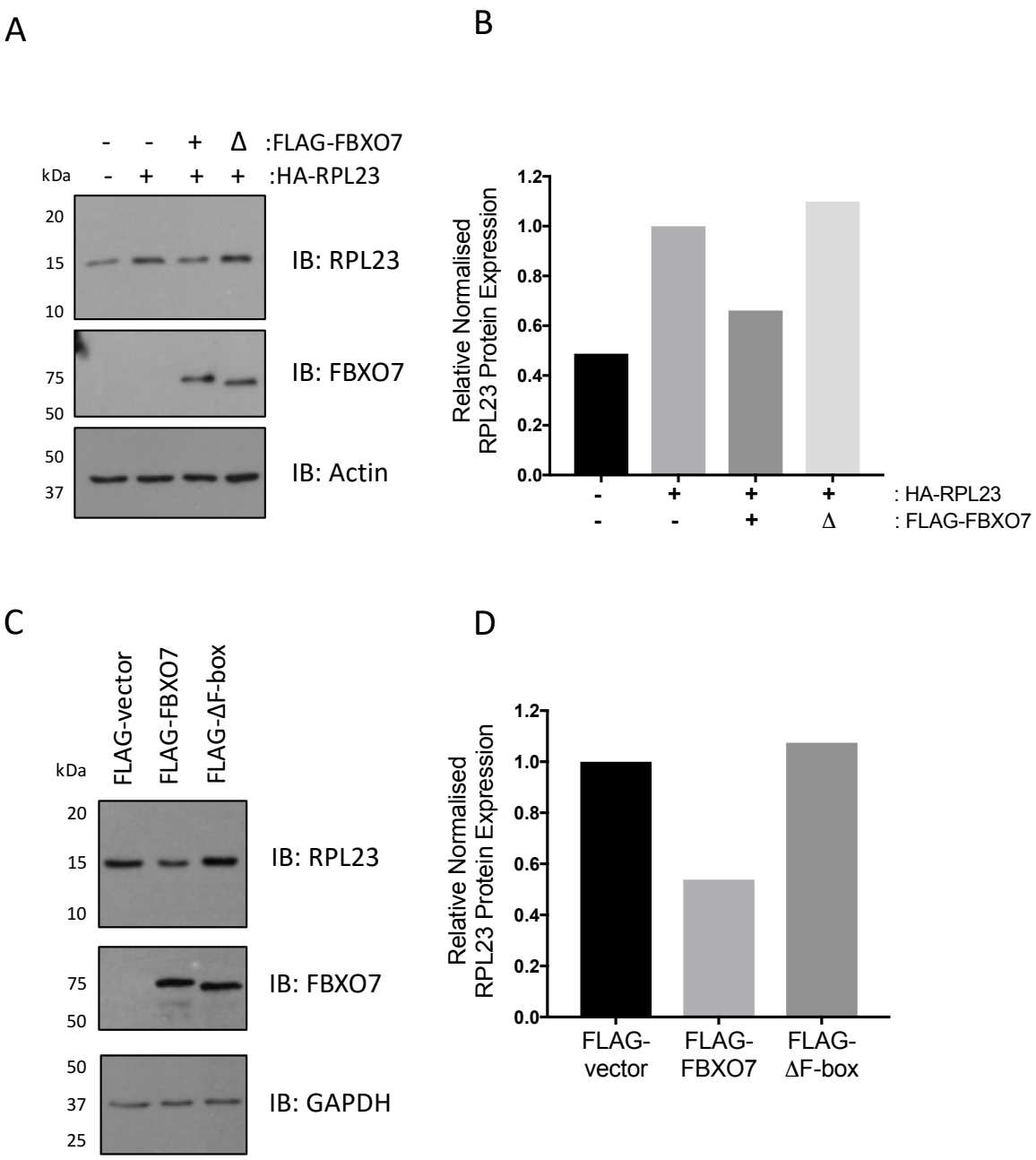

Figure 5.7 – RPL23 expression upon FBXO7 and ΔF-box over-expression. (A) Immunoblots of HEK293T lysates showing a downregulation of RPL23 levels when WT (FLAG-FBXO7) but not mutant FBXO7 (FLAG-ΔF-box) ligase is over-expressed (n=3). (B) Quantification of relative exogenous RPL23 expression showing a 33.9% decrease in expression when WT FBXO7 (FLAG-FBXO7) is overexpressed and a 9.9% increase in expression when mutant FBXO7 (FLAG-ΔF-box) is overexpressed (n=3) (C) Immunoblots of HEK293T lysates showing a downregulation of endogenous RPL23 levels when WT (FLAG-FBXO7) but not mutant FBXO7 (FLAG-ΔFbox) ligase is over-expressed. (D) Quantification of relative endogenous RPL23 expression showing a 46.2% decrease in expression when WT Fbxo7 (FLAG-FBXO7) is overexpressed and a 7.5% increase in expression when mutant FBXO7 (FLAG-ΔF-box) is overexpressed.

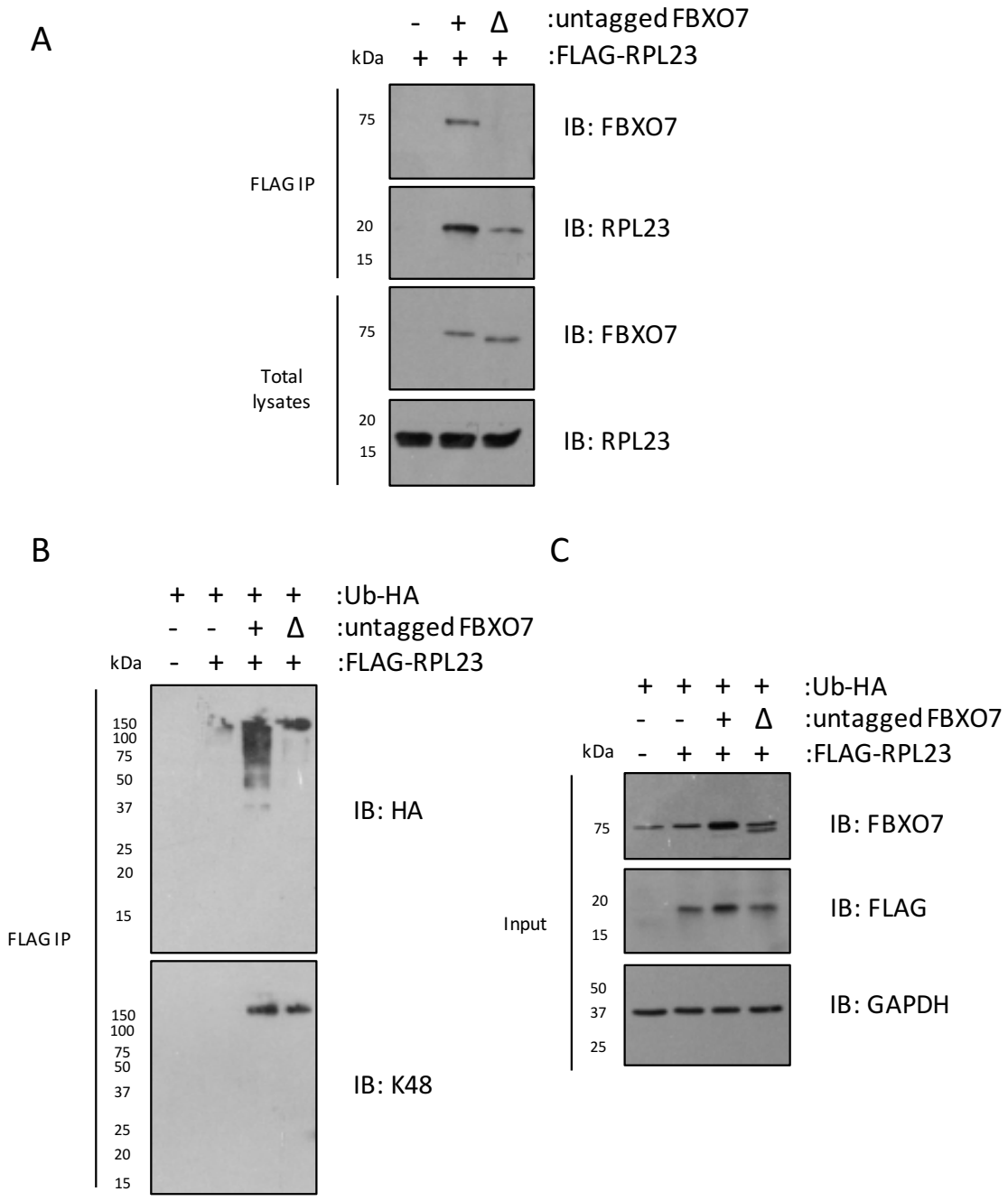

Figure 5.8 – FBXO7 interacts with and ubiquitinates RPL23 with K48 linkages. (A) FLAG IP from HEK293T cell lysates transfected with FLAG-vector control and FLAG-RPL23, in addition to untagged FBXO7 or ΔF-box. It shows that there is an interaction of FBXO7, but not ΔF-box, with RPL23. (n=3) (B) Ubiquitination assay in HEK293T cells, which were transfected with Ub-HA, untagged FBXO7 or ΔF-box, and FLAG-RPL23. The FLAG IP was immunoblotted for ubiquitin and K48 ubiquitin linkages. (C) The input of the ubiquitination assay was immunoblotted for FBXO7, FLAG and GAPDH as controls for the IP. (n=3)

5 – Discussion

There have only been a limited number of *Fbxo7* transgenic mouse models generated up to date, which are crucial to investigate FBXO7 pathophysiology of PD in a more physiological setting. Vingill *et al.* also published a report on systemic and conditional *Fbxo7* knockout mouse models, specifically utilising catecholaminergic and forebrain specific Cre mice.[330] Their systemic *Fbxo7* KO model exhibited weight loss, early-onset weakness and premature death.[330] This concurs with the systemic Zp3^{Cre}*Fbxo7*$^{-/-}$ mouse that we generated, which also presented with a runted phenotype. In both systemic mouse models, the causes of their severe phenotypes remain unknown.

The first aim of this chapter was to characterise the electrophysiology of the systemic Zp3^{Cre}*Fbxo7*$^{-/-}$ mouse brain sections, which remained untested in the Vingill *et al.* paper. Although it still remains to be fully elucidated to what extent genetic susceptibility to PD affects the electrophysiological properties of DA neurons, it has been shown that certain PD mouse models do exhibit altered firing patterns of DA neurons, prior to the onset of motor symptoms.[371,372] One particular study showed that knockout of *PINK1* results in neuronal hyperexcitability, characterised by irregular action potential firing and enhanced burst firing, attributed to reduced activity of small-conductance Ca^{2+}-activated potassium channels.[39] Interestingly, this phenotype was only observed in SNpc DA neurons, and not in the VTA DA neurons nor in substantia nigra pars reticulata (SNpr) GABAergic neurons.[39] These studies emphasise the importance of selective vulnerability of SNpc DA neurons in PD. In addition, FBXO7 and PINK1 have been previously shown to directly interact in Parkin-mediated mitophagy, so it is tempting to assume that they may be involved in other common pathways as well. The innervation of the striatum from the DA neurons of the SNpc occurs from E16 until day 60 postnatally (P60),[377] so these experiments could only be conducted on brains that were not completely innervated. Overall, my results suggest that there no differences in SNpc DA neuron electrophysiology at 2-3 weeks of age. However, as the electrophysiology recordings were only made in a total of six neurons, it is difficult to form robust conclusions at this stage, especially prior to quantifying the firing rate and tendency to burst against WT littermates. Overall, the neurons fired within the regular range and there were no noticeable changes towards hypo- or hyperexcitability. However, even if their physiology appears to remain unaffected by *Fbxo7* loss by 2-3 weeks of age, there may still be changes in their neurochemical content. Repetition of these recordings would

inform the next set of experiments, which could include downstream striatal recordings, tonic dopamine release measurements and whole-cell expression levels of NMDARs. It would also be interesting to repeat the electrophysiological characterisation in SNpc DA neurons of the conditional Dat^{Cre}*Fbxo7*$^{-/fl}$ mouse at different time points as certain phenotypes may only surface at an older age. This possibility is implied by the differing phenotypes of null and conditional KO mice examined at different ages, particularly in relation to TH positive DA cells of the striatum.

We were able to age and characterise the conditional Dat^{Cre}*Fbxo7*$^{-/fl}$ mouse model to reveal a complex Parkinson's-like DA degeneration phenotype. These mice presented with less TH+ innervation of the striatum at 6 weeks of age, decreased TH+ fibre density and TH+ cell body size in the SNpc at 12 weeks of age, and a reduction of TH+ DA neurons in the SNpc at 20 weeks of age. Furthermore, these mice also exhibited motor coordination defects at 20 weeks of age. At this stage, we cannot be certain whether it is a developmental defect or whether DA neurons develop properly but then there is a defect in their maintenance. The systemic null model perhaps suggests the latter, but it requires further investigation. It would be valuable to examine the brain of our current model at earlier time points but also to generate a temporally inducible conditional KO mouse, in which loss of *Fbxo7* could be induced post-innervation, which would also more closely mimic the disease onset of idiopathic PD. These models would indicate whether there is a developmental defect in neurite outgrowth, meaning cells never establish neuronal contacts, or whether it is a degenerative phenotype resulting in loss of neurons over time. Furthermore, proteins like LIM kinases, ephrins and GSK3β that are involved in neurite outgrowth, are also potential substrates of the SCF^{FBXO7} ligase and should be further investigated. As previously mentioned, Vingill *et al*. also recently generated two conditional FBXO7 knockout mice.[330] Their forebrain (*Nex*-Cre) conditional KO model showed severe motor dysfunction, hyperreflexia and spasticity.[330] Whereas, the catecholaminergic (*Th*-Cre) conditional KO model presented with progressive loss of motor function and reduced levels of dopamine in the striatum, but no TH+ cell loss as in our model. The differences may be due to the fact that the *Th*-Cre line has an earlier-onset and a wider recombination pattern compared to our *Dat*-Cre line, including in non-DA cells in regions outside than the ventral midbrain.

The second aim of this chapter was to determine the relationship between FBXO7 and RPL23. It was shown that RPL23 expression is significantly upregulated in DA neurons of the Dat^{Cre}*Fbxo7*$^{-/fl}$ mouse, suggesting that FBXO7 may negatively regulate RPL23. I determined that FBXO7 interacts and ubiquitinates RPL23 with K48 linked ubiquitin chains, targeting it for proteasomal degradation. In determining what effect this relationship may play in neuronal cell survival, and therefore contribute to the observed pathologies, it is important to note that RPL23 can inhibit MDM2, leading to p53 stabilisation and apoptosis.[375,376] One can therefore hypothesise that increased expression of RPL23, as seen in the absence of FBXO7 in the SNpc, would lead to increased p53 expression and cell death. This could be one possible explanation as to why there was no significant cell death of TH+ neurons in the SNpc at 6 weeks of age, but that accumulation of p53 over time and/or the significantly decreased striatal innervation could lead to cell death by 20 weeks of age. Furthermore, the lack of FBXO7 expression could also downregulate NF-κB-mediated cell survival pathway via the poly-ubiquitination of NRAGE.[378] At the same time, FBXO7 can also function as a negative regulator of NF-κB signalling,[318] so further experiments would be necessary to confirm.

Overall, these results suggest that multiple pathways may be regulated by *Fbxo7* in the midbrain of this mouse model, leading to the observed array of phenotypes. Immunoprecipitations showed that FLAG-RPL23 interacts with FBXO7 but not ΔF-box. It could be that FBXO7 and RPL23 interact via the F-box domain, however that seems to be unlikely. If RPL23 were to interact with FBXO7 via the same domain as Skp1, then this could hinder the recruitment of the rest of the E3 ligase subunits and thus interfere with the ubiquitination of RPL23. It is more likely that the lack of interaction is due to the fact that ΔF-box localises to the nucleus, unlike WT FBXO7 which is present in the cytoplasm. However, in order to test this experimentally, one would need to repeat the immunoprecipitation assay with different FBXO7 mutants, including those that localise to the cytoplasm but are still inactive as a ligase. In terms of other future experiments, it would be interesting to investigate the ubiquitination of RPL23 by testing *FBXO7* T22M, R378G and R498X PD mutant ligases. As PD mutations span most of the gene, these experiments could possibly suggest through which domain these two proteins interact and which potential pathogenic mechanism may be involved. Furthermore, it would be also valuable to test for RPL23 expression in the patient fibroblasts that I have

characterised and described in Chapter 3 of this thesis, especially as one of their observed phenotypes was increased apoptosis.

In conclusion, the Dat^{Cre}*Fbxo7*$^{-/fl}$ mouse model was able to recapitulate several important PD phenotypes, including motor coordination defects, decreased TH innervation of the striatum and loss of TH cells in the SNpc. Characterisation of this mouse also lead to the identification of RPL23 as a new ubiquitination substrate of FBXO7 and suggested an RPL23-MDM2-p53 based mechanism leading to neuronal cell death.

CHAPTER 6

CONCLUSION

FBXO7 plays a crucial role in many pathways that include ubiquitination (mediating both degradation and function), cell cycle regulation, proteasomal maturation, inflammation, and mitophagy under stress. Due to its involvement in so many processes and having varying effects in different cells types, FBXO7 can be quite a challenging protein to study. However, it is important to continue to research its loss-of-function effects in various models as it lies at the intersection of many potential pathways underlying Parkinson's disease pathogenesis.

In my thesis, I first characterised primary fibroblasts from a rare patient harbouring an FBXO7 mutation resulting in the loss of protein expression (Chapter 3). My main focus was to investigate parkin-independent roles of FBXO7 in mitochondrial biology, under basal conditions. Mitochondrial dysfunction seems to be at the centre of potential mechanisms that lead to both sporadic and familial PD pathogenesis. Some of the PD-contributing mitochondrial factors include mutations in mtDNA, mutations in nuclear DNA that are linked to mitochondria, changes in mitochondrial morphology, dynamics, and trafficking, or electron transport chain and oxidative phosphorylation defects.[8,166] I discovered several important phenotypes in FBXO7-deficient fibroblasts, which included a reduction in mitochondrial respiration, ETC complex activities, and mitochondrial RNAs expression (**Fig6.1A**). Importantly, I also observed similar phenotypes in MEFs from a systemic FBXO7 KO mouse model. Both patient fibroblasts and MEFs do not express full-length FBXO7, but it is unsure whether the patient is also a complete null or whether a truncated protein may still be made and functioning to a certain extent.

One of the key further experiments would be to complement back FBXO7 into these cell lines to hopefully observe a reversal of the phenotypes. This would provide a direct link between FBXO7 expression and the observed mitochondrial phenotypes. In addition to complementing back wild-type FBXO7, it would be also interesting to insert other pathogenic *FBXO7* mutations into FBXO7-null cells to investigate whether some phenotypes may be mutation specific. In order to elucidate the decrease in

mitochondrial complex activities and respiration, it would be important to check whether the subunits correctly assemble into functioning complexes. Blue-native SDS PAGE would show whether mitochondrial complexes are being formed properly or whether an assembly defect may be responsible for their decreased activities. Lastly, it would be also important to investigate mitochondrial translation and mitoribosome protein levels *in vivo*.

As it is known for FBXO7 to have cell-specific functions, I tried to recapitulate the findings from the patient fibroblasts and MEFs in a neuronal cell line (Chapter 4). I conducted experiments on both knockdown and knockout SH-SY5Y cell lines, which are widely used as an *in vitro* PD model. The shortcomings of using these lines to study the effects of FBXO7 were that some phenotypes proved to be transient and/or variable. This was possibly due to residual FBXO7 expression in the KD lines, clonal effects in the KO lines, and potential compensatory mechanisms in both models. Thus, I would refrain from working with these cell lines in the future but rather continue the line of inquiry into mitochondrial and cellular oxidative stress, mitochondrial function and lipid droplets in another model. For instance, it may prove valuable to create a patient-derived neuronal model to investigate the discovered phenotypes further. Differentiating patient fibroblasts into dopaminergic neurons via iPS reprogramming would combine the advantages of using patient fibroblasts (Chapter 3) and a neuronal environment (Chapter 4), hopefully providing a more accurate model of Parkinson's disease.

In parallel to these cellular models, I also contributed to the characterisation of systemic and conditional *Fbxo7* knockout mouse models (Chapter 5). We investigated whether these mouse models could recapitulate some of the hallmarks of PD pathogenesis in a more physiological environment. The conditional FBXO7 KO model was able to recapitulate several important PD phenotypes, including motor coordination defects, decreased TH innervation of the striatum and loss of TH cells in the substantia nigra pars compacta. Furthermore, I was able to identify and confirm RPL23 as a new K48-linked ubiquitination substrate of FBXO7, suggesting an RPL23-MDM2-p53 based mechanism leading to neuronal cell death in Parkinson's disease (**Fig6.1B**).

To further characterise the role of FBXO7 *in vivo* and check whether the remaining neurons are functional properly, I would conduct electrophysiological analysis of SNpc DA neurons in the conditional Dat^{Cre}*Fbxo7*$^{-/fl}$ mouse at different timepoints. Also, in order to confirm whether the defects are at the neurodevelopmental stage or rather in their maintenance, it would be valuable to examine the current model at earlier time points. I would also generate a temporally inducible conditional KO mouse. In this case, loss of *Fbxo7* could be induced post-innervation, which would more closely mimic the disease onset of idiopathic PD. These models would indicate whether there is a developmental defect in neurite outgrowth, meaning cells never establish neuronal contacts, or whether it is a degenerative phenotype resulting in loss of neurones over time. In terms of other future experiments, it would be interesting to investigate the ubiquitination of RPL23 by testing *FBXO7* T22M, R378G and R498X PD mutant ligases. As PD mutations span most of the gene, these experiments could possibly suggest through which domain these two proteins interact and which potential pathogenic mechanisms may be involved. Furthermore, it would be also valuable to test for RPL23 expression in the patient fibroblasts that I have characterised and described in Chapter 3 of this thesis, especially as one of their observed phenotypes was increased apoptosis.

Modelling human diseases in cellular and animal models is inherently difficult. However, it is vital to continue investigating the role of FBXO7, and other associated genes, in a variety of models to gain insight into pathogenic mechanisms underlying Parkinson's disease. The work I presented in this thesis revealed important roles of FBXO7 not only in basal mitochondrial biology, but also suggested potential pathways that may contribute to neurodegeneration in Parkinson's disease.

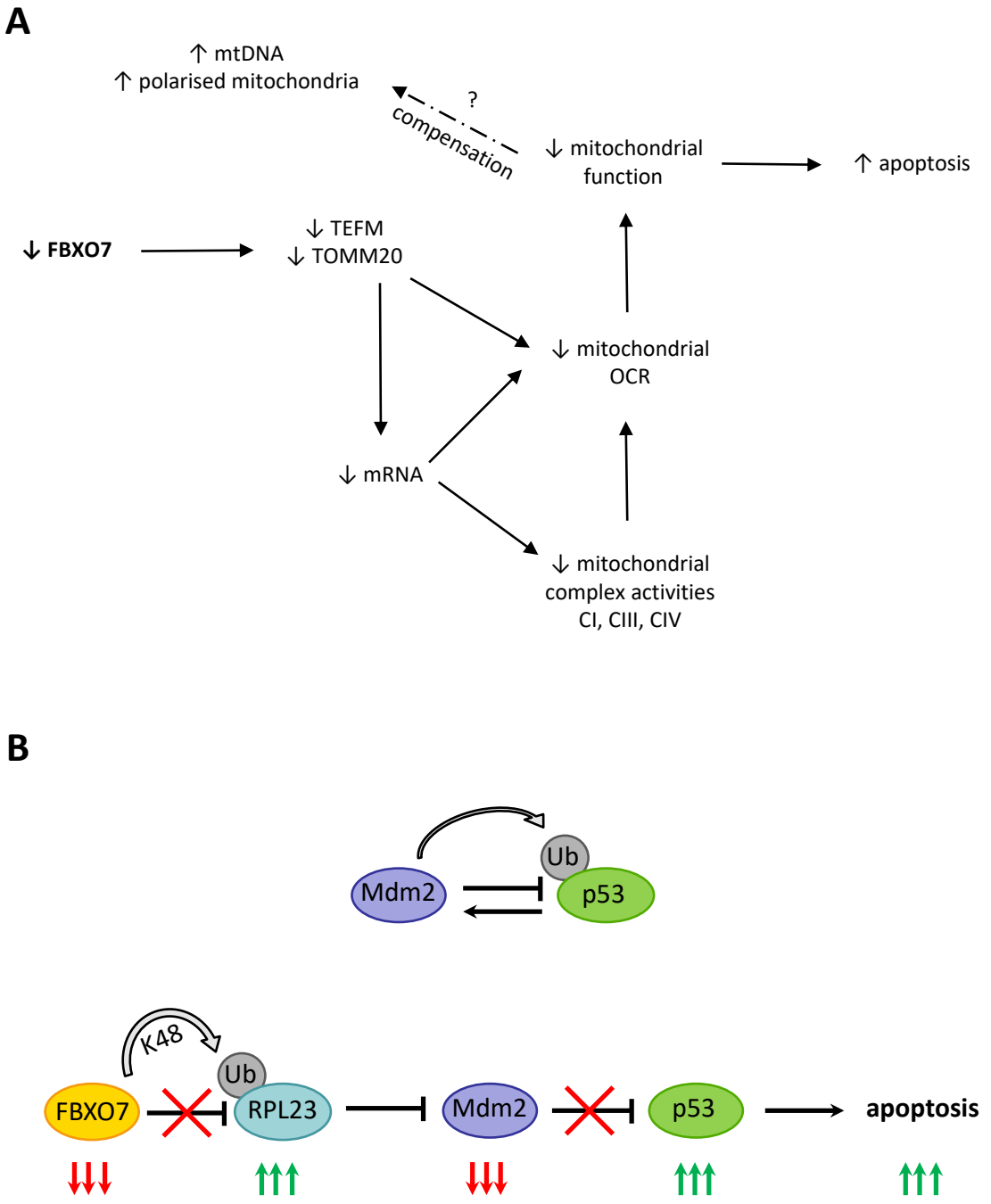

Figure 6.1 – Summary of main thesis findings. (A) A schematic showing potential roles that loss of FBXO7 expression has on various aspects of mitochondrial biology in patient fibroblast lines (and MEFs from a systemic *Fbxo7* KO mouse). (B) A model showing the Mdm2:p53 axis (negative feedback loop) under regular conditions and a proposed model of how loss of FBXO7 may dysregulate the axis via its the effect on RPL23.

REFERENCES

1. Parkinson James. An Essay on the Shaking Palsy (reprint of 1817 original). *J Neuropsychiatry Clin Neurosci* 14, 223–236 (2002).
2. Bonifati, V. Genetics of Parkinson's disease - state of the art, 2013. *Park. Relat. Disord.* 20, S23–S28 (2014).
3. Singleton, A. B., Farrer, M. J. & Bonifati, V. The genetics of Parkinson's disease: Progress and therapeutic implications. *Mov. Disord.* 28, 14–23 (2013).
4. Dauer, W. & Przedborski, S. Parkinson's Disease: Mechanisms and Models. *Neuron* 39, 889–909 (2003).
5. Yeragani, V. K., Tancer, M., Chokka, P. & Baker, G. B. Arvid Carlsson, and the story of dopamine. *Indian J. Psychiatry* 52, 87–8 (2010).
6. Bolam, J. P., Hanley, J. J., Booth, P. A. & Bevan, M. D. Synaptic organisation of the basal ganglia. *J. Anat.* 196 (Pt 4, 527–42 (2000).
7. Gaki, G. S. & Papavassiliou, A. G. Oxidative Stress-Induced Signaling Pathways Implicated in the Pathogenesis of Parkinson's Disease. *NeuroMolecular Med.* 16, 217–230 (2014).
8. Camilleri, A. & Vassallo, N. The Centrality of Mitochondria in the Pathogenesis and Treatment of Parkinson's Disease. *CNS Neurosci. Ther.* 20, 591–602 (2014).
9. Dexter, D. T. & Jenner, P. Parkinson disease: from pathology to molecular disease mechanisms. *Free Radic. Biol. Med.* 62, 132–144 (2013).
10. Mandel, S. A., Fishman, T. & Youdim, M. B. H. Gene and protein signatures in sporadic Parkinson's disease and a novel genetic model of PD. *Parkinsonism Relat. Disord.* 13, S242–S247 (2007).
11. Koutsilieri, E. & Riederer, P. Excitotoxicity and new antiglutamatergic strategies in Parkinson's disease and Alzheimer's disease. *Parkinsonism Relat. Disord.* 13 Suppl 3, S329-31 (2007).
12. Pires, A. O. *et al.* Old and new challenges in Parkinson's disease therapeutics. *Prog. Neurobiol.* 156, 69–89 (2017).
13. Katzenschlager, R. *et al.* Mucuna pruriens in Parkinson's disease: a double blind clinical and pharmacological study. *J. Neurol. Neurosurg. Psychiatry* 75, 1672–1677 (2004).
14. Damodaran, M. & Ramaswamy, R. Isolation of l -3:4-dihydroxyphenylalanine from the seeds of Mucuna pruriens. *Biochem. J.* 31, 2149–2152 (1937).
15. Factor, S. A. Current status of symptomatic medical therapy in Parkinson's disease. *Neurotherapeutics* 5, 164–180 (2008).
16. Schapira, A. H. V. Present and future drug treatment for Parkinson's disease. *J. Neurol. Neurosurg. Psychiatry* 76, 1472–8 (2005).
17. Smith, Y., Wichmann, T., Factor, S. A. & DeLong, M. R. Parkinson's Disease Therapeutics: New Developments and Challenges Since the Introduction of Levodopa. *Neuropsychopharmacology* 37, 213–246 (2012).
18. Klein, C. & Westenberger, A. Genetics of Parkinson's Disease. doi:10.1101/cshperspect.a008888
19. Deng, H., Wang, P. & Jankovic, J. The genetics of Parkinson disease. (2018). doi:10.1016/j.arr.2017.12.007
20. Polymeropoulos, M. H. *et al.* Mutation in the alpha-synuclein gene identified in families with Parkinson's disease. *Science* 276, 2045–7 (1997).
21. Ibáñez, P. *et al.* Causal relation between α-synuclein locus duplication as a cause of familial Parkinson's disease. *Lancet* 364, 1169–1171 (2004).
22. Golbe, L. I., Di Iorio, G., Bonavita, V., Miller, D. C. & Duvoisin, R. C. A large kindred with autosomal dominant Parkinson's disease. *Ann. Neurol.* 27, 276–82 (1990).
23. Houlden, H. & Singleton, A. B. The genetics and neuropathology of Parkinson's

disease. *Acta Neuropathol.* 124, 325–338 (2012).
24. Spillantini, M. G. *et al.* α-Synuclein in Lewy bodies. *Nature* 388, 839–840 (1997).
25. Funayama, M. *et al.* A new locus for Parkinson's disease (PARK8) maps to chromosome 12p11.2-q13.1. *Ann. Neurol.* 51, 296–301 (2002).
26. Zimprich, A. *et al.* Mutations in LRRK2 cause autosomal-dominant parkinsonism with pleomorphic pathology. *Neuron* 44, 601–7 (2004).
27. Healy, D. G. *et al.* Phenotype, genotype, and worldwide genetic penetrance of LRRK2-associated Parkinson's disease: a case-control study. *Lancet. Neurol.* 7, 583–90 (2008).
28. Sidransky, E. *et al.* Multicenter analysis of glucocerebrosidase mutations in Parkinson's disease. *N. Engl. J. Med.* 361, 1651–61 (2009).
29. Goker-Alpan, O. *et al.* The Spectrum of Parkinsonian Manifestations Associated With Glucocerebrosidase Mutations. *Arch. Neurol.* 65, 1353–7 (2008).
30. Tayebi, N. *et al.* Gaucher disease with parkinsonian manifestations: does glucocerebrosidase deficiency contribute to a vulnerability to parkinsonism? *Mol. Genet. Metab.* 79, 104–9 (2003).
31. Tayebi, N. *et al.* Gaucher disease and parkinsonism: a phenotypic and genotypic characterization. *Mol. Genet. Metab.* 73, 313–21 (2001).
32. Aharon-Peretz, J., Rosenbaum, H. & Gershoni-Baruch, R. Mutations in the Glucocerebrosidase Gene and Parkinson's Disease in Ashkenazi Jews. *N. Engl. J. Med.* 351, 1972–1977 (2004).
33. Kitada, T. *et al.* Mutations in the parkin gene cause autosomal recessive juvenile parkinsonism. *Nature* 392, 605–608 (1998).
34. Samaranch, L. *et al.* PINK1-linked parkinsonism is associated with Lewy body pathology. *Brain* 133, 1128–42 (2010).
35. Bonifati, V. *et al.* Early-onset parkinsonism associated with PINK1 mutations: Frequency, genotypes, and phenotypes. *Neurology* 65, 87–95 (2005).
36. Abou-Sleiman, P. M., Healy, D. G., Quinn, N., Lees, A. J. & Wood, N. W. The role of pathogenicDJ-1 mutations in Parkinson's disease. *Ann. Neurol.* 54, 283–286 (2003).
37. Bonifati, V. *et al.* Mutations in the DJ-1 gene associated with autosomal recessive early-onset parkinsonism. *Science* 299, 256–9 (2003).
38. Ramirez, A. *et al.* Hereditary parkinsonism with dementia is caused by mutations in ATP13A2, encoding a lysosomal type 5 P-type ATPase. *Nat. Genet.* 38, 1184–1191 (2006).
39. Paisan-Ruiz, C. *et al.* Characterization of PLA2G6 as a locus for dystonia-parkinsonism. *Ann. Neurol.* 65, 19–23 (2008).
40. Lin, C.-H., Chen, M.-L., Lai, T.-T., Tai, C.-H. & Wu, R.-M. Mutational analysis of FBXO7 gene in Parkinson's disease in a Taiwanese population. *Neurobiol. Aging* 34, 1713.e1-1713.e4 (2013).
41. Di Fonzo, A. *et al.* FBXO7 mutations cause autosomal recessive, early-onset parkinsonian-pyramidal syndrome. *Neurology* 72, 240–5 (2009).
42. Zhao, T. *et al.* FBXO7 immunoreactivity in α-synuclein-containing inclusions in Parkinson disease and multiple system atrophy. *J. Neuropathol. Exp. Neurol.* 72, 482–8 (2013).
43. Valente, E. M. *et al.* Hereditary Early-Onset Parkinson's Disease Caused by Mutations in PINK1. *Science (80-.).* 304, 1158–1160 (2004).
44. Bonifati, V. *et al.* DJ-1(PARK7), a novel gene for autosomal recessive, early onset parkinsonism. *Neurol. Sci.* 24, 159–160 (2003).
45. Strauss, K. M. *et al.* Loss of function mutations in the gene encoding Omi/HtrA2 in Parkinson's disease. *Hum. Mol. Genet.* 14, 2099–2111 (2005).
46. Shojaee, S. *et al.* Genome-wide linkage analysis of a Parkinsonian-pyramidal syndrome pedigree by 500 K SNP arrays. *Am. J. Hum. Genet.* 82, 1375–84 (2008).
47. Zimprich, A. *et al.* A Mutation in VPS35, Encoding a Subunit of the Retromer Complex,

Causes Late-Onset Parkinson Disease. *AJHG* 89, 168–175 (2011).
48. Vilariño-Güell, C. *et al.* VPS35 Mutations in Parkinson Disease. *AJHG* 89, 162–167 (2011).
49. Chartier-Harlin, M.-C. *et al.* Translation Initiator EIF4G1 Mutations in Familial Parkinson Disease. *Am. J. Hum. Genet.* 89, 398–406 (2011).
50. Edvardson, S. *et al.* A Deleterious Mutation in DNAJC6 Encoding the Neuronal-Specific Clathrin-Uncoating Co-Chaperone Auxilin, Is Associated with Juvenile Parkinsonism. *PLoS One* 7, e36458 (2012).
51. Köroğlu, Ç., Baysal, L., Cetinkaya, M., Karasoy, H. & Tolun, A. DNAJC6 is responsible for juvenile parkinsonism with phenotypic variability. *Parkinsonism Relat. Disord.* 19, 320–324 (2013).
52. Krebs, C. E. *et al.* The Sac1 domain of SYNJ1 identified mutated in a family with early-onset progressive parkinsonism with generalized seizures. *Hum. Mutat.* 34, 1200–1207 (2013).
53. Quadri, M. *et al.* Mutation in the SYNJ1 gene associated with autosomal recessive, early-onset Parkinsonism. *Hum. Mutat.* 34, 1208–15 (2013).
54. Deng, H.-X. *et al.* Identification of TMEM230 mutations in familial Parkinson's disease. *Nat. Genet.* 48, 733–739 (2016).
55. Funayama, M. *et al.* CHCHD2 mutations in autosomal dominant late-onset Parkinson's disease: a genome-wide linkage and sequencing study. *Lancet Neurol.* 14, 274–282 (2015).
56. Lesage, S. *et al.* Loss of VPS13C Function in Autosomal-Recessive Parkinsonism Causes Mitochondrial Dysfunction and Increases PINK1/Parkin-Dependent Mitophagy. *Am. J. Hum. Genet.* 98, 500–513 (2016).
57. Neudorfer, O. *et al.* Occurrence of Parkinson's syndrome in type I Gaucher disease. *QJM* 89, 691–4 (1996).
58. Creed, R. B. & Goldberg, M. S. New developments in genetic rat models of Parkinson's disease. *Mov. Disord.* (2018). doi:10.1002/mds.27296
59. Ungerstedt, U. 6-hydroxy-dopamine induced degeneration of central monoamine neurons. *Eur. J. Pharmacol.* 5, 107–10 (1968).
60. Blandini, F., Armentero, M.-T. & Martignoni, E. The 6-hydroxydopamine model: News from the past. *Parkinsonism Relat. Disord.* 14, S124–S129 (2008).
61. Lee, C. S., Sauer, H. & Bjorklund, A. Dopaminergic neuronal degeneration and motor impairments following axon terminal lesion by instrastriatal 6-hydroxydopamine in the rat. *Neuroscience* 72, 641–53 (1996).
62. Jackson-Lewis, V., Blesa, J. & Przedborski, S. Animal models of Parkinson's disease. *Park. Realt. Disord.* 18, S183–S185 (2012).
63. Langston, J. W., Ballard, P., Tetrud, J. W. & Irwin, I. Chronic Parkinsonism in humans due to a product of meperidine-analog synthesis. *Science* 219, 979–80 (1983).
64. Chiueh, C. C. *et al.* Neurochemical and behavioral effects of 1-methyl-4-phenyl-1,2,3,6-tetrahydropyridine (MPTP) in rat, guinea pig, and monkey. *Psychopharmacol. Bull.* 20, 548–53 (1984).
65. Cui, M. *et al.* The organic cation transporter-3 is a pivotal modulator of neurodegeneration in the nigrostriatal dopaminergic pathway. *Proc. Natl. Acad. Sci.* 106, 8043–8048 (2009).
66. Berry, C., La Vecchia, C. & Nicotera, P. Paraquat and Parkinson's disease. *Cell Death Differ.* 17, 1115–1125 (2010).
67. Greenamyre, J. T., Cannon, J. R., Drolet, R. & Mastroberardino, P.-G. Lessons from the rotenone model of Parkinson's disease. *Trends Pharmacol. Sci.* 31, 141-2-3 (2010).
68. Peng, J., Oo, M. L. & Andersen, J. K. Synergistic effects of environmental risk factors and gene mutations in Parkinson's disease accelerate age-related neurodegeneration. *J. Neurochem.* 115, 1363–1373 (2010).
69. Lu, X.-H. *et al.* Bacterial Artificial Chromosome Transgenic Mice Expressing a

Truncated Mutant Parkin Exhibit Age-Dependent Hypokinetic Motor Deficits, Dopaminergic Neuron Degeneration, and Accumulation of Proteinase K-Resistant -Synuclein. *J. Neurosci.* 29, 1962–1976 (2009).
70. Kitada, T., Tong, Y., Gautier, C. A. & Shen, J. Absence of nigral degeneration in aged parkin/DJ-1/PINK1 triple knockout mice. *J. Neurochem.* 111, 696–702 (2009).
71. Shin, J.-H. *et al.* PARIS (ZNF746) Repression of PGC-1α Contributes to Neurodegeneration in Parkinson's Disease. *Cell* 144, 689–702 (2011).
72. Goldberg, M. S. *et al.* Parkin-deficient Mice Exhibit Nigrostriatal Deficits but Not Loss of Dopaminergic Neurons. *J. Biol. Chem.* 278, 43628–43635 (2003).
73. Palacino, J. J. *et al.* Mitochondrial dysfunction and oxidative damage in parkin-deficient mice. *J. Biol. Chem.* 279, 18614–22 (2004).
74. Gispert, S. *et al.* Parkinson Phenotype in Aged PINK1-Deficient Mice Is Accompanied by Progressive Mitochondrial Dysfunction in Absence of Neurodegeneration. *PLoS One* 4, e5777 (2009).
75. Kim, R. H. *et al.* Hypersensitivity of DJ-1-deficient mice to 1-methyl-4-phenyl-1,2,3,6-tetrahydropyrindine (MPTP) and oxidative stress. *Proc. Natl. Acad. Sci.* 102, 5215–5220 (2005).
76. Chen, L. *et al.* Age-dependent motor deficits and dopaminergic dysfunction in DJ-1 null mice. *J. Biol. Chem.* 280, 21418–26 (2005).
77. Goldberg, M. S. *et al.* Nigrostriatal Dopaminergic Deficits and Hypokinesia Caused by Inactivation of the Familial Parkinsonism-Linked Gene DJ-1. *Neuron* 45, 489–496 (2005).
78. Dave, K. D. *et al.* Phenotypic characterization of recessive gene knockout rat models of Parkinson's disease. *Neurobiol. Dis.* 70, 190–203 (2014).
79. Vercammen, L. *et al.* Parkin Protects against Neurotoxicity in the 6-Hydroxydopamine Rat Model for Parkinson's Disease. *Mol. Ther.* 14, 716–723 (2006).
80. Villeneuve, L. M., Purnell, P. R., Boska, M. D. & Fox, H. S. Early Expression of Parkinson's Disease-Related Mitochondrial Abnormalities in PINK1 Knockout Rats. *Mol. Neurobiol.* 53, 171–186 (2016).
81. Sun, J., Kouranova, E., Cui, X., Mach, R. H. & Xu, J. Regulation of dopamine presynaptic markers and receptors in the striatum of DJ-1 and Pink1 knockout rats. *Neurosci. Lett.* 557 Pt B, 123–8 (2013).
82. Falkenburger, B. H., Saridaki, T. & Dinter, E. Cellular models for Parkinson's disease. *Journal of Neurochemistry* 139, 121–130 (2016).
83. Falkenburger, B. H. & Schulz, J. B. Limitations of cellular models in Parkinson's disease research. *J. Neural Transm. Suppl.* 261–8 (2006). doi:Review
84. Takahashi, K. & Yamanaka, S. Induction of Pluripotent Stem Cells from Mouse Embryonic and Adult Fibroblast Cultures by Defined Factors. *Cell* 126, 663–676 (2006).
85. Soldner, F. *et al.* Parkinson's Disease Patient-Derived Induced Pluripotent Stem Cells Free of Viral Reprogramming Factors. *Cell* 136, 964–977 (2009).
86. Gray, M. W., Burger, G. & Lang, B. F. Mitochondrial evolution. *Science* 283, 1476–81 (1999).
87. Falkenberg, M., Larsson, N.-O. & Gustafsson, C. M. DNA Replication and Transcription in Mammalian Mitochondria mtDNA: mitochondrial DNA. *Annu. Rev. Biochem.* 76, 679–99 (2007).
88. Gong, Z., Tas, E. & Muzumdar, R. Humanin and age-related diseases: A new link? *Front. Endocrinol. (Lausanne).* 5, 210 (2014).
89. Niikura, T., Chiba, T., Aiso, S., Matsuoka, M. & Nishimoto, I. Humanin: After the Discovery. *Mol. Neurobiol.* 30, 327–340 (2004).
90. Mokranjac, D. & Neupert, W. Protein import into mitochondria. *Biochem. Soc. Trans.* 33, 1019 (2005).
91. Shadel, G. S. & Clayton, D. A. Mitochondrial DNA maintenance in vertebrates. *Annu.*

Rev. Biochem. 66, 409–35 (1997).
92. Clayton, D. A. Replication and Transcription of Vertebrate Mitochondrial DNA. *Annu. Rev. Cell Biol.* 7, 453–478 (1991).
93. Montoya, J., Ojala, D. & Attardi, G. Distinctive features of the 5'-terminal sequences of the human mitochondrial mRNAs. *Nature* 290, 465–70 (1981).
94. Ojala, D., Montoya, J. & Attardi, G. tRNA punctuation model of RNA processing in human mitochondria. *Nature* 290, 470–4 (1981).
95. Stumpf, J. D. & Copeland, W. C. Mitochondrial DNA replication and disease: insights from DNA polymerase γ mutations. *Cell. Mol. Life Sci.* 68, 219–233 (2011).
96. Falkenberg, M. *et al.* Mitochondrial transcription factors B1 and B2 activate transcription of human mtDNA. *Nat. Genet.* 31, 289–294 (2002).
97. Minczuk, M. *et al.* TEFM (c17orf42) is necessary for transcription of human mtDNA. *Nucleic Acids Res.* 39, 4284–99 (2011).
98. Kornberg, H. Krebs and his trinity of cycles. *Nat. Rev. Mol. Cell Biol.* 1, 225–228 (2000).
99. Akram, M. Citric Acid Cycle and Role of its Intermediates in Metabolism. *Cell Biochem. Biophys.* 68, 475–478 (2014).
100. Nunes-Nesi, A., Araú Jo, W. L., Obata, T. & Fernie, A. R. Regulation of the mitochondrial tricarboxylic acid cycle. *Curr. Opin. Plant Biol.* 16, 335–343 (2013).
101. Lemarie, A. & Grimm, S. Mitochondrial respiratory chain complexes: apoptosis sensors mutated in cancer? *Oncogene* 30, 3985–4003 (2011).
102. Schultz, B. E. & Chan, S. I. Structures and Proton-Pumping Strategies of Mitochondrial Respiratory Enzymes. *Annu. Rev. Biophys. Biomol. Struct.* 30, 23–65 (2001).
103. Rutter, J., Winge, D. R. & Schiffman, J. D. Succinate dehydrogenase - Assembly, regulation and role in human disease. *Mitochondrion* 10, 393–401 (2010).
104. Sun, F., Zhou, Q., Pang, X., Xu, Y. & Rao, Z. Revealing various coupling of electron transfer and proton pumping in mitochondrial respiratory chain. *Curr. Opin. Struct. Biol.* 23, 526–538 (2013).
105. Hosler, J. P., Ferguson-Miller, S. & Mills, D. A. Energy Transduction: Proton Transfer Through the Respiratory Complexes. *Annu. Rev. Biochem.* 75, 165–187 (2006).
106. Perry, S., Norman, J., Barbieri, J., Brown, E. & Gelbard, H. Mitochondrial membrane potential probes and the proton gradient: a practical usage guide. *Biotechniques* 50, 98–115 (2011).
107. Balaban, R. S., Nemoto, S. & Finkel, T. Mitochondria, oxidants, and aging. *Cell* 120, 483–95 (2005).
108. Hirst, J. Mitochondrial Complex I. *Annu. Rev. Biochem.* 82, 551–575 (2013).
109. Wirth, C., Brandt, U., Hunte, C., Zickermann, V. & Zick, V. Structure and function of mitochondrial complex I. *BBA - Bioenerg.* 1857, 902–914 (2016).
110. Stroud, D. A. *et al.* Accessory subunits are integral for assembly and function of human mitochondrial complex I. *Nature* 538, 123–126 (2016).
111. Gottlieb, E. & Tomlinson, I. P. M. Mitochondrial tumour suppressors: a genetic and biochemical update. *Nat. Rev. Cancer* 5, 857–866 (2005).
112. Cecchini, G. Function and Structure of Complex II of the Respiratory Chain. *Annu. Rev. Biochem.* 72, 77–109 (2003).
113. Sun, F. *et al.* Crystal Structure of Mitochondrial Respiratory Membrane Protein Complex II. *Cell* 121, 1043–1057 (2005).
114. Yankovskaya, V. *et al.* Architecture of Succinate Dehydrogenase and Reactive Oxygen Species Generation. *Science (80-.).* 299, 700–704 (2003).
115. Lemarie, A., Huc, L., Pazarentzos, E., Mahul-Mellier, A.-L. & Grimm, S. Specific disintegration of complex II succinate:ubiquinone oxidoreductase links pH changes to oxidative stress for apoptosis induction. *Cell Death Differ.* 18, 338–49 (2011).
116. Hwang, M.-S., Rohlena, J., Dong, L.-F., Neuzil, J. & Grimm, S. Powerhouse down: Complex II dissociation in the respiratory chain. *Mitochondrion* 19, 20–28 (2014).
117. Hoekstra, A. S. & Bayley, J. P. The role of complex II in disease. *Biochim. Biophys. Acta* -

Bioenerg. 1827, 543–551 (2013).
118. Iwata, S. *et al.* Complete structure of the 11-subunit bovine mitochondrial cytochrome bc1 complex. *Science* 281, 64–71 (1998).
119. Mitchell, P. Possible molecular mechanisms of the protonmotive function of cytochrome systems. *J. Theor. Biol.* 62, 327–367 (1976).
120. Trumpower, B. L. The Protonmotive Q Cycle: Energy Transduction by Coupling of Proton Translocation to Electron Transfer by the Cytochrome bc1 Complex. *J. Biol. Chem.* 265, 11409–11412 (1990).
121. Khalfaoui-Hassani, B., Lanciano, P., Lee, D. W., Darrouzet, E. & Daldal, F. Recent advances in cytochrome bc1: Inter monomer electronic communication? *FEBS Letters* 586, 617–621 (2012).
122. Meunier, B., Fisher, N., Ransac, S., Mazat, J.-P. & Brasseur, G. Respiratory complex III dysfunction in humans and the use of yeast as a model organism to study mitochondrial myopathy and associated diseases. *Biochim. Biophys. Acta - Bioenerg.* 1827, 1346–1361 (2013).
123. Xia, D. *et al.* Structural analysis of cytochrome bc1 complexes: Implications to the mechanism of function. *Biochim. Biophys. Acta - Bioenerg.* 1827, 1278–1294 (2013).
124. Turrens, J. F., Alexandre, A. & Lehninger, A. L. Ubisemiquinone is the electron donor for superoxide formation by complex III of heart mitochondria. *Arch. Biochem. Biophys.* 237, 408–14 (1985).
125. Alexandre, A. & Lehninger, A. L. Bypasses of the antimycin a block of mitochondrial electron transport in relation to ubisemiquinone function. *Biochim. Biophys. Acta* 767, 120–9 (1984).
126. Campo, M. L., Kinnally, K. W. & Tedeschi, H. The effect of antimycin A on mouse liver inner mitochondrial membrane channel activity. *J. Biol. Chem.* 267, 8123–7 (1992).
127. Wanschers, B. F. J. *et al.* A mutation in the human CBP4 ortholog UQCC3 impairs complex III assembly, activity and cytochrome b stability. *Hum. Mol. Genet.* 23, 6356–6365 (2014).
128. Moslemi, A.-R. & Darin, N. Molecular genetic and clinical aspects of mitochondrial disorders in childhood. *Mitochondrion* 7, 241–52 (2007).
129. Vafai, S. B. & Mootha, V. K. Mitochondrial disorders as windows into an ancient organelle. *Nature* 491, 374–83 (2012).
130. Fernández-Vizarra, E. & Zeviani, M. Nuclear gene mutations as the cause of mitochondrial complex III deficiency. *Front. Genet.* 6, 134 (2015).
131. Kadenbach, B. & Hüttemann, M. The subunit composition and function of mammalian cytochrome c oxidase. *Mitochondrion* 24, 64–76 (2015).
132. Capaldi, R. A. Structure and function of cytochrome c oxidase. *Annu. Rev. Biochem.* 59, 569–596 (1990).
133. Rak, M. *et al.* Mitochondrial Cytochrome c Oxidase Deficiency. *Clin. Sci.* 130, 393–407 (2016).
134. Kadenbach, B., Ramzan, R. & Vogt, S. High efficiency versus maximal performance--the cause of oxidative stress in eukaryotes: a hypothesis. *Mitochondrion* 13, 1–6 (2013).
135. Srinivasan, S. & Avadhani, N. G. Cytochrome c oxidase dysfunction in oxidative stress. *Free Radic. Biol. Med.* 53, 1252–1263 (2012).
136. Capaldi, R. A., Aggeler, R., Turina, P. & Wilkens, S. Coupling between catalytic sites and the proton channel in F1F0-type ATPases. *Trends Biochem. Sci.* 19, 284–9 (1994).
137. Nijtmans, L. G., Klement, P., Houstěk, J. & van den Bogert, C. Assembly of mitochondrial ATP synthase in cultured human cells: implications for mitochondrial diseases. *Biochim. Biophys. Acta* 1272, 190–8 (1995).
138. Jonckheere, A. I., Smeitink, J. A. M. & Rodenburg, R. J. T. Mitochondrial ATP synthase: architecture, function and pathology. *J. Inherit. Metab. Dis.* 35, 211–225 (2012).
139. Devenish, R. J., Prescott, M., Boyle, G. M. & Nagley, P. The oligomycin axis of mitochondrial ATP synthase: OSCP and the proton channel. *J. Bioenerg. Biomembr.* 32,

507–15 (2000).
140. Zeth, K., Meins, T. & Vonrhein, C. Approaching the structure of human VDAC1, a key molecule in mitochondrial cross-talk. *J. Bioenerg. Biomembr.* 40, 127–132 (2008).
141. Shoshan-Barmatz, V., Ben-Hail, D., Admoni, L., Krelin, Y. & Tripathi, S. S. The mitochondrial voltage-dependent anion channel 1 in tumor cells. *Biochim. Biophys. Acta - Biomembr.* 1848, 2547–2575 (2015).
142. Waegemann, K., Popov-Čeleketić, D., Neupert, W., Azem, A. & Mokranjac, D. Cooperation of TOM and TIM23 Complexes during Translocation of Proteins into Mitochondria. *J. Mol. Biol.* 427, 1075–1084 (2015).
143. Ellenrieder, L., Mårtensson, C. U. & Becker, T. Biogenesis of mitochondrial outer membrane proteins, problems and diseases. *Biol. Chem.* 396, 1199–213 (2015).
144. Bauer, M. F., Hofmann, S., Neupert, W. & Brunner, M. Protein translocation into mitochondria: the role of TIM complexes. *Trends Cell Biol.* 10, 25–31 (2000).
145. Chacinska, A. *et al.* Essential role of Mia40 in import and assembly of mitochondrial intermembrane space proteins. *EMBO J.* 23, 3735–46 (2004).
146. Wrobel, L., Trojanowska, A., Sztolsztener, M. E. & Chacinska, A. Mitochondrial protein import: Mia40 facilitates Tim22 translocation into the inner membrane of mitochondria. *Mol. Biol. Cell* 24, 543–554 (2013).
147. Chan, D. C. Fusion and Fission: Interlinked Processes Critical for Mitochondrial Health. *Annu. Rev. Genet.* 46, 265–287 (2012).
148. Westermann, B. Mitochondrial fusion and fission in cell life and death. *Nat. Rev. Mol. Cell Biol.* 11, 872–884 (2010).
149. Lackner, L. L. & Nunnari, J. M. The molecular mechanism and cellular functions of mitochondrial division. *Biochim. Biophys. Acta - Mol. Basis Dis.* 1792, 1138–1144 (2009).
150. Hoppins, S. & Nunnari, J. The molecular mechanism of mitochondrial fusion. *Biochim. Biophys. Acta - Mol. Cell Res.* 1793, 20–26 (2009).
151. Smirnova, E., Griparic, L., Shurland, D. L. & van der Bliek, A. M. Dynamin-related protein Drp1 is required for mitochondrial division in mammalian cells. *Mol. Biol. Cell* 12, 2245–56 (2001).
152. Chen, H. *et al.* Mitofusins Mfn1 and Mfn2 coordinately regulate mitochondrial fusion and are essential for embryonic development. *J. Cell Biol.* 160, 189–200 (2003).
153. Wilson, R. H., Thurston, E. L. & Mitchell, R. Ultrastructural transformations in bean inner mitochondrial membranes. *Plant Physiol.* 51, 26–30 (1973).
154. Koopman, W. J. H. *et al.* Mitochondrial network complexity and pathological decrease in complex I activity are tightly correlated in isolated human complex I deficiency. *Am. J. Physiol. Physiol.* 289, C881–C890 (2005).
155. Morán, M. *et al.* Cellular pathophysiological consequences of BCS1L mutations in mitochondrial complex III enzyme deficiency. *Hum. Mutat.* 31, 930–41 (2010).
156. Sasarman, F. *et al.* LRPPRC and SLIRP Interact in a Ribonucleoprotein Complex That Regulates Posttranscriptional Gene Expression in Mitochondria. *Mol. Biol. Cell* 21, 1315–1323 (2010).
157. Pich, S. *et al.* The Charcot–Marie–Tooth type 2A gene product, Mfn2, up-regulates fuel oxidation through expression of OXPHOS system. *Hum. Mol. Genet.* 14, 1405–1415 (2005).
158. Agier, V. *et al.* Defective mitochondrial fusion, altered respiratory function, and distorted cristae structure in skin fibroblasts with heterozygous OPA1 mutations. *Biochim. Biophys. Acta - Mol. Basis Dis.* 1822, 1570–1580 (2012).
159. Guillery, O. *et al.* Modulation of mitochondrial morphology by bioenergetics defects in primary human fibroblasts. *Neuromuscul. Disord.* 18, 319–330 (2008).
160. Parone, P. A. *et al.* Preventing mitochondrial fission impairs mitochondrial function and leads to loss of mitochondrial DNA. *PLoS One* 3, e3257 (2008).
161. Rolland, S. G. *et al.* Impaired complex IV activity in response to loss of LRPPRC

function can be compensated by mitochondrial hyperfusion. *Proc. Natl. Acad. Sci.* 110, E2967–E2976 (2013).
162. Tondera, D. *et al.* SLP-2 is required for stress-induced mitochondrial hyperfusion. *EMBO J.* 28, 1589–600 (2009).
163. Gomes, L. C., Benedetto, G. Di & Scorrano, L. During autophagy mitochondria elongate, are spared from degradation and sustain cell viability. *Nat. Cell Biol.* 13, 589–598 (2011).
164. Rambold, A. S., Kostelecky, B., Elia, N. & Lippincott-Schwartz, J. Tubular network formation protects mitochondria from autophagosomal degradation during nutrient starvation. *Proc. Natl. Acad. Sci.* 108, 10190–10195 (2011).
165. Shutt, T., Geoffrion, M., Milne, R. & McBride, H. M. The intracellular redox state is a core determinant of mitochondrial fusion. *EMBO Rep.* 13, 909–915 (2012).
166. Bose, A. & Beal, M. F. Mitochondrial dysfunction in Parkinson's disease. *J. Neurochem.* 139, 216–231 (2016).
167. Ryan, B. J., Hoek, S., Fon, E. A. & Wade-Martins, R. Mitochondrial dysfunction and mitophagy in Parkinson's: from familial to sporadic disease. *Trends Biochem. Sci.* 40, 200–210 (2015).
168. Subramaniam, S. R. *et al.* Mitochondrial dysfunction and oxidative stress in Parkinson's disease. *Prog. Neurobiol.* 106–107, 17–32 (2013).
169. Nunnari, J. & Suomalainen, A. Mitochondria: In Sickness and in Health. *Cell* 148, 1145–1159 (2012).
170. Rugarli, E. I. & Langer, T. Mitochondrial quality control: a matter of life and death for neurons. *EMBO J.* 31, 1336–1349 (2012).
171. Pissadaki, E. K. & Bolam, J. P. The energy cost of action potential propagation in dopamine neurons: clues to susceptibility in Parkinson's disease. *Front. Comput. Neurosci.* 7, 13 (2013).
172. Bolam, J. P. & Pissadaki, E. K. Living on the edge with too many mouths to feed: why dopamine neurons die. *Mov. Disord.* 27, 1478–83 (2012).
173. Pickrell, A. M. & Youle, R. J. The Roles of PINK1, Parkin, and Mitochondrial Fidelity in Parkinson's Disease. *Neuron* 85, 257–273 (2015).
174. Lazarou, M., Jin, S. M., Kane, L. A. & Youle, R. J. Role of PINK1 Binding to the TOM Complex and Alternate Intracellular Membranes in Recruitment and Activation of the E3 Ligase Parkin. *Dev. Cell* 22, 320–333 (2012).
175. Hasson, S. A. *et al.* High-content genome-wide RNAi screens identify regulators of parkin upstream of mitophagy. *Nature* 504, 291–295 (2013).
176. Okatsu, K., Kimura, M., Oka, T., Tanaka, K. & Matsuda, N. Unconventional PINK1 localization to the outer membrane of depolarized mitochondria drives Parkin recruitment. *J. Cell Sci.* 128, 964–978 (2015).
177. Wood-Kaczmar, A. *et al.* PINK1 Is Necessary for Long Term Survival and Mitochondrial Function in Human Dopaminergic Neurons. *PLoS One* 3, e2455 (2008).
178. Dagda, R. K. *et al.* Loss of PINK1 Function Promotes Mitophagy through Effects on Oxidative Stress and Mitochondrial Fission. *J. Biol. Chem.* 284, 13843–13855 (2009).
179. Gegg, M. E., Cooper, J. M., Schapira, A. H. V. & Taanman, J.-W. Silencing of PINK1 Expression Affects Mitochondrial DNA and Oxidative Phosphorylation in DOPAMINERGIC Cells. *PLoS One* 4, e4756 (2009).
180. Wang, H.-L. *et al.* PARK6 PINK1 mutants are defective in maintaining mitochondrial membrane potential and inhibiting ROS formation of substantia nigra dopaminergic neurons. *Biochim. Biophys. Acta - Mol. Basis Dis.* 1812, 674–684 (2011).
181. Gautier, C. A., Kitada, T. & Shen, J. Loss of PINK1 causes mitochondrial functional defects and increased sensitivity to oxidative stress. *PNAS* 105, 11364–11369 (2008).
182. Morais, V. A. *et al.* PINK1 Loss-of-Function Mutations Affect Mitochondrial Complex I Activity via NdufA10 Ubiquinone Uncoupling. *Science (80-.).* 344, 203–207 (2014).
183. Pogson, J. H. *et al.* The Complex I Subunit NDUFA10 Selectively Rescues Drosophila

pink1 Mutants through a Mechanism Independent of Mitophagy. *PLoS Genet.* 10, e1004815 (2014).
184. Yang, Y. *et al.* Mitochondrial pathology and muscle and dopaminergic neuron degeneration caused by inactivation of Drosophila Pink1 is rescued by Parkin. *Proc. Natl. Acad. Sci. U. S. A.* 103, 10793–8 (2006).
185. Mortiboys, H. *et al.* Mitochondrial function and morphology are impaired in *parkin* -mutant fibroblasts. *Ann. Neurol.* 64, 555–565 (2008).
186. Taira, T. *et al.* DJ-1 has a role in antioxidative stress to prevent cell death. *EMBO Rep.* 5, 213–8 (2004).
187. Heo, J. Y. *et al.* DJ-1 null dopaminergic neuronal cells exhibit defects in mitochondrial function and structure: involvement of mitochondrial complex I assembly. *PLoS One* 7, e32629 (2012).
188. Thomas, K. J. *et al.* DJ-1 acts in parallel to the PINK1/parkin pathway to control mitochondrial function and autophagy. *Hum. Mol. Genet.* 20, 40–50 (2011).
189. Martin, L. J. *et al.* Parkinson's disease alpha-synuclein transgenic mice develop neuronal mitochondrial degeneration and cell death. *J. Neurosci.* 26, 41–50 (2006).
190. Choubey, V. *et al.* Mutant A53T alpha-synuclein induces neuronal death by increasing mitochondrial autophagy. *J. Biol. Chem.* 286, 10814–24 (2011).
191. Shavali, S., Brown-Borg, H. M., Ebadi, M. & Porter, J. Mitochondrial localization of alpha-synuclein protein in alpha-synuclein overexpressing cells. *Neurosci. Lett.* 439, 125–8 (2008).
192. Parihar, M. S., Parihar, A., Fujita, M., Hashimoto, M. & Ghafourifar, P. Mitochondrial association of alpha-synuclein causes oxidative stress. *Cell. Mol. Life Sci.* 65, 1272–1284 (2008).
193. Devi, L., Raghavendran, V., Prabhu, B. M., Avadhani, N. G. & Anandatheerthavarada, H. K. Mitochondrial Import and Accumulation of α-Synuclein Impair Complex I in Human Dopaminergic Neuronal Cultures and Parkinson Disease Brain. *J. Biol. Chem.* 283, 9089–9100 (2008).
194. Cole, N. B., DiEuliis, D., Leo, P., Mitchell, D. C. & Nussbaum, R. L. Mitochondrial translocation of α-synuclein is promoted by intracellular acidification. *Exp. Cell Res.* 314, 2076–2089 (2008).
195. Kamp, F. *et al.* Inhibition of mitochondrial fusion by α-synuclein is rescued by PINK1, Parkin and DJ-1. *EMBO J.* 29, 3571–3589 (2010).
196. Nakamura, K. *et al.* Direct membrane association drives mitochondrial fission by the Parkinson disease-associated protein alpha-synuclein. *J. Biol. Chem.* 286, 20710–26 (2011).
197. Biskup, S. *et al.* Localization of LRRK2 to membranous and vesicular structures in mammalian brain. *Ann. Neurol.* 60, 557–569 (2006).
198. Wang, X. *et al.* LRRK2 regulates mitochondrial dynamics and function through direct interaction with DLP1. *Hum. Mol. Genet.* 21, 1931–1944 (2012).
199. Iaccarino, C. *et al.* Apoptotic mechanisms in mutant LRRK2-mediated cell death. *Hum. Mol. Genet.* 16, 1319–26 (2007).
200. Simon, D. K. *et al.* Somatic mitochondrial DNA mutations in cortex and substantia nigra in aging and Parkinson's disease. *Neurobiol. Aging* 25, 71–81 (2004).
201. Gu, G. *et al.* Mitochondrial DNA deletions/rearrangements in parkinson disease and related neurodegenerative disorders. *J. Neuropathol. Exp. Neurol.* 61, 634–9 (2002).
202. Bender, A. *et al.* High levels of mitochondrial DNA deletions in substantia nigra neurons in aging and Parkinson disease. *Nat. Genet.* 38, 515–517 (2006).
203. Kraytsberg, Y. *et al.* Mitochondrial DNA deletions are abundant and cause functional impairment in aged human substantia nigra neurons. *Nat. Genet.* 38, 518–520 (2006).
204. Luoma, P. *et al.* Parkinsonism, premature menopause, and mitochondrial DNA polymerase γ mutations: clinical and molecular genetic study. *Lancet* 364, 875–882 (2004).

205. Trimmer, P. A. & Bennett, J. P. The cybrid model of sporadic Parkinson's disease. *Exp. Neurol.* 218, 320–5 (2009).
206. Pickrell, A. M., Pinto, M., Hida, A. & Moraes, C. T. Striatal dysfunctions associated with mitochondrial DNA damage in dopaminergic neurons in a mouse model of Parkinson's disease. *J. Neurosci.* 31, 17649–58 (2011).
207. Ekstrand, M. I. *et al.* Progressive parkinsonism in mice with respiratory-chain-deficient dopamine neurons. *Proc. Natl. Acad. Sci. U. S. A.* 104, 1325–30 (2007).
208. Schapira, A. H. *et al.* Mitochondrial complex I deficiency in Parkinson's disease. *J. Neurochem.* 54, 823–7 (1990).
209. Parker, W. D., Parks, J. K. & Swerdlow, R. H. Complex I deficiency in Parkinson's disease frontal cortex. *Brain Res.* 1189, 215–218 (2008).
210. Mizuno, Y., Suzuki, K., Sone, N. & Saitoh, T. Inhibition of mitochondrial respiration by 1-methyl-4-phenyl-1,2,3,6-tetrahydropyridine (MPTP) in mouse brain in vivo. *Neurosci. Lett.* 91, 349–353 (1988).
211. Richardson, J. R., Quan, Y., Sherer, T. B., Greenamyre, J. T. & Miller, G. W. Paraquat neurotoxicity is distinct from that of MPTP and rotenone. *Toxicol. Sci.* 88, 193–201 (2005).
212. Testa, C. M., Sherer, T. B. & Greenamyre, J. T. Rotenone induces oxidative stress and dopaminergic neuron damage in organotypic substantia nigra cultures. *Mol. Brain Res.* 134, 109–118 (2005).
213. Jackson-Lewis, V. & Przedborski, S. Protocol for the MPTP mouse model of Parkinson's disease. *Nat. Protoc.* 2, 141–151 (2007).
214. Burns, R. S. *et al.* A primate model of parkinsonism: selective destruction of dopaminergic neurons in the pars compacta of the substantia nigra by N-methyl-4-phenyl-1,2,3,6-tetrahydropyridine. *Proc. Natl. Acad. Sci. U. S. A.* 80, 4546–50 (1983).
215. Rojo, A. I. *et al.* Persistent penetration of MPTP through the nasal route induces Parkinson's disease in mice. *Eur. J. Neurosci.* 24, 1874–1884 (2006).
216. Ramsay, R. R., Salach, J. I. & Singer, T. P. Uptake of the neurotoxin 1-methyl-4-phenylpyridine (MPP+) by mitochondria and its relation to the inhibition of the mitochondrial oxidation of NAD+-linked substrates by MPP+. *Biochem. Biophys. Res. Commun.* 134, 743–8 (1986).
217. Mizuno, Y., Saitoh, T. & Sone, N. Inhibition of mitochondrial alpha-ketoglutarate dehydrogenase by 1-methyl-4-phenylpyridinium ion. *Biochem. Biophys. Res. Commun.* 143, 971–976 (1987).
218. Betarbet, R. *et al.* Chronic systemic pesticide exposure reproduces features of Parkinson's disease. *Nat. Neurosci.* 3, 1301–1306 (2000).
219. Alam, M. & Schmidt, W. J. Rotenone destroys dopaminergic neurons and induces parkinsonian symptoms in rats. *Behav. Brain Res.* 136, 317–24 (2002).
220. Höglinger, G. U. *et al.* Chronic systemic complex I inhibition induces a hypokinetic multisystem degeneration in rats. *J. Neurochem.* 84, 491–502 (2003).
221. Sherer, T. B., Kim, J. H., Betarbet, R. & Greenamyre, J. T. Subcutaneous rotenone exposure causes highly selective dopaminergic degeneration and alpha-synuclein aggregation. *Exp. Neurol.* 179, 9–16 (2003).
222. Masliah, E. *et al.* Dopaminergic loss and inclusion body formation in alpha-synuclein mice: implications for neurodegenerative disorders. *Science* 287, 1265–9 (2000).
223. Fujimoto, T. & Parton, R. G. Not just fat: the structure and function of the lipid droplet. *Cold Spring Harb. Perspect. Biol.* 3, a004838–a004838 (2011).
224. Singh, R. & Cuervo, A. M. Lipophagy: Connecting Autophagy and Lipid Metabolism. *Int. J. Cell Biol.* 2012, 1–12 (2012).
225. Murphy, S., Martin, S. & Parton, R. G. Lipid droplet-organelle interactions; sharing the fats. *Biochim. Biophys. Acta - Mol. Cell Biol. Lipids* 1791, 441–447 (2009).
226. Markgraf, D. F. *et al.* An ER Protein Functionally Couples Neutral Lipid Metabolism on Lipid Droplets to Membrane Lipid Synthesis in the ER. *Cell Rep.* 6, 44–55 (2014).

227. Martin, S. & Parton, R. G. Caveolin, cholesterol, and lipid bodies. *Semin. Cell Dev. Biol.* 16, 163–174 (2005).
228. Andersson, L. *et al.* PLD1 and ERK2 regulate cytosolic lipid droplet formation. *J. Cell Sci.* 119, 2246–2257 (2006).
229. Bostrom, P. *et al.* Cytosolic Lipid Droplets Increase in Size by Microtubule-Dependent Complex Formation. *Arterioscler. Thromb. Vasc. Biol.* 25, 1945–1951 (2005).
230. Boström, P. *et al.* SNARE proteins mediate fusion between cytosolic lipid droplets and are implicated in insulin sensitivity. *Nat. Cell Biol.* 9, 1286–1293 (2007).
231. Jacquier, N. *et al.* Lipid droplets are functionally connected to the endoplasmic reticulum in Saccharomyces cerevisiae. *J. Cell Sci.* 124, 2424–2437 (2011).
232. Jacquier, N., Mishra, S., Choudhary, V. & Schneiter, R. Expression of oleosin and perilipins in yeast promotes formation of lipid droplets from the endoplasmic reticulum. *J. Cell Sci.* 126, 5198–209 (2013).
233. Buhman, K. K., Chen, H. C. & Farese, R. V. The Enzymes of Neutral Lipid Synthesis. *J. Biol. Chem.* 276, 40369–40372 (2001).
234. Long, A. P. *et al.* Lipid Droplet De Novo Formation and Fission Are Linked to the Cell Cycle in Fission Yeast. *Traffic* 13, 705–714 (2012).
235. Wilfling, F., Haas, J. T., Walther, T. C. & Jr, R. V. F. Lipid droplet biogenesis. *Curr. Opin. Cell Biol.* 29, 39–45 (2014).
236. Pol, A., Gross, S. P. & Parton, R. G. Biogenesis of the multifunctional lipid droplet: Lipids, proteins, and sites. *J. Cell Biol.* 204, 635–646 (2014).
237. Wang, C.-W. Lipid droplets, lipophagy, and beyond. *Biochim. Biophys. Acta* 1861, 793–805 (2016).
238. Shibata, M. *et al.* The MAP1-LC3 conjugation system is involved in lipid droplet formation. *Biochem. Biophys. Res. Commun.* 382, 419–23 (2009).
239. Ohsaki, Y., Cheng, J., Fujita, A., Tokumoto, T. & Fujimoto, T. Cytoplasmic lipid droplets are sites of convergence of proteasomal and autophagic degradation of apolipoprotein B. *Mol. Biol. Cell* 17, 2674–83 (2006).
240. Singh, R. *et al.* Autophagy regulates lipid metabolism. *Nature* 458, 1131–1135 (2009).
241. Martinez-Vicente, M. *et al.* Cargo recognition failure is responsible for inefficient autophagy in Huntington's disease. *Nat. Neurosci.* 13, 567–76 (2010).
242. Kaushik, S. *et al.* Autophagy in hypothalamic AgRP neurons regulates food intake and energy balance. *Cell Metab.* 14, 173–183 (2011).
243. Martinez-Lopez, N., Athonvarangkul, D. & Singh, R. Autophagy and Aging. in *Advances in experimental medicine and biology* 847, 73–87 (Springer, New York, NY, 2015).
244. Kaushik, S. & Cuervo, A. M. Degradation of lipid droplet-associated proteins by chaperone-mediated autophagy facilitates lipolysis. *Nat. Cell Biol.* 17, 759–770 (2015).
245. Itabe, H., Yamaguchi, T., Nimura, S. & Sasabe, N. Perilipins: a diversity of intracellular lipid droplet proteins. *Lipids Health Dis.* 16, (2017).
246. Haemmerle, G. *et al.* ATGL-mediated fat catabolism regulates cardiac mitochondrial function via PPAR-α and PGC-1. *Nat. Med.* 17, 1076–1085 (2011).
247. Khan, S. A. *et al.* ATGL-catalyzed lipolysis regulates SIRT1 to control PGC-1α/PPAR-α signaling. *Diabetes* 64, 418–26 (2015).
248. Pu, J. *et al.* Interactomic study on interaction between lipid droplets and mitochondria. *Protein Cell* 2, 487–496 (2011).
249. Wang, H. *et al.* Perilipin 5, a lipid droplet-associated protein, provides physical and metabolic linkage to mitochondria. *J. Lipid Res.* 52, 2159–68 (2011).
250. Herms, A. *et al.* AMPK activation promotes lipid droplet dispersion on detyrosinated microtubules to increase mitochondrial fatty acid oxidation. *Nat. Commun.* 6, 7176 (2015).
251. Rambold, A. S., Cohen, S. & Lippincott-Schwartz, J. Fatty acid trafficking in starved cells: Regulation by lipid droplet lipolysis, autophagy, and mitochondrial fusion

dynamics. *Dev. Cell* 32, 678–692 (2015).
252. Barbosa, A. D. & Siniossoglou, S. Function of lipid droplet-organelle interactions in lipid homeostasis. *Biochim. Biophys. Acta - Mol. Cell Res.* 1864, 1459–1468 (2017).
253. Hörl, G. *et al.* Sequential synthesis and methylation of phosphatidylethanolamine promote lipid droplet biosynthesis and stability in tissue culture and in vivo. *J. Biol. Chem.* 286, 17338–17350 (2011).
254. Jin, Y., McFie, P. J., Banman, S. L., Brandt, C. & Stone, S. J. Diacylglycerol acyltransferase-2 (DGAT2) and monoacylglycerol acyltransferase-2 (MGAT2) interact to promote triacylglycerol synthesis. *J. Biol. Chem.* 289, 28237–28248 (2014).
255. Cole, N. B. *et al.* Lipid droplet binding and oligomerization properties of the Parkinson's disease protein alpha-synuclein. *J. Biol. Chem.* 277, 6344–52 (2002).
256. Kim, K.-Y. *et al.* Parkin is a lipid-responsive regulator of fat uptake in mice and mutant human cells. *J. Clin. Invest.* 121, 3701–12 (2011).
257. Papadopoulos, C. *et al.* Spastin Binds to Lipid Droplets and Affects Lipid Metabolism. *PLoS Genet.* 11, e1005149 (2015).
258. Liu, L. *et al.* Glial Lipid Droplets and ROS Induced by Mitochondrial Defects Promote Neurodegeneration. *Cell* 160, 177–190 (2015).
259. Vermeulen, K., Van Bockstaele, D. R. & Berneman, Z. N. The cell cycle: a review of regulation, deregulation and therapeutic targets in cancer. *Cell Prolif.* 36, 131–49 (2003).
260. Fisher, R. P. & Morgan, D. O. A novel cyclin associates with MO15/CDK7 to form the CDK-activating kinase. *Cell* 78, 713–24 (1994).
261. Evans, T., Rosenthal, E. T., Youngblom, J., Distel, D. & Hunt, T. Cyclin: a protein specified by maternal mRNA in sea urchin eggs that is destroyed at each cleavage division. *Cell* 33, 389–96 (1983).
262. Pines, J. Cyclins, CDKs and cancer. *Semin. Cancer Biol.* 6, 63–72 (1995).
263. Sherr, C. J. Growth factor-regulated G1 cyclins. *Stem Cells* 12 Suppl 1, 47-55–7 (1994).
264. Ohtsubo, M., Theodoras, A. M., Schumacher, J., Roberts, J. M. & Pagano, M. Human cyclin E, a nuclear protein essential for the G1-to-S phase transition. *Mol. Cell. Biol.* 15, 2612–24 (1995).
265. Girard, F., Strausfeld, U., Fernandez, A. & Lamb, N. J. Cyclin A is required for the onset of DNA replication in mammalian fibroblasts. *Cell* 67, 1169–79 (1991).
266. Walker, D. H. & Maller, J. L. Role for cyclin A in the dependence of mitosis on completion of DMA replication. *Nature* 354, 314–317 (1991).
267. King, R. W., Jackson, P. K. & Kirschner, M. W. Mitosis in Transition Review. *Cell* 79, 563–571 (1994).
268. Arellano, M. & Moreno, S. Regulation of CDK/cyclin complexes during the cell cycle. *Int. J. Biochem. Cell Biol.* 29, 559–73 (1997).
269. Morgan, D. O. Principles of CDK regulation. *Nature* 374, 131–134 (1995).
270. Lundberg, A. S. & Weinberg, R. A. Functional Inactivation of the Retinoblastoma Protein Requires Sequential Modification by at Least Two Distinct Cyclin-cdk Complexes. *Mol. Cell. Biol.* 18, 753–761 (1998).
271. Bracken, A. P., Ciro, M., Cocito, A. & Helin, K. E2F target genes: unraveling the biology. *Trends Biochem. Sci.* 29, 409–417 (2004).
272. Naito, M., Vongsa, S., Tsukune, N., Ohashi, A. & Takahashi, T. Promyelocytic leukemia zinc finger mediates glucocorticoid-induced cell cycle arrest in the chondroprogenitor cell line ATDC5. *Mol. Cell. Endocrinol.* 417, 114–123 (2015).
273. Choi, W.-I. *et al.* Role of promyelocytic leukemia zinc finger (PLZF) in cell proliferation and cyclin-dependent kinase inhibitor 1A (p21WAF/CDKN1A) gene repression. *J. Biol. Chem.* 289, 18625–40 (2014).
274. Karimian, A., Ahmadi, Y. & Yousefi, B. Multiple functions of p21 in cell cycle, apoptosis and transcriptional regulation after DNA damage. *DNA Repair (Amst).* 42, 63–71 (2016).

275. Jung, Y.-S., Qian, Y. & Chen, X. Examination of the expanding pathways for the regulation of p21 expression and activity. *Cell. Signal.* 22, 1003–1012 (2010).
276. Prives, C. & Hall, P. A. The p53 pathway. *J. Pathol.* 187, 112–126 (1999).
277. Niida, H. & Nakanishi, M. DNA damage checkpoints in mammals. *Mutagenesis* 21, 3–9 (2006).
278. Amaral, J. D., Xavier, J. M., Steer, C. J. & Rodrigues, C. M. The role of p53 in apoptosis. *Discov. Med.* 9, 145–52 (2010).
279. Ray, A., James, M. K., Larochelle, S., Fisher, R. P. & Blain, S. W. p27Kip1 Inhibits Cyclin D-Cyclin-Dependent Kinase 4 by Two Independent Modes. *Mol. Cell. Biol.* 29, 986–999 (2009).
280. Russo, A. A., Jeffrey, P. D., Patten, A. K., Massagué, J. & Pavletich, N. P. Crystal structure of the p27Kip1 cyclin-dependent-kinase inibitor bound to the cyclin A–Cdk2 complex. *Nature* 382, 325–331 (1996).
281. Polyak, K. *et al.* Cloning of p27Kip1, a cyclin-dependent kinase inhibitor and a potential mediator of extracellular antimitogenic signals. *Cell* 78, 59–66 (1994).
282. James, M. K., Ray, A., Leznova, D. & Blain, S. W. Differential Modification of p27Kip1 Controls Its Cyclin D-cdk4 Inhibitory Activity. *Mol. Cell. Biol.* 28, 498–510 (2008).
283. Aleem, E., Kiyokawa, H. & Kaldis, P. Cdc2–cyclin E complexes regulate the G1/S phase transition. *Nat. Cell Biol.* 7, 831–836 (2005).
284. Pardee, A. B. A restriction point for control of normal animal cell proliferation. *Proc. Natl. Acad. Sci. U. S. A.* 71, 1286–90 (1974).
285. Su, S. *et al.* Signalling networks in focus p27 Kip1 signaling: Transcriptional and post-translational regulation. *Int. J. Biochem. Cell Biol.* 68, 9–14 (2015).
286. Bahrami, A. R., Matin, M. M. & Andrews, P. W. The CDK inhibitor p27 enhances neural differentiation in pluripotent NTERA2 human EC cells, but does not permit differentiation of 2102Ep nullipotent human EC cells. *Mech. Dev.* 122, 1034–42 (2005).
287. Denicourt, C. & Dowdy, S. F. Cip/Kip proteins: More than just CDKs inhibitors. *Genes and Development* 18, 851–855 (2004).
288. McAllister, S. S., Becker-Hapak, M., Pintucci, G., Pagano, M. & Dowdy, S. F. Novel p27(kip1) C-terminal scatter domain mediates Rac-dependent cell migration independent of cell cycle arrest functions. *Mol. Cell. Biol.* 23, 216–28 (2003).
289. Gorbsky, G. J. Cell cycle checkpoints: Arresting progress in mitosis. *BioEssays* 19, 193–197 (1997).
290. Copani, A. *et al.* Activation of cell-cycle-associated proteins in neuronal death: a mandatory or dispensable path? *Trends Neurosci.* 24, 25–31 (2001).
291. Herrup, K., Neve, R., Ackerman, S. L. & Copani, A. Divide and Die: Cell Cycle Events as Triggers of Nerve Cell Death. *J. Neurosci.* 24, 9232–9239 (2004).
292. Hoglinger, G. U. *et al.* The pRb/E2F cell-cycle pathway mediates cell death in Parkinson's disease. *Proc. Natl. Acad. Sci.* 104, 3585–3590 (2007).
293. Jordan-Sciutto, K. L., Dorsey, R., Chalovich, E. M., Hammond, R. R. & Achim, C. L. Expression patterns of retinoblastoma protein in Parkinson disease. *J. Neuropathol. Exp. Neurol.* 62, 68–74 (2003).
294. Staropoli, J. F. *et al.* Parkin is a component of an SCF-like ubiquitin ligase complex and protects postmitotic neurons from kainate excitotoxicity. *Neuron* 37, 735–49 (2003).
295. Verdaguer, E. *et al.* Kainic acid-induced apoptosis in cerebellar granule neurons: an attempt at cell cycle re-entry. *Neuroreport* 13, 413–6 (2002).
296. Esteras, N. *et al.* G1/S Cell Cycle Checkpoint Dysfunction in Lymphoblasts from Sporadic Parkinson's Disease Patients. *Mol. Neurobiol.* 52, 386–398 (2015).
297. O'Flanagan, C. H., Morais, V. A., Wurst, W., De Strooper, B. & O'Neill, C. The Parkinson's gene PINK1 regulates cell cycle progression and promotes cancer-associated phenotypes. *Oncogene* 34, 1363–1374 (2015).
298. Hardwick, L. J. A., Ali, F. R., Azzarelli, R. & Philpott, A. Cell cycle regulation of

proliferation versus differentiation in the central nervous system. *Cell Tissue Res.* 359, 187–200 (2015).
299. Pauklin, S. & Vallier, L. The Cell-Cycle State of Stem Cells Determines Cell Fate Propensity. *Cell* 155, 135–147 (2013).
300. Ohnuma, S. & Harris, W. A. Neurogenesis and the cell cycle. *Neuron* 40, 199–208 (2003).
301. Calegari, F. & Huttner, W. B. An inhibition of cyclin-dependent kinases that lengthens, but does not arrest, neuroepithelial cell cycle induces premature neurogenesis. *J. Cell Sci.* 116, 4947–4955 (2003).
302. Li, V. C., Ballabeni, A. & Kirschner, M. W. Gap 1 phase length and mouse embryonic stem cell self-renewal. *Proc. Natl. Acad. Sci.* 109, 12550–12555 (2012).
303. Glickstein, S. B., Monaghan, J. A., Koeller, H. B., Jones, T. K. & Ross, M. E. Cyclin D2 is critical for intermediate progenitor cell proliferation in the embryonic cortex. *J. Neurosci.* 29, 9614–9624 (2009).
304. Kowalczyk, A. *et al.* The critical role of cyclin D2 in adult neurogenesis. *J. Mol. Cell Biol.* 167, 209–213 (2004).
305. Goto, T., Mitsuhashi, T. & Takahashi, T. Altered patterns of neuron production in the p27 knockout mouse. *Dev. Neurosci.* 26, 208–17 (2004).
306. Tarui, T. *et al.* Overexpression of p27 Kip 1, probability of cell cycle exit, and laminar destination of neocortical neurons. *Cereb. Cortex* 15, 1343–55 (2005).
307. Nguyen, L. *et al.* p27kip1 independently promotes neuronal differentiation and migration in the cerebral cortex. *Genes Dev.* 20, 1511–1524 (2006).
308. Meziane, E. K. E. K., Randle, S. J., Nelson, D. E., Lomonosov, M. & Laman, H. Knockdown of Fbxo7 reveals its regulatory role in proliferation and differentiation of haematopoietic precursor cells. *J. Cell Sci.* 124, 2175–86 (2011).
309. Laman, H. *et al.* Transforming activity of Fbxo7 is mediated specifically through regulation of cyclin D/cdk6. *EMBO J.* 24, 3104–3116 (2005).
310. Cenciarelli, C. *et al.* Identification of a family of human F-box proteins. *Curr. Biol.* 9, 1177–9 (1999).
311. Winston, J. T., Koepp, D. M., Zhu, C., Elledge, S. J. & Harper, J. W. A family of mammalian F-box proteins. *Curr. Biol.* 9, 1180–2 (1999).
312. Nelson, D. E., Randle, S. J. & Laman, H. Beyond ubiquitination: the atypical functions of Fbxo7 and other F-box proteins. *Open Biol.* 3, 130131–130131 (2013).
313. Kirk, R. *et al.* Structure of a Conserved Dimerization Domain within the F-box Protein Fbxo7 and the PI31 Proteasome Inhibitor. *J. Biol. Chem.* 283, 22325–22335 (2008).
314. Chau, V. *et al.* A multiubiquitin chain is confined to specific lysine in a targeted short-lived protein. *Science* 243, 1576–83 (1989).
315. Kirkin, V., McEwan, D. G., Novak, I. & Dikic, I. A Role for Ubiquitin in Selective Autophagy. *Mol. Cell* 34, 259–269 (2009).
316. Hsu, J.-M., Lee, Y.-C. G., Yu, C.-T. R. & Huang, C.-Y. F. Fbx7 functions in the SCF complex regulating Cdk1-cyclin B-phosphorylated hepatoma up-regulated protein (HURP) proteolysis by a proline-rich region. *J. Biol. Chem.* 279, 32592–602 (2004).
317. Chang, Y.-F., Cheng, C.-M., Chang, L.-K., Jong, Y.-J. & Yuo, C.-Y. The F-box protein Fbxo7 interacts with human inhibitor of apoptosis protein cIAP1 and promotes cIAP1 ubiquitination. *Biochem. Biophys. Res. Commun.* 342, 1022–6 (2006).
318. Kuiken, H. J. *et al.* Identification of F-box only protein 7 as a negative regulator of NF-kappaB signalling. *J. Cell. Mol. Med.* 16, 2140–2149 (2012).
319. Li, X., Thompson, D., Kumar, B. & DeMartino, G. N. Molecular and Cellular Roles of PI31 (PMSF1) in Regulation of Proteasome Function. *J. Biol. Chem.* 289, (2014).
320. Burchell, V. S. *et al.* The Parkinson's disease-linked proteins Fbxo7 and Parkin interact to mediate mitophagy. *Nat. Neurosci.* 16, 1257–65 (2013).
321. DAVISON, C. Pallido-pyramidal disease. *J. Neuropathol. Exp. Neurol.* 13, 50–9 (1954).
322. Joseph, S., Schulz, J. B. & Stegmüller, J. Mechanistic contributions of FBXO7 to

Parkinson disease. *J. Neurochem.* 144, 118–127 (2018).
323. Lohmann, E. *et al.* A new F-box protein 7 gene mutation causing typical Parkinson's disease. *Mov. Disord.* 30, 1130–1133 (2015).
324. Santoro, L. *et al.* Novel ATP13A2 (PARK9) homozygous mutation in a family with marked phenotype variability. *Neurogenetics* 12, 33–39 (2011).
325. Gündüz, A. *et al.* FBXO7-R498X mutation: phenotypic variability from chorea to early onset parkinsonism within a family. *Parkinsonism Relat. Disord.* 20, 1253–6 (2014).
326. Chen, C.-M. M. *et al.* FBXO7 Y52C polymorphism as a potential protective factor in Parkinson's disease. *PLoS One* 9, e101392 (2014).
327. Lennox, G., Lowe, J., Morrell, K., Landon, M. & Mayer, R. J. Ubiquitin is a component of neurofibrillary tangles in a variety of neurodegenerative diseases. *Neurosci. Lett.* 94, 211–7 (1988).
328. Lowe, J. *et al.* Ubiquitin is a common factor in intermediate filament inclusion bodies of diverse type in man, including those of Parkinson's disease, Pick's disease, and Alzheimer's disease, as well as Rosenthal fibres in cerebellar astrocytomas, cytoplasmic bodies in m. *J. Pathol.* 155, 9–15 (1988).
329. Snyder, H. *et al.* Aggregated and monomeric alpha-synuclein bind to the S6' proteasomal protein and inhibit proteasomal function. *J. Biol. Chem.* 278, 11753–9 (2003).
330. Vingill, S. *et al.* Loss of FBXO7 (PARK15) results in reduced proteasome activity and models a parkinsonism-like phenotype in mice. *EMBO J.* 35, 2008–2025 (2016).
331. McNaught, K. S. P., Belizaire, R., Jenner, P., Olanow, C. W. & Isacson, O. Selective loss of 20S proteasome alpha-subunits in the substantia nigra pars compacta in Parkinson's disease. *Neurosci. Lett.* 326, 155–8 (2002).
332. Wang, X.-F., Li, S., Chou, A. P. & Bronstein, J. M. Inhibitory effects of pesticides on proteasome activity: Implication in Parkinson's disease. *Neurobiol. Dis.* 23, 198–205 (2006).
333. Zhou, Z. D. *et al.* F-box protein 7 mutations promote protein aggregation in mitochondria and inhibit mitophagy. *Hum. Mol. Genet.* 24, 6314–6330 (2015).
334. Zhou, Z. D., Sathiyamoorthy, S., Angeles, D. C. & Tan, E. K. Linking F-box protein 7 and parkin to neuronal degeneration in Parkinson's disease (PD). *Mol. Brain* 9, 41 (2016).
335. Delgado-Camprubi, M., Esteras, N., Soutar, M. P., Plun-Favreau, H. & Abramov, A. Y. Deficiency of Parkinson's disease-related gene Fbxo7 is associated with impaired mitochondrial metabolism by PARP activation. *Cell Death Differ.* 24, 120–131 (2017).
336. Teixeira, F. R. *et al.* Gsk3 and Tomm20 are substrates of the SCFFbxo7/PARK15 ubiquitin ligase associated with Parkinson's disease. *Biochem. J.* 473, 3563–3580 (2016).
337. Zhao, T. *et al.* Dopaminergic Neuronal Loss and Dopamine-Dependent Locomotor Defects in Fbxo7-Deficient Zebrafish. *PLoS One* 7, e48911 (2012).
338. Doench, J. G. *et al.* Rational design of highly active sgRNAs for CRISPR-Cas9–mediated gene inactivation. *Nat. Biotechnol.* 32, 1262–1267 (2014).
339. Bugiani, M. *et al.* Clinical and molecular findings in children with complex I deficiency. *Biochim. Biophys. Acta - Bioenerg.* 1659, 136–147 (2004).
340. C.I. Ragan MTW, V.M. Darley-Usmar, P. . L. *Mitochondria: A Practical Approach*. (IRL Press, 1987).
341. Zheng, X. X., Shoffner, J. M., Voljavec, A. S. & Wallace, D. C. Evaluation of procedures for assaying oxidative phosphorylation enzyme activities in mitochondrial myopathy muscle biopsies. *Biochim. Biophys. Acta* 1019, 1–10 (1990).
342. Warthon, D. C. Cytochrome oxidase from beef heart mitochondria. *Methods Enzym.* 10, 245–250 (1967).
343. Srere, P. A. [1] Citrate synthase. [EC 4.1.3.7. Citrate oxaloacetate-lyase (CoA-acetylating)]. *Methods Enzymol.* 13, 3–11 (1969).
344. Gómez-Garre, P. *et al.* Systematic mutational analysis of FBXO7 in a Parkinson's

disease population from southern Spain. *Neurobiol. Aging* 35, 727.e5-727.e7 (2014).
345. Conedera, S. *et al.* FBXO7 mutations in Parkinson's disease and multiple system atrophy. *Neurobiol. Aging* 40, 192.e1-192.e5 (2016).
346. Tranchant, C., Koob, M. & Anheim, M. Parkinsonian-Pyramidal syndromes: A systematic review. *Parkinsonism Relat. Disord.* 39, 4–16 (2017).
347. Matsushime, H. *et al.* D-type cyclin-dependent kinase activity in mammalian cells. *Mol. Cell. Biol.* 14, 2066–76 (1994).
348. Chen, B. & Pollard, J. W. Cyclin D2 Compensates for the Loss of Cyclin D1 in Estrogen-Induced Mouse Uterine Epithelial Cell Proliferation. *Mol. Endocrinol.* 17, 1368–1381 (2003).
349. Oh, H., Kim, J. & Kim, J. Critical roles of Cyclin D1 in mouse embryonic fibroblast cell reprogramming. *FEBS J.* 283, 4549–4568 (2016).
350. Fernández-Vizarra, E., Enríquez, J. A., Pérez-Martos, A., Montoya, J. & Fernández-Silva, P. Tissue-specific differences in mitochondrial activity and biogenesis. *Mitochondrion* 11, 207–213 (2011).
351. Shoshan-Barmatz, V. & Golan, M. Mitochondrial VDAC1: function in cell life and death and a target for cancer therapy. *Curr. Med. Chem.* 19, 714–35 (2012).
352. Camara, A. K. S., Zhou, Y. F., Wen, P. C., Tajkhorshid, E. & Kwok, W. M. Mitochondrial VDAC1: A key gatekeeper as potential therapeutic target. *Frontiers in Physiology* 8, 460 (2017).
353. Tomasello, F. *et al.* Outer membrane VDAC1 controls permeability transition of the inner mitochondrial membrane in cellulo during stress-induced apoptosis. *Cell Res.* 19, 1363–1376 (2009).
354. D'Erchia, A. M. *et al.* Tissue-specific mtDNA abundance from exome data and its correlation with mitochondrial transcription, mass and respiratory activity. *Mitochondrion* 20, 13–21 (2015).
355. Nicholls, T. J. & Minczuk, M. In D-loop: 40 years of mitochondrial 7S DNA. *Exp. Gerontol.* 56, 175–181 (2014).
356. Posse, V., Shahzad, S., Falkenberg, M., Hallberg, B. M. & Gustafsson, C. M. TEFM is a potent stimulator of mitochondrial transcription elongation in vitro. *Nucleic Acids Res.* 43, 2615–2624 (2015).
357. Auburger, G. *et al.* Primary Skin Fibroblasts as a Model of Parkinson's Disease. *Mol Neurobiol* 46, 20–27 (2012).
358. Meyerson, M. & Harlow, E. Identification of G1 kinase activity for cdk6, a novel cyclin D partner. *Mol. Cell. Biol.* 14, 2077–86 (1994).
359. Krishna, A. *et al.* Systems genomics evaluation of the SH-SY5Y neuroblastoma cell line as a model for Parkinson's disease. *BMC Genomics* 15, 1154 (2014).
360. Marroquin, L. D., Hynes, J., Dykens, J. A., Jamieson, J. D. & Will, Y. Circumventing the Crabtree Effect: Replacing Media Glucose with Galactose Increases Susceptibility of HepG2 Cells to Mitochondrial Toxicants. *Toxicol. Sci.* 97, 539–547 (2007).
361. Elkalaf, M., Anděl, M. & Trnka, J. Low Glucose but Not Galactose Enhances Oxidative Mitochondrial Metabolism in C2C12 Myoblasts and Myotubes. *PLoS One* 8, (2013).
362. Marshall, K. D. & Baines, C. P. Necroptosis: is there a role for mitochondria? *Front. Physiol.* 5, 323 (2014).
363. Celardo, I., Martins, L. M. & Gandhi, S. Unravelling mitochondrial pathways to Parkinson's disease. *Br. J. Pharmacol.* 171, 1943–1957 (2014).
364. Liu, K. & Czaja, M. J. Regulation of lipid stores and metabolism by lipophagy. *Cell Death Differ.* 20, 3–11 (2013).
365. Gil-Perotin, S. *et al.* Roles of p53 and p27Kip1in the regulation of neurogenesis in the murine adult subventricular zone. *Eur. J. Neurosci.* 34, 1040–1052 (2011).
366. Andreu Z.H, M. Amir Khan, Pilar Gonzalez-Gómez, S. Negueruela, R. Hortigüela, J. San Emeterio, S. R. Ferrón, G. Martínez, A. Vidal, I. Fariñas, D. Chichung Lie, H. M. The Cyclin-Dependent Kinase Inhibitor p27 kip1 Regulates Radial Stem Cell Quiescence

and Neurogenesis in the Adult Hippocampus. *Stem Cells* 33, 219–229 (2015).
367. Tarui, T. *et al.* Overexpression of p27Kip1, Probability of Cell Cycle Exit, and Laminar Destination of Neocortical Neurons. *Cereb. Cortex* 15, 1343–1355 (2005).
368. Hoitzing, H., Johnston, I. G. & Jones, N. S. What is the function of mitochondrial networks? A theoretical assessment of hypotheses and proposal for future research. *Bioessays* 37, 687–700 (2015).
369. Lee, J., Giordano, S. & Zhang, J. Autophagy, mitochondria and oxidative stress: cross-talk and redox signalling. *Biochem. J.* 441, 523–40 (2012).
370. Patel, S. P., Randle, S. J., Gibbs, S., Cooke, A. & Laman, H. Opposing effects on the cell cycle of T lymphocytes by Fbxo7 via Cdk6 and p27. *Cell. Mol. Life Sci.* 74, 1553–1566 (2016).
371. Branch, S. Y. *et al.* Dopaminergic Neurons Exhibit an Age-Dependent Decline in Electrophysiological Parameters in the MitoPark Mouse Model of Parkinson's Disease. *J. Neurosci.* 36, 4026–37 (2016).
372. Good, C. H. *et al.* Impaired nigrostriatal function precedes behavioral deficits in a genetic mitochondrial model of Parkinson's disease. *FASEB J.* 25, 1333–44 (2011).
373. Grace, A. A. & Bunney, B. S. The control of firing pattern in nigral dopamine neurons: single spike firing. *J. Neurosci.* 4, 2866–76 (1984).
374. Poskanzer, K. E. & Molofsky, A. V. Dynamism of an Astrocyte In Vivo: Perspectives on Identity and Function. *Annu. Rev. Physiol* 801615, 1–16 (2018).
375. Zhou, X., Liao, W.-J., Liao, J.-M., Liao, P. & Lu, H. Ribosomal proteins: functions beyond the ribosome. *J. Mol. Cell Biol.* 7, 92–104 (2015).
376. Sung, M.-K., Reitsma, J. M., Sweredoski, M. J., Hess, S. & Deshaies, R. J. Ribosomal proteins produced in excess are degraded by the ubiquitin-proteasome system. *Mol. Biol. Cell* 27, 2642–2652 (2016).
377. Keller, H. H., Bartholini, G. & Pletscher, A. A. Spontaneous and drug-induced changes of cerebral dopamine turnober during postnatal development of rats. *Brain Res.* 64, 371–378 (1973).
378. Kang, J. & Chung, K. C. The F-box protein FBXO7 positively regulates bone morphogenetic protein-mediated signaling through Lys-63-specific ubiquitination of neurotrophin receptor-interacting MAGE (NRAGE). *Cell. Mol. Life Sci.* 72, 181–195 (2015).